THE UNIVERSITY *of* EDINBURGH

β-delayed neutron emission from r-process nuclei along the N=82 shell closure

Oscar Hall

Doctor of Philosophy
The University of Edinburgh
July 2020

Abstract

The rapid-neutron capture process (r-process) is thought to be responsible for the production of around half the elements heavier than iron. Despite first being proposed almost six decades ago, the astrophysical site of the r-process remains an open question. The multi-messenger observation of gravitational waves originating from a binary neutron star merger (GW170817) and its electromagnetic counterpart provided evidence indicating that a possible r-process had occurred, providing a possible answer to this question. The accurate modelling of the nucleosynthesis processes taking place in such mergers requires precise nuclear input data, including nuclear masses, β-decay half-lives, and β-delayed neutron emission probabilities. A challenge here is that for the exotic neutron-rich nuclei that are of importance to the r-process, relatively few values are known experimentally. There is, therefore, high demand for experimental measurements along the r-process path which can be used as inputs in r-process calculations. In addition to being used as inputs in nucleosynthesis calculations, experimentally measured values act as reference points for the development of theoretical models in regions far from stability.

This thesis presents the first measurement of the β-delayed neutron emission probabilities of 21 neutron-rich isotopes and improves upon the precision of a further four. In addition to this, measurements of the half-lives of 31 neutron-rich isotopes are presented. These neutron-rich isotopes are located along the $N = 82$ shell closure, a region that has been highlighted as being important in the production of the r-process $A = 130$ peak. These values, therefore, represent a significant contribution to the experimental data available for use in r-process calculations. The measurements were carried out at the Radioactive Ion Beam Factory in Japan, where the β-decays of neutron-rich ions were measured using the Advanced Implantation Detector Array in coincidence with their β-delayed neutrons that were measured using the BRIKEN neutron counter array.

Lay Summary

Elements are identified by the number of protons they have. Each element can have multiple configurations depending on the number of neutrons; these are known as isotopes. Isotopes can be either stable or unstable. Unstable nuclei will decay to stability by changing their configurations of protons and neutrons through different decay mechanisms. One of these decay mechanisms is β^--decay, in which isotopes change their configuration by converting a proton into a neutron and in the process release an electron and an anti-neutrino. If nuclei are very unstable, there is a chance that this decay can cause further changes to the configuration of the element, commonly in the form of the emission of either a further proton or neutron. If a neutron is emitted, the process is known as β-delayed neutron emission.

The rapid neutron capture process, or r-process, is thought to be responsible for the production of around half the elements heavier than iron. Despite being first proposed over 60 years ago, our understanding of the process is still lacking. Currently the r-process is understood to take place in explosive scenarios, with binary neutron star mergers being one of the most compelling astrophysical sites. In these explosive scenarios, highly exotic unstable nuclei are produced, which exist far from stability. Our ability to computationally model the process is limited by a lack of knowledge of the nuclear properties of these highly unstable nuclei. Of particular interest are the β-decay half-lives, β-delayed neutron emission probabilities and nuclear masses of isotopes along the r-process path.

This thesis details the measurement of β-delayed neutron emission probabilities of unstable nuclei along the r-process path. The values presented in this thesis provide crucial reference points for the development of future theoretical models in a region where the predictions of models are often not in agreement. The direct impact of these newly measured values on predicted r-process abundances is also

investigated by performing r-process calculations with and without them.

Declaration

I declare that this thesis was composed by myself, that the work contained herein is my own except where explicitly stated otherwise in the text, and that this work has not been submitted for any other degree or professional qualification except as specified.

(*Oscar Hall, July 2020*)

Acknowledgements

First and foremost, I would like to thank my supervisor, Prof. Philip Woods, for the help and guidance he has provided throughout my PhD. I would also like to thank my second supervisor, Prof. Thomas Davinson, for providing invaluable technical knowledge throughout the years, and also for his unrivalled knowledge of the best places to eat around RIKEN.

Thanks must also go to the staff and students of the University of Edinburgh Nuclear Physics Group for making the past few years with the group so enjoyable. In particular, I would like to thank the students of the PhD students office, for the friendly atmosphere they have always provided.

Thanks must go to the members of the BRIKEN collaboration for all of their contributions, both during and following the experiments. Without them this thesis would not have been possible. Special thanks must go to Alvaro Tolosa-Delgado for all of the conversations on the analysis of the data.

Thank you to Katie for your continual support and for ensuring that I still took time to make it into the mountains.

Finally thank you to my family, Carol, David and Alasdair, for always being there for me.

Contents

List of Figures

List of Tables

Chapter 1

Introduction

Other than hydrogen, helium and lithium produced during the Big Bang [2, 3], all of the elements that make up the universe were synthesised in stars and stellar environments. Within our solar system the relative abundances of the different elements form the solar abundance distribution, shown in Figure 1.1. The shape of the distribution is influenced by the nucleosynthesis processes that form the nuclides. Each process contributes different amounts to the total observed solar distribution; some processes produce characteristic features that stand out when looking at the distribution's shape. One of the most apparent features of the solar abundances is the "iron peak", spanning from $A \approx 40$ to $A \approx 60$ and peaking at ^{56}Fe [4]. The peak splits the solar abundance distribution into two regions. To the left of the peak, the production of nuclei is thought to predominantly take place in stars during their quiescent phase of stellar evolution. During this stage of a stars life-cycle successive burning stages take place, as fusion reactions produce gradually more massive elements. The most massive of stars, greater than 11 solar masses ($M_{\odot}$), are capable of producing elements up to and including the iron peak elements [4]. To the right is the region beyond the iron peak, where nucleosynthesis is no longer due to fusion reactions.

1.1 Nucleosynthesis beyond the iron peak

Much of the work done to study the nucleosynthesis of elements beyond the iron peak has been based on the ideas set out by Burbidge *et al.* [5] and Cameron

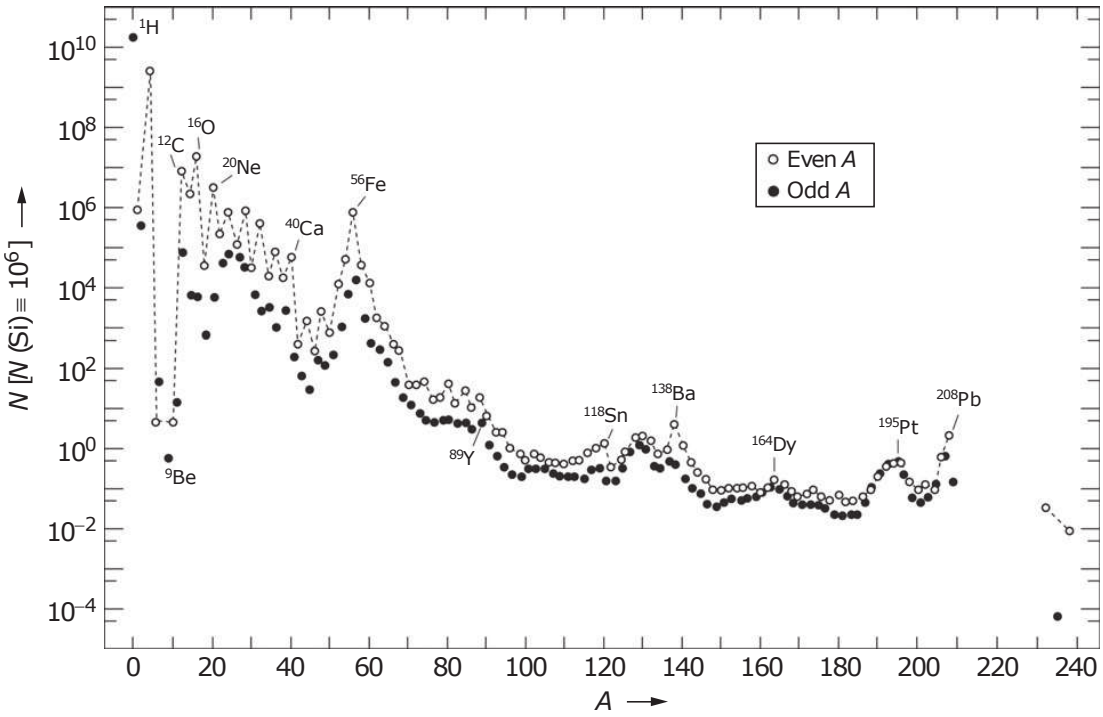

Figure 1.1 *Abundance distribution of the solar abundances N as a function of nucleon number A. Figure taken from [1].*

[6] in their 1957 papers on the nucleosynthesis of elements. One of the main conclusions of these works was that the production of the elements beyond the iron peak requires an abundance of free neutrons. The processes they proposed were informed by the shape of the abundance distribution beyond $A \sim 60$ and explained how features in the distribution were produced. The notable features they explained were a series of sharp peaks located at $A = 89$, 138 and 208 and broader peaks at $A = 80$, 130 and 194. Two processes were proposed to explain the development of these features. One of the processes proposed was the slow neutron-capture process, or s-process. The s-process was characterised by neutron-captures onto nuclei over timescales much longer than the β-decay half-lives of the majority of the unstable nuclei produced. For example, for nuclei with neutron-capture cross sections of ~ 100 mb a neutron capture time scale of a few tens of years is predicted [7]. The effect of neutron-captures followed by β-decays before further neutron-captures occur is a path that follows close to stability, with nuclei never capturing more than a couple of neutrons before decaying to stability. The second process presented was the rapid neutron-capture process, or r-process. The r-process differs from the s-process in that it is instead characterised by neutron-captures occurring over much shorter timescales than the β-decay half-lives of unstable nuclei produced. Successive neutron-captures

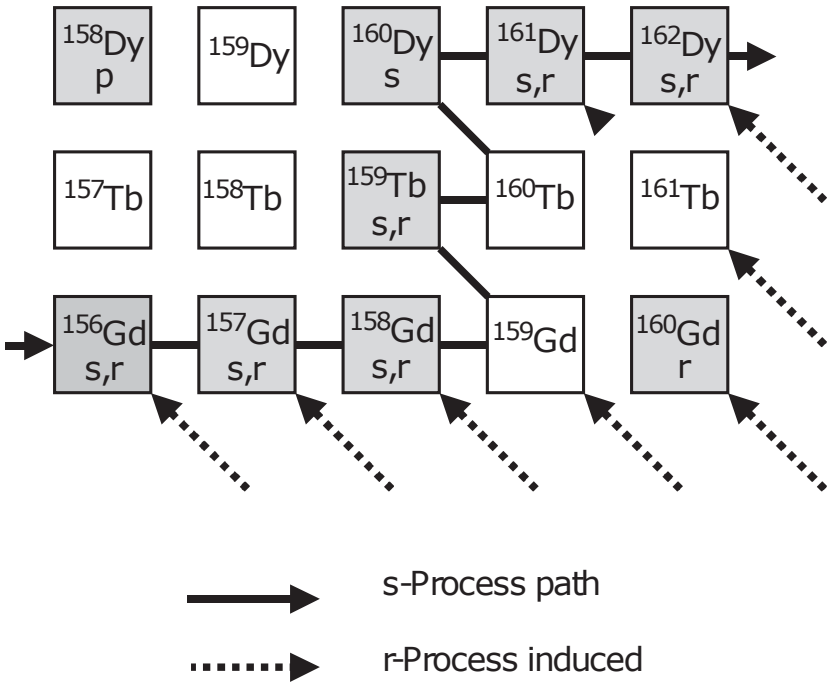

Figure 1.2 *Figure showing how s and r-process only nuclides can form. Stable nuclides are shaded in grey and labelled with either a 'p', 's', 'r' or 's,r' indicating whether they are produced by the p process, the s-process, the r-process or a combination of both the s and r processes respectively. Taken from [8].*

are able to occur before the unstable nuclei decay, leading to the production of increasingly neutron-rich isotopes. The path of the r-process, therefore, flows far from stability. Once the source of free neutrons is exhausted and neutron-captures cease, the unstable neutron-rich nuclei β-decay back to stability. More detailed discussions of the s-process and r-process can be found in sections 2.1 and 2.2 respectively.

While many of the nuclides produced by the s-process are also produced by the r-process, there exist some specific nuclides whose production can be attributed to a single process. The production of these s- and r-only nuclides is caused by stable nuclides that are separated from the s-process path by an unstable nuclide. An example of this is visible in Figure 1.2, where it can be seen that the stable nuclide ^{160}Gd is separated from the stable nuclides $^{156-158}$Gd by the unstable nuclide ^{159}Gd. Following the s-process path from ^{156}Gd, successive neutron-captures lead to the production of ^{159}Gd. If the half-life of unstable nuclei is comparable to or slower than the neutron capture time scale, branching can occur as the unstable nuclide either captures another neutron or β-decays, forming a competition between the two. In this example ^{159}Gd has a half-life of 18.479

hours [9], much shorter than the neutron capture timescale; therefore, ^{159}Gd β-decays before capturing additional neutrons. The s-process is, therefore, unable to bridge the gap to the stable nuclide ^{160}Gd and is unable to contribute to its abundance. Following the s-process path on from ^{159}Gd, its β-decay produces the nuclide ^{159}Tb, a nuclide that is produced in both the s and r-processes. The next stable nuclide encountered along the s-process path is ^{160}Dy, this nuclide is shielded from the β-decays of the r-process path by the stable, r-only nuclide ^{160}Gd. The production of ^{160}Dy can, therefore, be entirely attributed to the s-process and the production of ^{160}Gd entirely to the r-process. The presence of these s- and r-only nuclides are indicated in Figure 1.2 by the presence of "s" or "r" under the nuclide.

In Figure 1.2 we also see the isolated stable nuclide ^{158}Dy that does not lie on the s-process path and is also shielded from the influence of the r-process. The production of the nuclide ^{158}Dy and other isolated stable nuclides on the neutron-deficient side of stability cannot be attributed to neutron capture processes. A third process, the p-process, describes their production. The p-process occurs in the supernova of stars [10], where in these explosive events peak temperatures are reached in the range of 2.0 to 3.0 GK [10]. Under these conditions, the p-only nuclides, such as ^{158}Dy, can be produced by photo-disintegration reactions. In the hot conditions present in supernovae, highly energetic photons are able to remove nucleons from a nucleus through (γ,p), (γ,n) and (γ,α) photo-disintegration reactions. Photo-disintegration reactions acting on neutron-capture nuclei along the s-process path, present in a star prior to the supernova, can lead to the production of the isolated, neutron-deficient nuclides. For example, it can be seen in Figure 1.2 that successive (γ,n) reactions on Dy nuclides could produce the p-only nuclide of ^{158}Dy.

When comparing the distribution in abundances for isotopes of a specific element, it is found that p-only isotopes contribute little to the total abundances of an element and that no element has the majority of its abundance in a p-only isotope [11, 12]. Almost all of the abundances of elements heavier than iron is attributed to the s and r-processes. For nuclides that have contributions from both s- and r-processes, separating the contributions of each process poses a challenge. Separating the contributions from each process to the solar abundances requires that the contributions of one of the processes be accurately known. As the s-process follows a path close to stability, the nuclear properties and neutron-capture cross sections of nuclides along its path are accurately known.

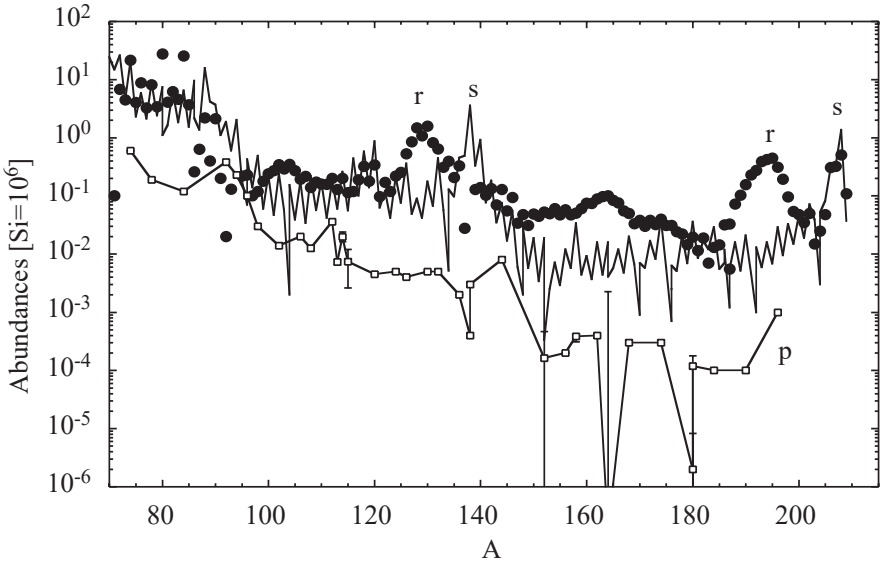

Figure 1.3 *Individual contributions to the solar abundances from the s-process (solid line), r-process (circles) and p-process contributions (squares). The contributions are taken from [13] and the figure is adapted from [14].*

Phenomenological models, described in more detail in Section 2.1, can then be used to calculate the s-process contributions to the solar abundances. The solar r-process abundances ($r_\odot$) are then found by subtracting the solar s-process abundances ($s_\odot$) from the total observed solar abundances ($Y_\odot$), such that:

$$r_\odot = Y_\odot - s_\odot. \tag{1.1}$$

The separated solar abundances from each of the three processes are shown in Figure 1.3, where it is seen that the p-process accounts for only a small percentage of the nuclei heavier than iron. The majority of the abundances are, as previously stated, a result of the s- and r-processes. From Figure 1.3 it can be seen that the s- and r-processes are each responsible for the production of just under half of the nuclei heavier than iron in the solar system.

1.2 r-process elements in old, metal-poor stars

Identification of large neutron-capture element abundances relative to iron in comparison with the Sun, in old, metal-poor stars began with the observation of an overabundance of neutron-capture elements in HD 115444 by Griffin *et al.* in 1982 [15]. In this star an enhancement in abundance of Eu was observed,

an element whose production is attributed primarily to the r-process[†]. Stars of extreme low metallicity ([Fe/H] < -2.5), like HD115444, are presumed to have been formed during the very earliest times of the galaxy, at a time and place where the environment had not been significantly enriched by the products of nuclear burning [15, 16]. This is backed up by estimates of the age of HD115444, which have been given at 15.6 ± 4 Gyr [17]. The composition of HD115444 and other metal-poor stars like it can, therefore, offer an insight into the composition of the very early galaxy.

When trying to measure the abundance distributions of stars, it is essential to measure as many elements as possible across the entire range of elements [16]. This is typically done by measuring absorption lines in stellar spectra that are caused as photons passing through the stellar-material are absorbed. Photons are absorbed as they interact with atoms in the stellar material, exciting the atoms present [18]. Each element has a selection of characteristic wavelengths that it is excited by, allowing the wavelengths absorbed to act as an identifier for the elements present. By fitting models to the intensity of the lines, the lines' wavelengths and the illuminating spectra, individual elements and their respective abundances can be determined. Low metallicity stars provide an excellent opportunity to measure the abundances of neutron-capture elements as there is little blending in the lines from lighter elements commonly present in higher metallicity stars [16].

Since the first observation by Griffin *et al.*, there has been a growing number of metal-poor stars exhibiting an overabundance of r-process elements discovered. The newly identified stars are given classification of either r-I or r-II, dependent on their [Eu/Fe] and [Ba/Eu] ratios [20]. Comprehensive studies of these stars have shown similarities between the relative abundances of neutron-capture elements in the stars and in the solar r-process abundances. The measured abundances of the observed neutron-capture elements in some of these metal-poor stars are plotted over the solar r-process abundances in Figure 1.4. For elements $Z > 56$, excellent agreement is seen between the stellar abundances and solar r-process abundances for all of the stars [21]. The lower panel of the figure highlights this agreement, showing the averaged residual between the stellar and solar abundances. For atomic numbers greater than 56, almost all of the values show agreement within uncertainties.

[†]While Eu is produced via both the s and r-processes, Figure 1.3 indicates the r-process is responsible for almost an order of magnitude more abundance in the $A = 160$ region where Eu is found.

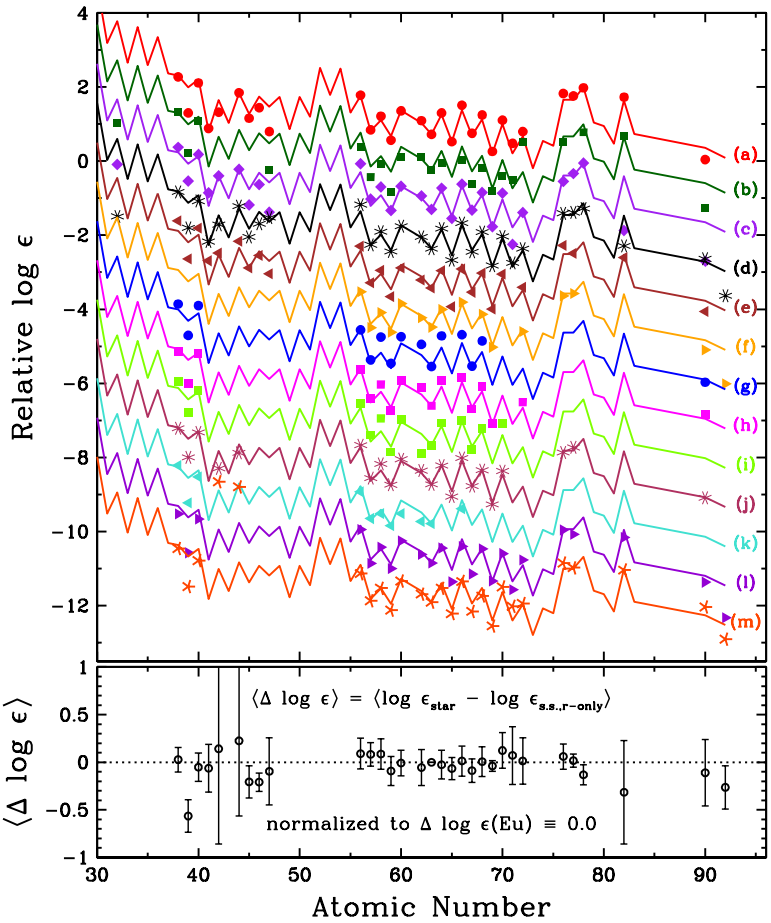

Figure 1.4 *The top panel shown neutron-capture abundances for 12 r-II stars (points) and then the scaled solar system r-process abundances (lines). Solar abundances were scaled to match at Eu ($Z = 63$) with a vertical offset applied for ease of visualising the data. The bottom panel shows the difference between the mean abundances of the 12 r-II stars and the solar system abundance. Adapted from [19] and references therein.*

While good agreements are seen between the stellar and solar abundances above $Z = 56$, the abundances of the lighter elements do not show the same excellent agreement. Instead, a greater spread in abundances is seen, with many of the residuals not agreeing with the solar r-process abundances. The fact that these old, metal-poor stars seem to match solar r-process abundances in one mass region but not another has been long used as evidence for the need for at least two different r-process sites [22–24]. One site would primarily be responsible for the production of the heavier r-process elements [16] and the second responsible for the lighter elements, with several theories attempting to explain this [22, 25].

1.3 *r*-process nucleosynthesis in core-collapse supernovae

The early works of Burbidge *et al.* [5] and Cameron [6] sought to associate the r-process with neutron-rich material in an exploding supernova. In particular, core-collapse supernovae were highlighted as a possible site of the r-process. First attempts at explaining the possibly occurring r-process nucleosynthesis were localised to the He burning layers surrounding the core of these massive stars following the supernova. The starting point of these explosive events is a massive star, about eight times more massive than the Sun, that has passed through successive burning stages at its core. By the time burning at the core ends, the core is predominantly comprised of iron, and fusion reactions no longer take place [26]. Lacking the outward pressure that was previously provided by the fusion reactions, the core begins to contract, undergoing rapid free-fall. The core falls at a speed of nearly a quarter of the speed of light, collapsing from about the size of the Earth to a hot, dense, neutron-rich proto-neutron star about 30 km in radius [26]. The core's collapse is eventually halted by the repulsion of the strong nuclear force, causing the inner core to rebound, sending a shockwave out through the star [27]. Early calculations of nucleosynthesis in the shock-heated layers surrounding the core showed promise in reproducing the abundance distribution of the r-process elements [28]. However, it is now known that the shockwave does not propagate through the whole star and, instead, the shockwave stalls due to photo-disintegration and neutrino losses dissipating the energy [26]. The rebounding shockwave then lacks the required energy to eject any matter from the inner layers of the star, where the conditions for a r-process are met [27]. The inner layers of core-collapse supernova can, therefore, be ruled out as a location for the r-process.

Another possible site that still involves core-collapse supernovae is in the neutrino-driven ejecta that follows the shockwave [29]. Following the shockwave the newly formed proto-neutron star releases a large flux of neutrinos over a few seconds, radiating around 10% of the proto-neutron stars rest mass (about 3×10^{53} erg) [26, 30]. The emitted neutrinos drive the ejection of matter, forming what is known as a neutrino-driven wind [31]. When modelling the possible nucleosynthesis that can occur in this environment, modellers find that the entropy of the expanding matter (S) and the electron fraction of the matter (Y_{e}) to be useful parameters [30, 32]. Under these conditions, the entropy of the environment represents the

number of macroscopic and microscopic states in the system. It is a function of the energy, volume and the number of particles of each species present [33]. As the entropy scales with the size of the system, it is commonly given in terms of per baryon and is denoted as s with units of k_{B} baryon^{-1}. By placing the entropy in units of per baryon comparisons can be made between systems containing different numbers of baryons, helpful for simulations involving different amounts of ejecta. The electron fraction of matter gives the number of electrons per baryon. For neutrally charged matter the electron fraction is equivalent to the proton fraction of the matter as the number of electrons equals the number of protons, allowing the ratio of protons to neutrons to be calculated. For example neutron-rich matter is defined as having $Y_{\mathrm{e}} < 0.5$. This is an important quantity as the r-process requires an abundance of neutrons. For more information on how these parameters are used in nucleosynthesis models, refer to section 2.2.2. Early calculations of nucleosynthesis in the conditions provided by a neutrino-driven wind showed promising results, reproducing the solar r-process abundances [34, 35].

While initial calculations of nucleosynthesis in the environment have been promising, they have not been without challenges. Hydrodynamical models of the neutrino-driven wind have shown that the ejecta are likely only moderately neutron-rich, with electron fractions of $Y_{\mathrm{e}} \sim 0.45$ [36]. In order for a robust r-process, where a robust r-process is described as an event capable of producing the solar r-process abundances, occurring under these conditions, entropies well in excess of those provided by the hydrodynamical models are required [37]. The low entropy conditions presented lead to a neutron to seed ratio that is not sufficient to support a robust r-process capable of producing the heaviest elements. Other calculations that have been able to produce heavy r-process elements have only been able to do so by artificially increasing the entropy of the wind [38]. Nucleosynthesis calculations, however, do point to the neutrino-driven winds as a likely site for the production of lighter r-process elements, such as Sr, Y and Zr [39, 40]. These are elements for which disagreements in abundance were seen between old, metal-poor stars and the solar r-process abundances, supporting claims of the possible existence of more than one r-process site.

1.4 r-process nucleosynthesis in binary neutron star mergers

The merger of two neutron stars has long been held as another possible site of the r-process. The idea was first proposed in 1974 by Lattimer and Schramm, who calculated that the mass of ejecta expected to be released in neutron-star black-hole mergers could account for the mass of r-process material in the galaxy [41]. The idea was later expanded to binary neutron-star mergers by Symbalisty and Schramm in 1982 [42]. In addition to the ejection of neutron-rich matter, a binary neutron star merger was theorised to release two forms of radiation that would be detectable on Earth. The first being gravitational waves [43]; predicted by general relativity to be released by the inspiral and coalescence of two compact objects [44]. Gravitational waves are detectable on Earth at facilities such as LIGO [45] and VIRGO [46]. The second source of radiation are bright gamma-ray bursts, which originate as matter from the stars is ejected at sub- and mildly relativistic speeds with prompt radio flares being detectable on Earth following the merger [47, 48].

General-relativistic simulations of mergers have identified two main mechanisms in which matter is ejected. First, an amount of matter can be ejected during the neutron-star merger. As the stars' surfaces approach one another, tidal forces peel away matter, ejecting it from the system [49]. Following this, as the surfaces come into contact, shock heating can lead to the further ejection of matter from the system [50]. The second mechanism for the ejection of matter occurs roughly a second following the merger, as a neutrino-driven wind forms. The wind forms as neutrinos, released during the merger, blow through an accretion disk that forms surrounding the merger remnant [51]. Depending on the masses of the two neutron stars and the properties of their orbit as they coalesce, the merger remnant can take on two forms. The merger remnant either collapses into a black hole if the masses of the neutron-stars is suitably large; or forms a metastable hypermassive neutron-star, supported by differential rotation and thermal pressure [52]. It should be noted that as the hypermassive neutron-star is only metastable, it will most likely eventually collapse, forming a black hole [53].

In the ejecta r-process nucleosynthesis is believed to occur as the ejected matter, no longer constrained by the gravitational force of the neutron stars, rapidly

expands and decompresses. The composition of the dynamically ejected matter is highly neutron-rich, with neutrons making up around $\sim 70\%$ of the baryons in the matter [52]. As the density decreases, unstable nuclei in the matter will undergo rapid β-decays, quickly heating the matter up to temperatures in excess of 10^9 K [54]. Initially, the ejecta will be optically opaque to the thermal radiation, and no radiation will be emitted. However, as the ejecta expands and the density decreases, the ejecta become optically transparent, allowing radiation to escape [53]. The ejecta continues to emit thermal radiation over a period of weeks, as continual heating is provided by the β-decays of the r-process nuclei [53]. The intensity and energy of the emitted radiation will change as the ejecta develops, producing a characteristic lightcurve that is dependent on the composition and density of the environment. Simulations of the lightcurves produced in the environment are around 1000 times brighter than novae events, giving them the term kilonovae [55]. These radioactively powered transient events are visible from Earth [56] and will continue to be visible over the days and weeks following the merger as the ejecta cool.

In August 2017 the LIGO and VIRGO detectors observed for the first time the gravitational wave signals of a binary neutron-star system inspiral, GW170817. Accompanying the observation of the gravitational waves was the independent detection of a gamma ray burst by the FermiGBM. Rapid sky localisation was carried out through analysis of the signals measured at each location, narrowing the signals' origin to a region of sky 31 deg^2 in area. The reduced search area, in turn, led to the discovery of SSS17a, an electromagnetic source not present in previous sky surveys. SSS17a was later confirmed to be the electromagnetic counterpart of the merger. The first detection of SSS17a occurred within 11 hours of the initial gravitational-wave measurement [44, 57]. Early identification of the kilonova allowed subsequent observations to be carried out over the following days. In doing this, the development of the spectra was measured as a function of time, allowing comparisons of the measured light curve to be made against various models [58–61]. The models compared calculated light curves, based on the estimated mass of the ejecta from the neutron-star merger and its opacity to determine the ejecta's composition.

The results of these models indicated the production of two groups of r-process nuclei, one lighter group of predominantly mass number $A \leq 130$ and one more massive group of $A \geq 130$ [62], or as some groups refer to it "lanthanide poor" and "lanthanide rich" [63–65]. Most recently groups have published results reporting

the identification of the neutron-capture element strontium in the ejecta [66]. The identification comes from the observation of absorption lines, present in the observed light curve, consistent with the presence of strontium in the matter. From these observations, the authors make the case that this establishes the origin of the r-process in the merger of two neutron stars. With the wealth of data provided by GW170817, a compelling case is made for some form of r-process to be taking place in neutron-star mergers. The amount of data available is expected to grow as further mergers are identified by LIGO and VIRGO, such as the event GW190425 which, although not accompanied by an electromagnetic counterpart, shows we can expect to observe more of these events [67]. Despite the growing wealth of data, questions still remain about the ability of neutron-star mergers to account for all of the r-process elements we observe. In our current understanding of neutron stars, they are one of the possible end products of core-collapse supernovae. The production of neutron stars and binary neutron-star mergers, therefore, requires supernovae to have previously taken place, which would enrich the surrounding environment with the products of stellar burning. This poses a problem for neutron stars being the dominant source of r-process nuclei, as it does not agree with the observed enrichment of r-process elements in old, metal-poor stars. If the r-process enrichment of these stars was the result of neutron-star mergers, an enrichment of iron elements released by the preceding supernovae would also be expected [68–70]. However, the metallicity of these stars points to their origin being at a time prior to any significant iron enrichment taking place. The origin of the r-process elements in these old metal-poor stars remains little understood. It can be seen then while significant progress has been made in narrowing down the site of the r-process, the exact process(es) that produced the solar r-process abundances remain an open question. Answering this question will require experimentalists, modellers and astronomers to work together to produce a detailed picture of how and where the r-process occurs.

Chapter 2

Theory

2.1 The *s*-process

For the obtained solar *r*-process abundances to be accurate, the solar *s*-process abundances must be accurate, and the mechanisms behind them well understood. This section focuses on the *s*-process and how our understanding of the process is used to obtain the solar *s*-process abundances.

In the works of Burbidge of *et al.* [5] and Cameron [6] the slow neutron-capture process (*s*-process) was proposed as a process capable of producing features evident in the solar system abundance distribution beyond the iron peak. Direct observational evidence for ongoing *s*-process nucleosynthesis in the galaxy has existed since 1952, with the detection of the radioactive element Tc in the spectrum of an Asymptotic Giant Branch (AGB) star of spectral type S by Merrill [71]. The half-life of ^{99}Tc is 2×10^5 yr [72], much less than the age of the star. The observation of this element is proof of ongoing nucleosynthesis, as for it to still exist in the stellar spectra it must have been produced since the star's formation. Identification of Tc in stellar spectra allowed the astrophysical site of the *s*-process to be identified, attributing it to the He burning layers of low mass AGB stars [4, 73, 74], stars that are at late stages in their evolutionary life-cycle. In these stars the conditions for the *s*-process to take place are reached, with neutron densities, n_{n}, of around 10^8 cm^{-3} and temperatures of 0.1 - 0.2 GK persisting for $\sim 10^4$ years [75]. Neutrons are provided in AGB stars via carbon burning [76] in

the reaction of:

$$^{13}\mathrm{C} + \alpha \rightarrow {}^{16}\mathrm{O} + \mathrm{n}. \tag{2.1}$$

When originally discussing the solar *s*-process abundance characteristics, Burbidge *et al.* noted that their ability to draw detailed conclusions was limited by the lack of reliable neutron-capture cross section information. Since then the number of experimentally measured neutron-capture cross sections has increased massively, with comprehensive evaluations of the known cross sections available [77]. The number of and precision to which neutron-capture cross sections are known also continues to improve, with collaborations such as n_TOF at CERN [78] continuing to measure these properties. Using these properties the classical approach to modelling the *s*-process abundances was to assume that a fraction G of the solar ^{56}Fe was irradiated by an exponential distribution of neutron exposures, τ_0 [79]. In these calculations, it is assumed that both the temperature and neutron density, n_n, are maintained at constant values. Under these conditions, the product of the neutron-capture cross section, the relative probability of a neutron incident on a nucleus being captured averaged over the energies present $\langle\sigma\rangle$, and the *s*-process abundance of a nuclide, N_s is given by [80]

$$\langle\sigma\rangle(A)N_s(A) = \frac{G \times N_\odot(^{56}\mathrm{Fe})}{\tau_0} \prod_{i=56}^{A} \left(1 + \frac{1}{\tau_0\langle\sigma\rangle_i}\right)^{-1} \tag{2.2}$$

where the two parameters G and τ_0 are found by fitting the abundances of the solar *s*-only nuclei. This just leaves the neutron-capture cross sections of the nuclides along the *s*-process path as the required inputs [81]. This classical approach gives a surprisingly good description of the *s*-process in the solar system. From it, one finds that equilibrium exists between neighbouring isotopes, such that

$$\sigma_{A-1}N_{A-1} = \sigma_A N_A, \tag{2.3}$$

with the product of cross sections and abundances remaining almost constant. It is also possible to explain the features observed in the abundance distribution such as the peaks at $A = 89$, 138 and 209, relating them to the closed neutron shells. Nuclides located at the closed neutron shells, at $N = 50$, 82 and 126, have reduced neutron capture cross sections. These small cross sections act as bottlenecks causing a build-up in abundances, generating the peaks of the abundance distribution [74].

Since the first classical calculations were performed, the availability of accurate

neutron-capture cross sections has shown inconsistencies with the classical model. These inconsistencies appear most clearly in the classical model's inability to account for s-process branching. These branchings occur when the half-life of nuclei becomes comparable to the neutron-capture cross section and competition forms between neutron captures and β-decays. The replacement of the classical model with the first generation of stellar models meant that these problems could be avoided [73]. These stellar models give a more accurate picture of the neutron exposures within the star and allow for the competition of neutron captures and β-decays. These stellar models also highlighted a region in which AGB stars could not account for all of the s-process abundances, a small region of nuclei with $A < 90$. A second weak s-process, complementary to the main s-process occurring in AGB stars, was found to occur in massive stars ($M > 8M_{\odot}$), which distribute the s-process material as they explode as supernovae [74]. In these massive stars, slow neutron captures are driven by the alpha capture of ^{22}Ne [82] in the reaction:

$$^{22}\mathrm{Ne} + \alpha \rightarrow {}^{25}\mathrm{Mg} + \mathrm{n}. \tag{2.4}$$

In contrast to the main s-process, the neutron flux is too low for reaction flow equilibrium to be achieved [83]. When this is combined with the very low neutron-capture cross sections of the elements of Fe to Sr, these elements act as bottlenecks to the flow of the weak s-process. The abundance of a nuclide, therefore, depends on how long the process spends at each bottleneck before it [84]. The abundances of the weak s-process, therefore, show great sensitivity to the neutron-capture cross sections of nuclei $A < 90$.

When calculating the solar r-process abundances, the main s-process plays the most significant role in determining the s-process abundances. The main s-process stretches from $A = 90$ up to $A = 209$ where $^{209}_{83}$Bi is reached. At this point, the s-process is no longer capable of producing more massive nuclei as nuclei produced by neutron-capture decay via alpha-particle emission, decreasing in mass number. The s-process is then not able to accrue nucleons and bridge the gap to the next stable element $^{232}_{90}$Th†, marking $^{209}_{83}$Bi as the upper limit of the s-process path. The abundances of the s-process nuclei can be calculated through either stellar nucleosynthesis models or the classical approach and subtracted from the total solar abundances to obtain the solar r-process abundances. Despite neglecting the contributions of the weak s-process, figure 2.1 shows

† $^{232}_{90}$Th is not truly stable, but its half-life is multiple times the age of the Earth so is often treated as if it was.

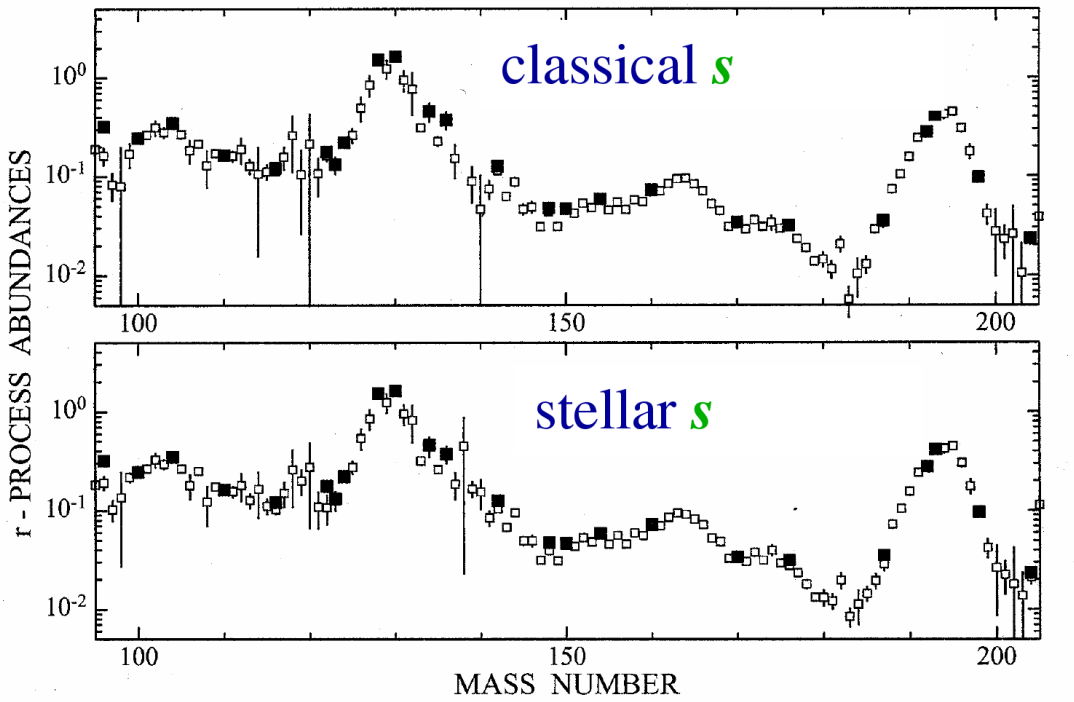

Figure 2.1 *Solar r-process abundances obtained via the residual method, $r_\odot = Y_\odot - s_\odot$, from classical s-process calculations and stellar s-process models [73]. Open squares are nuclei that are produced by both s and r-processes and closed squares indicate r-only nuclei. Figure taken from [74].*

that remarkable agreement in the solar r-process abundances obtained is found between the two methods.

2.2 The r-process

The rapid neutron-capture process, or r-process, was introduced in the previous chapter, where it was characterised by neutron-captures occurring at a much faster rate than the β-decays of unstable nuclei along its path. Successive neutron-captures are then able to occur before the unstable nuclei can β-decay, taking the path of the r-process through exotic, neutron-rich nuclei. The conditions required to support the high capture rates involve neutron densities of $n_\mathrm{n} > 10^{20}$ cm^{-3} and temperatures greater than 1 GK [85]. While the neutron-flux that facilitates the s-process lasts for tens of thousands of years, the neutron-flux for the r-process is believed to be present on the scale of a few seconds [86]. During this time unstable neutron-rich nuclei are produced through successive neutron-captures on seed nuclei, forming nuclei with progressively larger nucleon numbers.

Burbidge *et al.* proposed the r-process as the process that produces the broad peaks at $N = 80$, 130 and 194 [5]. The formation of the peaks was explained as an effect caused as the r-process path meets the closed neutron shells at $N = 50$, 82 and 126. For nuclides at the closed shells, a decrease in neutron-capture cross section is expected, this can cause a build-up in abundance as nuclei are unable to accrue more neutrons and must wait to β-decay before continuing the r-process path. The difference in location for the s- and r-process peaks can be explained by the different regions in which their paths meet the closed shells. While the s-process path meets the closed shells near stability, the r-process path meets these closed shells further from stability, where the proton to neutron ratio is small. As the proton to neutron ratio far from stability is lower than at stability, the nucleon number of the nuclei where the r-process meets the closed shells at $N = 82$ is lower than for the s-process.

Once the neutron-flux driving the captures ceases, a "freeze-out" occurs and the neutron-rich nuclei produced β-decay back towards stability. The abundance distribution of the r-process at freeze-out is then further modified by the occurrence of β-delayed neutron emission, which is when the β-decay of an nuclide also results in the prompt emission of one or more neutrons from the daughter nuclide. The conditions required to support such a high rate of neutron-captures are not found during a stars' quiescent lifetime, limiting the r-process to explosive, high-energy environments.

2.2.1 The canonical r-process approximation

Early methods of modelling the nucleosynthesis made use of what is now referred to as the canonical r-process approximation, first introduced by Seeger *et al.* in 1965 [79]. For the approximation, it is assumed that ^{56}Fe seed nuclei are subjected to neutron densities and temperatures that remain constant over the neutron irradiation time [87–89]. The temperatures and neutron densities are large enough such that neutron-captures and electromagnetic reactions occur at much greater rates than the β-decays. Under these conditions, a set of approximations can be used to obtain the r-process path and the relative abundances of the r-process elements along the path. Before these approximations are discussed, it is worth describing the properties used in these approximations. One of the key properties made use of in the approximations is the neutron separation energy of a nuclide, S_{n}. The neutron separation is the minimum energy required to remove a neutron

from the nucleus of a atom and is calculated as:

$$S_{\mathrm{n}}\left({}^{A}_{Z}X\right) = \left[m\left({}^{A-1}_{Z}X\right) + m_{\mathrm{n}} - m\left({}^{A}_{Z}X\right)\right]c^2 = B\left({}^{A}_{Z}X\right) - B\left({}^{A-1}_{Z}X\right), \tag{2.5}$$

where $m\left({}^{A}_{Z}X\right)$ is the neutral atomic mass of nuclide ${}^{A}_{Z}X$ and $B\left({}^{A}_{Z}X\right)$ is the binding energy of nuclide ${}^{A}_{Z}X$. Another property that is used is the electron fraction of the matter (Y_{e}). This property was introduced in chapter one as the number of electrons per baryon. It was also stated that for neutrally charged matter, the electron fraction is equal to the proton fraction and can be used to calculate the neutron fraction by:

$$Y_{\mathrm{p}} = Y_{\mathrm{e}} \tag{2.6}$$

$$Y_{\mathrm{n}} = 1 - Y_{\mathrm{p}} = 1 - Y_{\mathrm{e}}. \tag{2.7}$$

A final important property is the β-decay rate of a nuclide, it is most commonly used in the form of the decay constant (λ), where λ represents the probability of a single nucleus β-decaying in a unit of time. It is related to the half-life of an element ($t_{1/2}$), the amount of time taken for half of the nuclei present in a sample of a single nuclide to decay, by:

$$\lambda = \frac{\ln 2}{t_{1/2}}. \tag{2.8}$$

The total rate of decay, or activity A, of a sample is then given by $\lambda_i Y_i$, where Y_i is the number of nuclei of nuclide i present.

As stated previously, models of the canonical r-process begin with a seed nucleus of ^{56}Fe and a rate of neutron-captures much greater than the β-decay rate. The conditions required to necessitate this are high temperatures, $T \geq 2$ GK, and large neutron densities, $n_{\mathrm{n}} \geq 10^{20}$ cm^{-3}, [90] which are kept constant through the calculation. Neutron-capture reactions act to increase the mass number of nuclei by one; these are directly opposed by photo-disintegration reactions which remove a neutron from a nucleus. Photo-disintegration can occur when a photon interacts with a nucleus exciting it to a state above its neutron separation energy, S_{n}. The nucleus can then de-excite through the emission of one or more γ-rays or a neutron, reducing its nucleon number by one. The rate at which photo-disintegration reactions occur depends strongly on the temperature of the environment. To excite a nucleus to a state above its neutron separation energy requires a photon of energy greater than S_{n}. For photons originating from black

body radiation, a higher temperature environment will produce higher energy photons. A higher temperature environment or a lower S_{n} will, therefore, lead to an increased photo-disintegration rate.

When both neutron-captures and photo-disintegrations occur at a much faster rate than β-decays, a statistical equilibrium can be achieved between the (n,γ) and (γ,n) reactions of two neighbouring isotopes. When this occurs, a state of quasi-equilibrium known as (n,γ) $\rightleftharpoons$ (γ,n) equilibrium occurs along each of the isotopic chains where the abundance distribution for neighbouring isotopes is given by a Saha equation:

$$\begin{aligned}\frac{Y\left({}^{A+1}_{Z}X\right)}{Y\left({}^{A}_{Z}X\right)} &= \frac{n_{\mathrm{n}}\langle v\sigma_{\mathrm{n},\gamma}\left({}^{A}_{Z}X\right)\rangle}{\lambda_{\gamma,\mathrm{n}}\left({}^{A+1}_{Z}X\right)} \\ &= n_{\mathrm{n}}\left(\frac{2\pi\hbar^2}{m_{\mathrm{u}}k_{\mathrm{B}}T}\right)\left(\frac{A+1}{A}\right)^{3/2}\frac{G\left({}^{A+1}_{Z}X\right)}{2G\left({}^{A}_{Z}X\right)}\exp\left[\frac{S_{\mathrm{n}}\left({}^{A+1}_{Z}X\right)}{k_{\mathrm{B}}T}\right].\end{aligned} \tag{2.9}$$

Here $\langle v\sigma_{\mathrm{n},\gamma}\left({}^{A}_{Z}X\right)\rangle$ is the velocity averaged neutron-capture cross section, $\lambda_{\gamma,\mathrm{n}}$ is the photo-disintegration rate, T is temperature, $\hbar$ is the Planck constant, k_{B} is the Boltzmann constant and $G(Z,A)$ is the nuclear partition function [91]. When the small differences in partition functions between neighbouring isotopes are neglected, and taking into account that at high nucleon numbers $[(A+1)/\mathrm{A}]^{3/2}$ tends to 1, it is seen that Eq. 2.9 only depends on the neutron density, temperature and neutron separation energy. For a given neutron density and temperature, it can be seen that the isotope of maximum abundance along each isotopic chain will depend only on the neutron separation energy. This value will be the same for all isotopic chains, during the r-process this typically occurs at around 2 MeV [92]. The isotopes of maximum abundance along each isotopic chain are known as waiting point isotopes where the r-process must "wait" for a β-decay to progress to higher atomic numbers and link up to form the approximated path of the canonical r-process.

In order for matter in the r-process to reach larger atomic numbers it must β^--decay, changing a neutron to a proton, such that $(Z,A) \rightarrow (Z+1,A) + \mathrm{e} + \bar{\nu}_{\mathrm{e}}$. When (n,$\gamma$) $\rightleftharpoons$ (γ,n) has been established, the majority of an element's abundance is held in a single "waiting-point" isotope. The flow of nuclei out of the isotopic chain is dependent on the β-decay rate of the "waiting-point" isotope. Likewise, the flow of matter into an isotopic chain will be established by the waiting-point isotope of the previous element's isotopic chain. Given enough time a steady flow

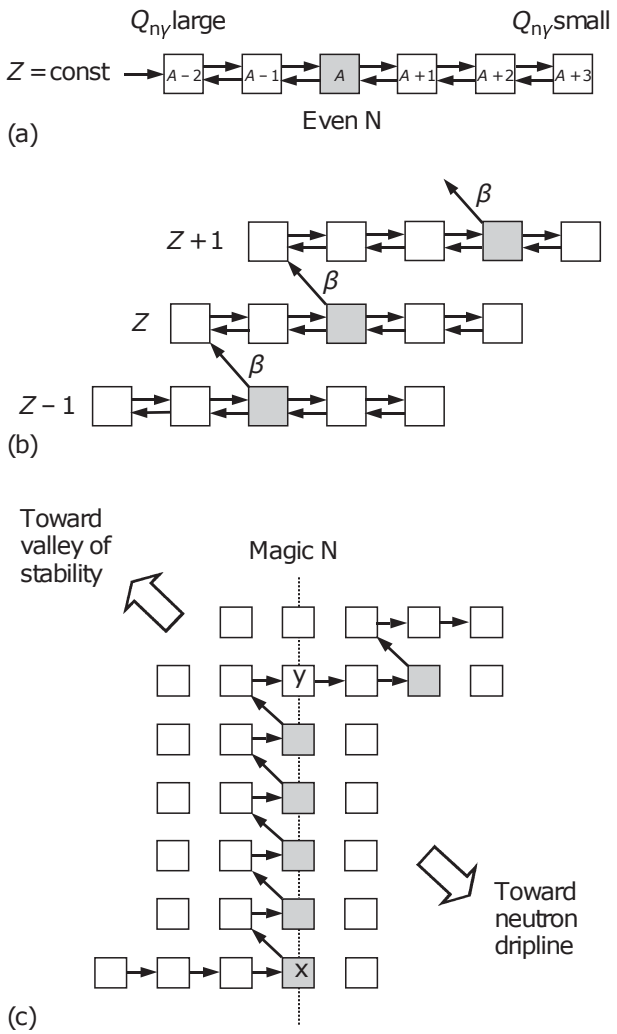

Figure 2.2 *Frame a) shows the balance between (n,γ) and (γ,n) along an isotopic chain. Frame b) shows that an increase in Z occurs from the β-decay of waiting point nuclei. Frame c) shows that when the r-process path reaches a closed neutron shell it ascends it like a ladder. Figure from [8]*

will form where the flow of matter into an isotopic chain will equal the flow out of it, such that

$$\frac{\mathrm{d}Y(Z,A)}{\mathrm{d}t} = 0 = \lambda(Z-1)Y(Z-1) - \lambda(Z)Y(Z). \tag{2.10}$$

By rearranging Eq. 2.10 to be of the form:

$$Y(Z) = \frac{\lambda(Z-1)Y(Z-1)}{\lambda(Z)}, \tag{2.11}$$

it can be seen that the abundance of a nuclide is inversely proportional to its decay constant λ. This equation can be solved for all of the waiting-point nuclides

along the r-process path, allowing their relative abundances to be calculated. The waiting point approximation holds best when the β-decay rates of isotopes are low in comparison to their neutron capture and photo-disintegration rates [90]. Therefore, the waiting point approximation is best achieved for high temperatures where the photo-disintegration rate pushes the waiting point to stability [90], where the half-lives of isotopes are longest. The benefit of this approximation is that the r-process abundances can be calculated using only the β-decay half-lives of the waiting point nuclides, limiting the amount of nuclear data required to perform calculations.

While the canonical r-process models make use of approximations, it is able to reproduce the features of the r-process abundances that we observe. The characteristic r-process peaks at $A \sim 130$ and $A \sim 195$ can be explained by the properties of nuclei with magic numbers of $N = 82$ and $N = 126$. A build-up of nuclei in these regions can be attributed to the rapid drop off in S_{n} beyond the magic numbers and the small β-decay rates of the nuclei with closed neutron shells causing a build-up in the abundance of nuclei.

2.2.2 Dynamic calculations of the r-process

While the canonical r-process has been used to model the nucleosynthesis of the r-process previously, it is limited in its application. The assumptions made to simplify the calculations and reduce the number of nuclear properties needed mean there is no flexibility in the model to account for changes in the environment's conditions. The requirement for neutron-captures to occur at a much greater rate than β-decays also places limitations on the scenarios in which it can be used. When performing calculations where the required conditions are not met the approximations begin to break down as competition forms between neutron-captures and β-decays, causing a "leakage" of matter from an isotopic chain through β-decays not at the waiting point [90]. As computational power has increased, and a more extensive range of nuclear properties have become available, more complex models of r-process nucleosynthesis have been made possible. These models are able to calculate the path of the r-process dynamically and do not require assumptions to be made about the path taken. The probabilities of reactions occurring are calculated as functions of nuclides' abundances, the temperature of the environment, and the free neutron density of the matter [93]. By calculating the probabilities of the reactions occurring over time, the

change in abundance of a nuclide can be propagated through the model. For r-process reactions networks, the abundance of a nuclide will be most heavily impacted by neutron-capture reactions, photo-disintegrations and β-decays, with the possibility of fission occurring at higher proton numbers. Each of these processes can either add to or subtract from the abundance of a nuclide. The rate of change in an nuclide's abundance is then given as the summation of all of these processes which can be written as [91]:

$$\begin{aligned}\frac{\mathrm{d}N\left({}^{A}_{Z}X\right)}{\mathrm{d}t} = {} & n_{\mathrm{n}}\langle v\sigma_{\mathrm{n},\gamma}\left({}^{A-1}_{Z}X\right)\rangle Y\left({}^{A-1}_{Z}X\right) + \lambda_{\gamma,\mathrm{n}}\left({}^{A+1}_{Z}X\right) N\left({}^{A+1}_{Z}X\right) \\ & + \sum_{i=0} \lambda_{\beta i}\left({}^{A+i}_{Z-1}X\right) N\left({}^{A+i}_{Z-1}X\right) - n_{\mathrm{n}}\langle v\sigma_{\mathrm{n},\gamma}\left({}^{A}_{Z}X\right)\rangle Y\left({}^{A}_{Z}X\right) \\ & - \lambda_{\gamma,\mathrm{n}}\left({}^{A}_{Z}X\right) N\left({}^{A}_{Z}X\right) - \sum_{i=0} \lambda_{\beta i}\left({}^{A}_{Z}X\right) N\left({}^{A}_{Z}X\right)\end{aligned} \tag{2.12}$$

where $N\left({}^{A}_{Z}X\right)$ is the number of nuclide ${}^{A}_{Z}X$ present, n_{n} is the neutron number density, $\langle\sigma_{\mathrm{n},\gamma}\left({}^{A}_{Z}X\right)\rangle$ is the thermally averaged neutron capture cross section, $\lambda_{\gamma,\mathrm{n}}\left({}^{A}_{Z}X\right)$ is the photo-disintegration probability, and $\lambda_{\beta i}\left({}^{A}_{Z}X\right)$ is the decay-constant for β-decays followed by the emission of i neutrons. The full reaction network is obtained by solving Eq. 2.12 for all nuclides present in the r-process.

Before the reaction network can be propagated, the initial abundances of the nuclides present in the matter must be known. While early calculations assumed an initial seed of ^{56}Fe [87–89], modern calculations calculate the initial abundance distribution based upon the composition of the matter and the conditions present in the environment. A common property of many of the possible sites for the r-process is their origin in explosive or high-energy environments. Most calculations of the r-process, therefore, begin under very high initial temperatures. Under these conditions, reactions that were not energetically favourable and unlikely to occur in a star become more likely. At very high temperatures, in excess of 2 GK [94], almost all reactions are energetically favourable. When this occurs, a balance can be achieved between the rates of a reaction progressing in one direction and its reverse direction. When the reverse reaction rates balance all of the forward strong and electromagnetic reaction rates in the system, the system is said to be in Nuclear Statistical Equilibrium (NSE) [90]. Weak processes such as β-decay are commonly ignored from NSE as their reverse reactions are extremely improbable, as neutrinos produced by the forward process are effectively lost from the system due to their low interaction cross sections.

One of the outcomes of NSE is that, given enough time, any nucleus can be

transformed into any other nucleus under the conditions present [94]. Another way of thinking about this is that a nucleus can be formed out of its constituent protons and neutrons such that:

$$ {}^{A}_{Z}X \rightleftharpoons Z\mathrm{p} + (A - Z)\mathrm{n} \tag{2.13} $$

Under the conditions of NSE the system will tend towards its lowest energy configuration, which may change with temperature and density [94]. For example, for densities of less than 10^7 g/cm^3, the iron group nuclei are the most stable due to their large binding energies per nucleon. However, when the temperature is raised to 7 GK, iron nuclei are converted into helium nuclei. While the iron group nuclei still have the greatest binding energy per nucleon, the He nuclei are formed in conditions in which electrons present in the system form a degenerate gas with a high Fermi energy. The system can then maintain its minimum energy by minimising the energy of the nuclei and electrons together [94]. For systems under NSE, it is therefore beneficial to specify a relationship between the total number of neutrons and protons present in the system, the conditions of the environment and the abundances of nuclei present. This relationship can be given as:

$$ N\left({}^{A}_{Z}X\right) = \frac{G\left({}^{A}_{Z}X\right) A^{3/2}}{2^A} \left(\frac{2\pi\hbar^2}{m_\mathrm{u} kT}\right)^{3(A-1)/2} \left(\frac{\rho}{m_\mathrm{u}}\right)^{A-1} Y_\mathrm{n}^{A-Z} Y_\mathrm{p}^{Z} \exp\left(\frac{B\left({}^{A}_{Z}X\right)}{kT}\right). \tag{2.14} $$

Here m_u is the atomic mass unit ($m_\mathrm{u} = 931$ MeV $\cdot$ c^{-2}), ρ is the density of the system, $B\left({}^{A}_{Z}X\right)$ is the nuclear binding energy of the nucleus ${}^{A}_{Z}X$ [91] and Y_p and Y_n are again the proton and neutron fractions of the system and are defined as they were in Eqs. 2.6 and 2.7. Considering Eqs. 2.14, 2.6 and 2.7 together it can be seen that the final yield of an nuclide in NSE depends only on its binding energy and the temperature, density and Y_e of the environment and not any reaction rates.

For NSE occurring under r-process conditions ($T > 6$ GK), clusters of nuclei form in two major groups: a lighter group formed of protons, neutrons and alpha particles; and a more massive group of ^{12}C nuclei and heavier [92]. As the matter that makes up the system expands, it begins to cool, causing the system to drop out of NSE. As the system drops out of NSE the temperature is still high enough that charged particle reactions are still favourable. Matter is then able to flow from the lighter group to the heavier group through reactions such as $3\alpha \rightarrow {}^{12}\mathrm{C}+\gamma$ and $\alpha+\alpha+\mathrm{n} \rightarrow {}^{9}\mathrm{Be}$ followed by $\alpha+{}^{9}\mathrm{Be} \rightarrow {}^{12}\mathrm{C}+\mathrm{n}$ and also back along the inverse

reactions. As the matter continues to cool, charged particle reactions freeze out, becoming energetically unlikely, and the r-process begins from the resulting seed abundance distribution.

In addition to the increased computational cost of performing dynamic reaction network calculations, there is an increased data requirement. This increased data requirement takes the form of the nuclear properties that must be known for all nuclides in the network. Whereas calculations based on the canonical approximation may only involve a few hundred nuclei, some of the very first dynamic calculations carried out included a total of 6033 nuclei [90]. These nuclei ranged from stability to the neutron drip line, the point at which the neutron separation energy of nuclides becomes less than zero. For each of these nuclides, their masses, β-decay Q-values, β-decay half-lives, β-delayed neutron emission probabilities, and neutron capture cross sections must be known.

2.3 Obtaining the nuclear properties for r-process calculations

Whether a r-process is being calculated using the canonical waiting point approximation method or with a full dynamic reaction network, a large number of nuclear properties are required. This amount can vary from a few hundred nuclei used in the canonical r-process to the thousands used in dynamic calculations. The values of most importance for r-process calculations are nuclear masses and β-decay properties. Near stability these properties are relatively well known for nuclei, however, for nuclei far from stability there exist far fewer measurements. Currently the sheer number of values needed to perform r-process calculations outmeasures the extent of experimentally measured values. For large amounts of the values used in r-process calculations, theoretical predictions are used. For values near to stability, there is a wealth of nuclear data to base models on and optimise their outputs. However, as the models extend away from stability to regions where fewer measurements are available, the values predicted by different models diverge sometimes giving drastically different results [95].

2.3.1 β-decay properties for use in r-process calculations

β-decay properties play an important role throughout the r-process, with β-decay rates determining the rate at which the r-process path proceeds under (n,γ) $\rightleftharpoons$ (γ,n) equilibrium. The energy given off by β-decays also plays a significant role in the heating of the matter and is believed to contribute significantly to the radiation emitted by kilonova [53]. β-delayed neutron emission also plays a key role in the r-process through two mechanisms. The first is that as the neutron-flux powering the r-process stops and β-decays start to occur, delayed neutron emission acts as an important secondary source of free neutrons, allowing delayed neutron capture after the primary source of neutrons has ceased. Secondly, during freeze-out, as matter decays to stability, the delayed emission of neutrons continues to shape the r-process abundance distributions, determining the final abundances.

At present, only a small amount of the β-decay lifetimes that are required for r-process calculations are known. The amount of β-delayed neutron emission probabilities currently known is even smaller in comparison. Where experimentally measured values are not available, r-process calculations must make use of theoretical models. In recent years shell-model calculations, performed using the diagonalisation shell model code NATHAN [96, 97], have been able to reproduce experimentally measured half-lives with reasonable accuracy [98]. However, these calculations are limited to nuclides near to, or at, neutron shell closures where an inert core can be used to simplify calculations. The limited nuclides for which these calculations can be currently be performed means they are not ideal for providing values for use in r-process calculations. Instead, global models capable of producing half-lives for a wide range of nuclei are used.

The Quasiparticle Random Phase Approximation (QRPA) employed by Moller *et al.* [99] is one of the most commonly used models for calculating nuclear properties for use in r-process calculations. The starting point for the QRPA calculations is the ground-state properties of nuclei, which are calculated using the Finite Range Droplet Model (FRDM) that is discussed in more detail in Section 2.3.2. Moller *et al.* have used the QRPA to perform calculations of gross β-decay properties, which have been released in three iterations. The first iteration was released in 1997 and included the β-decay properties of 8979 nuclei ranging from ^{16}O to ^{339}136 [100]. In 2003 a new revision of the data table was released, FRDM+QRPA2003 [99], which had the inclusion of the gross theory for

the first-forbidden (ff) part of the β-decay. In first-forbidden decays, the parities of the initial and final states are different. For the parity of the nucleus to change the electron or neutrino must be emitted with an odd value of the orbital angular momentum relative to the nucleus [75]. In 2019 a new revision of the data table was again released [101], the methods used to calculate the half-lives remained the same, however, a new version of the FRDM was used to determine the ground-state properties of the nuclei. The most commonly used version of the model is FRDM+QRPA2003, which is commonly used to provide the nuclear properties for r-process calculations.

In the QRPA half-lives are calculated using the β-strength function ($S_\beta(E_i)$) of nuclei. The β-strength function is determined by the level density of excited states in the daughter nucleus [102] and describes the probability of β-decay to states in the vicinity of excitation energy E_i [75]. The half-life is calculated as a summation over all states and is written as [99]:

$$\frac{1}{T_{1/2}} = \sum_{E_i=0}^{Q_\beta} S_\beta\left(E_i\right) \times f\left(Z, R, Q_\beta - E_i\right), \tag{2.15}$$

where $S_\beta\left(E_i\right)$ is the β-strength function and f is the Fermi function which depends on Z, the nuclear radius R, and $Q_\beta - E_i$ the energy difference between the β-decay Q-value, which is defined as and the energy of the excited state the decay proceeds to. Where the β-decay Q-value is given by

$$Q_\beta = \left[m\left({}^{A}_{Z}X\right) - m\left({}^{A}_{Z+1}X\right) - m_\mathrm{e}\right] c^2, \tag{2.16}$$

where m_e is the mass of an electron. The Fermi function is included to incorporate the influence of the nuclear Coulomb field during the decay process [75]. For models using the QRPA, wave functions describing the parent and daughter nuclei are used as the starting point for calculating S_β [103, 104].

Figure 2.3 shows the ratio of experimentally measured half-lives to those predicted by FRDM+QRPA2003. In the figure, the two panels show the ratio of the calculated and experimental β-decay half-lives are plotted against the experimental β-decay half-life. The top panel is produced using calculated half-lives that do not include the first-forbidden term, whereas, the bottom panel uses half-lives calculated with the inclusion of the first-forbidden term. It is observed that across the range of half-lives plotted, the ratio between the measured half-lives and the calculated half-lives typically falls within an order of

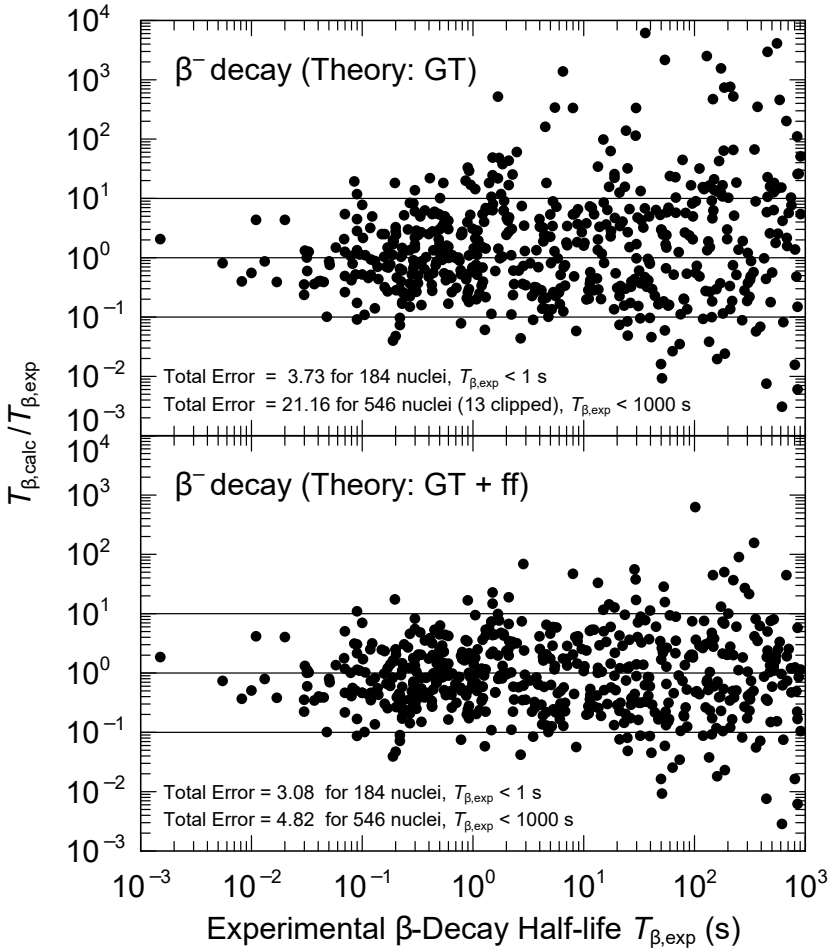

Figure 2.3 *Ratio of experimentally measured β-decay half-lives to theoretical values calculated using the QRPA, for nuclei including and above ^{16}O in size. Figure adapted from [99].*

magnitude shown by the lines running across from 10^1 and 10^{-1} on Figure 2.3. A narrower distribution in the ratio is also seen for calculations including the ff term, indicating an improvement in the calculated half-lives.

In addition to calculating half-lives, the QRPA is used to calculate the β-delayed neutron emission probabilities ($P_{\rm n}$) of nuclei. In the FRDM+QRPA2003 models, the $P_{\rm n}$ value is calculated as the probability of a β-decay proceeding to a state above the neutron separation energy of the daughter. Under this method of calculating the $P_{\rm 1n}$ value, the possibility of a nucleus excited to a state above its single neutron separation energy de-exciting via γ-emission is neglected, and all de-excitations are assumed to occur via particle emission. The $P_{\rm 1n}$ value can then

be given as [99]:

$$P_{\mathrm{n}} = \frac{\sum_{E_i=S_{\mathrm{n}}}^{Q_\beta} S_\beta\left(E_i\right) \times f\left(Z, R, Q_\beta - E_i\right)}{\sum_{E_i=0}^{Q_\beta} S_\beta\left(E_i\right) \times f\left(Z, R, Q_\beta - E_i\right)}. \tag{2.17}$$

In the 2019 revision of FRDM+QRPA, the model was updated to include a Hauser-Feshbach (HF) framework to handle the de-excitation of excited states statistically. Within the framework de-excitation via γ-emission is no longer neglected and competition is allowed between γ-decay and neutron emission. The overall effect that the inclusion of the HF framework has on the predicted P_{n} values is a decrease in emission probability for most nuclides, in particular those that can emit more than one neutron [105].

A second theory that has been used to produce a data table of β-decay properties utilises a fully self-consistent model to calculate the properties. In this model, the ground state of all nuclei is calculated with the relativistic Hartree-Bogoliubov (RHB) model, and excited states are obtained within the proton-neutron relativistic quasiparticle random phase approximation (pn-RQRPA) [106]. The author has highlighted two key differences between this model and the FRDM+QRPA model of Moller *et al.*. The first is that the model used by Moller *et al.* uses QRPA calculations based on a schematic interaction on top of the FRDM, making it hard to maintain consistency between the models used. Conversely, in the model employed for the RHB+pnRQRPA model, the residual interaction used for the pnRQRPA calculations is derived from the same density functional that is used for the ground state calculations. In this method, consistency is ensured between the properties used in the calculations. The second key difference is in the treatment of first-forbidden decays, whereas FRDM+QRPA2003 only treats the first-forbidden term macroscopically, using the statistical gross theory model to obtain contributions. The method employed by RHB+pnRQRPA treats the decays fully microscopically, treating them equally to Gamow-Teller transitions.

A final theory that has only been used in the calculation of β-delayed neutron emission probabilities, and not in the calculation of half-lives, is the effective density model [107]. It is based on the assumption that the β-strength function is proportional to the effective level density,

$$S_\beta(E) \sim \rho(E) = \frac{\exp\left(a_d\sqrt{E}\right)}{E^{3/2}}, \tag{2.18}$$

where a_d is a phenomenological effective parameter. The systematics of the a_d parameter are obtained from experimental measurements of $P_{\rm n}$ values and extrapolated to nuclei for which this has not been measured. The total β-delayed neutron emission probability of a nuclide is then calculated as [107]

$$P_{\rm n} = \frac{\int_{S_{\rm n}}^{Q_\beta} \exp(a_d\sqrt{E})E^{-3/2}f(Z+1, Q_\beta - E)\mathrm{d}E}{\int_{0}^{Q_\beta} \exp(a_d\sqrt{E})E^{-3/2}f(Z+1, Q_\beta - E)\mathrm{d}E} \tag{2.19}$$

where Z is the parent nuclide's atomic number and f is again a Fermi function. The model used masses calculated using the HFB-21 mass model [108] to obtain Q-values and $S_{\rm n}$ values for use in its calculation. The HFB mass model is described in more detail in the following section.

2.3.2 Nuclear masses for use in *r*-process calculations

While this thesis is focused on the β-decay properties of neutron-rich nuclei, it has been shown above that these values depend strongly on nuclear masses and as such a discussion on the models used for calculating nuclear masses is included. Nuclear masses are one of the most fundamental properties of nuclei. They are used extensively in the determination of almost all quantities of interest for r-process calculations, where they are used to calculate neutron separation energies and reaction Q-values. Neutron separation energies are crucial in the determination of neutron capture and photo-disintegration rates and Q-values play a large role in the determination of β-decay rates and the heating it produces, and also in β-delayed neutron emission probabilities. The importance of accurate nuclear masses can be seen in Eq. 2.14, which shows an exponential dependence on the binding energy of nuclei in the determination of NSE yields. The need for accurate masses continues throughout the r-process through to the determination of (n,γ) $\rightleftharpoons$ (γ,n) equilibrium points where Eq. 2.9 includes an exponential dependence on the $S_{\rm n}$ values of nuclei.

At present around 2353 masses have been measured and published in the atomic mass evaluation [109, 110], a number which is short of the many thousands needed for r-process calculations. Almost all of the masses used in a r-process calculation must then be obtained from theoretical predictions. Two examples of methods in which nuclear masses are calculated are described here: i) a combination of macroscopic and microscopic terms and ii) a fully microscopic treatment of the system. The Finite-Range Droplet Model (FRDM) [111, 112] is one of the

most commonly used macroscopic-microscopic hybrid models in the calculation of nuclear masses. In the macroscopic-microscopic method, the total potential energy of the nucleus is calculated as a function of shape, proton number Z, and neutron number N. It is calculated as the sum of a macroscopic term and a microscopic term, which represents the shell-plus-pairing correction [111]. The parameters used in the model are determined from an optimised fit of the experimentally measured ground-state masses of 2149 nuclei ranging from ^{16}O to $^{265}_{106}$Sg and $^{264}_{108}$Hs. The model has a RMS error of 0.56 MeV when reproducing the masses of the data it is optimised using. The Hartree-Fock-Bogoliubov (HFB) model [113] is the leading example of a model that uses a fully microscopic method for calculating nuclear masses, using density functionals based on Skyrme-type or Gogny-type effective interactions to determine the potential of the nucleus. The parameters used in the model are optimised through the fit of experimentally measured values, similarly to the FRDM approach, with the most recent models achieving a RMS error of less than 0.5 MeV [113] when reproducing the range of fitted masses. As new data becomes available, further revisions are made to these models, and the parameters are changed as new data is included in the optimisation. A range of different data sets can, therefore, be found for the HFB model ranging from the first revision HFB-1 [114, 115] to more recent revisions HFB-26 [113, 116].

While many of the models are able to reproduce experimental data with RMS errors of less than 1 MeV for most nuclei, this does not necessarily mean that they are able to predict unknown values accurately. Reference [117] investigates the predictive power of mass models by comparing the masses predicted by models optimised using the AME2003 to newly measured masses in AME2012. No strong correlations were found between a model's error in reproducing measured values and its predictive powers; this makes it hard to determine the true uncertainty in masses for nuclei far from stability. It was also found that the predictive powers of any single model are not uniform across its entire range but varies across regions of the nuclear chart.

2.4 Uncertainties in r-process predictions

As the previous section outlines, it has been shown that theoretical values can be calculated for the nuclear properties used in r-process calculations. However, these calculations often have large uncertainties associated with them,

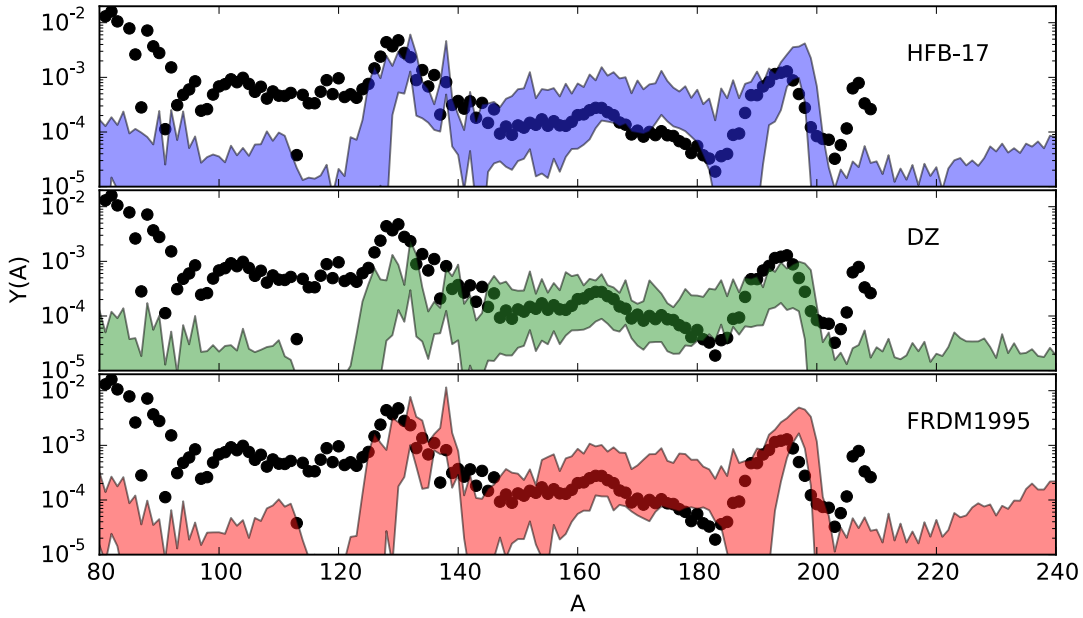

Figure 2.4 *Uncertainty bands on calculated r-process abundances with rates from FRDM-QRPA and Q-values from three mass models. Figure adapted from [119].*

especially in regions lacking experimental data. When using these values to calculate r-process abundances, the effects of these uncertainties should be considered. Monte-Carlo studies performed in recent years by Mumpower, Surman and Aprahamian [95, 118–120], have sought to investigate the effects these uncertainties can have on calculated r-process abundances. To test the uncertainties of calculated r-process abundances that can be attributed to the uncertainties associated with β-decay rates, they performed Monte-Carlo variations of the β-decay rates in the calculations. For each run, the initial trajectory of the r-process calculation was fixed to ensure all differences came from the change in rate. For each run, each of the β-decay rates present in the reaction network were varied by a multiplicative factor with a variation that was motivated by the standard deviation shown in Figure 2.3, these multiplicative factors varied over a range of 10^{-1} and 10^{1}.

The results of the calculations are shown in Figure 2.4 in which the uncertainty bands are plotted alongside solar r-process abundances. It is worth noting that the three models referred to in the plot – HFB-17, DZ and FRDM1995 – were only used for the prediction of masses and that for all three tests the rates were obtained from FRDM+QRPA 2003 [99]. For each of the plots, the isotopic abundances are scaled to the rare Earth region. It can be seen that for all of the

plots, most of the rare Earth region and much of the structure around $A \sim 130$ lie within the uncertainty bands. The authors noted that the magnitude of the uncertainty bands are all of the same order of magnitude and that the current error bars on the models are all too large to distinguish between the predictions of different nuclear models. They also noted that that in order to improve the predictability of r-process simulations, advances in the description of neutron-rich nuclei must be achieved [95].

2.5 Sensitivity studies and the need for experimental data

As shown in the previous section, much of our ability to make predictions about the r-process is hindered by the uncertainties attributed to theoretical values used as inputs in calculations. There has recently been an increased demand for precise experimental data of r-process nuclei, in an effort to reduce these uncertainties [119, 121, 122]. The benefits of increased measurements in the region are twofold: i) the measured values can be used as direct inputs in r-process calculations where they are available and ii) measurements out from stability allow for further reference points in the optimisation of theoretical models in the region.

With such a large amount of nuclear properties currently not experimentally measured, it can be challenging for experimentalists to know in which regions of the nuclear chart to focus their measurements. To aid in this modellers carry out sensitivity studies in which the sensitivity of the final abundance distribution to the properties of specific nuclei is gauged [123–125]. These studies highlight the nuclear properties and nuclides, which play the largest roles in determining the final abundances of the r-process. Experimentalists can then perform measurements targeting these highlighted nuclei and properties, constraining the uncertainties associated with them and improving the predictability of r-process calculations.

Mumpower *et al.* performed sensitivity studies, investigating which nuclides' β-decay rates and β-delayed neutron emission probabilities have the greatest impact on the final r-process abundances. The sensitivity studies were performed by first carrying out a r-process calculation, using nuclear masses from FRDM95 [111], β-decay rates from FRDM+QRPA 2003 [99] and neutron capture rates

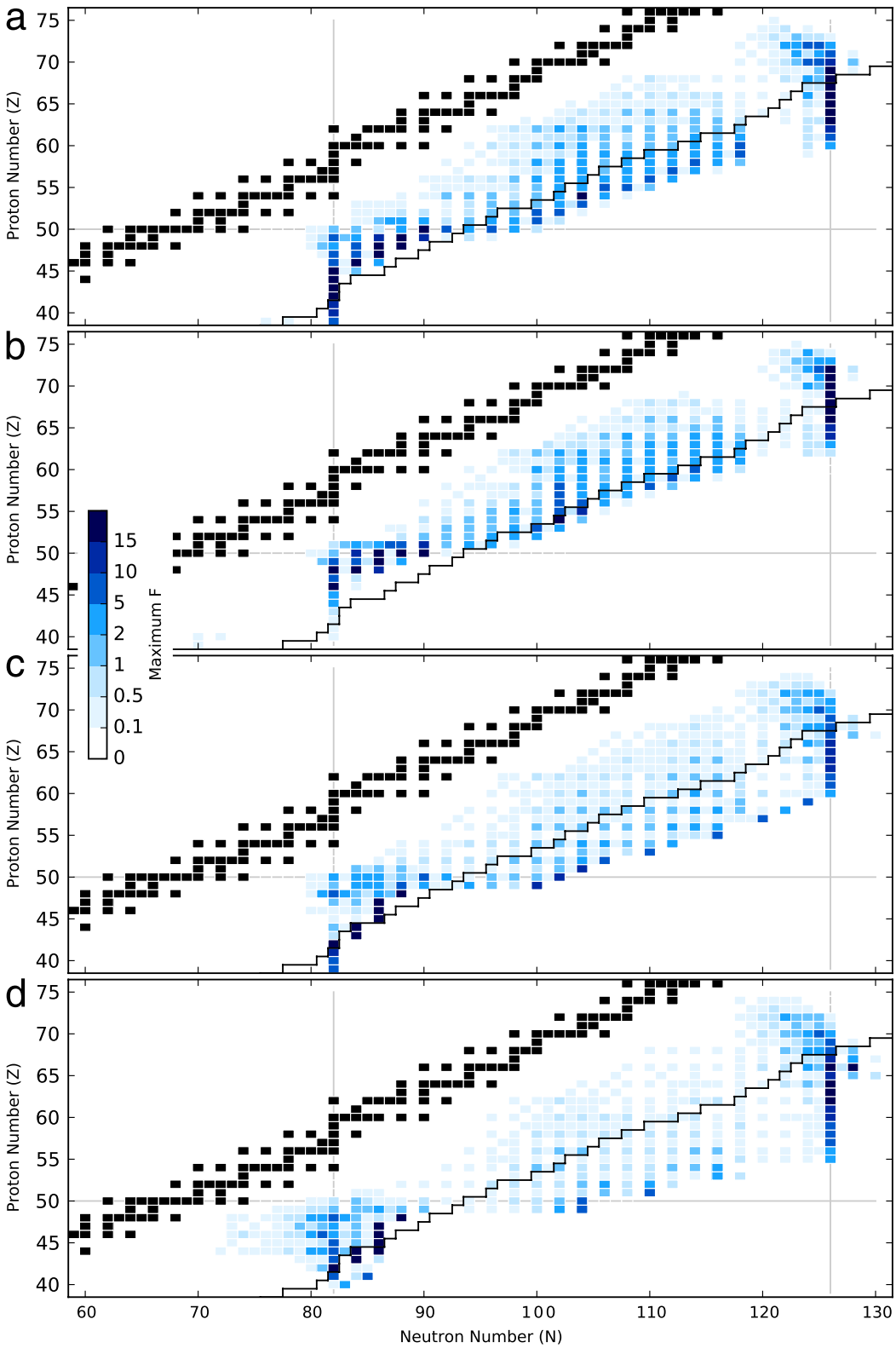

Figure 2.5 *Impact of individual β-decay rates on calculated r-process abundances in four astrophysical environments (a) low entropy hot wind, (b) high entropy hot wind, (c) cold wind and (d) neutron-star merger. Black line represents the estimated region accessible to FRIB. Figure from [95] based on data from [123]*

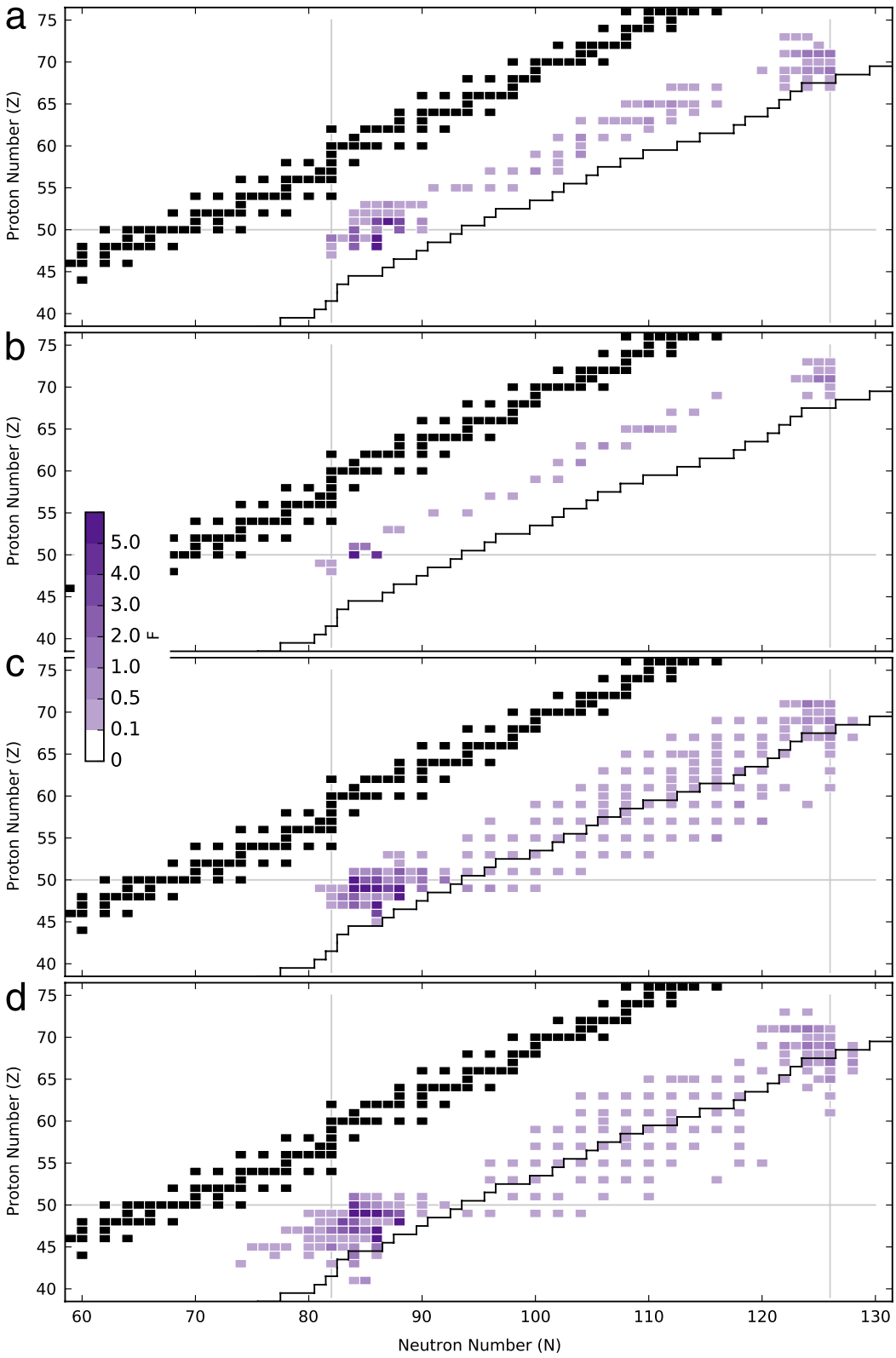

Figure 2.6 *Impact of individual β-delayed neutron emission probabilities on calculated r-process abundances in four astrophysical environments (a) low entropy hot wind, (b) high entropy hot wind, (c) cold wind and (d) neutron-star merger. Black line represents the estimated region accessible to FRIB. Figure from [95] based on data from [125]*

from NON-SMOKER [126]. The calculation was used to obtain a base version of the r-process distribution, against which further calculations can be compared in order to determine changes in abundance. The calculation was then repeated with either the half-life or P_{n} value of a single nuclide's value changed. For half-lives, individual rates were varied by a factor of 10. For P_{n} values, the delayed neutron emission channel was removed by setting the $P_{\mathrm{n}} = 0$. The difference in abundances between the two runs was used to calculate an impact factor F, which is defined as:

$$F = 100 \times \sum_{A} |X(A) - X_{\mathrm{baseline}}(A)| \tag{2.20}$$

where $X(A)$ represents the final mass fraction of an isobar A from the varied run and $X_{\mathrm{baseline}}(A)$ is the final mass fraction of isobar A in the baseline calculation. Impact factors were measured for the half-lives and P_{n} values of nuclides in the region of $40 \leq Z \leq 75$ and $70 \leq N \leq 130$. The sensitivity studies were performed for four different trajectories of initial r-process conditions (a, b, c and d), relating to different astrophysical environments. Trajectories a and b represent low and high entropy hot neutrino driven winds respectively, conditions which could be found in core-collapse supernovae. Trajectory c represents cold neutrino driven wind and trajectory d represents the trajectory set by a binary neutron star merger.

The results of the β-decay rate investigation are presented in Figure 2.5. The greatest impact factors are observed for nuclides at the closed neutron shells at $N = 82$ and $N = 126$, followed by the nuclides that fall along the early r-process path. This is seen to be the case for all four sets of initial conditions and is attributed to the fact that at early stages in the r-process the steady flow condition holds well. Sensitivity to β-decay rates are observed to a lesser extent closer to stability, indicating the continued importance of β-decay rates during freeze-out as matter decays back to stability.

The results of the β-delayed neutron emission study are shown in Figure 2.6. In section 2.3.1 it was stated that β-delayed neutron emission plays two key roles in late stages of the r-process: i) acting as a source of additional free neutrons and ii) shaping the final abundance distributions. Turning off just a single β-delayed neutron emitter is unlikely to affect the total number of free neutrons available, and so any effects that were seen in the study are going to be due to the shaping during freeze-out. The effects of individual P_{n} values were found by

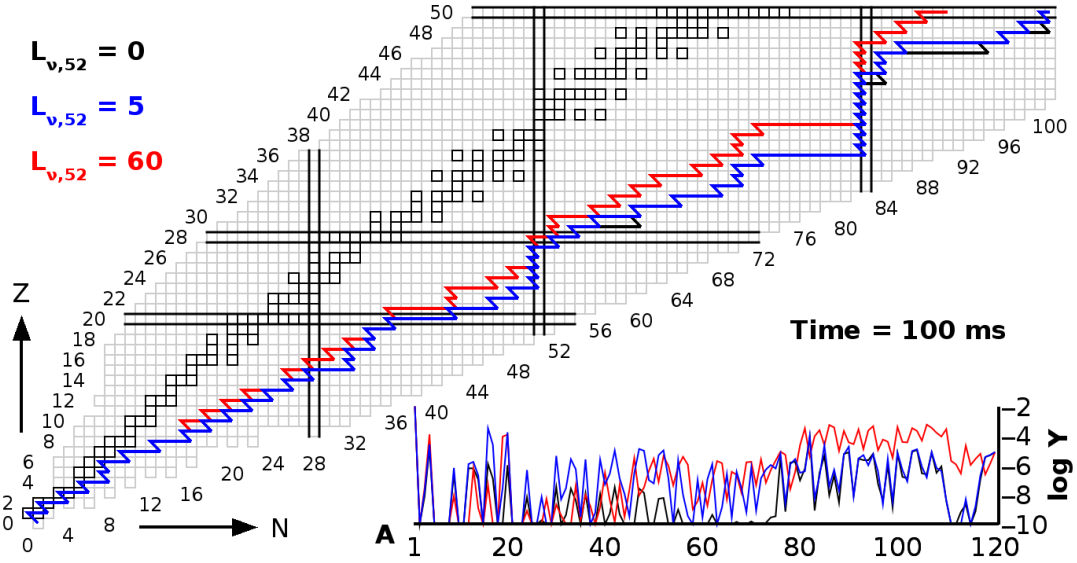

Figure 2.7 *Calculated r-process paths for different neutrino luminosities in a neutron-star black hole merger. Figure adapted from [36]*

systematically setting the P_{n} of each nuclide to zero. It should be noted that the scale of Figure 2.6 is different from Figure 2.5 and the impact factor F tends to be much smaller. This is expected as P_{n} values are expected only to vary the local abundance distributions. The global measure used in the study, therefore, is a poor measure of any effective change. The location of maximum impact being observed at the closed neutron shells at $N = 82$ and $N = 126$ is also expected, this can be attributed to the build-up in abundances that occurs as the r-process path meets them. Little impact is seen for nuclides near to stability, as the Q_{β} value of these nuclei is unlikely to be larger than their daughter's neutron separation energy. The population of states above the daughter's neutron separation is, therefore, very unlikely; making β-delayed neutron emission very unlikely in these nuclei.

2.6 The region around the $N = 82$ shell closure

In the previous section, the sensitivity of r-process calculations to nuclear properties was shown as a method of determining individual nuclides that have a large impact on the final r-process abundances. Of particular importance were the half-lives and β-delayed neutron emission probabilities of nuclides around the closed neutron shells at $N = 82$, and 126. In section 2.2 it was explained that the

production of the r-process abundance peaks at $A = 80$, 130 and, 194 are related to the r-process path meeting the closed shells and that the reduced neutron-capture cross sections of nuclides along these closed shells caused a build-up in abundance. Figure 2.7 shows calculated r-process paths, differing only in the neutrino luminosity, for a black hole neutron-star merger. A common feature of all the paths is that they become trapped at the closed neutron shells and forced to β-decay before further neutrons can be captured. The paths are only able to break out of the neutron shells once the neutron-capture rate can compete with the β-decay rate. Accurate measurements of the nuclear properties for the nuclei along these closed neutron shells will help to drastically reduce the uncertainties associated with r-process calculations.

In recent years the number of half-lives published for nuclei near the closed neutron shells has increased, with experiments performed using the EURICA [127] and Griffin [128, 129] setups. There have also been a growing number of masses measured for these nuclei, with measurements carried out at facilities such as Jyväskylä [130] and CARIBU [131]. However, there are still very few measurements of the β-delayed neutron emission probabilities of these nuclei. Without accurate measurements of the β-delayed neutron emission probabilities of nuclei near the closed neutron shells, r-process calculations will be unable to reproduce the shaping of the final abundances and also the late-stage neutron-captures facilitated by delayed neutron emission. The experiment presented in this thesis provides much needed nuclear data on the β-delayed neutron emission probabilities of nuclei around the closed neutron shell at $N = 82$. For many of the nuclei studied, only the half-lives were previously known. This work, therefore, represents a significant contribution to the available neutron emission probabilities for use in r-process calculations.

The experiment presented in this thesis was performed in 2017 by the BRIKEN collaboration [132] at the Radioactive Ion Beam Factory (RIBF). The elements measured in the experiment ranged from Ru ($Z = 44$) to Ba ($Z = 56$) including nuclides along the $N = 82$ shell closure and then higher mass nuclei beyond $N = 82$ that are of importance when the r-process path escapes the $N = 82$ closed shell and neutron-captures dominate. The half-lives and β-delayed neutron emission probabilities presented in this thesis are of the nuclides that are in the range of $Z < 50$ and $N \leq 82$. Nuclides with $Z > 50$ and $N > 82$, also measured in the experiment, have been analysed by other PhD students. The β-delayed neutron emission probabilities of the nuclides included in this thesis, in

particular of $^{125-126}$Rh and $^{127-128}$Pd, have a direct impact on the final abundances of ^{125,126,127,128,130}Te isotopes and, therefore, on the location of the $A = 130$ r-process peak.

Chapter 3

Exotic Beam Production at the Radioactive Ion Beam Facility

3.1 Radioactive ion production

The production of exotic nuclei, for use in experiments, is commonly achieved through the break up of massive nuclei such as uranium or through fusion reactions involving lighter nuclei. Projectile fragmentation and in-flight fission are two of the primary break-up methods used. Both methods are capable of producing a wide range of unstable nuclei. Before these nuclei are used in experiments, it is common to separate and focus the nuclei, restricting the large range of nuclides produced to a group centred on a region of interest.

3.1.1 Projectile fragmentation

Projectile-fragmentation reactions were first pioneered as a method of producing light neutron-rich nuclei in the 1970s. The work carried out at the Lawrence Berkeley Laboratory used highly energetic (212 MeV/u) medium mass nuclei (^{48}Ca) to create light nuclei close to the limit of stability [133–135]. The reaction mechanism involves the bombardment of relativistic heavy nuclei onto lighter target nuclei. During the interaction, a small amount of excitation is imparted to the projectile, which is enough to cause nucleons to be emitted from the nucleus without causing significant changes to its velocity or direction [135].

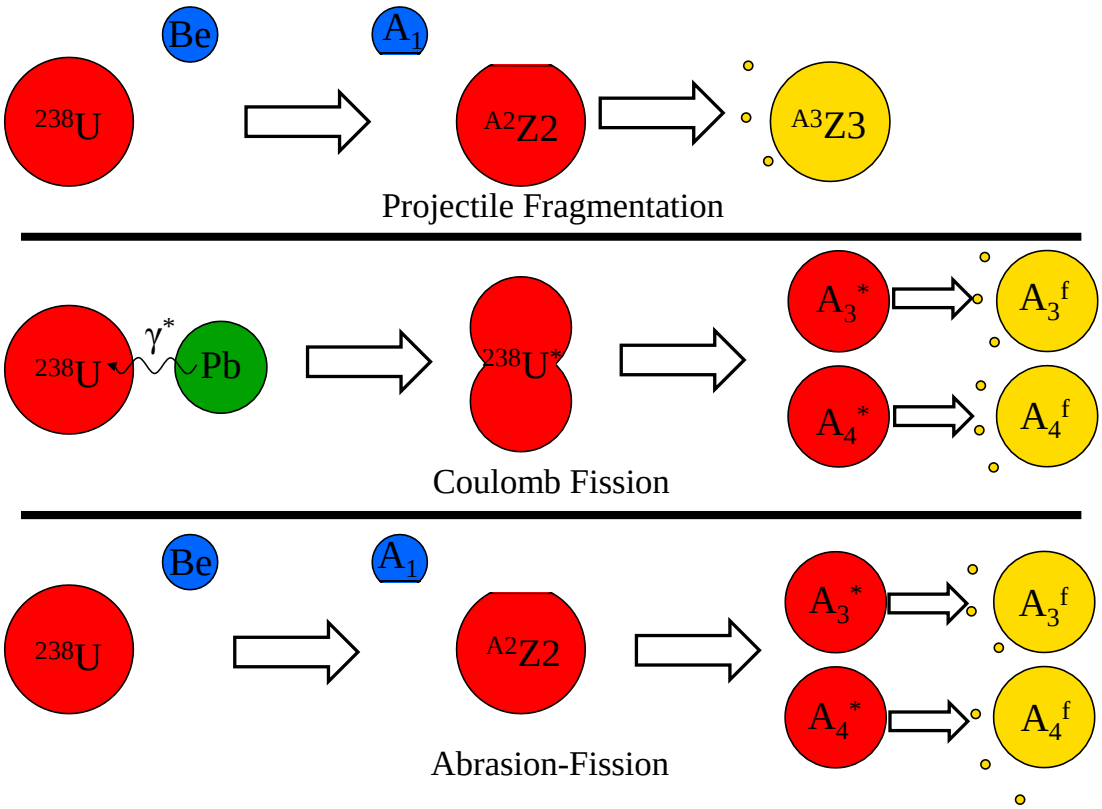

Figure 3.1 *Diagram showing three methods of radioactive beam production commonly employed. In all three methods,* ^{238}U *is used as the primary beam ion. In projectile fragmentation and Abrasion-Fission the uranium ion is incident on a light target nuclei such as beryllium. Whereas, in Coulomb fission, the uranium is incident on a heavy target nuclei such as lead. In projectile fragmentation* $A_3 \leq A_2 < 238$ *and* $Z_3 \leq Z_2 \leq 88$*. In Coulomb Fission* $A_3 + A_4 = 238$*. Finally, in abrasion-fission* $A_3 + A_4 < 238$*.*

One of the first models developed to describe this phenomenon is that of "Abrasion - Ablation" [136], where the production of the forward-focused fragments occurs in a two-step process. As the heavy ion collides with the target nuclei the overlapping volume of the heavy ion is sheared away in the process of "abrasion". The remaining part of the heavy ion, known as the spectator, remains unchanged in its direction. The amount of material sheared off in the abrasion process is determined by an impact parameter, which describes the overlapping volume of the heavy ion and target nuclei. The spectator nucleus is left in an excited state after the "abrasion", and this excitation energy is lost through particle emission in the process of "ablation". The excitation energy the spectator nucleus gains is determined by the change in the shape of its surface term as it is left deformed after the abrasion [136]. The top panel of Figure 3.1 shows a diagram of how the Abrasion-Ablation model works, in the example a

uranium ion impinges upon a beryllium target. After interacting with the target, the uranium ion has had part sheared away and de-excites by the emission of nucleons. The combination of the impact parameter and the amount of excitation energy determines the final isotopic distribution of produced ions. Fragmentation cross sections are largest for fragments that are just below the mass of the initial nucleus and decrease exponentially with smaller atomic mass numbers.

3.1.2 In-flight fission

While projectile fragmentation is used in the study of neutron-rich light mass nuclei, it is not as well suited to the study of heavy neutron-rich nuclei. For high mass nuclei, the fragmentation yield is largest for neutron-deficient nuclei [137]. Nuclear fission is instead used as a source of neutron-rich nuclei. The first in-flight fission reactions were performed in GSI by Bernas *et al.* in the 1990s, and across their first two studies a total of 117 new nuclides were discovered [138–140]. While fission had previously been used in the production of neutron-rich nuclei [141], there are many challenges when using it to study nuclei of higher masses. One of the most significant challenges is that at the low energies involved it becomes challenging to separate nuclides due to the limitations in resolving power of Z [138]. The limitation is a result of the relatively low energies given to the fission products, making it hard to observe them without stopping them in a detector. In addition to this, broad charge state distributions of the fission products and their isotropic production make the identification and study of nuclei in the high-mass regime almost impossible [142]. In-flight fission helps to alleviate a number of these issues. While the fission products are emitted isotropically in the centre of mass frame of the fissile nucleus, fission products via in-flight fission are observed to be emitted in a tight cone around the beam axis in the laboratory frame. This cone forms as the energies given to the fission products in the fission process are small in comparison to the beam energy. Another benefit is that by using the fissile nucleus as the primary beam ion, the primary ion can have all, or almost all, electrons removed before interacting with the production target. By removing all, or most of, the electrons before the fission process occurs, products are, consequently, more likely to be produced with no, or few, electrons. The charge state distributions of the products are therefore drastically reduced, making identification of the fission products easier than if there was a broad charge state distribution.

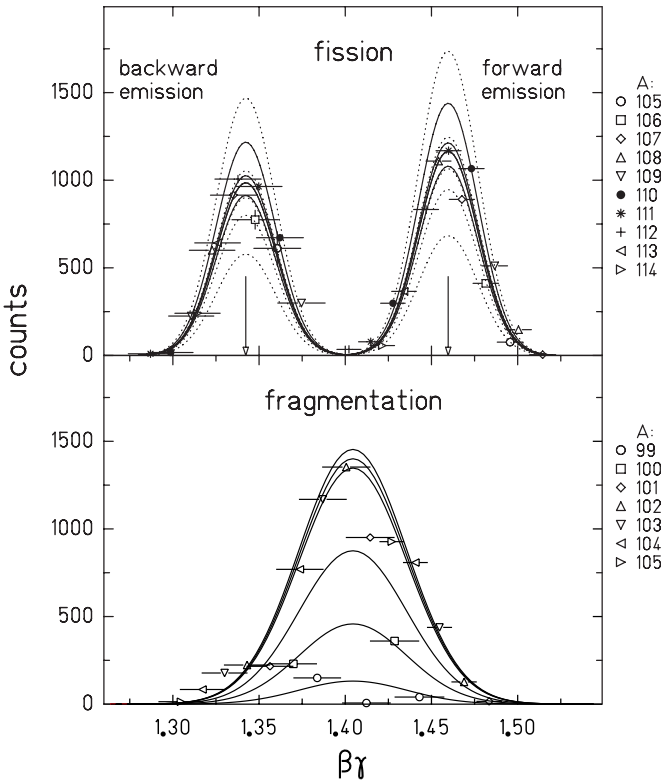

Figure 3.2 *Comparison between the double-humped velocity distribution of fission products and the centrally peaking velocity distribution of fragmentation products. Figure taken from [143].*

In contrast to projectile fragmentation, where the velocities of the fragmentation products are centred around the primary beam velocity, the velocity distribution of fission products shows a double-humped structure above and below the primary beam velocity. A comparison of the two distributions is shown in Figure 3.2. This results from the combination of the isotropic distribution of products emitted by fission and the momentum acceptances of the separators used to identify them. The momentum acceptance of separators limits the nuclei observed to those emitted either forwards or backwards with respect to the beam axis. The kinetic energy, given to the nuclei by the fission process, then either adds to or subtracts from the beam energy, leading to the double-humped structure.

Two different interaction mechanisms between the projectile ion and target ion can cause the projectile ion to undergo fission. The first is via Coulomb fission of the uranium projectile. In Coulomb fission, there is a large impact parameter between the projectile ion and target ion, meaning a large overlapping volume. The long-range Coulomb interaction dominates between the projectile and target, and a virtual photon is exchanged between the target and projectile ion, exciting the uranium projectile to an excited state [144, 145]. The excited uranium then

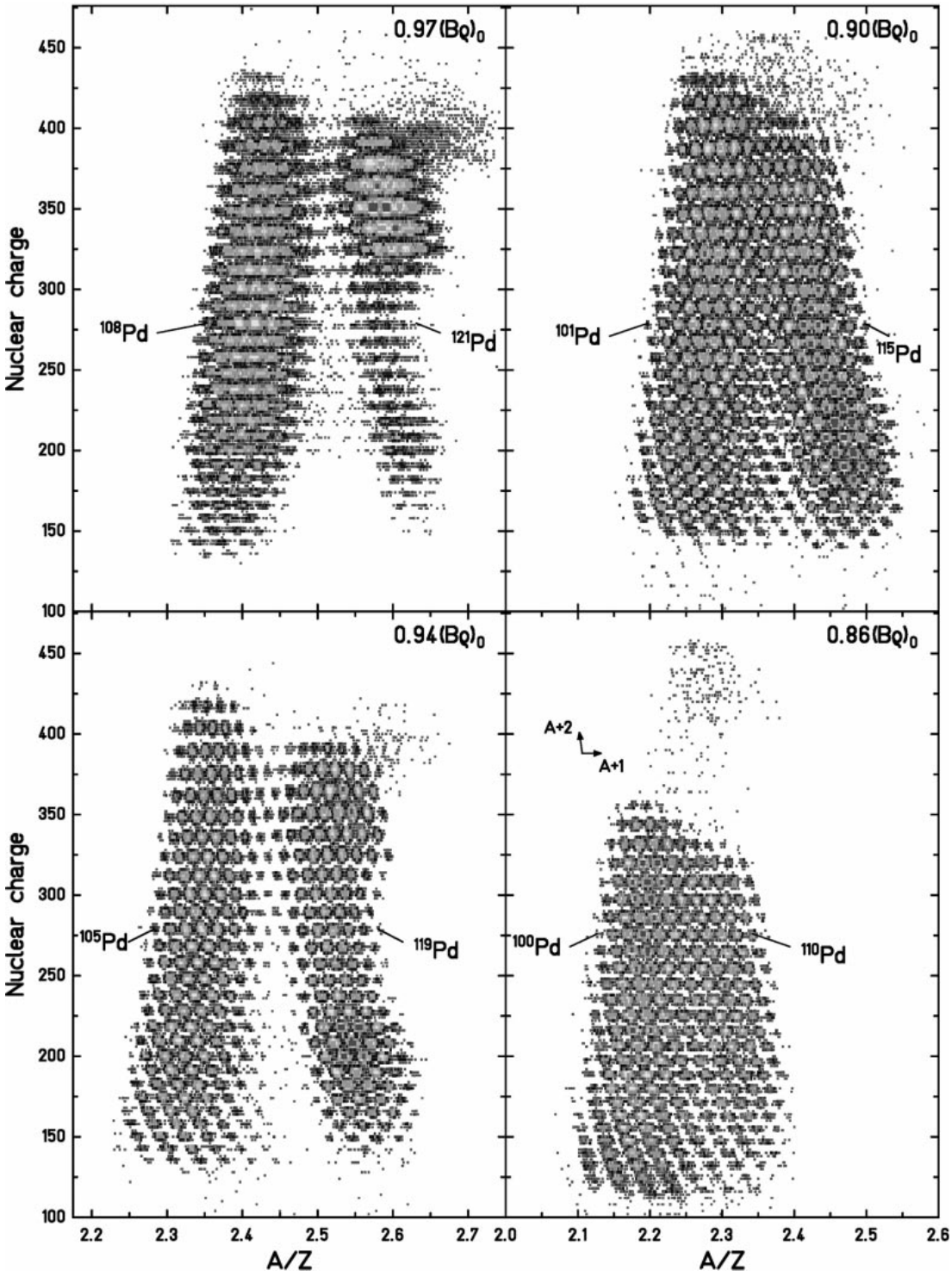

Figure 3.3 *Nuclei produced during the ^{238}U+^{208}Pb reaction gated on different product momenta. Two groups are present at each momentum, a high mass group on the right and a lower mass group on the left. Figure taken from [143].*

has the possibility of undergoing fission to de-excite. A second fission process is through abrasion induced fission. Here, a small impact parameter exists between the uranium projectile and the target. As the uranium passes through the target a small amount of the uranium is sheared away, leaving the projectile in a highly excited state. As the abraded and excited nuclei de-excite through particle emission, it has the chance to undergo fission with a finite probability. Figure 3.1 shows a step by step breakdown of how each of the two fission processes proceeds. It has been found that Coulomb induced fission dominates the excitation at lower energies and that Abrasion-Fission leads to higher excitation energies [139, 146].

The different velocity distributions of in-flight fission and projectile fragmentation products allow for the separation of products from each of the processes. Figure 3.3 shows particle identification plots produced using different momentum cuts on the fission products, obtained from the in-flight fission of uranium [143]. The top two panels in the figure show two groups of nuclei attributed to fission, with the group on the left comprises high-energy fission products emitted in the forward direction, and the left-hand side comprises backwards emitted low-energy fission. The lower plots also include fragmentation products with backwards high-energy fission on the right and the fragmentation products on the left.

3.2 Particle identification methods

Both projectile fragmentation and in-flight fission produce RI beams made up of multiple species of nuclei. This can be seen in the panels on Figure 3.3, where each of the blobs on a panel represents a different nuclide. For most experiments, it is desired that the nuclei produced are identified before being used in the experiment. Nuclei are identified by their atomic number, Z, and their mass number, A. Determination of these quantities is commonly achieved through a combination of energy loss measurements and measurements of the momentum of the ions.

The atomic number, Z, of a nuclide can be determined by measuring the amount of energy lost as it passes through matter [147, 148]. The rate at which a high-energy heavy-ion loses energy as it interacts with matter is given by a relativistic version of the Bethe-Bloch equation [149]:

$$\frac{\mathrm{d}E}{\mathrm{d}x} = \frac{4\pi \mathrm{e}^4 Z^2}{m_\mathrm{e} v^2} N z \left[\ln \frac{2 m_\mathrm{e} v^2}{I} - \ln\left(1-\beta^2\right) - \beta^2 \right]. \tag{3.1}$$

Here Z is the ion's atomic number, v is its velocity (which is related to β and γ by $v = \beta c$ and $\gamma = 1/\sqrt{1-\beta^2}$ with c being the speed of light), m_{e} is the mass of an electron and e is the elementary charge. z is the atomic number of the material, N is its atomic density and I is its mean excitation potential. From Eq. 3.1 it can be seen that for ions travelling through the same material their energy loss relative to each other will depend only on their atomic number, Z, and their velocity. Therefore, for ions where their velocities are known the relative atomic numbers of each ion can easily be determined from energy loss measurements.

The velocity of ion is often determined by measuring its Time-Of-Flight (TOF) over a known track length L. If both the TOF and track length are known, the velocity is given to be:

$$v = \beta c = \frac{L}{TOF}. \tag{3.2}$$

In fragment separators used in the identification of fission and fragmentation products, the track that is taken by the ions is not a straight line but often involves multiple bends that are created by large dipole magnets. The bending radius of an ion in a magnetic field depends on its magnetic rigidity ($B\rho$), which is defined to be the momentum of a particle divided by its charge Q. Ions travelling with different momentum will, therefore, travel over different paths. By determining the path that an ion takes through a separator, its magnetic rigidity and momentum can thus be found. If both the $B\rho$ and velocity of an ion are measured simultaneously, they can be combined to calculate the mass of an nuclide as a fraction of its charge (A/Q), where:

$$\frac{A}{Q} = \frac{B\rho}{\beta\gamma}\frac{c}{m_{\mathrm{u}}}. \tag{3.3}$$

For fully stripped ions, which have no electrons remaining, $Q = Z$ and this can be combined with the values obtained from the energy loss measurements to identify ions. Identification of ions is then performed using a plot of the atomic number Z against the mass/charge ratio A/Q, an example particle identfication plot is shown in Figure 3.3.

3.3 The Radioactive Ion Beam Factory

The Radioactive Ion Beam Factory, or more simply RIBF, is a world-leading facility for the production of RI beams [150, 151]. Run by the Nishina Centre,

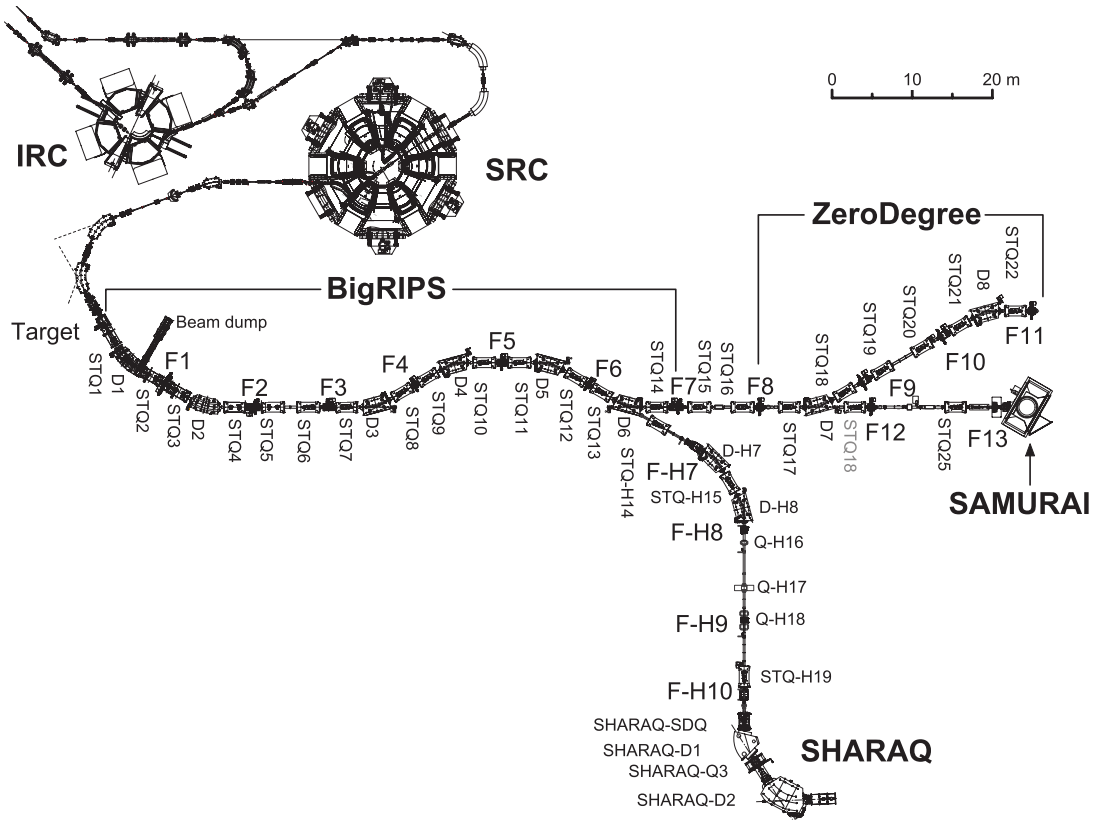

Figure 3.4 *Schematic layout of the RI Beam Factory. Adapted from [152].*

at RIKEN Japan, this world-leading facility came online in 2007 and underwent further upgrades that were carried out until 2012. With primary beam energies of up to 440 MeV/u for light ions and 350 MeV/u for very heavy ions, near relativistic energies are available for the production of RI beams using a wide range of primary beam nuclei. The RI beams produced at the facility are separated, focused and identified using the superconducting fragment separator, BigRIPS, before being delivered to experimental setups located within the factory.

3.3.1 Primary beam production

For the production of heavy neutron-rich nuclei, a high primary beam intensity is wanted as the production cross sections of exotic nuclei are often small. At the RIBF ^{238}U is chosen as the primary beam nucleus for the production of the heaviest beams. Intense primary beam currents are produced via a 28 GHz superconducting electron cyclotron resonance ion source (SC-ECRIS), which is capable of producing $^{238}U^{35+}$ ion beams of a few pμA [153, 154]. After being extracted from the SC-ECRIS the highly charged uranium ion beam is injected

into the RIKEN ring cyclotron (RRC), where it is accelerated to an energy of 11 MeV/u [155]. Upon extraction from the RRC, the beam passes through a stripper foil, removing electrons, taking the charge state of the uranium ions from 35+ to 71+. In order to further accelerate the uranium ions to the 350 MeV/u relativistic energy needed for particle identification, a high-power heavy-ion booster system is used. The high-power heavy-ion booster system comprises three ring cyclotrons. The first cyclotron in the system is the fixed frequency cyclotron (fRC), from which uranium ions are extracted at an energy 50.7 MeV/u. Following the fRC the ions are passed through a stripper foil, leaving the uranium ions with just four electrons taking them to a charge state to 88+. The second cyclotron is the Intermediate stage Ring Cyclotron (IRC), which accelerates $^{238}U^{88+}$ to 127 MeV/u before being extracted. The third and final cyclotron is the superconducting ring cyclotron (SRC) [156], the first of its kind, capable of accelerating the $^{238}U^{88+}$ to the final beam energy of 350 MeV/u.

3.3.2 Radioactive ion production

To create the radioactive ions in-flight fission through the abrasion-fission process is utilised. The uranium ions impinge upon a 740 mg/cm^2 (4 mm) thick beryllium target. Beryllium is chosen as the target element as it has a small impact parameter associated with it. This minimises the chances of Coulomb induced fission occurring, allowing Abrasion-fission to dominate. In addition to having a low impact parameter, Beryllium is a good choice of target material as it has a large heat capacity [163, 164]. This allows it to dissipate the large amounts of heat deposited into the target as a result of the high primary beam intensity. To further aid in heat dissipation, a rotating target is used. The rotating target stops the intense primary beams impinging on a single location, spreading the heat across the surface of the target [164].

As the uranium ions pass through the target, small amounts of nuclei are abraded from the uranium ion, leaving it in an excited state. The abraded ions then de-excite via fission processes, producing a wide range of radioactive nuclei. The large forward momentum of the primary beam causes the fission products to travel forwards in a tight cone once through the target. The resulting fission products will have a range of Z and A values, with a distribution given by their fission cross sections. A plot of fission cross sections measured at BigRIPS for ^{238}U + ^{9}Be is shown in Fig. 3.5. In the figure, the upper panel is for even Z

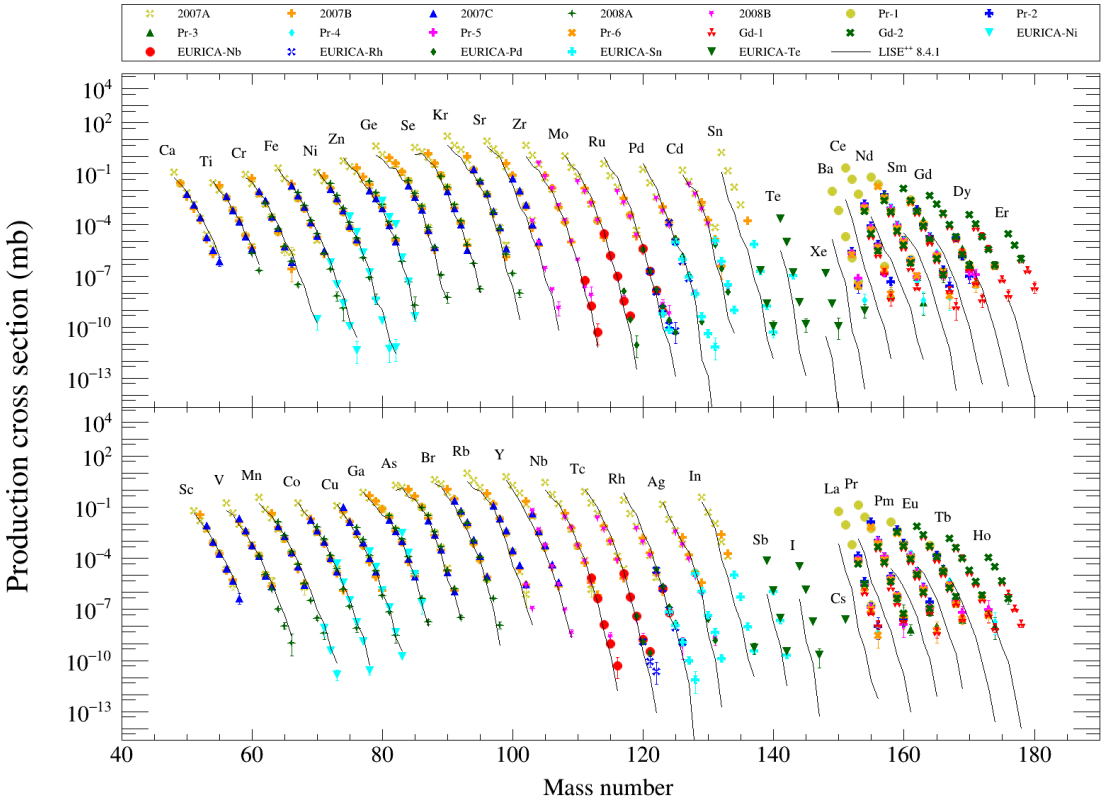

Figure 3.5 *Fission cross sections for ^{238}U+Be measured at BigRIPS. The top panel shows the cross sections of even Z nuclei and the bottom panel odd Z nuclei. Adapted from [157] which includes data from [158–162]*

nuclei, and the bottom panel is for odd Z nuclei. The cross sections can be seen to drop for increasing mass number for each nuclide. This is one of the reasons intense primary beam currents are required for the production of neutron-rich nuclei.

3.4 The radioactive ion beam separator

After passing through the production target, the resulting beam is a mixture of radioactive nuclei produced via fission and fragmentation and the remaining unreacted primary beam. The intensity of this beam is still considerable, with an intensity close to the primary beam intensity, much larger than is feasible for use in experiments. The broad distribution of nuclear species produced means that for experiments only looking to study a few different nuclei, there is a significant background. By separating the beam and focusing solely on a small selection of nuclides, more usable rates can be achieved while also allowing identification of

the nuclei to be carried out.

The Radioactive-Isotope beam Separator BigRIPS is part of a new generation of in-flight particle separators. BigRIPS is characterised by its large acceptances and its two-stage design [165]. The large acceptances ensure that BigRIPS has high collection efficiencies not just for fragmentation processes but also for fission processes, where products are created with a large momentum spread. The collection efficiency for fission products is around 50% [152]. Its two-stage design allows for excellent separation of particles and the delivery of tagged radioactive ion beams with identification of individual ions.

The two-stage design of BigRIPS utilises six room-temperature dipole magnets and fourteen Superconducting Triplet Quadrupoles (STQs) to separate and focus the beam. The dipole magnets have a bending angle of 30 deg and a mean bending radius of 6m [166]. Along the length of the separator there are six intermediary focus points before the final focus at F7. Figure 3.4 shows a schematic of BigRIPS with the dipole magnets labelled as D1-6, the STQs labelled as STQ1-14 and the focal points F1-7. The total length of the separator is 78.2m [152]. The large acceptances of BigRIPS are achieved through the use of large apertures in the STQs. The acceptances of ±40mr horizontally and ±50mr vertically, and the momentum acceptance of ±3%, are comparable to the spreads of fission fragments in the energy region, allowing BigRIPS to achieve its high collection efficiency.

Each of the stages in BigRIPS is designed as a mirror-symmetric achromatic system. Mirror-symmetric means that an ion's trajectory is a mirror about the symmetry axis of each stage and achromatic means that the focus point of the ions does not depend on an ion's momentum. The first stage of BigRIPS is designed to carry out the production and separation of nuclides between the production target and the intermediate focus F2, forming a two bend achromatic system with a momentum dispersive focus at F2. The second stage, which is used for the identification of ions, runs from F2-F7 forming a four bend system with dispersive focal points at F4, F5 and F6 [152].

3.4.1 Particle separation

In the first stage, fragments are separated by a combination of magnetic analysis and energy loss techniques. The first stage of the selection is carried out by the first dipole after the production target, which selects ions by their magnetic

rigidity, reducing the number of nuclei transported to nuclides around a specific A/Q value. Wanted A/Q values are steered onto a wedge-shaped degrader, while unwanted fragments are steered into a beam dump. A wedge-shaped degrader is used so that the system remains achromatic. To do this, the dispersive coefficient of the ions must remain constant before and after the degrader. This is achieved as higher energy ions are steered onto the thicker portion of the degrader, and so they lose the same amount of energy as lower energy ions travelling through the thinner part [152]. The wedge-shaped degrader causes the momentum distribution between different values of Z to broaden. Another stage of separation is then carried out by the second dipole magnet, further refining the A/Q selection of the fission products. The combined use of both techniques is known as momentum-loss achromat [167]. A telescopic matching system, made up of STQ4 and STQ5 between D2 and D3, transports the separated beam from the first stage to the second stage.

3.4.2 Particle identification

The identification of ions is carried out in the second stage of BigRIPS. The reduced rate in the second stage, achieved by the separation carried out in the first stage, allows for individual ions to be identified as they pass through the second stage. Identified ions are said to be "tagged", indicating that their Z and A/Q values have been measured. Particle identification in BigRIPS is carried out via the implementation of the $TOF - B\rho - \Delta E$ method. During particle identification, each of these quantities is measured as an ion passes through the separator. Precise measurement of each of these quantities is essential for the accurate identification of high Z RI beams.

Determination of A/Q in BigRIPS

The determination of an ion's A/Q is carried out by the simultaneous measurements of the ion's TOF and also its $B\rho$, which, when combined, can be related to the absolute value of A/Q by Eq. 3.3. Measurement of an ion's TOF is carried out over the full length of the second stage of BigRIPS. The long path length of the ions, 46.6m, allows for high resolution TOF measurements to be performed. This is a requirement for high resolution A/Q determination, needed in the identification of heavy nuclei where A/Q only varies slightly between neighbouring

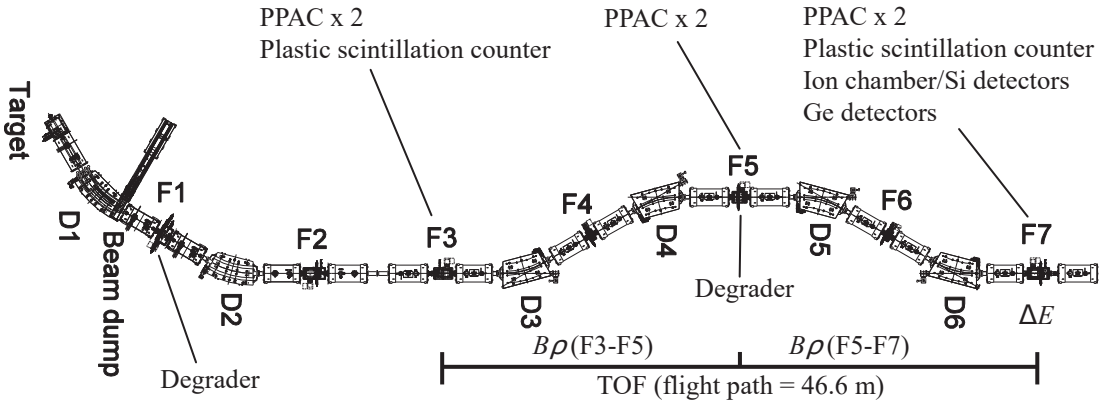

Figure 3.6 *Schematic layout of the beamlime detectors in BigRIPS. Adapted from [149]*

isotopes. The start and stop signals for the measurements are produced by thin plastic scintillators, located at the focal points of F3 and F7 [149]. From the TOF the velocity of an ion can be determined if its path through the separator is known. The reconstruction of an ion's path through the separator is also used in the determination of the ion's magnetic rigidity. The path of the ion is reconstructed from measurements of its position and trajectory at each of the focal points of along the second stage. The measurements of the ion's position and trajectory are performed using position-sensitive plate avalanche counters (PPACs) [149]. The measurements from the PPACs are used in combination with experimentally determined third-order ion-optical transfer matrices to determine the exact path taken by ions through the separator. Ions that travel along the central path of the accelerator are defined to have the central $B\rho$ of the setting, which is determined from measurements of the magnetic fields in each of the dipoles using NMR probes. From the central $B\rho$ value, the magnetic rigidities of the other ions can be determined.

The identification methods employed in BigRIPS are also designed to determine if nuclei undergo nuclear reactions as they travel through the separator. Ions that undergo reactions as they pass through the separator are unwanted as the particle identification of these ions can no longer be relied upon to be accurate. Identification of these events is achieved by carrying out two independent measurements of an ion's magnetic rigidity, and thus its A/Q, as it passes through the separator. By determining the A/Q of an ion as it passes from F3 to F5, and then again as it passes from F5 to F7, the two values can be checked for consistency. If there is a change in an ion's A/Q between the two regions, it indicates a possible reaction taking place, and the ion can then be rejected from

the data analysis.

Determination of Z

The determination of an ion's atomic number as it passes through BigRIPS is achieved through energy loss measurements carried out in the separator. The Bethe-Bloch equation, given in Eq. 3.1, shows the energy loss of an ion as it interacts with matter is proportional to both the atomic number and velocity of the ion. The measurements of ions' velocities are achieved through the TOF measurements mentioned previously. Energy loss measurements are carried out at F7 after the TOF has been measured to avoid interfering with the measurement. The energy loss measurements are sometimes performed using a silicon detector telescope, but most commonly a multi-sampling ionisation chamber (MUSIC) [168] is used. The MUSIC detector comprises twelve anodes and thirteen cathodes that are aligned alternatively. The anodes are connected in pairs with each of the six signals being read out individually, providing energy loss measurements across the six regions that make up the anode pairs [168]. The ΔE measurements are combined with the velocity measured from the TOF to determine the relative Z values of ions in the separator.

The particle identification is produced in the form of a plot of Z against A/Q for each of the ions through the separator. At this stage, it is important to verify the particle identification assigned to ions. This is achieved through the use of Germanium detectors, located at F7. By stopping ions at the detector, characteristic γ rays can be identified. Nuclei that have a relatively long-lived isomer, with half-lives on the order of a few μs, are well suited for this and often chosen. The verification of a single nuclide's identification allows all of the surrounding nuclei in the PID to be also verified.

3.5 The ZeroDegree spectrometer

Transportation of the tagged beam, from the focal point at F7 to the experimental area at F11, is carried out by the ZeroDegree spectrometer. The ZeroDegree spectrometer consists of two dipole magnets and six STQs, indicated as D7-D8 and STQ17-22 in Figure 3.4 are of the same design as those used in BigRIPS. The ZeroDegree spectrometer makes up a two bend achromatic system with anti-

mirror symmetry. A telescopic matching section, between F7 and F8, joins the spectrometer to the second stage of BigRIPS. For experiments that are carried out at F11 and F12, the ZeroDegree spectrometer is used to transport and focus the beam onto the experimental setups. In addition to being able to transport the beam, the spectrometer can be used in the study of nuclear reaction measurements with RI beams. When this is done, a target is placed at F8 and surrounded with γ ray detectors. The spectrometer can then be used to identify ions, using the same methods as BigRIPS, in coincidence with γ-rays measured at F8.

Chapter 4

Advanced Implantation Detector Array

Many of the nuclei involved in the r-process have short half-lives, ranging from tens of milliseconds to a few seconds. In order to study the β-decay properties of these short-lived nuclei, they must be measured as soon as they are created. The Advanced Implantation Detector Array (AIDA) is a state of the art silicon semiconductor array designed to study the β-decay properties of these short-lived nuclei at RI beam facilities.

4.1 β-decay spectroscopy measurements

Decay spectroscopy measurements allow the determination of a nuclides's half-life and provide the opportunity to study the excited states of the daughter nucleus. For the case of half-life measurements, a radioactive ion will be identified as it passes through a fragment separator before being implanted into a detector. The measurement of an implant in the detector provides a start time from which the time taken for the subsequent decays to take place can be measured. By combining the time differences between implants of a specific nuclide and its decays, a time distribution is formed which represents the half-life of the implanted nuclide.

The silicon detectors used in AIDA are sensitive to charged particles, and as such are well suited to the measurement of both implanted ions and the β-electrons

emitted in decays. They are also sensitive to any charged particle emission that may accompany a β-decay, such as β-delayed proton emission or β-delayed alpha emission. In order to measure non-charged particle/radiation emission, in coincidence with β-decays, the AIDA setup can be paired with other detector systems such as γ-ray and neutron detectors. By carrying out measurements of these emissions in coincidence with the β-decay measurements in AIDA, it is possible to calculate the probabilities of the various emission types occurring with a decay.

4.1.1 Experimental requirements

When carrying out decay measurements at RI beam facilities, the exotic nuclei are often delivered directly from a fragment separator to the silicon detector. This has the benefit of allowing the study of short half-lives that would otherwise decay between the time they were created and transported to a detector system. The energies of ions leaving the fragment separator are in the range of tens of GeV, most of which will be deposited in the silicon as they are implanted, whereas the subsequent decays of the nuclei will be much lower in energy, on the range of a few keV to several MeV. In order to be sensitive to both the high-energy implant events and the low-energy decays, the system must have a broad dynamic range spanning several orders of magnitude. The short-lifetimes and high energies of the implanted ions also place a second requirement on the system: the electronics used must be able to recover from a multi-GeV implant in time to be sensitive to the subsequent decay.

When using AIDA in conjunction with other detection systems, the emitted radiation measured is likely to be distributed isotropically in 4π around the implantation detectors. To obtain the highest detection efficiency for the radiation emitted, it is necessary to have detectors surrounding the implantation location. The compact design of the AIDA system is therefore crucial in allowing for the maximum solid angle coverage of the other detector systems. In addition to the compact design, the chances of the emitted radiation/particles scattering have been minimised by using a minimal amount of material to surround the detectors.

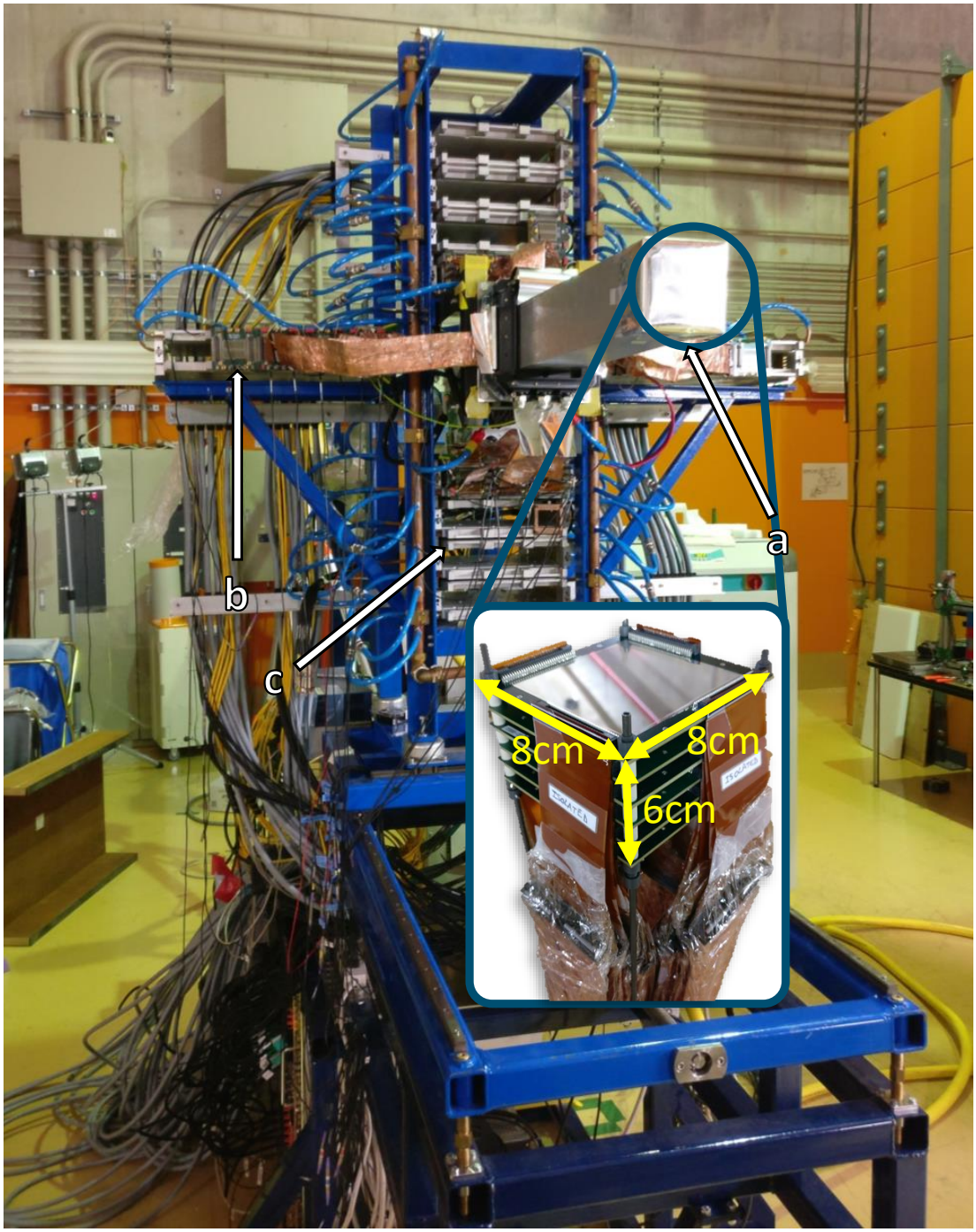

Figure 4.1 *Photograph of the full AIDA assembly. a) Shows the snout, inside which the 6 DSSDs are located (See Section 4.2.1). b) Shows an adapter card, to which the DSSD cabling gets connected (See Section 4.2.4). c) Shows a aluminium water cooling crate, for temperature control of the FEE modules (See Section 4.2.3).*

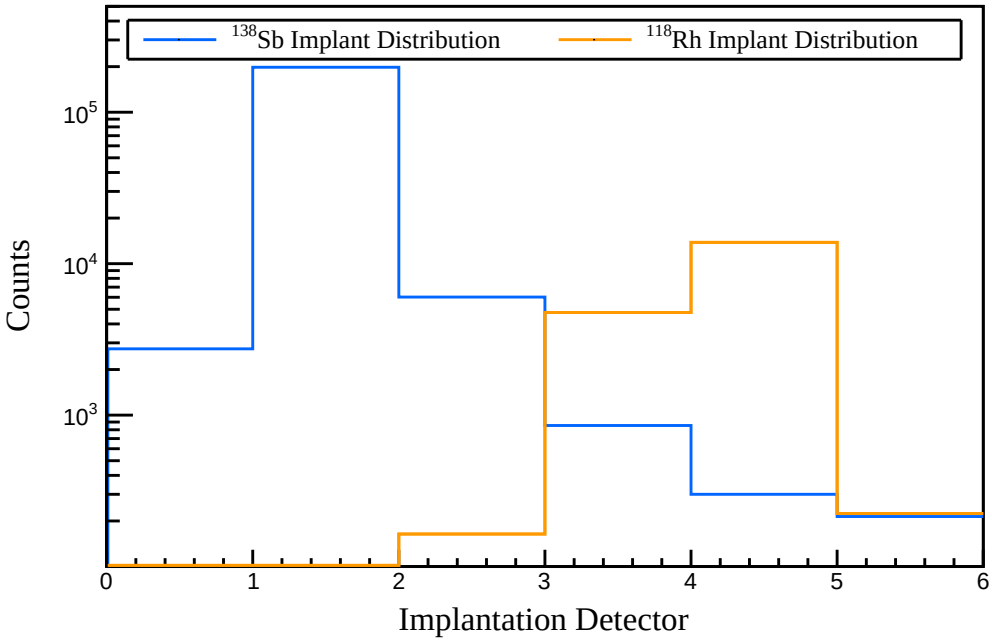

Figure 4.2 *Implantation range of different nuclides in AIDA from experiment RIBF128. High Z elements are stopped nearer to the front of the stack than lower Z elements.*

4.2 Design of the array

4.2.1 Double-sided Silicon Strip Detectors

As the energies of ions leaving the fragment separator can be up to several GeV, detectors with a high stopping power are needed in order to stop the ion within their bulk. Silicon detectors are well suited to this task. The fact that they can be produced in a range of thicknesses provides a flexible amount of stopping power while maintaining a good energy resolution for the study of β-decay properties. The detectors used in AIDA have a nominal thickness of 1 mm, which alone is not enough to stop the multi-GeV implants. However, the detectors can be combined in a stack to allow a flexible amount of stopping power, depending on the experimental requirements. The amount of energy implanted by an ion in a detector is proportional to the ion's atomic number; for RI beams containing multiple elements the stopping power of each detector will vary depending on the nuclide. This allows for the implanted ions to be spread among the layers of detectors, with high Z ions stopping near the front and lower Z ions stopping further back. An example of this is shown in Figure 4.2, where it can be seen that

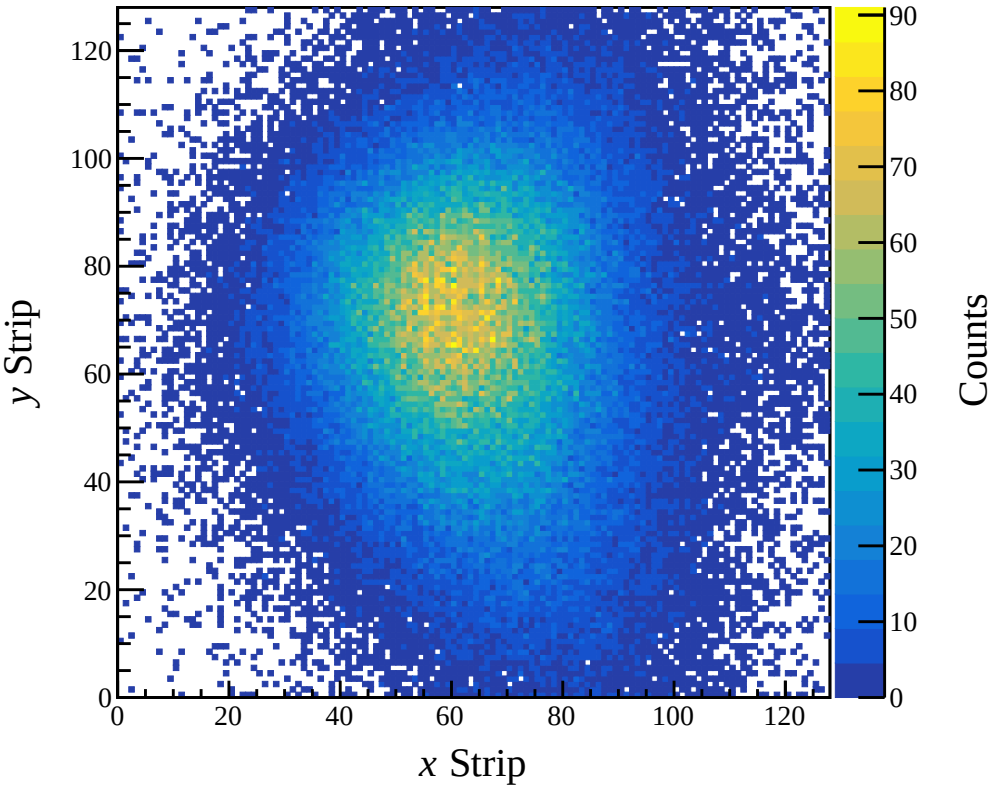

Figure 4.3 *The implantation profile over the surface of a detector in the AIDA detector stack.*

^{138}Sb ($Z = 51$) stops predominantly in the second detector and ^{118}Rh ($Z = 45$) stops across the fourth and fifth detectors.

The silicon detectors are used to perform implant-decay correlations, which are carried out by detecting both the implanted ions and their subsequent decays. Implant and decay events can be clearly distinguished by the different amounts of energy deposited in the silicon, with implants depositing substantial amounts of energy and decays comparatively depositing much smaller amounts. For half-life measurements, the time between the implants and their decays is of interest. It is therefore required to be able to attribute a decay to its parent ion. If the average rate of implantation events in the detector is similar to the rate of decays, it can become challenging to identify which decays are correlated to which implant, limiting the implantation rate. Double-Sided Silicon Strip Detectors (DSSDs) [170, 171] can be used to allow large implantation rates across the detector. Each side of a DSSD is separated into individual strips, arranged orthogonally to one another on each side. In this layout, one side forms the x-plane and one side the y-plane. The positions of implants and decays can be matched to specific locations

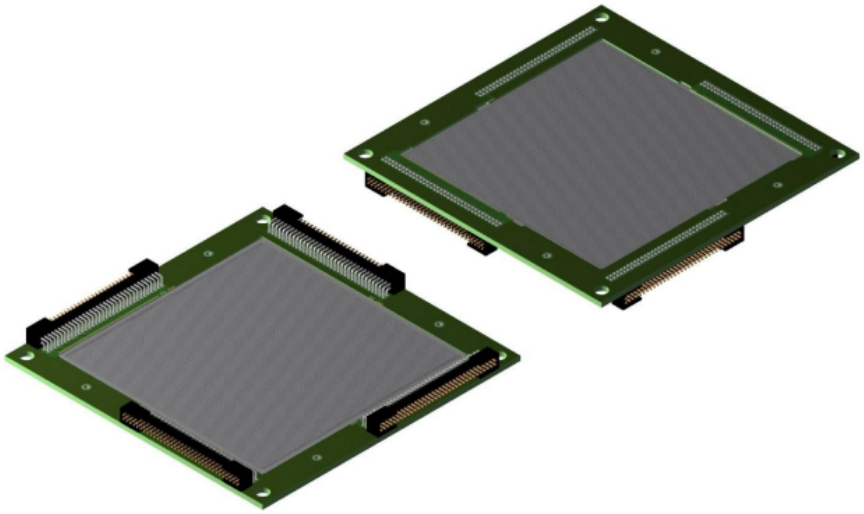

(a)

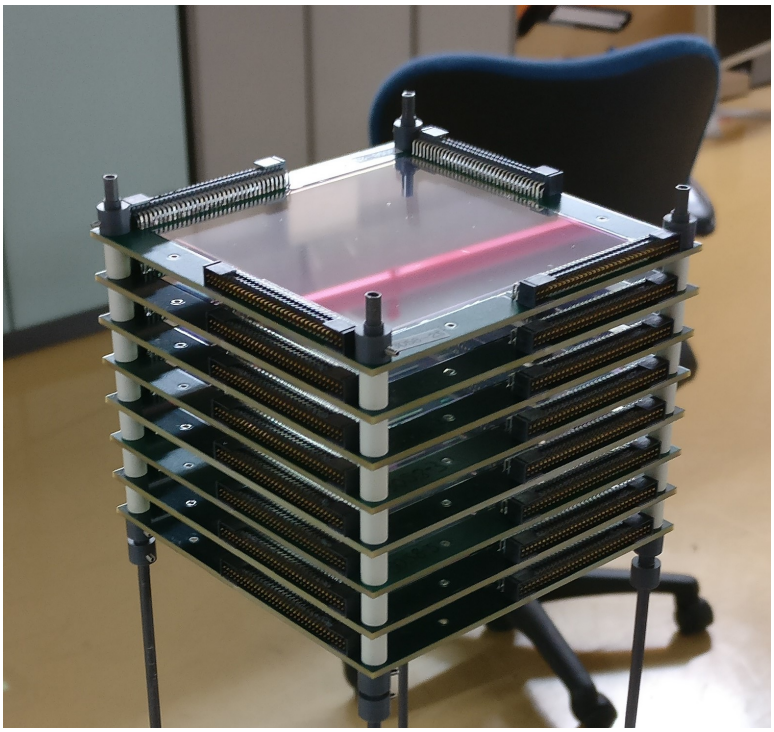

(b)

Figure 4.4 *a) Rendering of a single BB18 DSSD design used in AIDA, produced by Micron Semiconductors Ltd. Image from [169]. b) Photo of an assembled detector stack with no cabling connected.*

on the detector by pairing the front and back events. An example implantation profile across the detector is shown in Figure 4.3, where it can be seen that much of the detector's surface is used. By spreading an implantation profile across the surface of the detector, implants need only be correlated with decays occurring at the same location on the detector. This allows for an increased implantation rate across the detector while still being able to correlate decays to their parent implants.

Micron Semiconductors Ltd produces the detectors used in AIDA. Built upon 6″ wafer technology each detector has an active area of 7.63 cm × 7.63 cm and a nominal thickness of 1 mm. The detectors are segmented into 128 strips per side of the detector, with a strip pitch of 560 μm and an inter-strip separation of 50 μm. Signals from strips are read out individually from the detector over high-density connectors. There are four 68-pin connectors located on the DSSD, one at each corner. Each connector is responsible for the collection of 64 channels of data, with the four remaining pins providing a high-voltage connection to the bias ring and optional grounding connectors. The stack of detectors, as shown in Figure 4.4b, are mounted on titanium rods with a spacing of 10 mm between detector faces. The assembled stack is placed within a protective aluminium "snout", which can be seen labelled "a" in Figure 4.1, that has outer dimensions of 10.6 cm × 10.6 cm.

4.2.2 Application Specific Integrated Circuits (ASICs)

The maximum amount of energy that can be deposited in a single detector corresponds to the amount of energy deposited as a ^{238}U ion is stopped in 1 mm of silicon, which is 17 GeV. For lighter ions, this energy is less with ions such as ^{120}Sn depositing 7 GeV max per detector. The upper limit of the energy deposition by uranium sets the full-scale energy range required to ensure that all energies of implants are recorded during an experiment. As the energy deposited per implant is much greater than the energy expected to occur from decays, which can range from 25 keV to 20 MeV, a scale where the minimum energy expected is almost one-millionth the maximum energy deposited is needed. To provide a good energy resolution across the broad range of expected energies presents a challenge in the electronic handling of signals within AIDA.

In order to meet these requirements, a 16-channel Application Specific Integrated Circuit (ASIC) was designed to handle the readout of the detectors. The ASIC

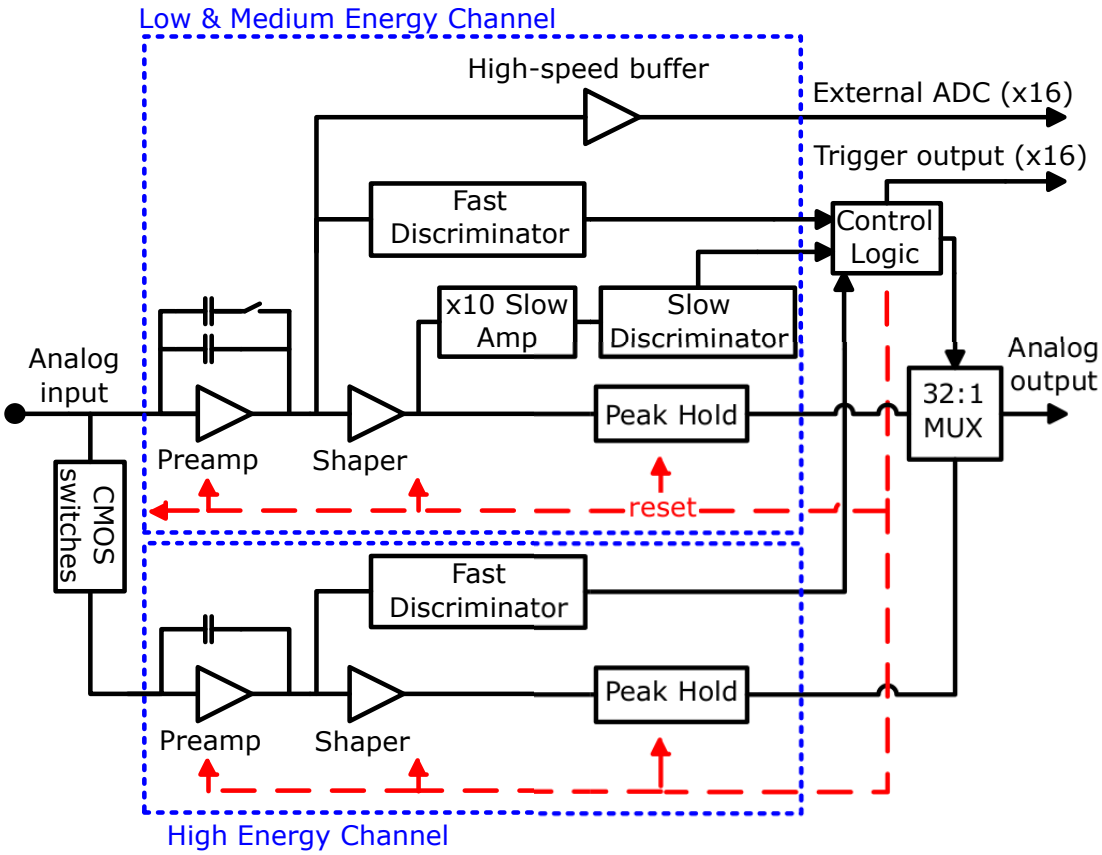

Figure 4.5 *Simplified block diagram of the ASIC circuitry. Adapted from [172].*

has been optimised to achieve a high dynamic range, with fast recovery from implant signals, excellent linearity and good noise performance [172]. One of the characteristic features of the AIDA ASIC is in its front end, where each of the sixteen input channels has two dedicated preamplifiers. The first of these preamplifiers has a selectable gain for the processing of low/medium energy signals ($<$ 20MeV/$<$ 1 GeV), and is directly connected to the channel input. The second preamplifier has much lower gain and is for the processing of implant signals ($<$ 20 GeV). Connection to the input node is achieved via a bypass link. The bypass link ensures that for low-energy signals, only the low-energy/high-gain preamplifier is connected to the channel input. However, when a high-energy signal is deposited in the channel, the high-gain preamplifier saturates, causing a rapid change of the input node voltage. The voltage fluctuation is sensed by a comparator that operates a CMOS bypass switch, providing a low impedance path for the input charge into the high-energy/low-gain preamplifier. Once the charge has been integrated with the high-energy/low-gain preamplifier, the path is disconnected by the CMOS bypass switch, and a reset signal is sent to the low-energy/high-gain preamplifier. This speeds up recovery from the implant

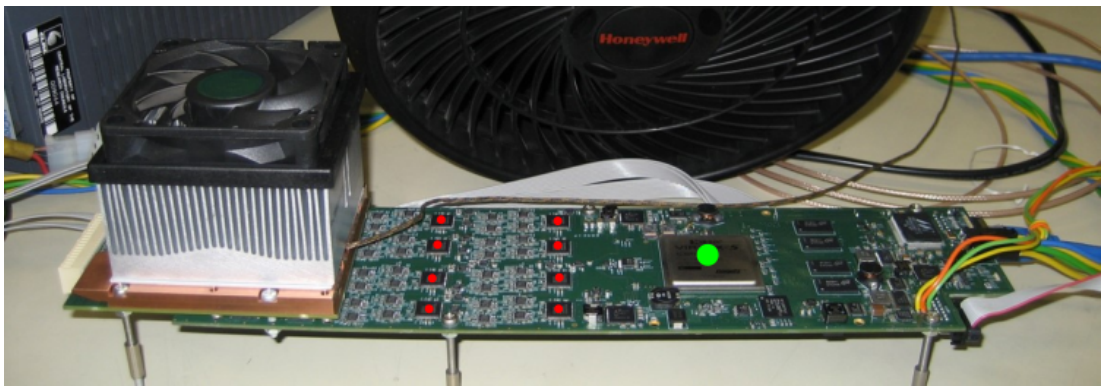

Figure 4.6 *A photograph of a prototype FEE64 module. The green dot is the location of the Field Programmable Gate Array. Each of the eight red dots is a 14-bit, eight-channel* 50×10^6 *samples per second ADCs. The ASICs are located on a mezzanine board which covered by a copper heat sink with aluminium cooling fins on the left-hand side of the board.*

signal and allows the low-energy channel to be sensitive to decays within a few microseconds of an implant event. This allows for fast implant-decay correlations for short-lived nuclei.

A simplified block diagram of the ASIC design is shown in Figure 4.5. Here it is seen that for both high and low gain channels after the preamplifier the signals are passed into a CR-RC filter shaper before being fed into a peak-hold. The shaper has a selectable shaping time that ranges from 0.5 μs to 8 μs in 16 steps, allowing the shaping time to be tailored to the experimental demands and the quality of the detectors as they deteriorate through radiation damage. Both the high and low energy peak-hold circuits are connected to a 32:1 multiplexer which links the peak-hold to the analogue output of the ASIC. The multiplexer has a readout time of 2μs meaning that adjacent channels will have a 2 μs increment in the times at which they are recorded.

4.2.3 Front End Electronics (FEE) Modules

The electronics that handle the data output of the AIDA ASIC are mounted on a module that is known as the Front End Electronics (FEE) module. Each FEE64 card is responsible for handling the signals from 64 channels of instrumentation, half the number of strips per side of the detector. The FEE64 modules contain all of the electronics used in the processing of the signals and act as their own independent data acquisition systems.

Mounted to the front of each FEE64 card is a small mezzanine board, on which four ASICs are located, providing inputs for 64 channels of instrumentation. On the FEE64 card, each ASIC module has its own dedicated 16 bit ADC, responsible for its multiplexed readout. In addition to this, there are eight 14-bit eight-channel 50×10^6 samples per second ADCs for the readout of the low energy channel preamplifiers. Between the ADCs and the analogue outputs of the ASICs are groups of op-amps (operational amplifiers), which work to process the signal such that the voltages and impedances of the ASIC analogue outputs match the FADC inputs. A photograph of a prototype FEE card is shown in Figure 4.6 though the mezzanine board is below a copper heat sink and fan.

The data processing, the building of events, and the control of the FEE64 is handled by a Field Programmable Gate Array (FPGA). Running custom firmware, developed by STFC Daresbury Laboratory (STFC-DL), each FEE64 module acts as its own independent data acquisition system. The remainder of the card is used for the input and output of data, and power for the FEE64. The delivery of external clock, reset and synchronisation signals are provided to the FEE64 by a mini-HDMI (High-Definition Multimedia Interface) cable connection. Power is delivered to the FEE64 over a six-pin connector. Data is output, as a data stream, from the FEE64 over a gigabit Ethernet connection. Finally, a JTAG connection is included for optional monitoring of the FEE64 system console through an external device.

FEE64 cards are sandwiched in pairs between two aluminium heat sinks, shown in Figure 4.7, that cover the length of the FEE card. The mezzanine boards are mounted and have a separate copper heat sink for each card. The fully assembled FEE64 modules, shown in Figure 4.7b, are placed into aluminium crates housed in the AIDA support frame. Heat is dissipated from the heat-sinks via a water-cooling loop running through the aluminium crates, that is maintained at a constant 20°C by a chiller.

4.2.4 Adapter board

Adapter boards act as an interface between the detector cabling and the FEE64 modules. In addition to connecting the detector's cabling to the electronics, they provide a useful location for the placement of grounding, bias and test input connections to the system. Each adapter board supports up to two detectors being connected to it via Kapton cables and features 2x ERNI connectors (J2

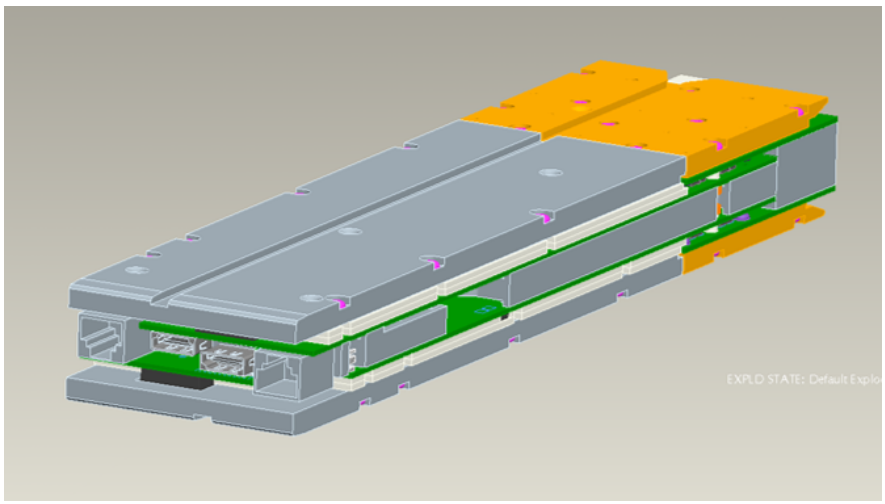

(a)

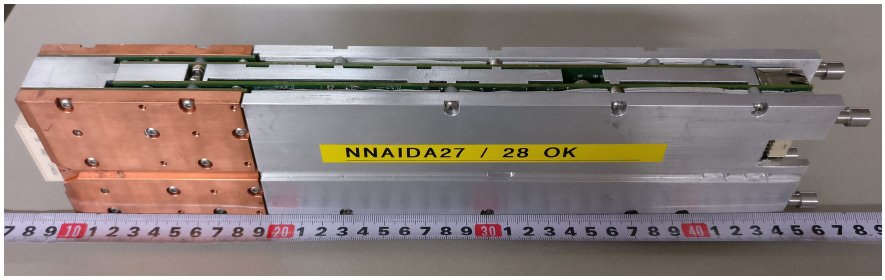

(b)

Figure 4.7 *Rendering and photograph of the complete FEE64 assembly.*

and J4 on Figure 4.8) on the back, onto which the FEE64 cards are connected in pairs. Biasing can be applied to detectors via two LEMO connectors (J9 and J10), which can be seen in the lower left and lower right of the adapter boards. Two additional LEMO connectors (J7 and J8) are found in the lower middle of the board, which allows for the input and output of a test signal for easy daisy-chaining between adapter boards.

Grounding between the FEE64 assembly and the adapter boards is achieved through the use of gold plated through-holes, located in the four corners of the card, that are used to house the bolts securing the board to the FEE. An additional ground connection is located in the top middle of the board, allowing grounding connections to be made to other components such as DSSD cable sleeves. Early revisions of the board provided this ground via a plated through-hole with a bolt through it. In later revisions, this has been replaced with a LEMO connector. Jumper pins (LK-1 through LK-6) provide optional ground connections between the PCB and DSSD and also the front and back field plates.

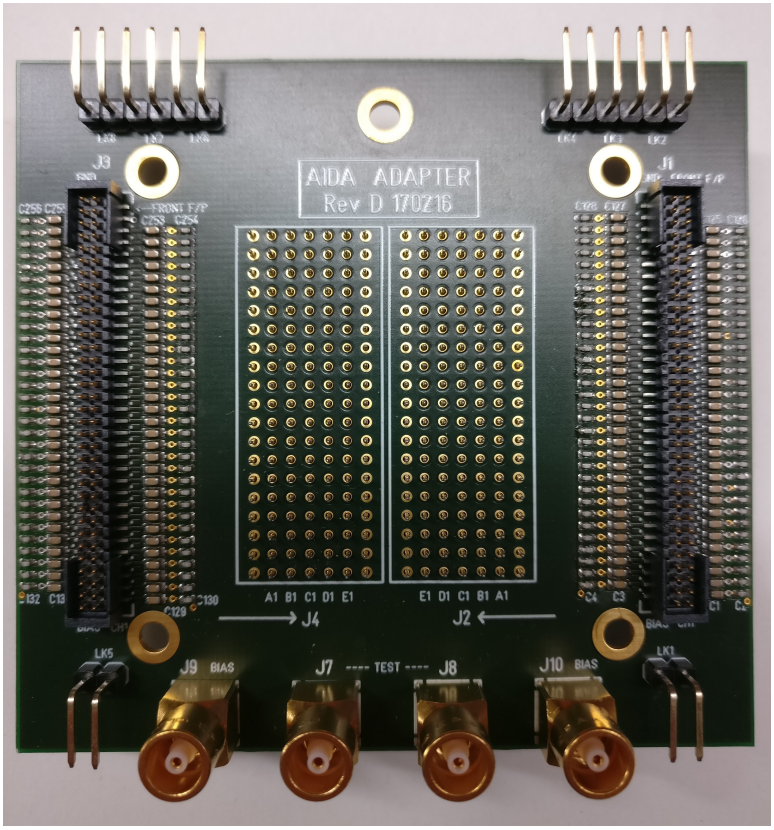

Figure 4.8 *Photograph of an AIDA adapter board from Revision D*

4.2.5 Timestamp distribution and data handling

As each FEE64 card acts as an independent DAQ-system, synchronicity must be maintained between all of the FEE64 for the duration of the experiment. This ensures that when the datastreams of the various FEE64 cards are merged, time ordering of the data is maintained and correlations can be made between the various FEE64 cards. This is important as it allows the localisation of events across the detector. To ensure this synchronicity is maintained, MACB modules designed by STFC-DL are used to distribute a common clock between all of the FEE64s. This clock can either be a 50 MHz clock generated by a MACB module in stand-alone operation or an external clock provided to the MACB module.

Each MACB module can be connected up to a maximum of four FEE64 modules. When distributing timestamps to more than four FEE64 modules, a hierarchical system of MACB modules must be used. Each MACB module has on it 5 HDMI Type-C ports numbered 0 through 4. The first port, 0, connects to the next level up in the hierarchy and the following four connect to either FEE64 cards or MACB modules lower down in the hierarchy. The number of levels in the

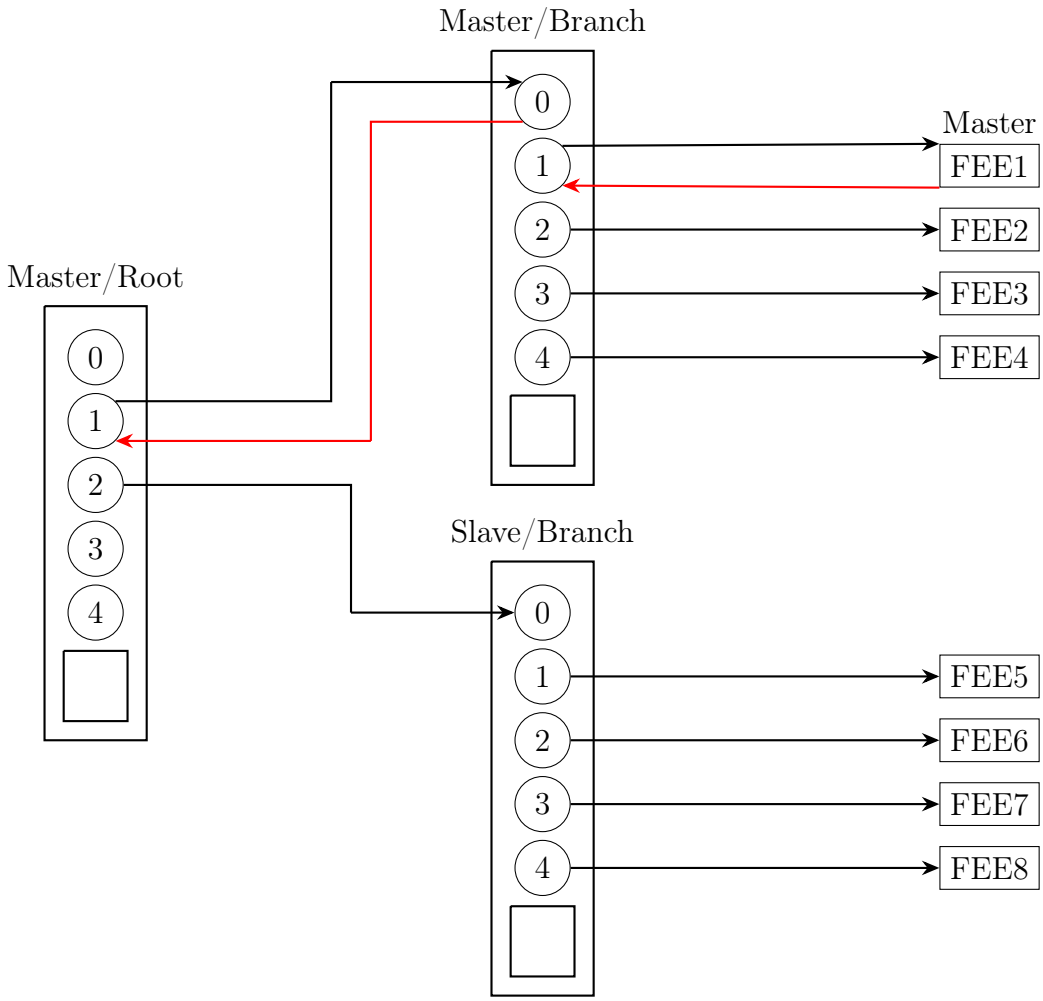

Figure 4.9 *Diagram showing the hierarchical distribution of timestamps between FEEs using the MACB modules*

hierarchy can be extended multiple times to allow for large amounts of FEE64 cards to be connected *i.e.* one level for up to four cards, two levels for up to sixteen cards, three levels for up to sixty-four cards *etc.*. The cabling between MACB modules and the FEE64 modules will produce small amounts of delay in the signal. It is, therefore, necessary that all FEE64 modules in the system are on the same level of the hierarchy, such that any signal delay is the same for all FEE64. The FEE64 modules will then always be connected to MACB modules in the lowest level of the hierarchy.

Depending on its role and position in the hierarchy, a MACB can be configured in several different ways with different terms used to describe them. To explain the terms, it is useful to do so in the context of a hierarchy of two levels involving 5 MACB modules and 16 FEE64 cards. The module in the top-level of the hierarchy is known as the root module; it is responsible for distributing the clock, whether

from its own internal clock or an externally connected one. HDMI connectors 1-4 will be connected to connector 0 on the next level of MACB modules; as these modules are not the top-level, they are known as branch connections. Branch connections will receive and pass on all clock and sync signals that they receive.

When multiple FEE64 cards are being used, one will be defined as the master card. The master FEE64 card will generate sync pulses, used to maintain synchronicity between the FEE64, which are sent out via the Sync return line. The Sync pulse will be received by the master MACB module which will then redistribute it to all of the FEE64, the master FEE64 will then receive the sync pulse again at the same time as all other cards, via the Sync Line. The Master FEE64 is also responsible for generating the Correlation Scaler, a 25 MHz clock that can be externally distributed, allowing AIDA to be synchronised with external systems. Requests for the correlation scaler are made through the Master/Root MACB module and handled by the Master FEE64. The master FEE64 will always be connected to port 1 on a MACB module, and if the MACB module is not the top-level of the hierarchy all the MACB modules along the chain will be connected to port 1 of the next level up branch. All MACB modules in this chain are known as master modules. If a MACB has no connection to the master FEE64, it is said to be operating as a slave. In this mode, all four HDMI output ports on the MACB behave the same in that they receive sync pulses but never generate them and only receive the FEE64 clock.

4.2.6 Hardware control and data merging

Hardware control for each of the FEE64s is carried out over a gigabit network connection. While each FEE64 can be individually controlled via telnet/RSH (Remote Shell) protocols; for ease of use, a GUI (Graphical User Interface) has been developed by STFC-DL for interacting with all FEE64s at once. The GUI itself is the front end of a server program, running on the embedded CPU of the FEE64 FPGA, based on the MIDAS data acquisition system [173]. Through the GUI, the user is able to adjust the hardware parameters of the ASICs, view live histograms from each of the FEE64s and start and stop data acquisition.

A separate server, called the TapeServer, is used for the writing of the data to disk. One of the primary roles of this server is taking the individual data streams, from each of the FEE64s, and merging them into one single data stream that can be written to file. The merging of the data is kept synchronised by aligning sync

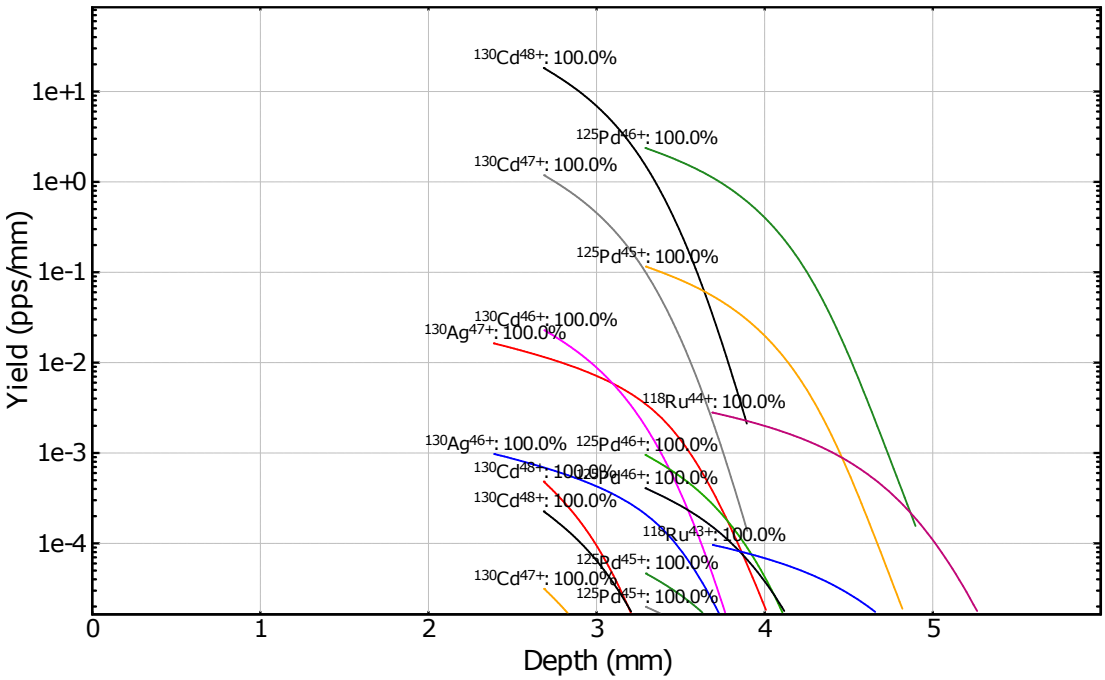

Figure 4.10 *Depth calculations performed in Lise++ of ions, expected in experiment RIBF128, that will be implanted into the silicon detector stack. The penetration depth shown here is with the addition of 6mm of aluminium degrader placed before AIDA at F11.*

statements in each data stream, which are generated when a FEE64 receives a sync pulse. The time period between sync pulses is 2.62144 ms (2^{18} ns). Having the sync items repeat at such a short timescale ensures that even with low data rates synchronicity between the data streams is maintained. The TapeServer runs on a high-performance workstation operating on Scientific Linux 6. The high core count of the CPU inside the workstation ensures there is enough processing power not to cause bottlenecks in the writing of data to file. To ensure a high-speed connection between the FEEs and the workstation gigabit Ethernet connections are used between the FEE64s and the workstation.

4.3 AIDA configuration for experiment RIBF128

Before running the experiment, Lise++ simulations were carried out to determine the expected rates of fragments at F11, the last focal point of the separator before AIDA. Another outcome of these simulations is that the energy of the ions as they leave F11 is calculated. From the simulations, it was decided that for the experiment, six silicon detectors would be used in the AIDA detector stack. This

is based on the range distribution of ions in AIDA, calculated using Lise++ and is shown in Figure 4.10. The shape of the stopping distribution is dependent on the energy distribution of the implanted ions, which is determined by the setting and acceptance of the fragment separator. In this experiment the slits of the fragment separator were set to remove low-energy ions from the beam, which resulted in the implanted ions having an energy distribution that resembles a tail pulse, with a steep rise on the low-energy side of the peak and a long decay beyond the peak to higher energies. This energy distribution is reflected in the stopping range of the ions, where a sharp peak is seen in the range distribution as ions in the peak stop, with a decreasing distribution to deeper implantation depths/higher energies. As the low-energy ions are cut before reaching the detector stack, few ions stop in the first couple of mm of the detector stack and fragments are implanted across the central four detectors. The first detector can then be used as a confirmation of an implant and the last detector to be used as a veto, for ions that are of high enough energy to traverse the stack without stopping.

In addition to the stopping power of the detectors, additional aluminium degraders can be used to fine-tune the implantation depth of the ions. By using aluminium degraders (less than 1 mm thick), the depth over which implanted ions penetrate can be carefully controlled. This is particularly useful when the Lise++ simulations show that most of the ions will be stopping in a single detector. By adding in a degrader of 0.5 mm it is possible to spread the implantation of ions over two detectors which lowers the beta rate in the individual stopping detectors or centre the implantation profile of an individual ion in a single detector. For the initial running of the experiment, it was decided that an initial degrader thickness of 6 mm would be used. As can be seen in Figure 4.10 this thickness results in the central nuclide of ^{130}Ag being deposited in the centre of the stack, while maintaining enough stopping power to ensure that even the lighter nuclides, such as ^{118}Ru, are stopped in the final detector. If further fine-tuning was needed during the experiment, additional degraders were located on motor arms, allowing degraders to be added or removed from the beam path remotely without having to interrupt the beam.

Light ions that are produced by the fragmentation of ^{238}U will often accompany the beam through to F11 and will be incident on the detector stack. These ions will typically be elements such as carbon and oxygen, which when travelling through the detector stack will not deposit enough energy to trigger an implant event due to their low Z and large energies. Instead, these ions will deposit

energies in the range of 3-20 MeV, triggering as events in the low energy ADCs as they pass through the detector stack. In order to determine when these events occur, a scintillator detector is placed behind the AIDA detectors which can be used as a veto for these high energy ions passing through the detector stack.

The settings used for the ASICs during the experiment are defined in a settings folder on the server. Almost all of the ASIC settings are kept the same between experiments, but the two that are most likely to be changed are the shaping time and threshold of the low-energy channels. The shaping time of the AIDA ASICs was chosen to be 8 μs. This value was chosen based on previous experience from commissioning experiments that showed an 8 μs shaping time gave the best noise performance. The ASIC thresholds used for the low-energy channels in the experiment were set to values that corresponded to energies of around 100 keV. This value was chosen as it provides a good β-detection efficiency while not saturating the data rate with detector noise.

Chapter 5

Neutron Detection with the BRIKEN Array

The energies of neutrons released via β-delayed neutron emission can range from hundreds of keV to several MeV. To measure the percentage of β-decays that result in the emission of a neutron requires a neutron detector with a high, constant neutron detection efficiency over this broad energy range. This chapter focuses on the design of the BRIKEN neutron detector array, which was carried out by members of the BRIKEN collaboration and detailed in the paper Tarifeño *et al.* [174].

5.1 Neutron detection for β-delayed neutron measurements

As neutrons are neutral particles, their interactions with matter are not governed by Coulombic interactions, and as such, they do not produce primary ionisation as they pass through matter. Consequently, neutrons are not detected directly and are instead detected through indirect methods. Often this is done through the use of a nuclear reaction involving the neutron, which produces a charged particle that can be directly detected.

5.1.1 Detection of neutrons through the ^{3}He(n,p)^{3}H reaction

The reaction of ^{3}He(n,p)^{3}H is often used as an indirect method of detecting neutrons. The positive Q-value of 0.764 MeV allows the reaction to take place with no minimum threshold energy, allowing sensitivity to very low-energy neutrons. The Q-value is released during the reaction and shared between the emitted proton and triton, both of which can be directly detected. Another reaction that is sometimes used is ^{10}B(n,α)^{7}Li; it is less favoured than that of ^{3}He for multiple reasons. For thermal neutrons the conversion cross section for ^{3}He is large at 5333 barn, whereas ^{10}B has a conversion cross section of 3840 barn, just 75% of the value for ^{3}He [75]. Secondly, ^{3}He can be used at a much higher pressure, up to 1500 kPa, whereas the maximum pressure obtainable for ^{10}B is 200 kPa [175], allowing for a much larger density of atoms. Both of these factors together lead to ^{3}He detectors having a much greater detection efficiency of thermal neutrons than similarly sized ^{10}B detectors. For both the conversion of neutrons by ^{3}He and by ^{10}B, the cross section drops off with $E^{-\frac{1}{2}}$ dependence [176]. Therefore, while providing high conversion efficiencies for low-energy neutrons, the efficiency quickly drops with increasing neutron energy. To have high conversion efficiencies for high-energy neutrons, it is then necessary to lower their energies through the use of moderators.

As ^{3}He is a noble gas it cannot be formed into a solid compound and as such is used as a gas. Detectors conventionally achieve this by using ^{3}He as the fill gas in a proportional counter. As the energy of the neutron is likely negligible, owing to the low cross section at higher energies, the maximum energy deposition seen in a counter will be equal to the Q-value of the reaction. If both reaction products are detected, the full Q-value will be detected. However, one of the two products may not be detected, allowing for a range in energies to be deposited. If the size of the chamber is short in comparison to the range of the proton or triton, some events will not deposit their full energy in the gas. When this happens, the particle will strike the wall of the chamber, producing a small pulse of charge. This is known as the wall effect and in smaller detectors can have a significant effect [177].

5.1.2 Experimental requirements

When carrying out measurements of β-delayed neutron probabilities a common method of extracting the P_{1n} is to compare the number of observed neutrons with the number of observed β-decays. The P_{1n} value can then be written as

$$P_{1n} = \frac{\bar{\varepsilon}_\beta}{\bar{\varepsilon}_n} \frac{N_n}{N_\beta} \tag{5.1}$$

where $\bar{\varepsilon}_\beta$ and $\bar{\varepsilon}_n$ are β and neutron-detection efficiencies that are averaged over all beta and neutron energies respectively [174].

This simple method only holds for cases where the neutron background is low. When the neutron background rate becomes comparable to or greater than the beta-delayed neutron rate, it becomes necessary to observe neutrons in coincidence with β-decays. In this case Eq. 5.1 becomes

$$P_{1n} = \frac{\bar{\varepsilon}_\beta}{\bar{\varepsilon}_n \bar{\varepsilon}'_\beta} \frac{N_{\beta n}}{N_\beta} \tag{5.2}$$

where $\bar{\varepsilon}'_\beta$ is the β detection efficiency averaged only over the neutron unbound energies and $N_{\beta n}$ is the number of neutrons observed in coincidence with a β-decay. Here the number of neutrons observed accompanying a β depends not only on the neutron detection efficiency but also the β-detection efficiency.

As the neutron energy distributions for most of the nuclei are *a priori* unknown, it is desirable to have a flat, or constant, neutron detection efficiency across their expected energy range. A constant neutron detection efficiency can then be used when extracting the P_{1n} value, allowing the application of Eq. 5.2 in its simple form without needing an energy dependence. β-delayed neutrons can be released with energies spanning a range up to the $Q_{\beta n}$ of the nuclei studied. This can range from 100s of keV to several MeV for the most exotic of nuclei, a range over which it can be challenging to maintain a flat efficiency.

The total detection efficiency of a system does not just depend on a detector's ability to detect incident neutrons, but also on the geometry of the detectors. Ideally, a system would be made up with a solid angle covering all of 4π, such that particles released in any direction will be incident on a detector. However, this is unfeasible as gaps must be left in the system for entry of the beam and other detector systems. These openings place a maximum limit on the achievable detection efficiency.

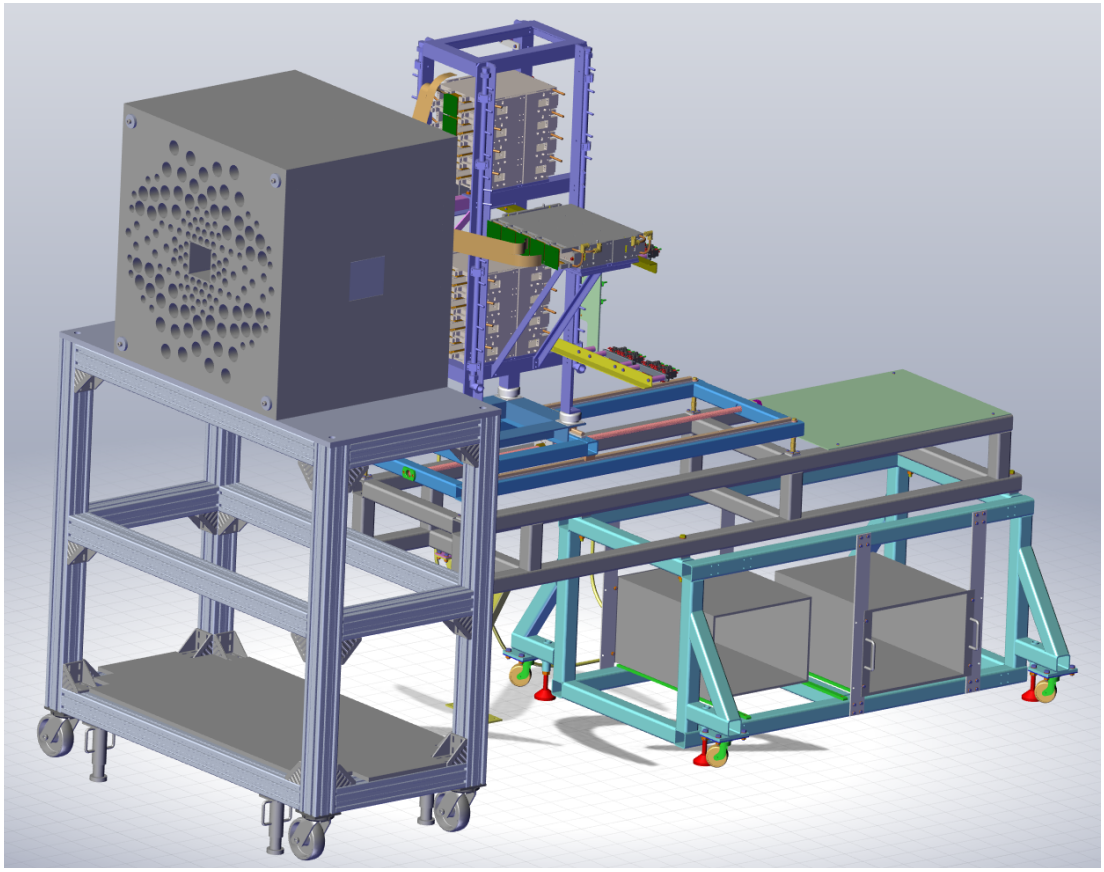

Figure 5.1 *Technical drawing of the combined BRIKEN and AIDA setup, showing the layout of cutouts in the HDPE moderator for the ^{3}He counters and the central cutout for the beam/AIDA. On the sides cutouts can be seen which will house the Clover detectors.*

5.2 BRIKEN neutron counter array

BRIKEN is an international collaboration formed with the aim of studying β-delayed neutrons at RIKEN (BRIKEN). Neutron detection is carried out using a large number of ^{3}He counters, housed inside a large High-Density Polyethylene (HDPE) moderator. The β-delayed neutrons are detected in coincidence with β-decays in the AIDA detector system.

5.2.1 Optimisation of design

The ^{3}He tubes used in the BRIKEN neutron detector array come from different parts of the collaboration. This has meant a number of different tube types have been used, with different dimensions and pressures of ^{3}He inside. A summary of

Table 5.1 *Parameters of the ^{3}He tubes available for BRIKEN adapted from [174]*

Manufacturer	Type	Pressure [atm]	Diameter [cm]	Length [cm]	Active Length [cm]	Past Setup	Number of Counters
LND Inc.	B	8	2.54	67.6	60.0	BELEN [178–181]	42
	R	10					10
GE Reuter Stokes	I	10	2.54	74.6	60.96	3Hen [182, 183]	17
	K	10	5.08	69.79	60.96		64
	E	5	2.54	39.63	30.0		26
—	N	4	3.0	60	50.0	Flerov [184]	20
Total number of counters for the BRIKEN detector							**179**

the properties of the tubes is provided in Table 5.1. When planning the layout of counters in BRIKEN, the properties of each counter must be taken into account, as the efficiencies of counters will vary with their pressure and dimensions.

In addition to the ^{3}He counters, two Clover detectors were made available to the collaboration. Each detector comprises four High Purity Germanium (HPGe) crystals, which can be used to measure γ-rays in coincidence with observed β-decays and neutrons. By having gamma measurements in coincidence with the decays, gamma-ray spectroscopy physics is possible [182].

The HDPE moderator has outer dimensions of $90 \times 90 \times 90$ cm^3 and is made up of HDPE slices, each 5cm thick. The moderator has cutouts along the beam axis which allow the insertion of AIDA, enabling the double-sided silicon strip detectors to be located at the centre of the moderator. The cutout is just larger than the outer dimensions of the AIDA detector housing. By minimising this distance, losses in geometric efficiency are limited.

The design of an array with such a large number of counters of different sizes and properties is a time-consuming task. Extensive Monte-Carlo (MC) studies were carried out by Tarifeño *et al.* [174] to aid in the design process. The results of these MC studies informed the design process of the BRIKEN neutron detector array. To carry out the MC studies GEANT4 [185] simulations were used. The simulations made use of passive and active volumes available in GEANT4 to represent the parts of the BRIKEN array. The customisation of GEANT4 allowed the moderator density to be 0.95 g/cm^3 and the dimensions and properties of the

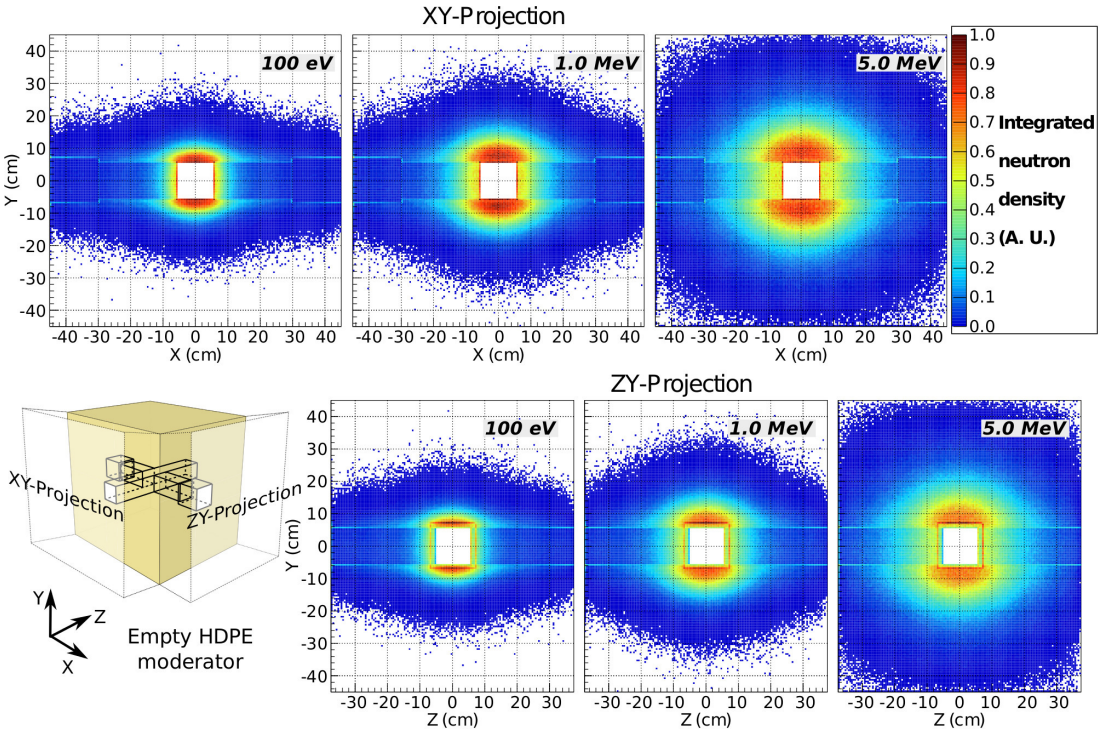

Figure 5.2 *Outcome of a MC simulation showing the positions of neutrons within the HDPE volume at the point they are moderated to below 1 eV. Adapted from [174]*

counters to be those provided by their manufacturers.

Neutrons are moderated as they pass through the HDPE in a series of scattering reactions. It is important to understand the positions of the neutrons within the moderator at the point that their energy has reduced to an amount such that the ^{3}He cross section is large; this informs where counters should be placed for the highest neutron detection efficiency. In order to do this, the particle tracking functionality of GEANT4 was used. By setting up a simulation with an empty moderator; neutrons of discrete energies were then tracked from the centre and through the moderator until they either escaped or were captured via (n,γ) reactions with nuclei in the moderator. Moderated neutron energies of less than 1 eV were then computed, and a neutron density plot throughout the moderator was produced, see Figure 5.2.

The neutron density plots show that along the central beam axis, there is a region of zero neutron density; this corresponds to the cutouts for AIDA and additional γ-ray detectors. Neutrons can escape without moderation through these cutouts, having the effect of reducing the symmetry of the neutron density. In both the XY-projection and the ZY-projection an oval distribution is seen. A wider

distribution of neutrons is seen in the X and Z planes than in the Y plane. For neutrons at 100 eV, the neutron density is shown to be at its peak up to around 4 cm from the edge of the AIDA entrance holes whereas at 5.0 MeV this region is shown to extend out to around 15 cm from the edge. The regions beyond this peak area drop off to an almost constant density. As a result of this, counters placed near the central holes will be necessary to reach a high neutron efficiency, but counters are also needed further away to maintain a flat efficiency out to 5.0 MeV.

Based on the outcome of the simulations, the following was assumed for the parametrisation of the counter array distribution [174]:

1. All counters will be placed along the Z-axis (Parallel to the AIDA axis)
2. The counters will be distributed in an oval shape around the AIDA detector stack
3. Counters will be closely packed around the AIDA snout hole, with the 2.54 cm diameter counters making up the innermost rings and the 5.08 cm diameter counters making up the outer rings. This has the added benefit that the sudden failure on an inner ring has a minimal cost on the overall efficiency.

With a set of general assumptions about how the counters should be arranged throughout, the moderator simulations were set up with the counters in place to test the various configurations. As a way of comparing the different layouts to one another, a set of parameters of merit were defined:

1. Average neutron detection efficiency
2. Efficiency flatness as a function of reduced number of geometric variables.

The simulations were carried out by defining a source of monoenergetic neutrons at the centre of the moderator, active volumes of ^{3}He were placed around the moderator in which the moderated neutrons could be converted. A detected neutron was defined to be a deposition of between 150 keV and 900 keV, a typical energy range for a ^{3}He counter. The neutron detection efficiency of a given detector layout could then be taken to be the number of neutrons observed as a fraction of the number of neutrons emitted. By repeating this process for multiple

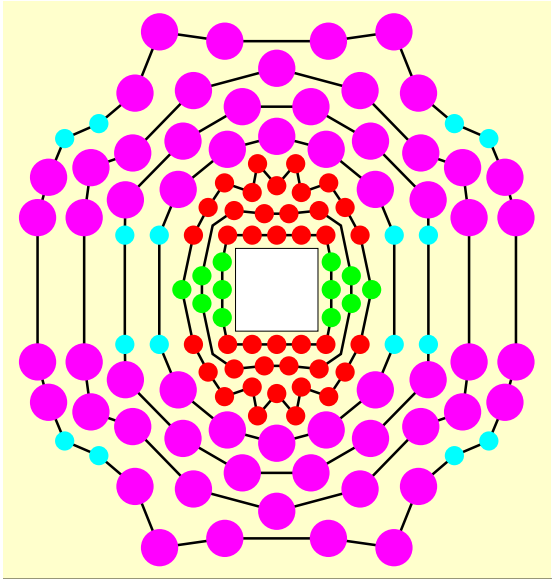

Figure 5.3 *Schematic layout of the ^{3}He counters in the HDPE moderator surrounding the AIDA hole. The colour indicates the counter type: Small red dots - Type B; Small blue dots - Type I; Large pink dots - Type K; Small green dots - Type E. Properties of tubes are shown in Table 5.1. Adapted from [186]*

neutron energies, a measure of the efficiency as a function of neutron energy could be gained.

5.2.2 Hybrid BRIKEN array

A hybrid design using both neutron and γ-ray detectors was settled upon for use in experiments, with the two γ-ray detectors placed perpendicular to the beam in alignment with the centre of the AIDA detector stack. The small loss in neutron efficiency over a system with no γ-ray detectors, $\sim$7% at 1 MeV [174], is outweighed by the ability to perform simultaneous γ-ray spectroscopy measurements such as the identification of short-lived isomeric states in nuclei [187]. The γ-ray detectors used were Clover-detectors which comprise four germanium crystals per detector that can be individually read out [188].

With the addition of the Clover detectors, the choice of counter that can be used around the Clover is limited to those counters short enough that they can be inserted fully and not interfere with the placement or operation of the Clover. Type E counters are used as their short length allows them to be inserted from the front and back of the moderator, either side of the Clover. The finalised counter distribution for the hybrid model can be seen in Figure 5.3.

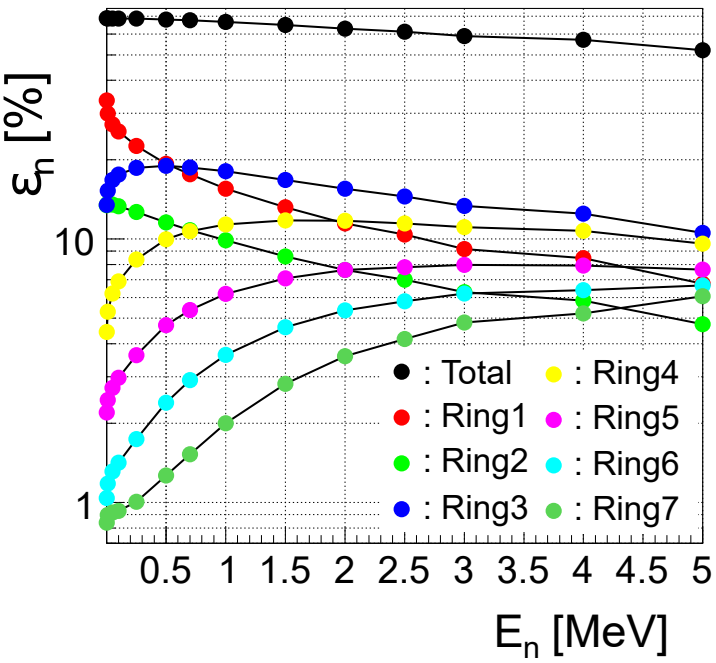

Figure 5.4 *Total efficiency and the efficiency of each ring of ^{3}He counters as a function of energy. With 1 being the innermost and 7 being the outermost, in the hybrid detector array setup. Adapted from [186]*

The finalised design has an average neutron detection efficiency of 66.8% for single neutrons up to 5 MeV in energy. The total efficiency as a function of energy is shown in Figure 5.4, where the contributions of each counter ring are also shown. At lower neutron energies the innermost rings are shown to be responsible for contributing most to the neutron efficiency of the array with the innermost ring having an efficiency of around 30%. Whereas with increasing neutron energies, the efficiency of the outer rings increases and the inner rings decrease in efficiency as the neutrons penetrate the moderator further before being detected in the outer rings.

Chapter 6

Data Analysis

In order to extract the half-lives and β-delayed neutron emission probabilities of nuclei, the production of individual decay curves for each of the nuclides is required. Production of the decay curves requires that the data from the three detector systems are synchronised and the events correlated in time. The produced decay curves can then be fit, and the values of interest extracted from the fits. This chapter discusses the production of the decay curves and the fitting method used to obtain the final results.

6.1 AIDASort - Sorting the AIDA raw data

Traditional DAQs, used in nuclear physics experiments, run on a trigger which signals the start of data taking across all channels. This trigger is usually generated when a signal in a channel is recorded above a defined threshold. An event is then created when the information in all channels is recorded at the same time. While this method is useful for allowing correlations between multiple channels to be easily formed, it has the effect of increasing the dead time as the entire system must wait for the event window (data taking) to end before it can trigger again.

A method to reduce the dead time of the system, first introduced by the Gamma Recoil Electron Alpha Tagging (GREAT) spectrometer, is to use what is known as a triggerless DAQ [189]. In this mode of operation rather than a global trigger signalling data acquisition to take place across all channels, each ADC is instead

self-triggered. This reduces the dead time as ADCs will now only process data when a signal in the channel is above the threshold. The downside of this method is that any correlations between ADCs that would be recorded in a single event are now lost. However, by pairing the ADC data with a timestamp, these correlations can be reconstructed in post-processing by comparing timestamps.

As each FEE64 in AIDA acts as a triggerless DAQ, the merged data stream produced by the TapeServer consists of a time-ordered list of ADC data items. Each item includes information on its FEE64 and channel of origin and the timestamp at which it was recorded. AIDASort is a program, written by the author, which takes the raw data stream and builds it into full events representing the decays and implants taking place within the detector. The processes carried out in the program can be split into four main sections: unpacking and event building, calibration, clustering, and writing to file.

6.1.1 AIDA raw data

The raw data from AIDA is recorded in the GREAT data format [190]. Originally designed to be used as part of the first triggerless DAQ [189], the structure of the data format has been updated over the years to accommodate the features needed for the running of AIDA. The raw data files form a time-ordered list of data items which are stored in 64 kB blocks. These blocks are formed from a series of 32-bit data word pairs, that together form one 64-bit data item. These data items can be of the form of an ADC data item or an information data item, such as a correlation scaler. ADC data items contain the data output from the ADCs. The first 32-bit word is split into multiple parts and contains the ADC value, a flag indicating whether it is a high or low-energy event, the channel and the FEE64 from which the data originated. The second word then contains information on the timestamp at which the event was recorded.

Information data items are used to keep track of the status of each of the FEE64s and also in keeping the full timestamp updated. The 48-bit timestamp used by the MIDAS DAQ, to stamp data items, would take up too large a portion of the data in a single 64-bit data item. It is therefore split into two components: the bottom 28 bits, or least significant bit, which is included with every data item and the upper 20 bits, the most significant bit, which is regularly updated via an information data item. The AIDA clock runs at a rate of 100 MHz which will cycle through the lower 28-bits every 2.68435 seconds; the most significant

Table 6.1 *Bit positions of the data contained in the two 32 bit words of an ADC data item.*

Word 1

Bit Position	31	30	29	28	27 to 16	15 to 0
Field Value	1	1	Fail	Veto	Channel Identification	ADC data

Word 2

Bit Position	31 to 28	27 to 0
Field Value	Empty	Timestamp 27:0

part of the timestamp must, therefore, be updated at a rate faster than this. In order to ensure that the upper part of the timestamp is kept up to date in the data stream SYNC100 items, containing the upper 20 bits, are sent every 2^{18} clock cycles such that 1024 SYNC100 pulses are sent in the time it takes for the lower 28 bits to rollover. Another information data item that is of importance to the analysis of the data is the correlation scaler. Sent as three 16-bit words the correlation scaler is a 48-bit timestamp on a common clock across all data acquisition systems used in the experiment. By working out the offset between the internal AIDA timestamp and that of the correlation scaler, it is possible to synchronise events across multiple systems.

6.1.2 Unpacking and event building

During the unpacking and event building stage, the raw time-ordered data is read into the program and grouped into events based on the time structure of the data items. The unpacker sorts the data blocks, separating the 64-bit data words from one another and forming them into the two 32-bit words that make up a full data item. A list of paired unsigned integers stores the unpacked data words. An unpacker class then receives the paired 32-bit words. Each 32-bit word contains multiple pieces of information, assigned to different bit positions, the unpacker separates these pieces of information and stores them as variables in a C++ class. Table 6.1 shows the data structure of the two 32 bit words that make up an ADC data item. Two types of classes are used to store the data items; one for ADC data items and one for information data items. Both classes are created in the same method taking the two 32-bit words as input in addition to the upper 20 bits of the timestamp. The 32-bit words are then broken up inside the class and assigned to variables that are accessible in the analysis, and the full timestamp of the item is formed from the two parts.

An event builder function takes the list of time-ordered data items from the unpacker and forms these into discrete events. For the program, an event is defined as all the ADC data items that fall within 2 μs of the previous data item. The separation time of 2 μs was chosen as this is the time between successive readouts of the multiplexer in the AIDA ASICs.

After an event has been formed the timestamps of the items that make up the event undergo two corrections. First, a correction is applied to correct for the multiplexed output of the ASIC. The amount corrected is determined from the number of items originating from the ADC and subtracting integer multiples of 2 μs from the timestamp depending on how many events have come before it. For example, the first event has no time removed; the second has 2 μs subtracted; the third 4 μs and so on up to a maximum of 30 μs for the sixteenth item. The effect the multiplexer has on the time distribution of outputs is best observed in a time difference plot between implantation times in AIDA and the time of the ion in BigRIPS. An example plot of the uncorrected data is shown in Figure 6.1a where it is seen that after a sharp peak at 13.7 μs there are a series of following peaks each separated by 2 μs decaying in amplitude. A corrected plot is also shown in Figure 6.1b where it can be seen that the initial location of the peak does not change at 13.7 μs but all implants now occur in the following 4 μs. The second correction aligns the item timestamp to the correlation scaler by applying an offset calculated as the difference between the two clocks.

After a data item has been formed and has had its timestamp corrected, the item is inserted into one of two lists depending on whether the data item has a high-energy flag present or not. The type of event is then categorised depending on the contents of the two lists when closing the event window. Firstly, if there is more than one item in the high-energy list, the event is categorised as an implantation event, and only the high-energy list is passed on to be calibrated. If this condition is not met, and the low-energy list contains more items than half the number of strips in the system, the event is identified as a pulser event and histograms are filled with the data. Finally, if neither condition is met the event is identified as a low-energy event, and the low-energy list is passed on to the calibrator.

6.1.3 Energy calibration and geometry

During the energy calibration, the ADC data is taken from units of ADC channel and put into units of keV for items using the high-gain channels and MeV for items

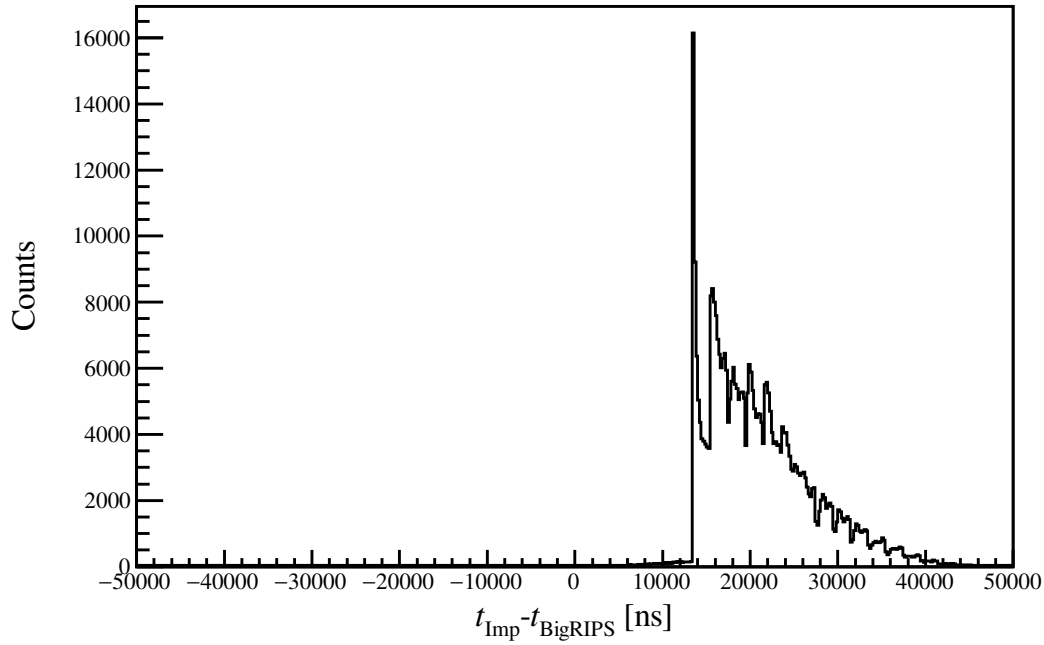

(a)

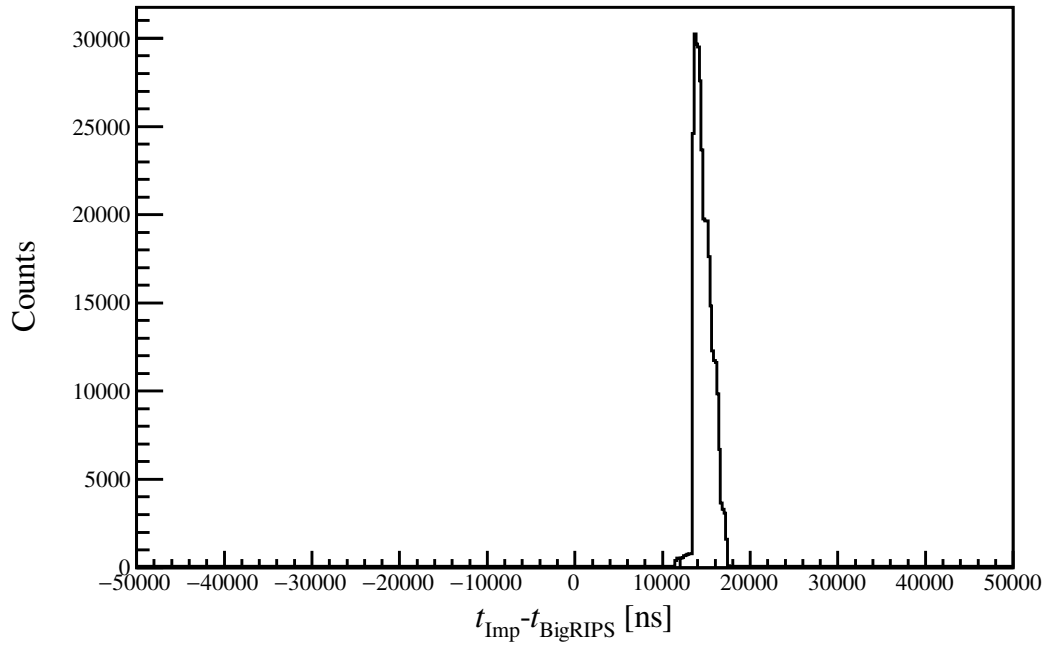

(b)

Figure 6.1 *a) Shows the time difference plot between uncorrected implant events being registered in AIDA and ions being detected in BigRIPS. A peak at 13 μs is observed with further peaks of lessening amplitudes being separated by 2 μs out to 45 μs. b) Shows a similar time difference plot but this time the implant timestamps have been corrected for the multiplexed output. A single peak is now observed at 13 μs with all implants being contained within 4 μs.*

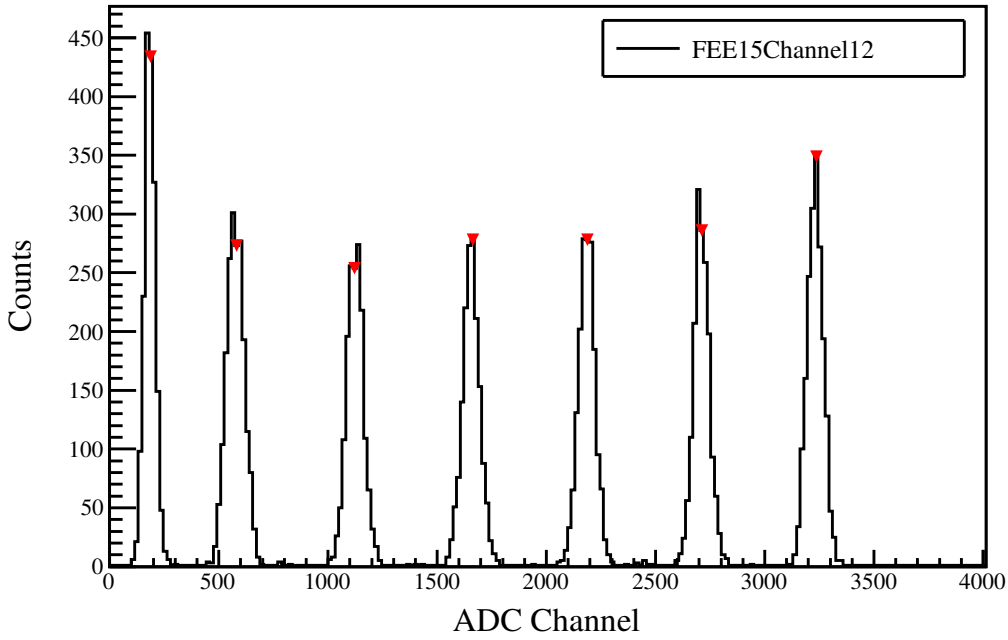

Figure 6.2 *Example channel spectra for a pulser walk-through. Red triangles are placed at the fitted centres of the six pulser peaks. The peaks, from right to left, relate to pulser amplitudes of 12000, 10000, 8000, 6000, 4000 and 2000 arbitrary units. The peak visible at 200 is noise above the ASIC threshold and not related to the pulser.*

using the low-gain preamplifiers. A constant gain is applied to each strip, which is determined by the charge sensitive preamplifier feedback capacitors used that can vary in capacitance by around $\sim 3\%$. A correction for the ADC offset is then applied which varies per channel in each FEE64. The ADC offset represents the difference between the ADC zero point and the ADC value obtained when there is no input signal. The zero point offset of each channel is found by performing a pulser walk-through. In a pulser walk-through, multiple signals of known relative amplitudes are fed into the individual channels, generating a spectrum of peaks for each channel, an example of which is shown in Figure 6.2. A linear ADC response over the region of interest is assumed, and a straight-line fit is applied to the measured positions of the pulser signals. The offset returned by the straight-line fit is the ADC offset.

During the calibration, the geometry of the system is applied to the data. The FEE64 and channel that the data is recorded with are mapped to information describing DSSD, side and strip of origin. The values of which are assigned from a FEE64 to DSSD and side map. After calibration the data items are stored in a list with a multi-tiered sort; first sorting by DSSD, then by detector side and

finally by strip, such that adjacent strips are located next to each other in the list.

6.1.4 Event clustering and localisation

As a β-electron can have a range in silicon greater than that of the strip pitch of the detector, for example, a 1 MeV electron has a range of 2.3 mm in Si [191], a decay event will likely not be confined to a single strip and instead deposit energy over multiple adjacent strips. In this instance, to obtain the total amount of energy deposited into the detector by the β-electron the energy deposited across each of the strips needs to be summed. The strips that are summed together are grouped in a cluster. Nominally a cluster is defined as a group of adjacent strips in a single side of a DSSD that all fire within the same event window. The requirement for all of the strips to be adjacent comes from the fact that it is not physical for a β-electron to cross a strip without depositing enough energy to trigger the channel. To reduce the chances of noise items being added to the cluster, a time window requiring all strips to be within 4000 ns of each other is applied.

The position of events is then determined by matching clusters from the front side of the detector with clusters from the back, such that the front provides a x position and the back provides a y. Clusters are matched on the condition of an equal energy cut, restricting the clusters to be within 150 keV energy of one another. The width of the window is determined by the resolution of the front and back sides of the detector, which is estimated using the locus that forms as high-energy light ions pass through the silicon. Figure 6.3 shows an example of this where a locus is seen along $y = x$. These ions are typically single strip events of low intensity that deposit a range of energies in the silicon from < 1 MeV up to 10 MeV as they pass through the detector stack.

For event windows containing low-energy events, clusters are paired in every DSSD in which data items are present, whereas for high-energy event windows clustering is only carried out in the stopping layer of an implant as only the final position of the implant is required for performing implant-β correlations. The stopping layer of an implantation event is defined to be the last detector in which there are no downstream high-energy data items and at least one high-energy data item in each upstream layers. Also, for the requirement of obtaining a position, the stopping layer must contain a high-energy data item in each side. Once the

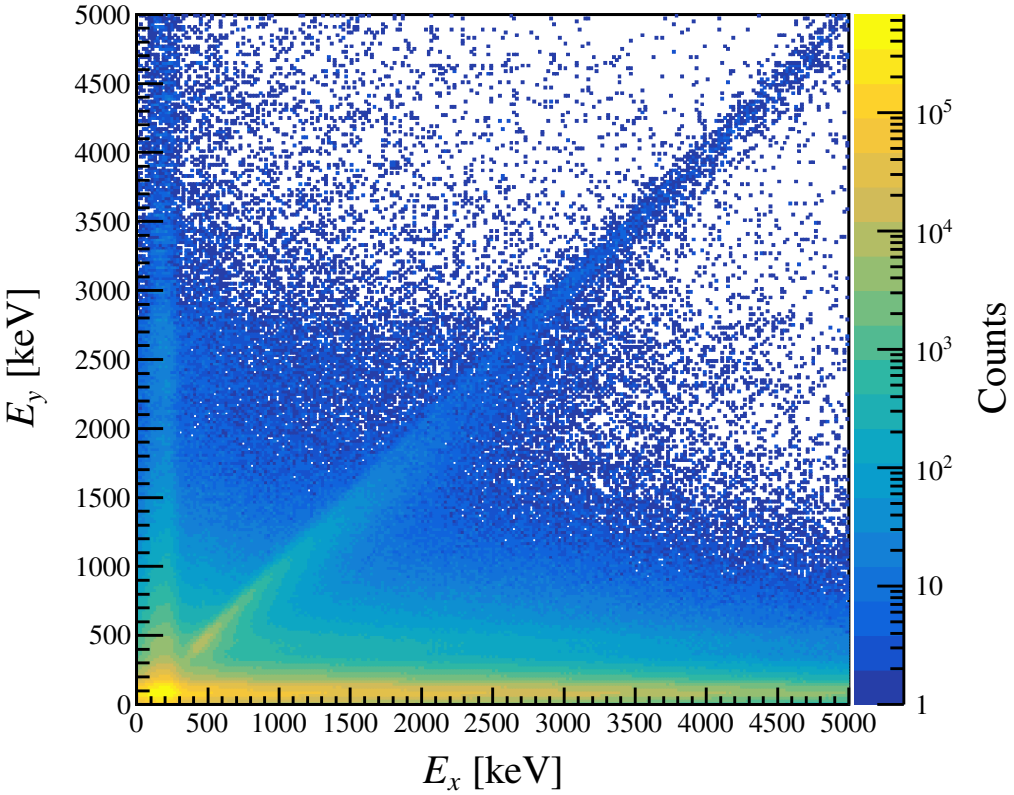

Figure 6.3 *Energy of x clusters against the energy of y clusters. The locus stretching from ∼400 keV to 5000 keV is caused by light ions passing through the detector.*

stopping layer of an implant event has been determined, clustering is carried out using the same method as described above. In the case of high-energy events, the window on the equal energy condition is much larger than that for low-energy events, for example, during this experiment a width of ±3000 MeV was used.

6.1.5 Writing to file

The paired front and back clusters are combined to form the final data item that will be written to file. The final output event contains information on the energies, positions, multiplicities and sizes of the clusters that are combined to produce it. The inclusion of these pieces of energy allows for selective conditions to be applied to the data during the later stages of the analysis.

The CERN ROOT [192] data format, used as the output file format of the sort, is a standard format used in nuclear physics experiments owing to its flexibility

in output structure. As part of the ROOT framework, a large number of libraries are available that allow the visualisation of data through histogram production and the analysis of data through dedicated analysis tools such as fitting functions. These features make the ROOT data format a well-suited choice for the storing of the sorted data.

6.2 BRIKEN Sort - Sorting the raw BRIKEN data

The BRIKEN DAQ is responsible for the collection of data from multiple detector systems. The data collected is split into three groups: i) neutron, for data originating in any of the 148 neutron counters, ii) gamma, for data from the 8 Clover channels and iii) ancillary, for data from any of the beamline detectors used in the analysis. The BRIKEN DAQ used is a triggerless system known as GasificTL [193], which makes use of SIS3302 VME digitisers [194] instead of the FEE64 modules used in AIDA. Each digitiser module has eight self-triggering channels which run at a 100 MHz sampling rate and are coupled with a 16-bit ADC. A triggerless DAQ is crucial in reducing dead time in the counter array, owing to the long moderation time of neutrons. As a result of the moderation time, neutrons are not observed simultaneously with a decay. Instead, they show a decreasing distribution over the 200 μs following a decay, as seen in Figure 6.4. For cases in which two neutrons are expected to be observed this would require an event window of 200 μs in length to reliably measure both during the same event window. In addition to a long window causing considerable dead time per neutron event [178], the number of random neutrons detected from background sources, also included within the event windows, would be larger making correlations harder to perform later in the analysis.

When a channel registers a signal above the threshold, the signal is processed. The amplitude of the signal is then is stored with the timestamp at which it was recorded. This information is stored in the 64 MB of onboard memory that each channel has in the digitiser. In order to allow the digitisers to continue writing to their memory banks while data is being simultaneously read, the memory banks are split in two. The split memory bank allows one bank to be available for writing while the other is available for reading. The effect of this is a reduction in dead time as there are no losses in writing time while data is read from the

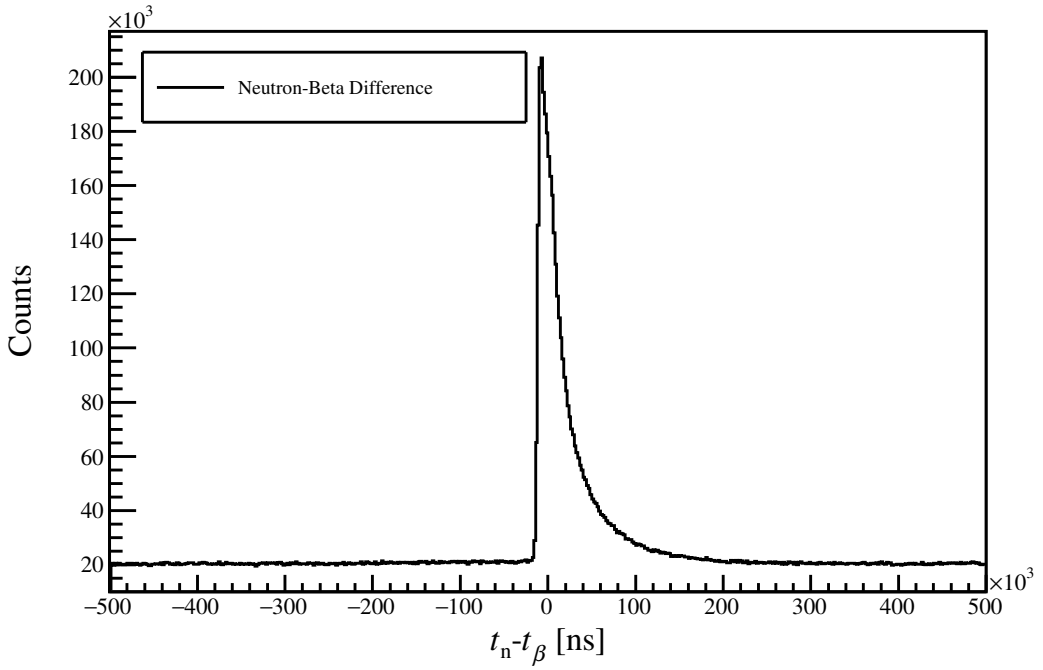

Figure 6.4 *Histogram showing the time difference between decay events being measured in AIDA and neutrons being recorded in the BRIKEN neutron counters*

system. Data is read from the modules by a PC over an optical link. The DAQ system, running on the PC, is responsible for determining when a bank will be read. The data stored in the swapped banks is read out in blocks, where each block is a time-ordered list of data from a single channel. While each block is in time order, the timestamps from block to block will not necessarily be in order, destroying any event information.

The time structure of events in the BRIKEN DAQ is reconstructed when the list mode data files are analysed using the BRIKEN Sort program. As the blocks of data are read in from each channel, they are broken up and constructed into events containing information on which detector channel the event took place in, the calibrated energy of the signal and also the timestamp the event was recorded. The processed events are then placed in a time-ordered list before being written to an output file. The timestamp of events written to file is aligned to the same correlation scaler used in AIDA.

The CERN ROOT data format is once again used for the storing of the final data. The structure of the TTree is more complicated than in the case of AIDA though as at this stage events are split into three categories: neutrons for events recorded within the ^{3}He counters, gamma for events recorded in the Clover and

ancillary for events recorded in the beamline plastic detectors. The final time-ordered ROOT file is then ready for further analysis and correlations with the other detector systems.

6.3 BigRIPS ANAROOT - Sorting the raw BigRIPS data

The output of the BigRIPS DAQ is a file containing the information from each of the beamline detectors used to carry out the identification of particles. A separate program ANAROOT [195], produced by RIBF, is then used to process the raw files and carry out the particle identification. The output of the ANAROOT program is a ROOT file in which each event represents an ion that has passed through BigRIPS. Each entry contains information on the ion's A/Q and Z value which are calculated using the procedures discussed in section 3.4.2. Information on the ion's velocity, which is given as $\beta = {}^{v}/_{c}$, and the timestamp as it passed through BigRIPS is also included. The timestamp given is also aligned to the correlation scaler.

6.4 Data merging

The outputs of the three detector systems are merged to produce a single data file which contains the events from all three systems as a single time-ordered list. During the merging process, correlations are performed between the various detector systems in both time and space. The correlations performed, and the criteria that define them, are user-defined in a configuration file. The merger program takes the configuration file as an input, in addition to the files to be merged. The merger program was developed by members of the BRIKEN collaboration [196], based at IFIC (Instituto de Física Corpuscular), with input from the author on required features and bug fixes. The program, written in C++, makes use of multi-threaded functions to handle the simultaneous data reading of the files and an additional thread for writing the final output to file. The ROOT file format is used as the final output of the program allowing for the use of the ROOT libraries in the analysis of the merged data. The merger allows for correlations to be performed in time between all of the different data structures

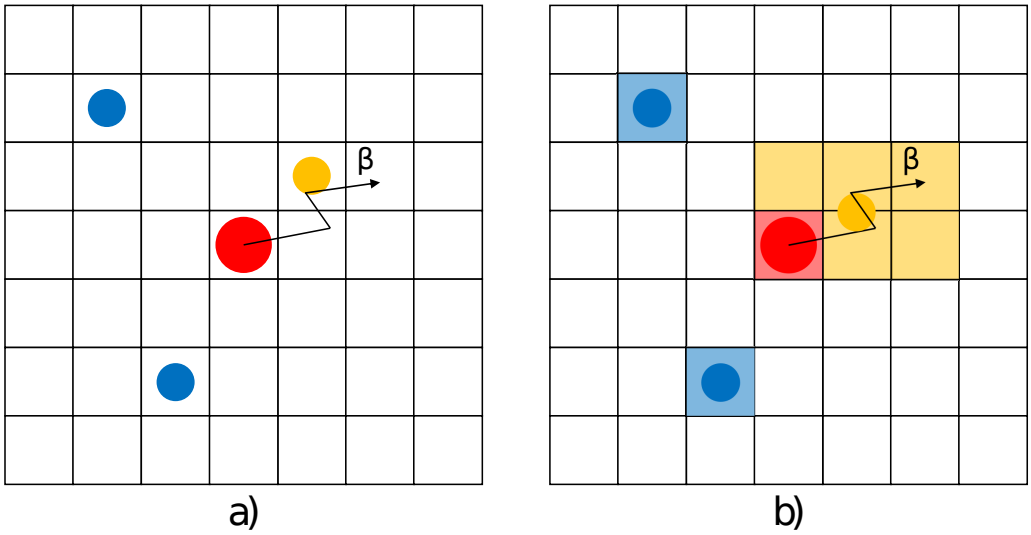

Figure 6.5 *Comparison between the old correlation method of performing correlations within a 7×7 square (a) and the new method (b). In both images the red circle indicates an implant particle, the orange circle a beta particle and the blue circles as noise events.*

that make up the combined data streams, these being: implant, beta, neutron, gamma, ancillary and BigRIPS events. The correlation methods employed will now be discussed.

6.4.1 Implant-β correlations

Decay events are assigned to nuclides by correlating the low-energy decay event with an identified high-energy implant. The correlations performed, use the position data of both the implants and decays to restrict the areas over which correlations are carried out. Implantation events have a well-defined location with most implantation events forming clusters of 2×2 strips in area or less. However, the position of decays is often less well defined, with β-particles having a range of up to a few millimetres in silicon. The area over which correlations need to be carried out can thus be drastically reduced from the entire surface of the detector to just a few millimetres surrounding an implant.

The previous method used to perform these correlations involved assigning the locations of both the implant and the decay events to single points. These points were calculated based on the energy depositions in each of the strips forming a cluster, with the largest energy depositions having the most weighting on the calculated position of the event. Decay events would then be correlated with an

implant if their position fell within a specific area around the implant, typically a 7×7 pixel square centred on the implant. This method, while providing a high β-detection efficiency, the percentage of implants which have a decay associated, has the downside that it also includes large amounts of background in the correlations. Noise events are typically low-energy events occurring just above the hardware threshold of the ASICs. As they require a random event in each side of the detector to pass an equal energy cut they are most commonly single-pixel events, *i.e.* made up of a single strip from each side of the detector. A correlation method sensitive to noise events will produce decay curves with a significant background underneath the decay signal, which can cause issues when trying to fit decay curves with low statistics as the signal to noise ratio becomes low. An example of the old method is shown in Figure 6.5a. Here it is observed that a red implant centred in the square emits a single beta particle which has its position calculated to be one pixel away. Also included in the area around the implant are two noise events which are localised to single pixels. These noise events are separated from the implant but still fall inside the 7×7 area, correlating them to the implant.

A new methodology was developed to reduce the amount of background correlated with implants [197]. Based on physical assumptions about the energy depositions of β-particles in the detector, the new methodology makes full use of the location data available for both the implants and decays. Instead of being assigned to single points, implants and decays are confined to areas defined by the strips that fire. For example, if three x strips fire and two y strips fire the resulting area will be a 3×2 rectangle. Next, it is reasoned that the area of an implant should be overlapping or adjacent to the area of the decay. This implies that there can be no gaps between the two events as a β-particle traversing the width of a pixel should deposit enough energy to register above the hardware threshold of the slow comparators. This has the effect of rejecting correlations with noise events that are separated from the implant pixel that would have been previously correlated, which can be seen in Figure 6.5b where the β-particle is still correlated but the noise events are now rejected. Tests carried out have shown that this methodology has the effect of increasing the signal to noise ratio when producing decay curves in comparison to the previous method.

6.4.2 Time based correlations

The common timestamp used in the output of the sorting programs for each system allows for correlations between the systems in time to be carried out. It is only in the case of implant-β correlations that spatial correlations need to be taken into account. For the other types of correlations performed, conditions are only placed on the time between the events taking place in each of the systems. The time range over which correlations are performed will vary depending on the intended application for the correlated data. For example, when identifying an implant, a prompt correlation between an event in BigRIPS and the implant will be expected. Therefore, a short correlation window is used. However, when assigning a decay to an implant, the time at which it will occur cannot be determined so a much longer correlation window will be used.

In addition to the wanted correlations, some random correlations may also be included. An example of this would be a β-decay being correlated with a neutron originating from the decay of a different ion. The rate at which random correlations are made can be estimated by performing correlations both after and before an event. As any correlations that are made before the event cannot be as a consequence of the event, they can be identified as a random correlation. Assuming a constant rate of randoms, the rate of correlations performed before an event, or backwards in time, can be taken to be the random rate following the event. A case where this can be easily justified is the detection of a decay event before an implant has been detected. The decay event here must be randomly correlated as it cannot be of the ion that is yet to be implanted. Therefore any decays that are seen backwards in time are random correlations.

6.4.3 Time windows used for correlations

Implant-BigRIPS - Particle identification

The correlation plot between implants and particle identification events in BigRIPS is one of the most well-constrained plots in terms of event windows. As all ions typically tend to be travelling with a velocity of around 0.64 c, the time difference between events in BigRIPS and AIDA is negligible, and implants appear instantaneously. However, this is not seen in the correlation plot where a delay of 13.7 μs appears, as seen in Figure 6.1b. This difference can be put down

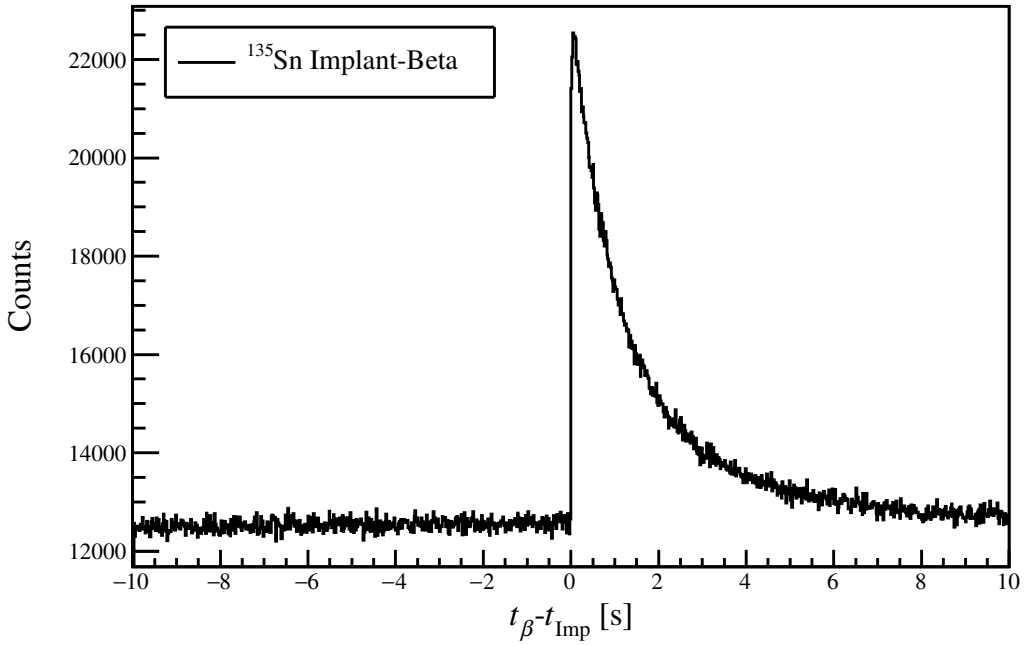

Figure 6.6 *Decay curve of ^{135}Sn one of the longest half-lives in the setting, showing that after 10 s the activity has reached the background rate*

to a combination of the shaping time of the AIDA ASICs and the delay in signals being read out by the ASIC multiplexers. A correlation window of ± 100 μs is used between implant events and BigRIPS events. While this is much larger than the anticipated time difference between implant events and BigRIPS events, it does not have a significant background component as the mean time difference between implants is much larger than this window size.

β-Implant

The time windows used for the correlations between implant events and β events are the longest used in the analysis of this experimental data. They were decided upon by looking at the half-lives of the nuclei expected in the experiment. In addition to the parent's half-life, the half-lives of the daughters and granddaughters must be taken into account. This is done as the decays of the daughters and granddaughters will also correlate to the parent nuclide. A time window of ± 10 seconds was chosen as the region out to -10 seconds allows for an accurate determination of the random background, and by $+10$ seconds the activity will have decayed back to the random background rate as can be seen in Figure 6.6.

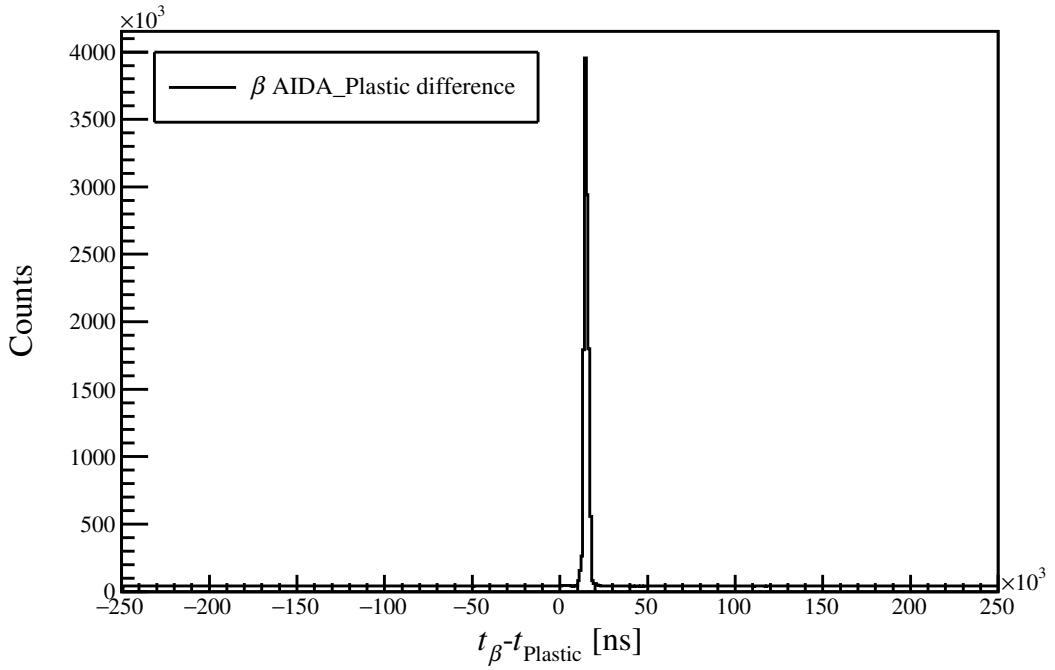

Figure 6.7 *Time difference plot between β detection time and AIDA_Plastic detection time. The 13.4 μs delay between the two events is caused by the shaping and signal processing time of the ASICs in AIDA.*

β-neutron

The time window used in the correlation of β and neutron events needs to take into account the moderation time of the neutrons. A correlation plot showing the distribution of times between β and neutron events is shown in Figure 6.4. From the figure, a peak in the neutron-beta time difference can be seen at -13.7 μs, again caused by the shaping time of the AIDA ASICs. The peak then decays until it has mostly recovered to the random rate at $+200$ μs indicating that most neutrons are detected within 200 μs of the decay from which they originate. The window used is again symmetrical about 0s, allowing the determination of the random neutron rate by looking at neutrons that are detected before a decay. In order to allow correlations between neutrons and other data structures also correlated with β-events, a larger window of ± 1000 μs is used to ensure that the events in the neutron and ancillary detectors both fall within the correlation plots in the time region of interest surrounding a beta event.

β-Ancillary

The ancillary detectors mainly comprise beamline detectors that are used to produce vetoes for events in AIDA and BRIKEN. They are typically scintillator detectors that produce a signal as an ion passes through them, making them useful for determining whether an ion was present at a given time. An example of an ancillary detector is the AIDA Plastic, a thick (10mm) scintillator that is located behind the AIDA detector stack. It is commonly used to determine if an event passes through the detector stack or is stopped within its bulk. The correlation plots between low-energy events in AIDA and the ancillary detectors often show a prompt coincidence indicating the presence of beam-induced events in AIDA. This is evidenced in the correlation plot of β-events and the AIDA Plastic, shown in Figure 6.7, where a narrow peak is observed at 13.7 μs showing events that have passed through the detector stack depositing energy in each layer but not stopped. To allow correlations between ancillary detectors and neutron events to be performed, the same long $\pm$1000 μs correlation window that is used for β-neutron correlations is used again.

6.5 Analysis methodology for the extraction of half-lives and β-delayed neutron emission probabilities

The extraction of half-lives, $t_{1/2}$, and β-delayed neutron emission probabilities, P_{1n}, from the data is achieved by fitting decay curves generated for each ion. By measuring not just the total number of decays, but also those that come in coincidence with a β-delayed neutron, accurate P_{1n} values can be obtained for the nuclei that are studied.

6.5.1 Particle identification of implants

Decay events are assigned to nuclei based upon the particle identification of their correlated implant. This particle identification comes from the correlation of implantation events in AIDA with identified ions in BigRIPS. As both of these data-types are low noise the correlations are simple to produce as an implant

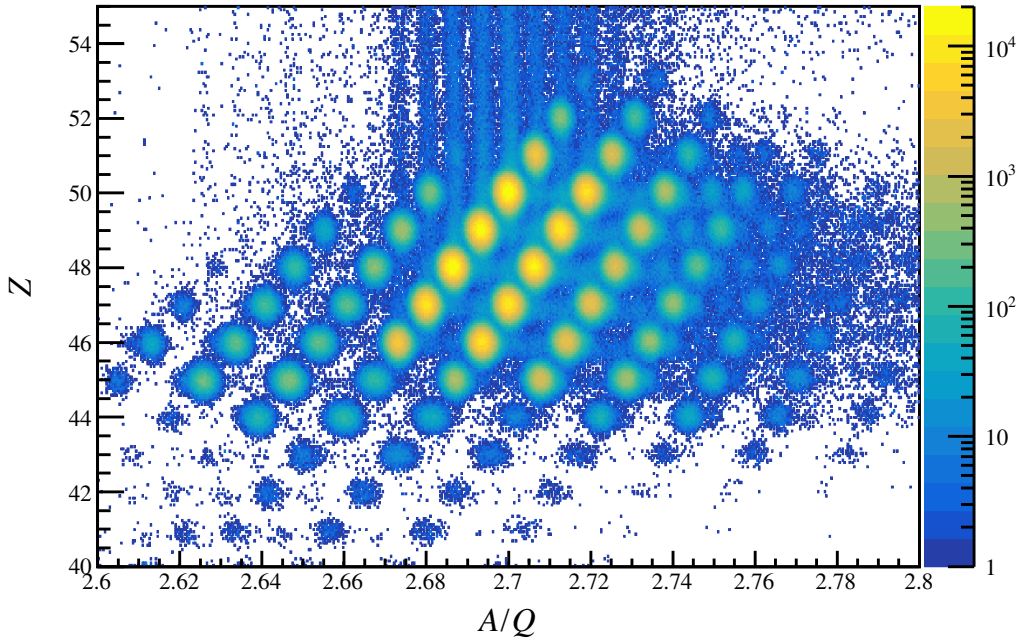

Figure 6.8 *Particle identification plot for all of the ions implanted in the AIDA detector stack during the high intensity run.*

will only be correlated with one BigRIPS event with a very narrow correlation distribution, as seen in Figure 6.1b. A particle identification plot of the implants detected in AIDA is produced in terms of the A/Q and Z values measured by BigRIPS. The final particle identification plot, for the experiment, is shown in Figure 6.8. The PID shows good resolution in both A/Q and Z, allowing clear identification of ions in AIDA. At this stage, the PID has been calibrated and verified through isomer tagging at F7 by the BigRIPS group. With the particle identification confirmed, cuts can be placed onto the data assigning implant events to their respective nuclides.

6.5.2 Determination of beam-induced background events

In addition to the nuclei of interest, the RI beam is often accompanied by many light ions produced in the fragmentation/fission processes and reactions occurring along the beamline. As these ions are typically light, they do not deposit enough energy in the silicon to register as an implantation event and instead register as low-energy events. The effect of these events is in the contribution of background to the decay curves and an increase in the neutron background rate, as neutrons often accompany them. In order to be able to reject these background events

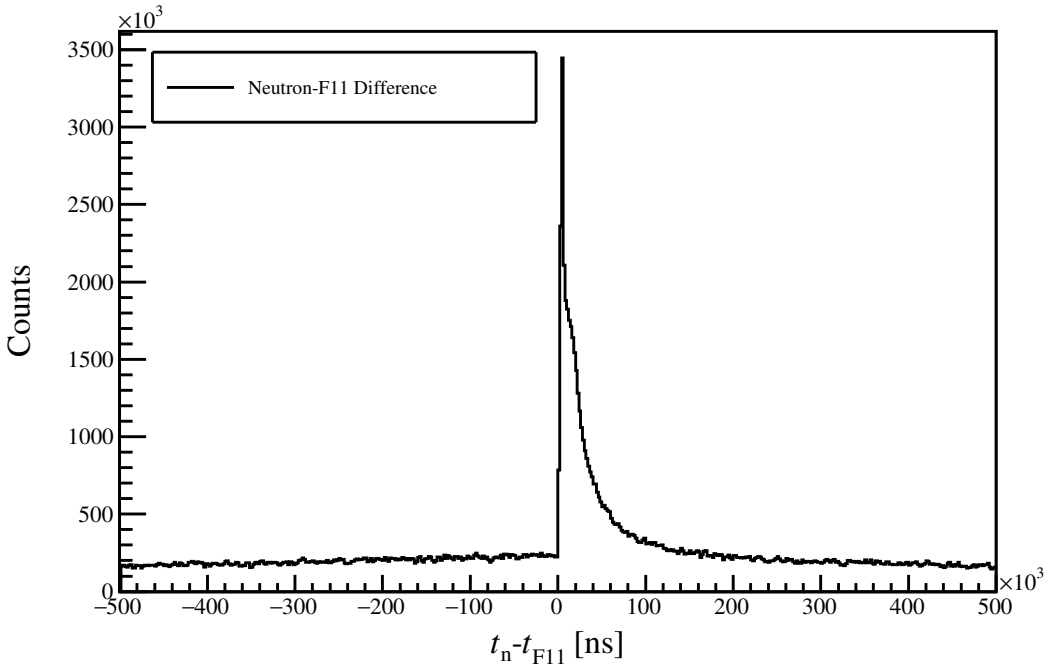

Figure 6.9 *Time difference between events being detected in a neutron counter and ions being registered at F11 by the F11 scintillator.*

from the final data, it is desirable to be able to identify when these beam induced events have occurred. Beamline detectors are used to achieve this by performing correlations between the beamline detectors and betas or neutrons. The two primary ancillary detectors used to determine beam-induced events are the plastic scintillator at F11 and the plastic scintillator located behind the AIDA detector stack.

F11 vetoes

The F11 plastic scintillator is a thin (1 mm) plastic scintillator, located at F11 just as ions leave the zero-degree spectrometer. Signals registered from the scintillator are read out by two photomultiplier tubes (PMTs), one on the left and one on the right side. Signals in the scintillator will be produced whenever a charged particle passes through depositing energy.

By looking at neutrons in coincidence with signals in the F11 scintillator, shown in Figure 6.9, a clear coincidence is seen with a peak at 0 μs followed by the exponential decay of counts out to 200 μs caused by the moderation time of the neutrons. From this, it can be seen that in addition to ions coming down the beamline there are neutrons, likely caused during the fragmentation of the ^{238}U

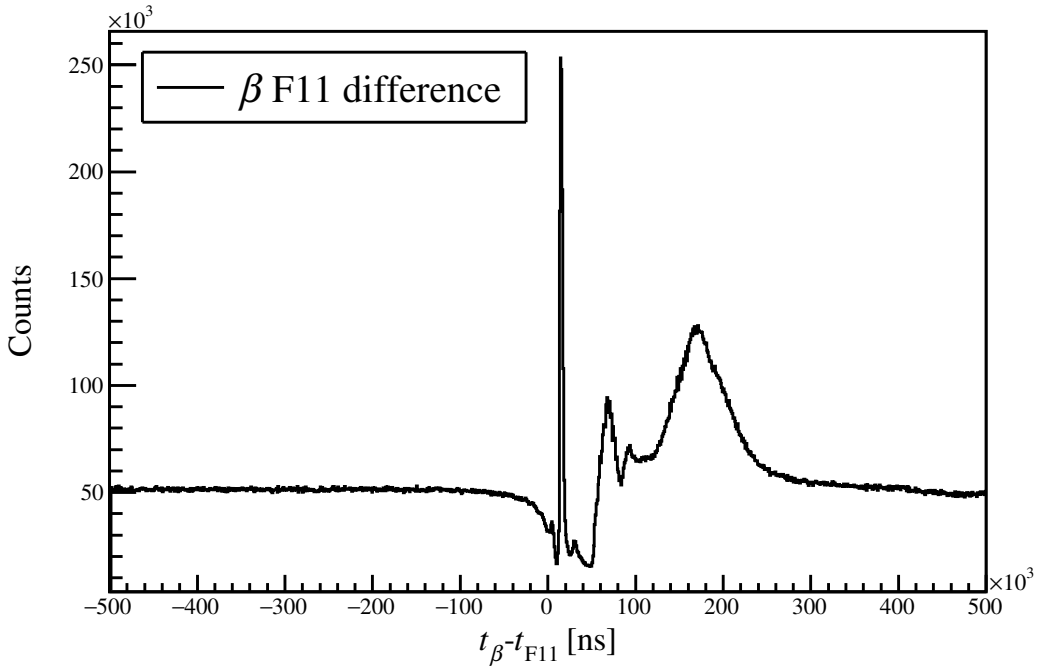

Figure 6.10 *Time difference between low-energy events detected in AIDA and ions being registered at F11 by the F11 scintillator.*

primary beam or nuclear reactions occurring along the beamline. As a result of this, a veto of 200 μs is placed on neutrons following an F11 event to reject these beam induced events. This has the effect of artificially increasing the dead time on the neutron system by 4%, but is required to be able to correlate neutrons with β events accurately.

For the correlation plot of β events and the F11 scintillator, shown in Figure 6.10, three processes are occurring that produce features in the correlation plot. The first feature is evidenced by the dip in events from $-40\,\mu$s to $50\,\mu$s, this is caused by the AIDASort software rejecting low-energy events when a high-energy event is present within the event window. The second feature caused by implants is the two peaks at $60\,\mu$s and $170\,\mu$s, which are spurious decay events caused by the repeat triggering of ASICs. The final feature results in the sharp peak of events at $17\,\mu$s, which is caused by light ions accompanying the beam. As mentioned previously, these do not trigger implantation events in AIDA, so there is no rejection of these events from the sort program. To reject all of these events in coincidence with the F11 signal a veto on beta events is placed from $-20\,\mu$s to $+280\,\mu$s at which the beta background rate has recovered to its pre-F11 signal rate.

AIDA Plastic vetoes

The correlation plot between events in the neutron counters and events in the AIDA plastic takes on the same distribution as the neutron-F11 scintillator correlation plot but with fewer events. The decrease in events is expected as the rate in the AIDA plastic is less than the rate at F11, as implants are stopped within the detector stack and do not produce signals in the plastic.

The correlation plot between low-energy events in AIDA and the AIDA Plastic, shown in Figure 6.7, shows the same sharp peak at 13.7 μs that is observed in the F11 scintillator correlation plot. This gives further evidence to the fact that this peak is the result of light ions, such as carbon and oxygen the accompany the fission fragments, passing through the detector stack. There is, however, no decrease in events or broad secondary peaks as the ions that cause these are stopped within the detector bulk.

6.5.3 Decay curves

The half-life of an nuclide implanted in AIDA can be found by measuring the activity, A, of decays following an implant using the relationship between the number of nuclei implanted of that nuclide, N, and its decay constant, λ, such that the activity is given by $A = N\lambda$. By forming histograms of the time difference between implants and their correlated decays, a measure of the activity as a function of time can be obtained. If the number of implanted ions is also known the decay constant of the nuclide can be determined, which can be related to the half-life by:

$$t_{1/2} = \frac{\ln 2}{\lambda} \tag{6.1}$$

To determine the P_{1n} value of the nuclide, we are also interested in the number of decays that are accompanied by the detection of a β-delayed neutron. A second decay curve can then be defined such that all β events must be in coincidence with a single β-delayed neutron. The difference in activity between the two defined histograms can be used to determine the number of decays that result in a neutron emission and the total number of decays, allowing the P_{1n} value of an nuclide to be calculated.

In total to obtain the $t_{1/2}$, P_{1n} and P_{2n} values of an nuclide, three histograms are

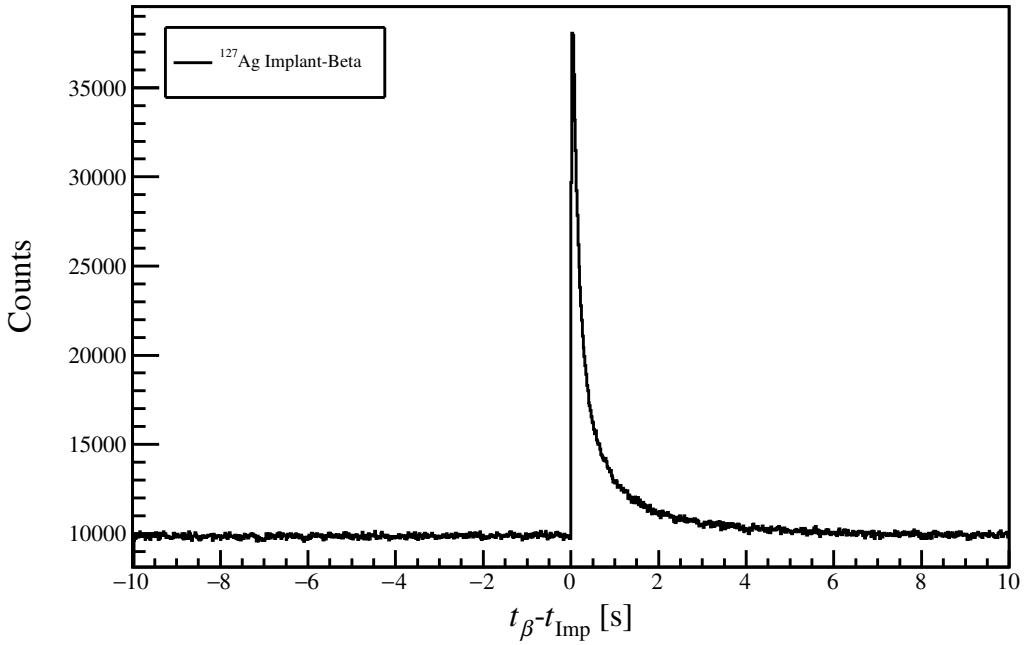

(a)

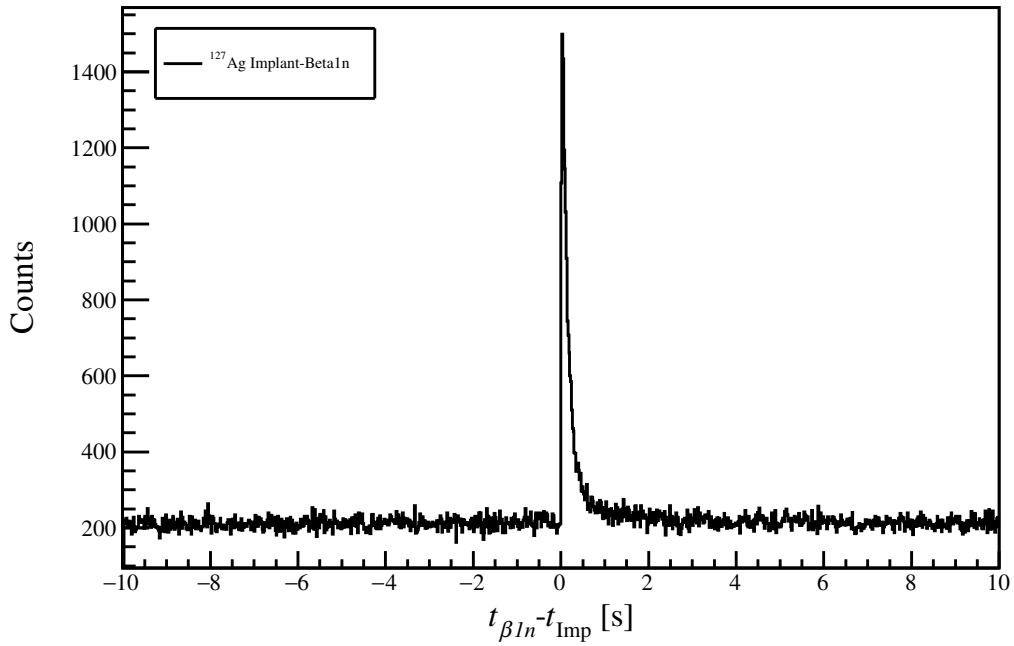

(b)

Figure 6.11 *a) Decay curve for ^{127}Ag produced from the time differences between ^{127}Ag implants and their correlated decays. b) Decay curve gated on decays accompanied by a single neutron within 200 μs of the decay.*

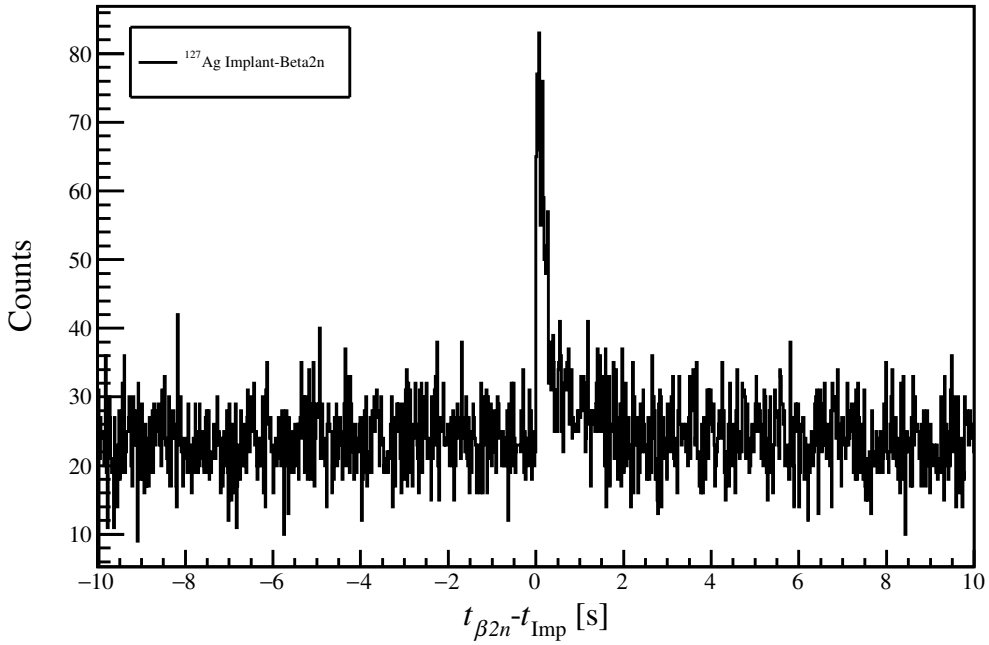

(c)

Figure 6.11 *c) Decay curve for ^{127}Ag produced from the time differences between ^{127}Ag implants and their correlated decays; gated on decays that have two neutrons within 200 μs of the decay.*

created. Firstly, an implant-β correlation plot with only the cuts coming from the vetoes of the beam-induced background. Secondly, an implant-β correlation plot but with a single-neutron cut applied, here β-events are required to be measured with a single neutron occurring within 200 μs of the decay. Finally, a decay curve with the requirement of two neutrons occurring within 200 μs of the decay. Examples of these three decay curves are shown in Figures 6.11a, 6.11b and 6.11c respectively.

While all of the information, needed to extract the $t_{1/2}$, $P_{1\mathrm{n}}$ and $P_{2\mathrm{n}}$ values, is contained within the three decay curves mentioned previously, additional factors need to be considered. In addition to the decays of the parent nuclide, decays of daughter nuclides and from background sources will also contribute to the decay curve. All of these contributions must be fully accounted for before extracting the final values.

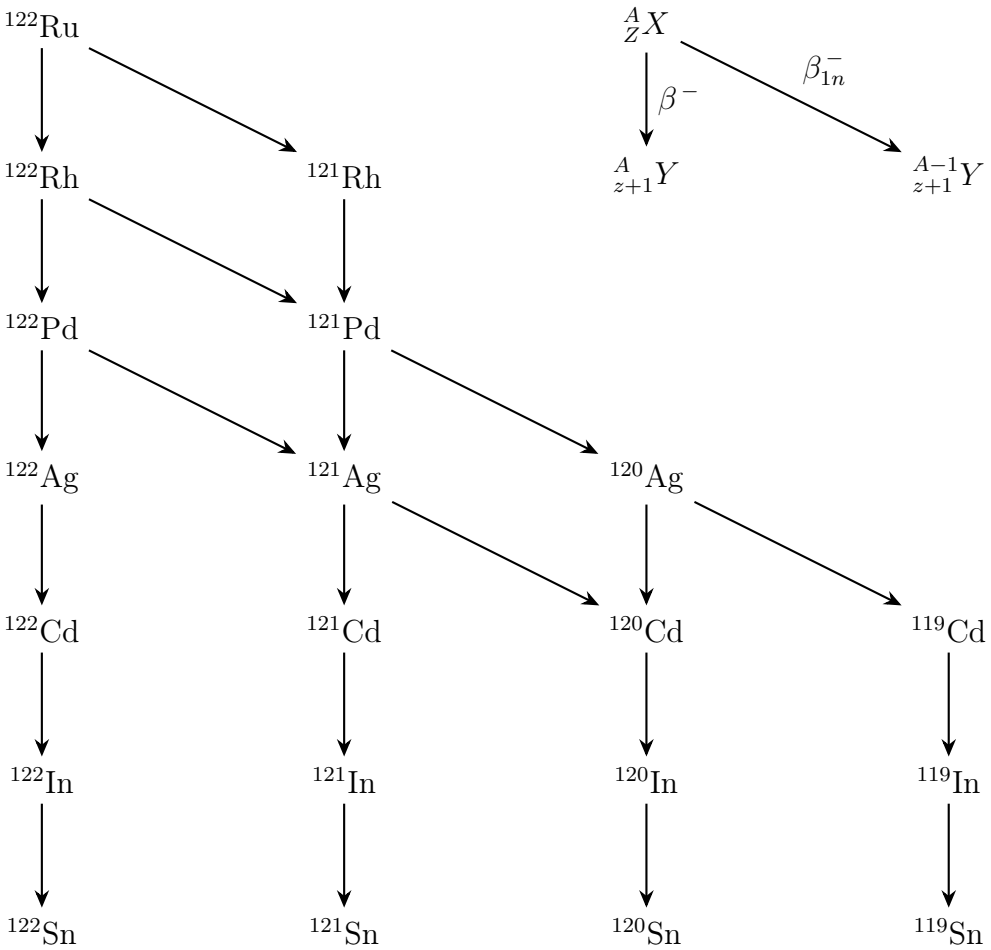

Figure 6.12 *The full decay path that is implemented in the Bateman Equations that are used in the fitting of ^{122}Ru where each arrow represents a permitted decay path according to literature. Half-lives and P_n values of nuclei other than ^{122}Ru are fixed to their literature values.*

6.5.4 Bateman equations

The correlated implant-β decay curves, when gated on an individual nuclide, comprise all of the decays associated with an implant. As these nuclei are far from stability, the daughter nuclei will undergo successive decays until stability is reached. These decays are all localised to the same region of the detector, and will all correlate with the original implant. Fitting the activity of the resulting curves requires the activity of all the contributions to be calculated as a function of time. The Bateman equations are used to calculate this.

The equations were devised by Henry Bateman and presented as "The solution of a system of differential equations occurring in the theory of radioactive transformations." [198]. They begin from the starting point that the rate of

change in the number of a particular species, $\frac{\mathrm{d}N_1}{\mathrm{d}t}$, is the combination of its production rate and its destruction rate. For a species undergoing radioactive decay, its destruction rate is given by its activity, A. A nuclide's activity is calculated as the product of its decay constant, λ, and its abundance at a time, t. Likewise, its production rate is given by the activity of the decay that produces it.

$$\begin{aligned} \frac{\mathrm{d}N_1}{\mathrm{d}t} &= -\lambda_1 N_1 \\ \frac{\mathrm{d}N_i}{\mathrm{d}t} &= -\lambda_{i-1} N_{i-1} - \lambda_i N_i \quad (i = 2, n) \end{aligned} \tag{6.2}$$

Where the subscript 1 indicates the parent nuclide and i indicates nuclides along a decay chain. In order to solve these equations for an entire decay chain the amount of each species, N_i, present at each time, t, must be known. The solution provided by Bateman assumes a non-zero abundance of the parent species and zero abundance of nuclides along the decay chain at time $t = 0$ such that

$$N_1(0) \neq 0 \quad \text{and} \quad N_i(0) = 0 \quad \text{when} \quad i > 1 \tag{6.3}$$

The abundance of each species, N, present at a time t can then be calculated to be

$$N_n(t) = \frac{N_1(0)}{\lambda_n} \sum_{i=1}^{n} \lambda_i \alpha_i \exp[-\lambda_i t] \tag{6.4}$$

where

$$\alpha_i = \prod_{j=1 \neq i}^{n} \frac{\lambda_j}{(\lambda_j - \lambda_i)} \tag{6.5}$$

This equation however assumes that all decays progress along the same linear decay chain with no branching points. In order to account for the branching that occurs when a nuclide has multiple decay products, *e.g.* β-decay and β-delayed neutron emission, the probability of each product being produced need to be taken into account. When this is done Eq. 6.4 can be rewritten as:

$$N_k(t) = N_1 \prod_{i=1}^{k-1} (b_{i,i+1} \lambda_i) \times \sum_{i=1}^{k} \frac{\exp(-\lambda_i t)}{\prod_{j=1 \neq i}^{k} (\lambda_j - \lambda_i)} \tag{6.6}$$

where $b_{i,i+1}$ represents the branching ratio between N_i and N_{i+1} and can be written as

$$b_{i,i+1} = P^i_{1n}, P^i_{2n} \text{ or } 1 - P^i_{1n} - P^i_{2n} \tag{6.7}$$

dependent on whether the decay is a β-event accompanied by a single, two or no β-delayed neutrons. The functions that describe the activity of the decay chains

as a function of time are given as:

$$\begin{aligned} f_\beta(t) &= \sum_{i\in\beta} \bar{\varepsilon}^i_\beta \lambda_i N_i(t) \\ f_{\beta 1n}(t) &= \sum_{j\in\beta 1n} \bar{\varepsilon}^j_\beta \bar{\varepsilon}^j_n P^j_{1n} \lambda_j N_j(t) \\ f_{\beta 2n}(t) &= \sum_{k\in\beta 2n} \bar{\varepsilon}^k_\beta (\bar{\varepsilon}^k_n)^2 P^k_{2n} \lambda_k N_k(t) \end{aligned} \tag{6.8}$$

where $f_\beta(t)$ is the function for all betas correlated with an implant, $f_{\beta 1n}(t)$ is the function for all betas accompanied by a single delayed neutron correlated with an implant and $f_{\beta 2n}(t)$ is the same but for betas accompanied by two delayed neutrons.

6.5.5 Background correction

The Bateman equations describe the activity just from the decays originating from nuclides along the parent's decay path back to stability. The histograms produced also have contributions from randomly correlated events which serve to act as a background in the decay curve. To accurately fit the data, this background must be understood. The fitting of which is discussed in this section.

Random β background

Low-energy events that are correlated with an implant but do not originate from the decay of an implanted ion form a significant source of background in the decay curves. These events come from several sources: i) β-decays originating from the decays of other ions implanted in the same region, ii) light ions that pass through the detectors accompanying the beam and iii) detector noise. The effect of these unwanted correlations is a steady source of background which limits the lowest level of activities to which AIDA is sensitive. In order to reduce the contributions to the histograms from these background sources, a robust correlation method with good noise rejection is needed for implants and β-events such as the method described in Sec 6.4.1. The random background component is determined by performing correlations backwards in time. In this region, the only contributions to the histogram are from β-events and noise that are unrelated to the implanted ion. The time distribution of events backwards in time can then be studied to

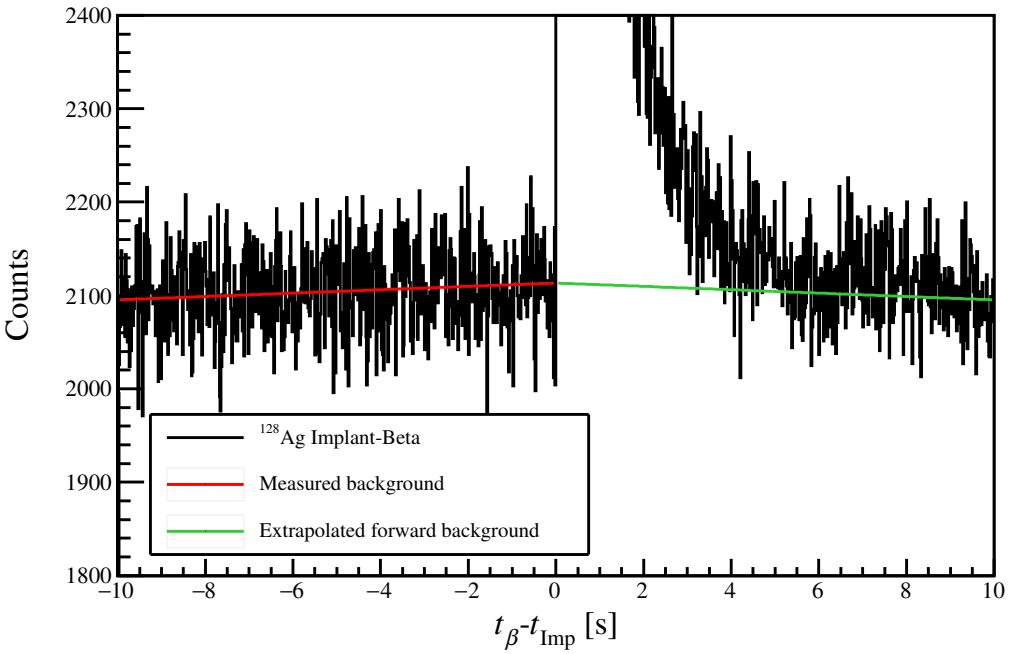

Figure 6.13 *The measure background using backward correlations for the decay curve for ^{128}Ag is shown in red along with the extrapolated background at forward times in green.*

determine the background rate, an example of this for the case of ^{128}Ag is shown in Figure 6.13.

From Figure 6.13 it is observed that this background rate is not constant and in fact shows a slight positive slope at negative times, $t < 0$. It has been determined that this is due to interruptions in the beam intensity throughout the experiment. During all experiments at RIKEN-RIBF, it has been observed that there are frequent beam interruptions. During the interruptions, the beam drops for times ranging from less than a second to many minutes. These losses of beam cause the β activity in the detector to decrease, while the beam is absent, resulting in fewer correlations occurring between implants and betas than when the beam is on. When the beam returns the β activity in the detectors increases causing an increased rate of correlations, the increased correlations first occur at short time differences from an implant and then move to longer times as time progresses. Frequent beam interruptions result in times closer to 0 s seeing more correlations than those further out as this process repeats. As a result of this, the fitted background rate at negative times is taken to be symmetrical about $t = 0$ s and a mirror function is applied at positive times. Monte-Carlo simulations carried out, by the BRIKEN group, following the initial

commissioning experiment have verified that a mirror function is suitable [199]. Another method of verification also taken was to investigate the production of decay curves where beam interruptions had been removed from the data stream with 10s either side. When this was done a flat background was obtained at the cost of a significant reduction in statistics. Results obtained using the reduced data were in statistical agreement with those obtained using a mirrored background. As such, a mirrored background was employed in the analysis of this thesis data.

Neutron background

Neutrons not originating from the decays of nuclides along the implanted ion's decay chain can also form a significant source of background. These neutrons come from several sources: i) decays of other nuclei, ii) beam induced neutrons, iii) background neutrons in the environment and iv) detector noise, such as gamma-like events in the counters. The number of these background events can be minimised through the use of proper shielding of detectors, determination of beam-induced neutrons and proper detector noise reduction.

While these steps can be taken to minimise the number of unwanted neutron correlations, they cannot be completely removed from the data. An accurate method of determining the contributions of random neutrons to the decays that make up the histograms is then essential in determining the precise number of neutrons measured in coincidence with the decay of the parent nuclide [199]. The method presented here and used in the analysis of the data makes use of the assumption that the number of random neutrons that come in a time window $\Delta_{t\beta\mathrm{n}}$ before a β is on average the same as the number that come in the window $\Delta_{t\beta\mathrm{n}}$ afterwards. In order for this assumption to hold true, the random neutron background rate must be flat over a period of a few hundred microseconds surrounding a decay. Looking at times $t < 0$ in Figure 6.4 shows this to be true.

To determine the contribution of random neutrons to one neutron gated decay curves, a new implant-β histogram, $h_{\mathrm{i}\beta 1\mathrm{nBW}}$, can be produced with the condition that a single neutron must arrive within the time window $\Delta_{t\beta\mathrm{n}}$ before the decay, where $\Delta_{t\beta\mathrm{n}} = 200\,\mu$s. This histogram shown in Figure 6.14a can be seen to take the same shape as the ungated implant-β histogram, $h_{\mathrm{i}\beta}$, scaled by a factor r_1.

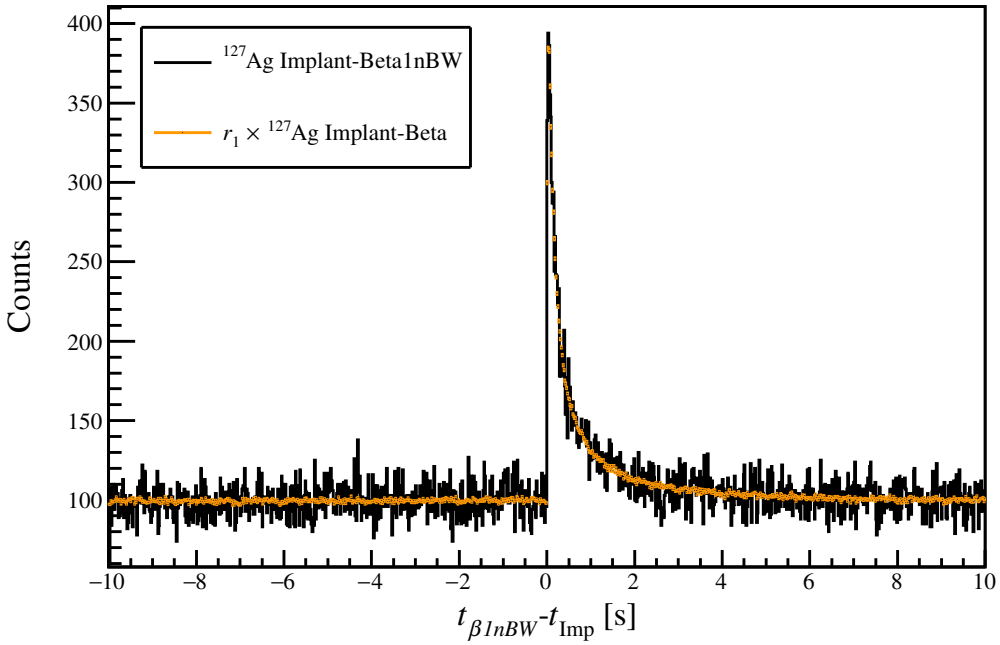

(a)

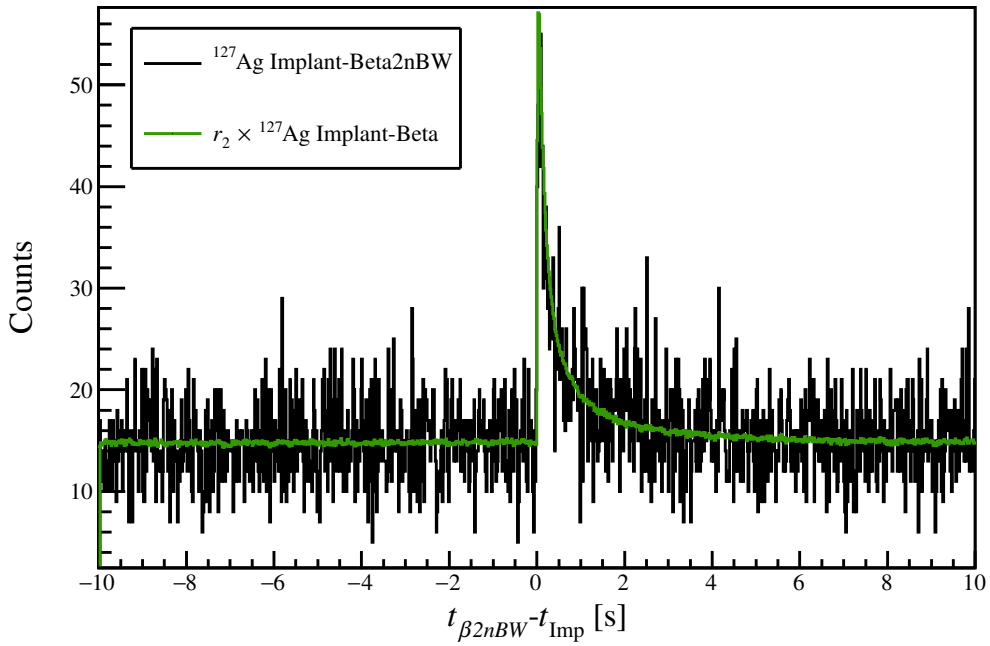

(b)

Figure 6.14 *a) Decay curve for ^{127}Ag produced from the time differences between ^{127}Ag implants and their correlated decays, gated on decays accompanied by a single neutron occurring within 200 μs prior to the decay with the scaled ^{127}Ag histogram overlayed. b) Decay curve gated on two neutrons occurring within 200 μs prior to the decay.*

Where r_1 is given by:

$$r_1 = \frac{\int_{-10\,\mathrm{s}}^{+10\,\mathrm{s}} h_{\mathrm{i}\beta 1\mathrm{nBW}}(t)\,\mathrm{d}t}{\int_{-10\,\mathrm{s}}^{+10\,\mathrm{s}} h_{\mathrm{i}\beta}(t)\,\mathrm{d}t} \tag{6.9}$$

and represents the probability of a single random neutron being correlated with a β event. The value of r_1 is determined with high precision as the full amount of statistics available per nuclide are used. The value is nuclide dependent and will shift by a few percent for each nuclide, depending on both the implantation rate and P_n value of the parent nuclide.

The probability of two random neutron coincidences occurring is determined using the same method, but with the condition of two neutrons coming within the window $\Delta_{t\beta\mathrm{n}}$. The new histogram $h_{\mathrm{i}\beta 2\mathrm{nBW}}$ is shown in Figure 6.14b. The shape of this histogram is also seen to take the form of a scaled implant-β histogram, with a scaling factor of r_2. Similarly to r_1 the factor r_2 is given by

$$r_2 = \frac{\int_{-10\,\mathrm{s}}^{+10\,\mathrm{s}} h_{ii\beta 2\mathrm{nBW}}(t)\,\mathrm{d}t}{\int_{-10\,\mathrm{s}}^{+10\,\mathrm{s}} h_{\mathrm{i}\beta}(t)\,\mathrm{d}t} \tag{6.10}$$

and represents the probability of two random neutrons being correlated with a β event. It can be seen that the probability of having two randomly correlated neutrons is much smaller than that of one random neutron as in the present example r_2 is around seven times smaller. It can also be taken that the total probability of any amount of random neutrons being correlated is given by $r = r_1 + r_2$.

The probabilities of random single- and two-neutron correlations can then be included in the fit function applied to the histograms. For the case of decays followed by the release of a single neutron, the correlation of random neutrons will have two effects on the histogram $h_{\mathrm{i}\beta 1\mathrm{n}}$. The first being that it will lead to an increase in counts in the implant-$\beta_{1\mathrm{n}}$ histograms caused by random neutrons correlating with β events that do not directly result in the emission of a β-delayed neutron. These events take on a time distribution which is given as the difference between all events that make up the decay chain, $f_{\mathrm{i}\beta}$, and those that result in the emission of a neutron, $f_{\mathrm{i}\beta 1\mathrm{n}}$, scaled by the factor r_1. The second effect is a loss of counts caused by the addition of a random neutron to β events that already correlate to the delayed emission of a single neutron. This causes a reduction in the number of correlated neutrons by a factor of r, the total random neutron rate, reducing the number of truly correlated neutrons by a factor of $(1-r)f_{\mathrm{i}\beta 1\mathrm{n}}$. The measured histogram can then be given as the sum of both these effects plus

the uncorrelated β background, $h_{\mathrm{iu}\beta 1\mathrm{n}}$, and after rearrangement can be written as:

$$h_{\mathrm{i}\beta 1\mathrm{n}}(t) = (1 - r - r_1) f_{\mathrm{i}\beta 1\mathrm{n}}(t) + r_1 f_{\mathrm{i}\beta}(t) + h_{\mathrm{ui}\beta 1\mathrm{n}}(t). \tag{6.11}$$

The case for the detection of two neutrons is treated in much the same way. Random neutrons cause both an increase in random counts in the implant-$\beta_{2\mathrm{n}}$ histogram and a decrease in the number of true correlations. The corrections needed for the two-neutron case becomes slightly more complicated as the increase in counts comes from two sources: β events that do not result in the emission of any neutrons but correlate with two random neutrons and also β events that result in the emission of one neutron but also correlate with a single random neutron. The full derivation of the correction terms is given in Appendix A of reference [199], but here the final histogram terms are given as:

$$\begin{aligned} h_{\mathrm{i}\beta 1\mathrm{n}}(t) =& (1 - r - r_1) f_{\mathrm{i}\beta 1\mathrm{n}}(t) + r_1 f_{\mathrm{i}\beta}(t) \\ &+ (2r_e(1 - r - r_1) - r_1) f_{\mathrm{i}\beta 2\mathrm{n}}(t) + h_{\mathrm{ui}\beta 1\mathrm{n}}(t) \end{aligned} \tag{6.12}$$

$$\begin{aligned} h_{\mathrm{i}\beta 2\mathrm{n}}(t) =& (1 - r - r_2 + 2r_e(r_1 - r_2)) f_{\mathrm{i}\beta 2\mathrm{n}}(t) \\ &+ (r_1 - r_2) f_{\mathrm{i}\beta 1\mathrm{n}}(t) + r_2 f_{\mathrm{i}\beta}(t) + h_{\mathrm{ui}\beta 2\mathrm{n}}(t) \end{aligned} \tag{6.13}$$

where $r_e = (1 - \bar{\varepsilon}_{2n})/\bar{\varepsilon}_{2n}$.

6.5.6 Fitting procedure

In order to simplify the equations that are fit to the data, the $f_{\mathrm{i}\beta x\mathrm{n}}$ terms are substituted for the data held in the histograms apart from the histogram being fit. With these terms substituted the functions can be written as:

$$\begin{aligned} h_{\mathrm{i}\beta}(t) =& f_{\mathrm{i}\beta} + h_{\mathrm{ui}\beta} \\ h_{\mathrm{i}\beta 1\mathrm{n}}(t) =& -\frac{d_0}{d_1} h_{\mathrm{i}\beta}(t) + \frac{1}{d_1} f_{\mathrm{i}\beta 1\mathrm{n}}(t) - \frac{d_2}{d_1} h_{\mathrm{i}\beta 2\mathrm{n}}(t) + \tilde{h}_{\mathrm{ui}\beta 1\mathrm{n}}(t) \\ h_{\mathrm{i}\beta 2\mathrm{n}}(t) =& -\frac{e_0}{e_1} h_{\mathrm{i}\beta}(t) - \frac{e_1}{e_2} h_{\mathrm{i}\beta 1\mathrm{n}}(t) + \frac{1}{e_1} f_{\mathrm{i}\beta 2\mathrm{n}}(t) + \tilde{h}_{\mathrm{ui}\beta 2\mathrm{n}}(t) \end{aligned} \tag{6.14}$$

with $\tilde{h}_{\mathrm{ui}\beta 1\mathrm{n}}(t)$ and $\tilde{h}_{\mathrm{ui}\beta 2\mathrm{n}}(t)$ being the uncorrelated background remaining after applying corrections. The full derivation of the equations and definitions of the d_ν and e_ν coefficients can be found in Appendix A of reference [199].

A global fit is then carried out on the three histograms using a shared set of parameters. From this global fit, the half-life and β-delayed neutron emission probability of the parent nuclide is obtained.

Fitting Parameters

In order to fully implement the Bateman equations, as they are in Eq. 6.8, accurate information is needed on the half-lives and P_{n} values for all nuclides that make up the parent's decay chain. The values used in the decay chain were adopted from evaluated reference sources such as ENSDF [200] for both half-lives and P_{n} values. In the cases where the latest evaluation had not been updated in many years, other sources such as NDS [201], which are updated more frequently, were also checked. If a nuclide along a decay chain was also included as a parent nuclide in this experiment, the half-life and $P_{1\mathrm{n}}$ value obtained in this thesis was used. The reason for this is that often any measurement of a P_n value was the first measurement; therefore, to accurately model the branching ratio of the decay, the new measurement should be used.

In addition to the parameters relating to the daughters an accurate understanding of the neutron detection efficiency is needed as this has a direct link on both the $P_{1\mathrm{n}}$ and $P_{2\mathrm{n}}$ values obtained from the Bateman equations (Eq. 6.8). While we have a nominal neutron detection efficiency of 66.8(20)%, obtained from simulations of the array [199], this needs to be normalised to take into account losses in efficiency from multiple sources. The first is the effect of a finite window on the correlation time of the neutrons. As a result of the moderation time of neutrons, not all neutrons will be detected within 200 μs of a decay. In total, the 200 μs window will catch only 98.9% of the neutrons following the decay resulting in a decrease in the effective neutron efficiency of the system. While the window can be widened to increase the percentage of neutrons measured this also increases the amount of randomly correlated neutrons, an effect that must be minimised.

The second effect is caused by the dead time of the neutron counters themselves. As each channel runs as a triggerless system the dead time of the counter is greatly reduced, though an effect is still observed as each channel will have its own independent dead time. In order to determine the dead time of the entire system, a weighted average of the dead time in each channel was performed, treating the counter array as a non-paralysable system. The dead time of each

channel can be determined by comparing the number of pulser events observed in each channel to a reference channel in which only the pulser is present which is taken to have zero dead time. The correction factor for the dead time of the system can then be calculated to be:

$$C_{\mathrm{DT}} = \sum_{i}^{n=\#\mathrm{tubes}} \frac{n_i \frac{p_i}{p_{\mathrm{m}}}}{n_{\mathrm{Total}}} \tag{6.15}$$

where n_i is the number of neutrons detected in counter i, p_i is the number of pulser events observed in tube i, p_{m} is the number of pulser events in the master pulser channel and n_{Total} is the total number of neutrons in all tubes. This value is dependent on the rate of neutrons in the counters and as such two values were obtained: 0.9983 for the high intensity run and 0.9979 for the low intensity run.

The last source of change in the neutron efficiency comes from the veto applied to neutrons in coincidence with signals in the F11 scintillator. The 200 μs veto applied with every F11 scintillator event has the effect of increasing the dead time of the neutron detectors. This reduction takes the form of:

$$C_{\mathrm{veto}} = \exp\left(-R_{\mathrm{F11}}\Delta_{\mathrm{F11}}\right) \tag{6.16}$$

where R_{F11} is the F11 scintillator rate and Δ_{F11} is the length of time the veto applied for following an event in the F11 scintillator. For the high-intensity setting, this produces a correction factor of 0.961. Combining all of these sources of reduction to the neutron efficiency gives a final average neutron efficiency of 63.3(18)% for the high-intensity setting.

The β-detection efficiency, while included in the fit function, is fixed at a value of 1.0 during the fit. The reason for this is that it can instead be obtained from the value of N_0 returned from the fit. When this is done, the returned N_0 by the fit equation will be the number of decays attributed to the parent nuclide. The β-detection efficiency can then be calculated as N_0 divided by the total number of implants. While the fit function has the ability to use different β detection efficiencies for each nuclide in the decay chain, this feature is not utilised and all efficiencies are taken to be that of the parent. The reason for this is the distribution of β energies for each nuclide are mostly unknown so efficiencies would end up being based on theoretical β strength functions which are not guaranteed to describe the energies of the β-events well.

Fitting range of the decay curves

As the rate of decays is highest immediately following the implant, at time $t = 0$ in the implant-β correlations, it is desirable to start the fit as close to this point in time as possible to make the most of the available statistics. Unfortunately for many of the fits carried out the initial time at which it is possible to carry out a fit is often $t_\beta - t_{\mathrm{Imp}} \geq 50\,\mathrm{ms}$. During the analysis of the experimental data, it became apparent that at times of around 40 ms after an implant an amount of noise was seen in the implant-β decay curves which caused issues with the fitting. The cause of this noise was later determined to be due to the AC coupling capacitors on the adapter boards responding to high-energy deposits in the silicon causing a retriggering of ADCs. With no way of removing this noise through cuts or vetoes, it meant that for some nuclei the fits had to be started after 40 ms. New adaptor boards have been fitted and tested, and this issue is no longer seen. As large depositions of energy cause this problem, it was not seen for all ions. Depending on their implantation depth into the silicon and the amount of energy deposited in the final layer, not all nuclei were susceptible to this problem. For these nuclei, shorter timescales could be used in the fit. The limiting time range for these nuclei then became a shortage of events at times close to zero seconds. This lack of events is possibly caused by the effects of the vetoes applied to data following an implantation event. An example of the fits returned during the simultaneous fitting of the three decay curves is shown in Figure 6.15, where the fits are shown for ^{127}Ag. Also included in the figures are the contributions of the individual nuclides to the fit. The yellow line relating to ^{126}Cd in the single-neutron and two-neutron gated histograms shows the contributions of random neutrons to the fit as ^{126}Cd has no neutron emission probability itself.

6.6 Uncertainties associated with the extracted results

Owing to the complex nature of the fitting functions used to extract the half-lives and neutron emission probabilities of the nuclei care must be taken when assigning uncertainties to the final values. In addition to the statistical uncertainty associated with the fit, systematic uncertainties must be taken into account. These systematic uncertainties come from values used in the fitting function, which are not definitive in value and have uncertainty in themselves. They can be

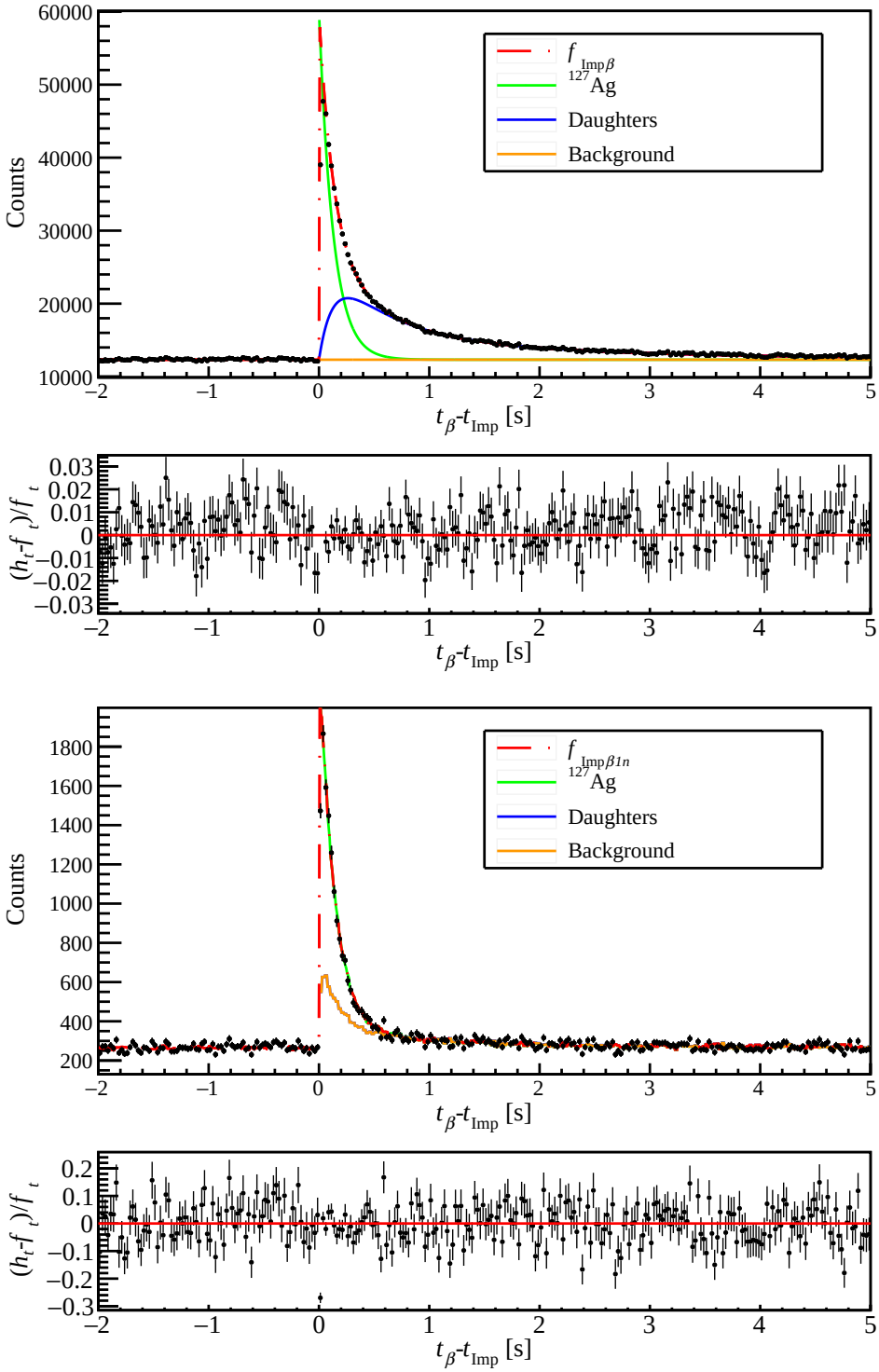
Counts
$f_{\mathrm{Imp}\beta}$
^{127}Ag
Daughters
Background
t_β-t_{Imp} [s]
$(h_t$-$f_t)/f_t$
$f_{\mathrm{Imp}\beta 1n}$

Figure 6.15

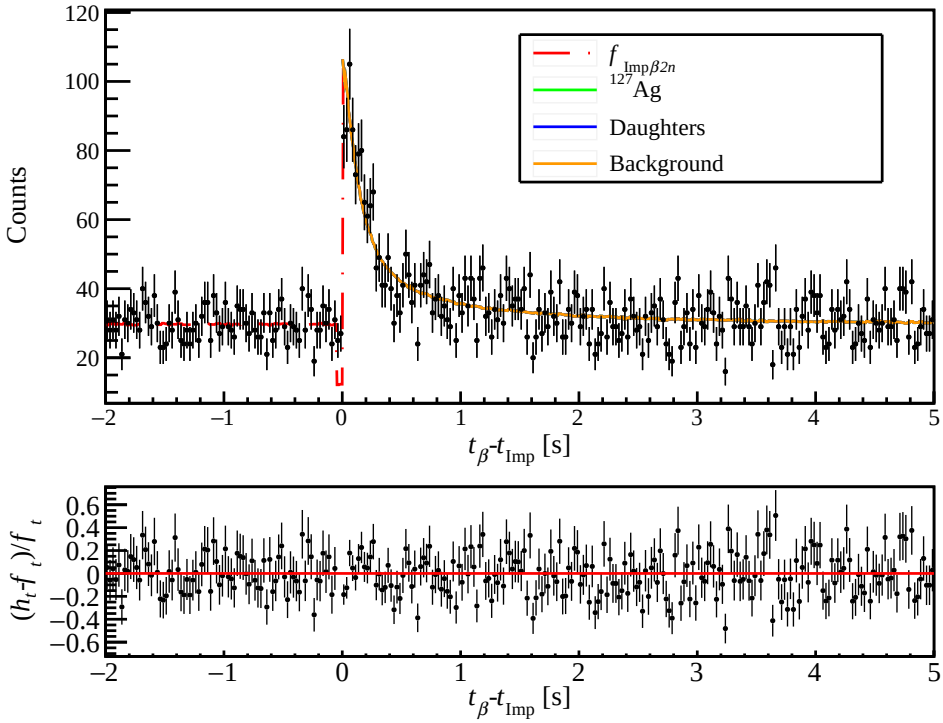

Figure 6.15 *Fits obtained from the simultaneous fitting of ungated (previous page top), single-neutron gated (previous page bottom) and two neutron gated (this page) ^{127}Ag decay curves. Below each of the fits are reduced residuals, which are calculated as the function subtracted divided by the value of the function at each point.*

split into two groups, the uncertainty that is attributed to the neutron efficiency and the uncertainty that is associated with the half-lives and neutron emission probabilities of the nuclides included in the decay chain.

The impact of these uncertainties on the final extracted values was accessed through the use of a Monte Carlo fitting method that was carried out for the groups of systematic uncertainties. In the first group, the neutron-efficiency used in the fit was randomly varied over a Gaussian distribution using the previously calculated central value and width corresponding to a 3% uncertainty. In the second group, each of the daughter values was simultaneously varied over Gaussian distributions centred on their reported values with a width equal to the uncertainty associated with the literature measurements. The fits were run 1000 times for each of the groups, and the results were placed in a histogram.

The results of the Monte Carlo fitting method often produced an approximate Gaussian centred on a mean value. By fitting the resulting Gaussian and obtaining the standard deviation, an uncertainty was attributed to both the

neutron detection efficiency and the decay chain parameters. These uncertainties are combined in quadrature with the statistical uncertainty of the fit using the central values of each parameter to give the final uncertainty associated with the measurement. For most cases, it was found that the uncertainties were dominated by the statistical uncertainty followed by the uncertainties in the decay chain and finally the neutron efficiency.

6.7 Verification of the fitting procedure

It is crucial to verify that the methodology, used to extract the $t_{1/2}$ and P_{1n} values, is accurate and consistent in the values that are obtained. Two tests were performed to ensure that the results obtained were accurate.

6.7.1 Comparison to known P_{1n} emitters

One of the first methods used to verify the results was the comparison of values obtained to previously measured values. A nuclide was identified that was present in both the literature and the experimental data. The nuclide of ^{135}Sn was identified as a good choice for several reasons: i) two previous measurements have published simultaneous measurements of $t_{1/2}$ and P_{1n} values with good precision, ii) it is present in the data with good statistics and iii) there are no isomers that exist along the decay chain. The half-lives and P_{1n} values found in literature and those obtained during this test are shown in Table 6.2, it can be seen that there is excellent agreement between the previously reported values and those obtained here. The uncertainties given alongside the values obtained here represent only the statistical error as the full uncertainty study, detailed in the previous section, was not performed for this nuclide.

$t_{1/2}$ [ms]	P_{1n} [%]	Source
450(50)	25(7)	[202]
525(25)	21(3)	[203]
517(3)Stat	19(2)Stat	This Work

Table 6.2 *Comparison of measurements of the $t_{1/2}$ and P_{1n} value of ^{135}Sn from previous literature and those obtained using the analysis methodology laid out in this chapter.*

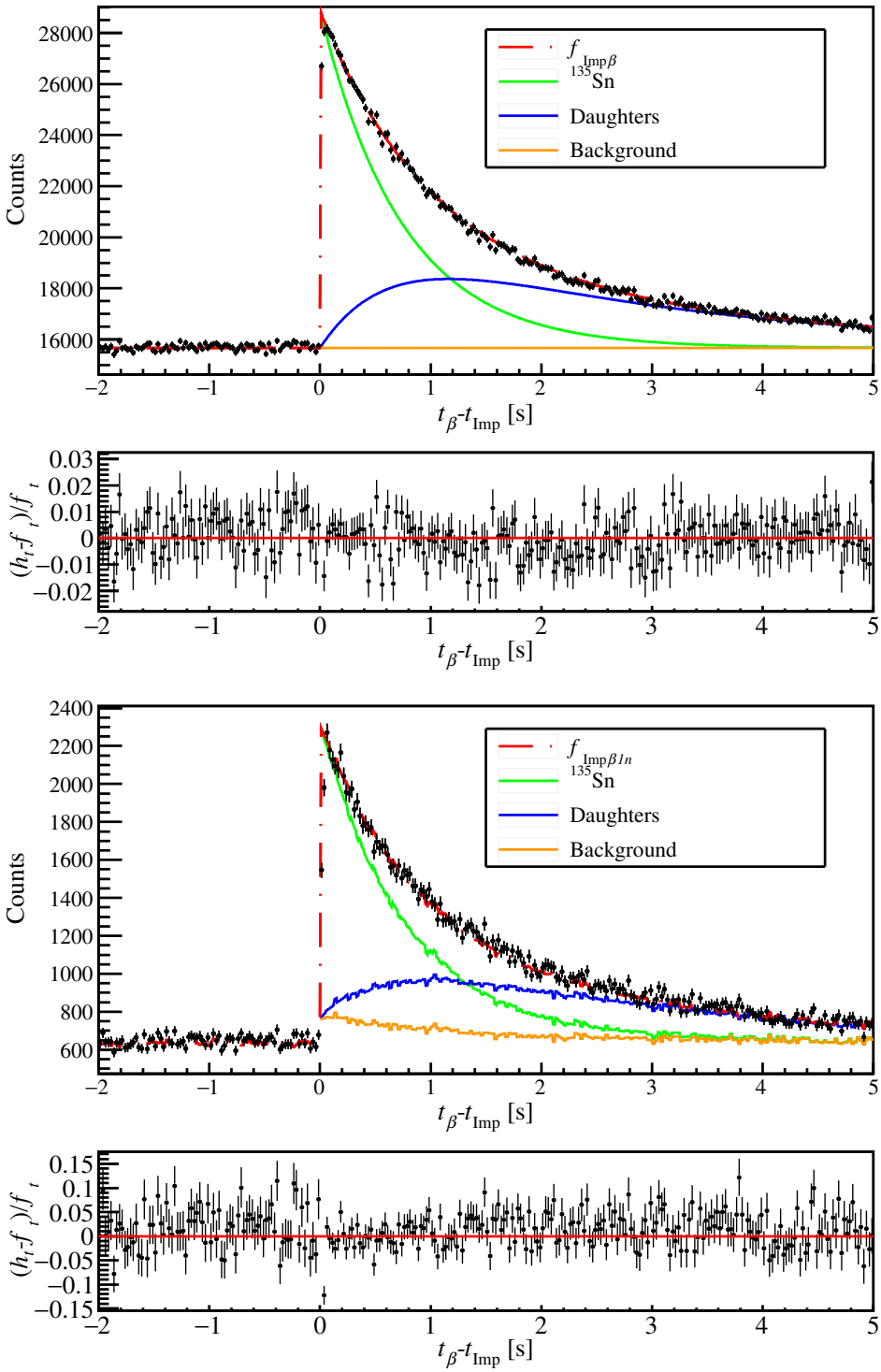

Figure 6.16 *Fits of the ^{135}Sn decay curves obtained to verify the analysis methodology. Top panel is the ungated decay curve and the bottom panel is the single-neutron gated. Below each of the fits the reduced residuals are shown. The residuals are calculated as the function subtracted from the data, divided by the value of the function at each point.*

6.7.2 Monte Carlo simulation studies

Another method used in the verification of the fit program was through the fitting of simulated data. A simple Monte Carlo program was written that would propagate the decay chain of a nuclide and produce the histograms used in the analysis. This allowed every parameter used in the decay chain to be set at a known fixed value. The method used to propagate the decay chain in the simulation was capable of branching when β-delayed neutron emission occurs. The branching ratio was set as a probability equal to the P_{1n} of the decaying nuclide. In addition to this, effects such as the neutron detection efficiency, a random neutron rate and continuous β background were also included.

The nuclide of ^{127}Ag was chosen to be the parent nuclide and the decay chain calculated back to stability. Values of 89 ms and 8.5% were used as the inputs for the half-life and β-delayed neutron emission probability, respectively. The simulation was run for a total number of 100,000 ^{127}Ag nuclei. The rate of single random neutrons was set by a probability of 0.0098 per decay event, and for two random neutrons, the probability was 0.0015. Three decay curves were produced for fitting: the ungated decay curve, a single-neutron gated curve and the two-neutron gated curve. Also produced were histograms gated on single random and two random neutrons, so that r_1 and r_2 could be determined by the fitting function. The fit function was then used to extract the half-life and β-delayed neutron emission probability from the simulated curves. The values obtained by the fit were 90(1) ms and 8.6(3)% where the uncertainties on the values are purely statistical from the fit. These values are in excellent agreement with those used in the input of the simulation, with the input values falling within the statistical uncertainties of the fit.

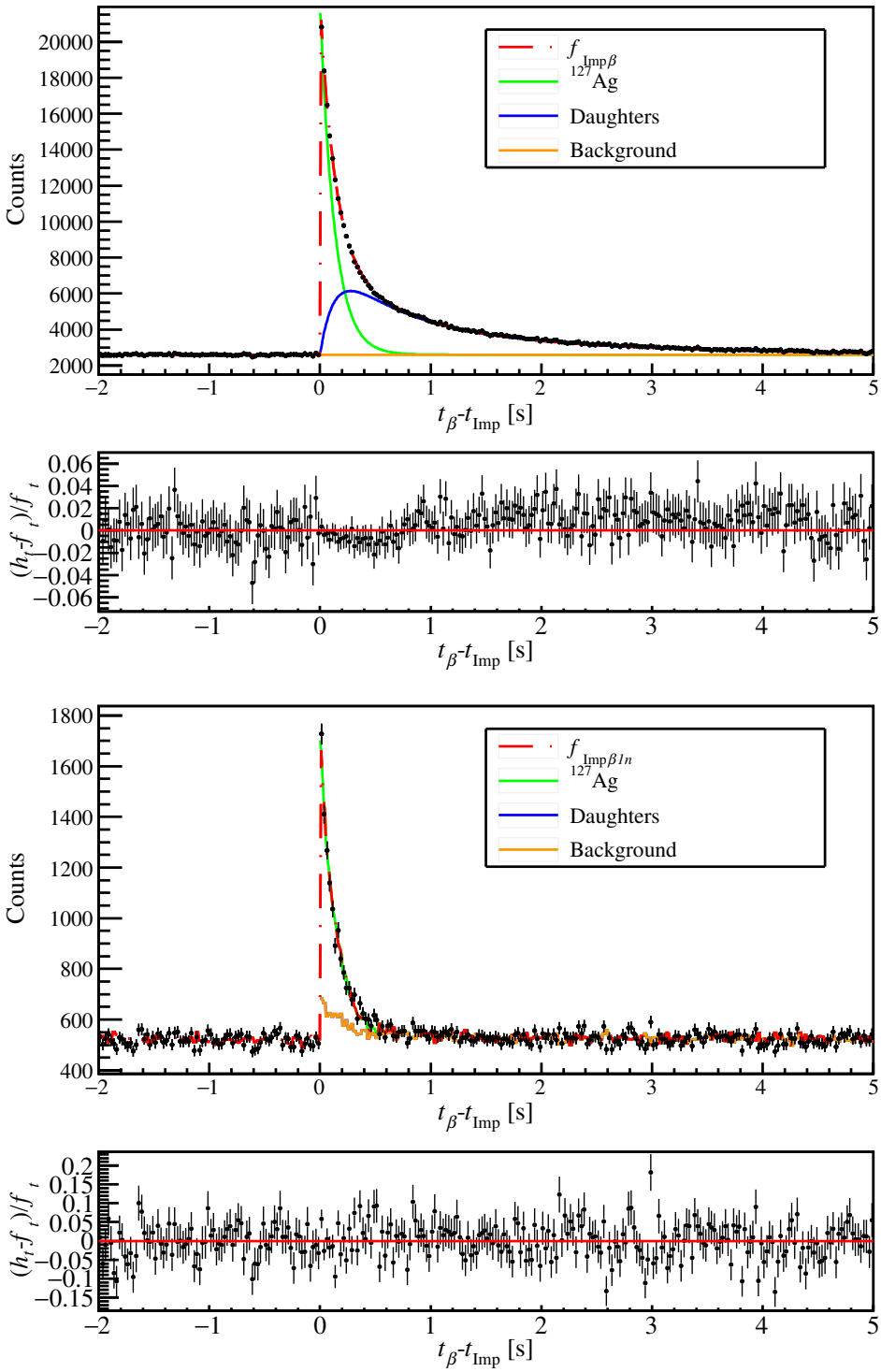

Figure 6.17 *Fits of the simulated ^{127}Ag decay curves. Top panel is the ungated decay curve and the bottom panel is the single-neutron gated. Below each of the fits the reduced residuals are shown. The reduced residuals are calculated as the function subtracted from the data, divided by the value of the function at each point.*

Chapter 7

Results and Discussion

The main scientific aim of experiment RIBF128 and this thesis was the measurement of the β-delayed neutron emission probabilities of nuclides around the $N = 82$ shell closure. In addition to obtaining the delayed neutron emission probabilities, the half-lives of the nuclides are also obtained and included here. Results from this experiment form part of a more extensive experimental campaign, performed by the BRIKEN collaboration, to study these β-decay properties for nuclides across the nuclear chart that have been highlighted to be of importance to the r-process. Presented in this chapter are the half-lives and β-delayed neutron emission probabilities for nuclides of Ruthenium ($Z = 44$) to Cadmium ($Z = 48$). The values were obtained using the analysis methodology discussed in the previous chapter.

7.1 Final results

The half-lives, $t_{1/2}$, and β-delayed neutron emission probabilities, P_{1n} obtained in the analysis of experiment RIBF128 are presented below in Table 7.1. Also recorded in the table are literature values, where they exist, that have been taken from peer-reviewed journals. The uncertainties presented alongside the data are the combined statistical and systematic uncertainties. A small number of measurements that overlap with the nuclides presented here have been presented in earlier theses [204, 205]. The measurements have not been included in the table below as they have not been peer-reviewed. Instead, these measurements

have been presented and discussed in comparisson with the results of this work in Appendix A.

Table 7.1 *Half-lives and P_{1n} values measured in RIBF128 alongside literature values. ◊ indicates values for which a long-lived isomeric state has been measured previously in the parent nuclide, the state information is given in the nuclide column.*

	$T_{1/2}$ [ms]		P_{1n} [%]		
Nuclide	This Work	Literature	This Work	Literature	Ref.
^{116}Ru	200(11)	204(6)	0	-	[127]
		204^{+32}_{-29}		-	[206]
^{117}Ru	162(9)	151(3)	2.4(10)	-	[127]
		142^{+18}_{-17}		-	[206]
^{118}Ru	98(10)	99(3)	1.5(19)	-	[127]
		123^{+48}_{-35}		-	[206]
^{119}Ru	57(13)	69.5(20)	6(5)	-	[127]
^{120}Ru	48(17)	45(2)	6(3)	-	[127]
^{121}Ru	37(5)	29(2)	13(4)	-	[127]
^{118}Rh	294(17)	285(10)	2.1(9)	-	[127]
		266^{+22}_{-21}		3.1(14)	[206]
		300(60)		-	[207]
^{119}Rh	192(12)	190(6)	3.4(9)	-	[127]
		171(18)		6.4(16)	[206]
^{120}Rh	150(15)	131(5)	7.2(16)	-	[127]
		136^{+14}_{-13}		≤ 5.4	[206]
		120(10)		-	[208]
^{121}Rh	73(2)	76(5)	13.4(8)	-	[127]
		151^{+67}_{-58}		-	[206]
^{122}Rh	52.4(15)	51(6)	11.3(7)	-	[127]
^{123}Rh	42.2(18)	42(4)	24.2(14)	-	[127]
^{124}Rh	35(3)	40(2)	28(5)	-	[127]
^{121}Pd	290(20)	290(1)	0	-	[127]
		285(24)		≤ 0.8	[206]
^{122}Pd	203(12)	195(5)	0.7(8)	-	[127]
		175(16)		≤ 2.5	[206]
^{123}Pd	114(2)	108(1)	1.4(3)	-	[127]
		174^{+38}_{-34}		-	[206]

Continued on next page

	$T_{1/2}$ [ms]		P_{1n} [%]		
Nuclide	This Work	Literature	This Work	Literature	Ref.
^{124}Pd	94(3)	88(15)	0.89(3)	-	[127]
		38^{+38}_{-19}		-	[206]
^{125}Pd	64.4(17)	57(10)	3.7(4)	-	[127]
^{126}Pd	51(3)	48.6(12)	4.9(9)	-	[127]
		48.6(12)		-	[209]
^{127}Pd	39(5)	38(2)	9(3)	-	[127]
^{128}Pd	53(10)	35(3)	10(7)	-	[127]
^{124}Ag	205(17)	180(3)	2.3(11)	-	[127]
		191(28)		-	[210]
		540(80)		-	[211]
		170(30)		-	[212]
		172(5)		-	[213]
		187^{+15}_{-14}		1.3(9)	[206]
^{125}Ag	146(11)	150(8)	2.2(11)	-	[127]
		166(7)		-	[213]
^{126}Ag	103.2(14)	98(5)	3.8(2)	-	[127]
		92(9)		-	[210]
		107(12)		-	[213]
		95		-	[214]
^{127}Ag	89.1(9)	89(2)	5.5(2)	-	[127]
		109(25)		-	[213]
^{128}Ag	67.4(16)	59(5)	9.3(5)	-	[127]
^{129}Ag	57(3)	52(4)	17.7(15)	-	[127]
		46^{+5}_{-9}		-	[215]
^{127}Cd	340(30)	330(20)	0.2(6)	-	[127]
		430(3)		-	[216]
		300(30)		-	[217]
^{128}Cd	243(11)	245(5)	0.7(7)	-	[127]
		246.2(21)		-	[128]
		260(20)		-	[217]
		340(30)		-	[216]
^{129}Cd	160.1(13)	154.5(20)	1.65(13)		[127]
◊ $3/2^+$		157(8)		-	[128]

Continued on next page

	$T_{1/2}$ [ms]		P_{1n} [%]		
Nuclide	This Work	Literature	This Work	Literature	Ref.
◊ $11/2^+$		147(3)		-	[128]
		155(3)		-	[218]
^{130}Cd	135.5(17)	127(2)	3.2(2)	-	[127]
		126(4)		-	[128]
		162(7)		3.5(10)	[219]
		195(35)		-	[220]

7.2 Discussion of half-lives

From looking at the data in Table 7.1 it is clear that on average, the half-lives obtained during the experiment are in excellent in agreement with previous measurements. A notable source of comparison is the half-lives published by Lorusso *et al.* [127] in 2015 on an experiment also performed at RIKEN, as comparisons can be made for all nuclei measured in this work. For many of the half-lives measured in this work, Lorusso *et al.* forms the only other measurement making this work a good validation of these previously published results. In order to more easily compare the half-lives presented in this work and those in Lorusso *et al.*, the half-lives have been plotted next to each other with their respective error bars in Figure 7.1. From the figure, it can be seen that there is good agreement between the data sets with no discernible systematic differences between the two. The agreement between these two sets gives confidence to these measurements of very neutron-rich nuclei.

7.2.1 Systematic evolution of half-lives

It is often of interest to see how the half-lives of an element's isotopes evolve with increasing neutron number. To do this, Figure 7.2 shows the half-lives measured in this thesis against their isotope's neutron number. When looking at the figure, a similar trend can be seen across all the isotopic chains, with the half-lives showing a steep decrease in the half-life at first but then a more gradual change in the rate as they become more neutron-rich. $^{128}_{46}$Pd^{82} appears as an exception to the trend, where an increase in the half-life from $^{127}_{46}$Pd^{81} is observed. The

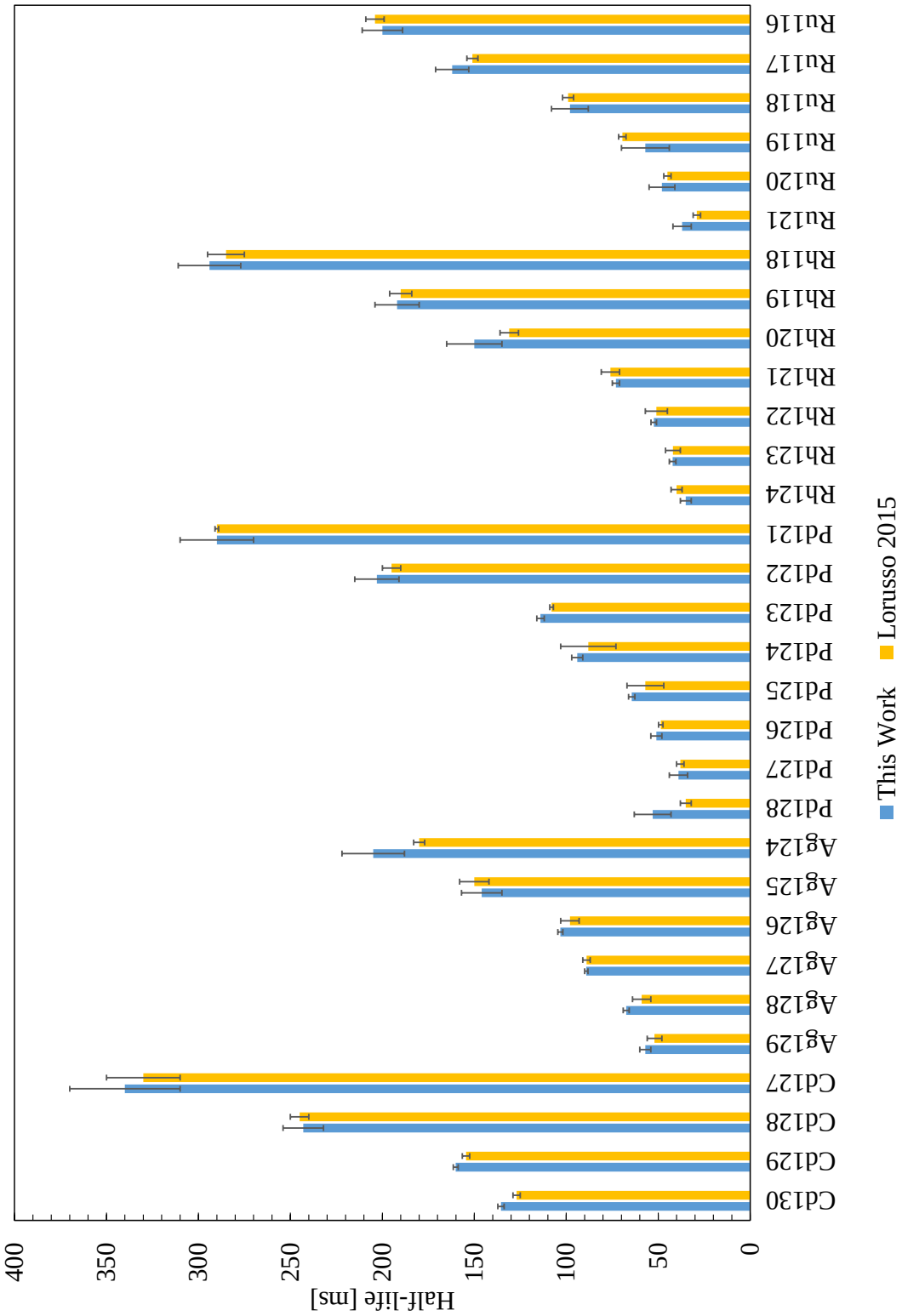

Figure 7.1 *Comparison between measured half-lives in this work and those published in Lorusso 2015 [127]. Errors bars are the combined statistical and systematic errors.*

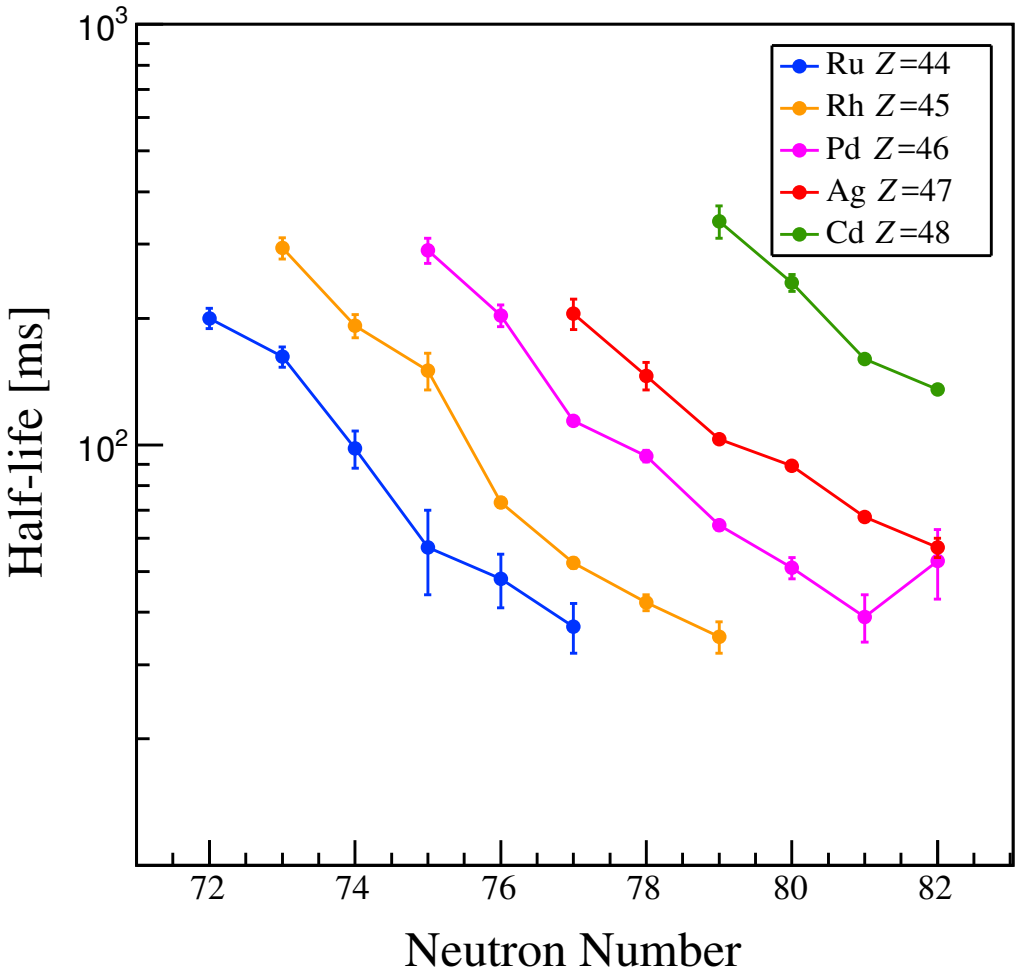

Figure 7.2 *The development of the half-life measured in this work with increasing neutron number for each of the isotopic chains.*

location of this increase is at the closed, $N = 82$, neutron shell. When looking at the literature half-lives reported for $^{126}_{45}\mathrm{Rh}^{81}$ and $^{127}_{45}\mathrm{Rh}^{82}$, the neighbouring element to Pd, a similar increase in half-life is observed [127] upon reaching the $N = 82$ shell closure. The behaviour in $^{128}_{46}\mathrm{Pd}^{82}$ could then be a structure effect that is observed at lower atomic numbers but disappears when approaching the $Z = 50$ closed proton shell. In addition to $^{128}_{46}\mathrm{Pd}^{82}$ two other $N = 82$ nuclides are included in this data set, them being $^{129}_{47}\mathrm{Ag}^{82}$ and $^{130}_{48}\mathrm{Cd}^{82}$, neither of which appear to show any deviations in the trend of decreasing half-life.

When looking at the half-lives presented in Table 7.1, the half-lives of this work and Lorusso *et al.* are often the two most precise values. A weighted average of the half-lives measured in this work and those of Lorusso *et al.* is included in Figure 7.3. The same downward trend continues to be observed for all elements.

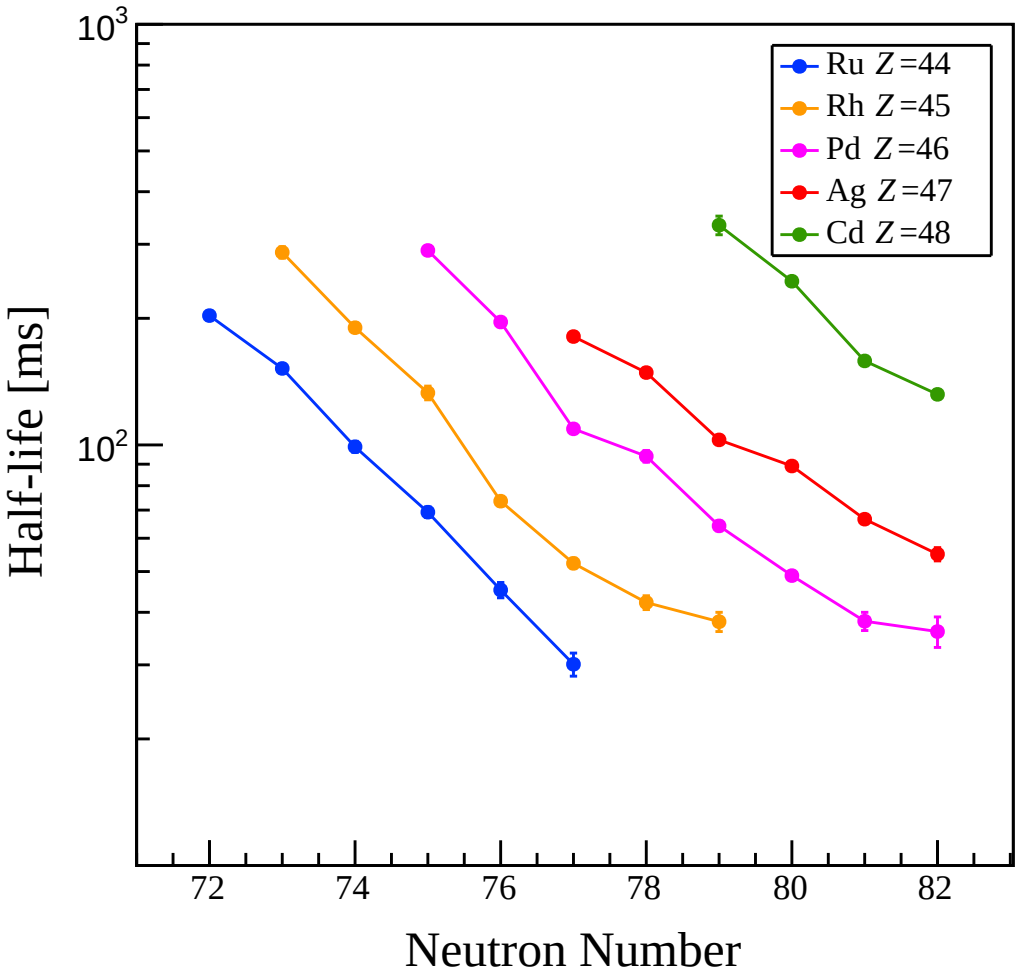

Figure 7.3 *Weighted averages of half-lives measured in this work and of Lorusso et al. plotted as a function of neutron number.*

Performing a weighted average also has the effect of bringing the half-life of ^{128}Pd down such that it is less than ^{127}Pd. While the half-life no longer increases between ^{128}Pd and ^{127}Pd, a change in the trend is still observed. The smooth decreasing half-life that was previously observed begins to level out as the rate of change in the half-life decreases.

7.2.2 Comparisons to theory

By comparing the half-lives and trends in the half-lives predicted by theoretical models to the half-lives measured in this thesis, the ability of the models to predict values in this region can be tested. This is of importance as in some

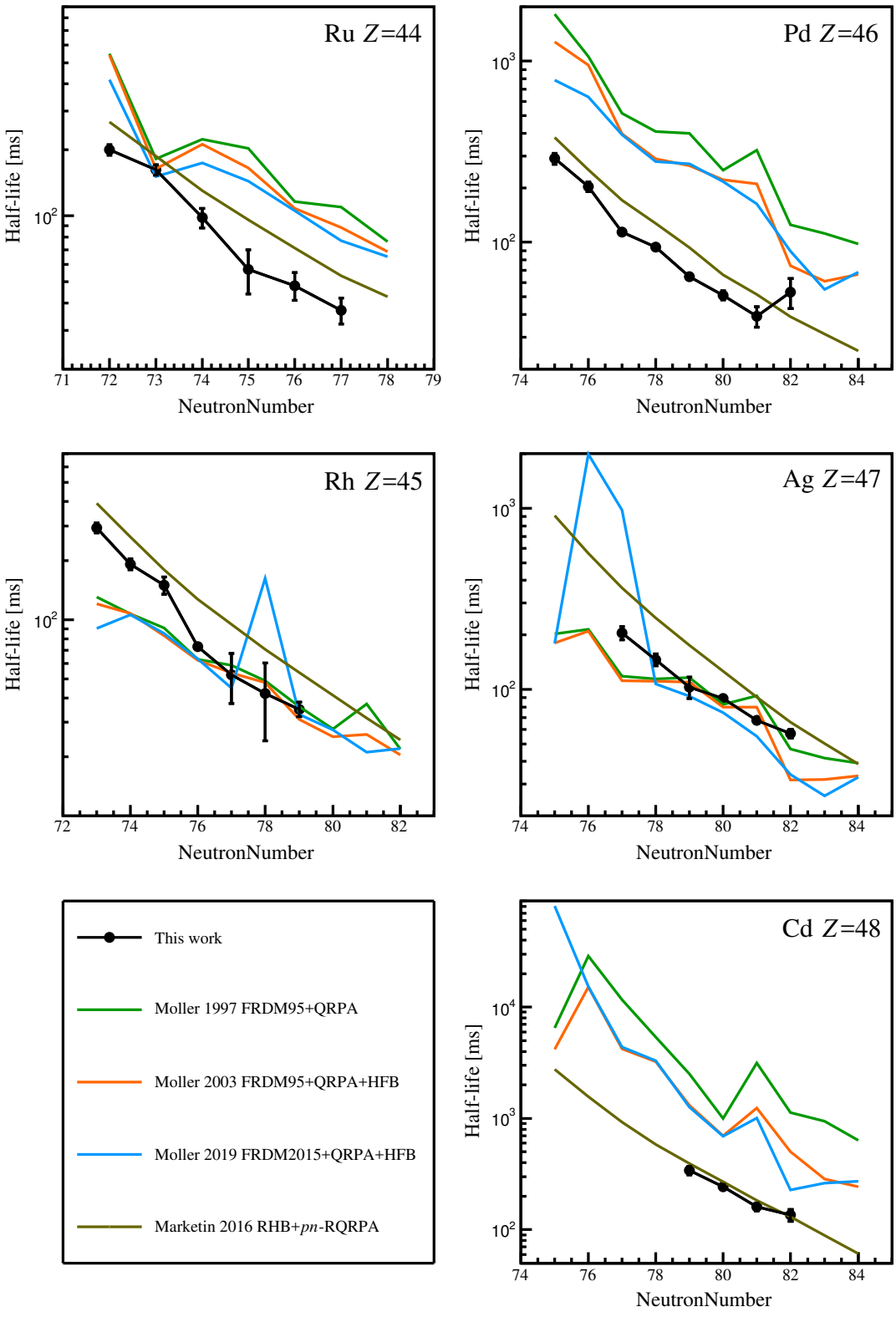

Figure 7.4 *Comparison of the measured beta-decay half-lives alongside a selection of theoretical predictions. References for the models can be found as: Möller 1997 [100], Möller 2003 [99], Möller 2019 [101] and Marketin 2016 [106].*

cases the half-lives presented here are at, or near, the limits of experimentally measured values. Calculations involving nuclides beyond those presented here will have to use predicted values. In Figure 7.4, the half-lives measured in this work are plotted alongside half-lives predicted from four models. The first three models chosen were based on the FRDM+QRPA produced by Möller *et al.*. The FRDM+QRPA models included are the original model from 1997 [100], the 2003 revision [99] and the most recent revision released in 2019 [101]. Of these three data sets, the 2003 revision is of particular interest as the half-lives calculated in it are commonly used as the base values for r-process calculations. The final half-life model included is the RHB+pn-RQRPA, produced by Marketin [106], and introduced in section 2.3.1. From section 2.3.1 it can be recalled that the key differences between the FRDM+QRPA and RHB+pn-RQRPA models are that the FRDM+QRPA uses a hybrid macroscopic-microscopic approach to determine the ground state properties of the nuclei, whereas, the RHB+pn-RQRPA model uses a fully self-consistent microscopic approach.

From Figure 7.4, it can be seen that the values predicted by FRDM+QRPA appear to show a better agreement for odd values of Z than for even values. This is especially seen to be the case for Pd, $Z = 46$, where the half-lives predicted are on average five times larger in FRDM+QRPA 2019 than those measured here. It is also interesting to note that with each new version of the FRDM+QRPA model, the model better reproduces the experimentally measured data, barring a couple of extreme cases such as Rh $N = 78$. Another feature common to the model is odd-even fluctuations which are not observed to the same extent in the data. This has previously been put down to the neglecting of particle-particle (pp) interactions, which results in the destruction of odd-even symmetry in the QRPA [221]. In contrast, the half-lives predicted by Marketin *et al.* show no evidence of odd-even staggering and instead show a smooth decrease in the half-life. However, the smoothness predicted by the model means that it is not able to replicate steps in the half-life, examples of this can be seen for Ru N=74 and Rh $N = 75$. On average, the half-lives predicted using the RHB+pn-RQRPA method show a much better agreement to the measured values for all values of Z than those predicted using FRDM+QRPA.

7.3 β-delayed neutron emission probabilities

Many of the P_{1n} values presented in this work are presented for the first time, with 23 of the P_{1n} values shown here not appearing previously in peer-reviewed sources. Previously published P_{1n} values are primarily found for some of the less neutron-rich Rh and Pd nuclides, where comparisons can be made with the work of Montes *et al.* [206]. For these nuclides, a good agreement can be seen between the two experiments with the majority of P_{1n} values being within uncertainties of one another. The good agreement found with these previous measurements, along with the tests carried out in section 6.7 give confidence to the values presented here for the more neutron-rich nuclides.

7.3.1 Systematic evolution of β-delayed neutron emission probabilities

Figure 7.5 shows the measured P_{1n} values as a function of neutron number. It can be seen that along all the isotopic chains, a gradual increase in P_{1n} is observed with increasing neutron number. However, there are nuclides where deviations from this trend are observed, such as Rh at $Z = 77$ and Ru at $Z = 74$. Another trend observed is that elements that have a higher proton number have a smaller P_{1n} value at a given neutron number than those with fewer protons, this is expected as the elements with a higher Z are likely less far from stability. Groupings in the P_{1n} values can also be seen between elements at each neutron number. For example, at $N = 77$, it is observed that the values presented for Ru and Rh are very close to one another and separated from these are the values for Pd and Ag which again show similarities. These pairings are observed at all neutron numbers with the only points where it is not observed occurring at the deviations mentioned previously of Rh and Ru. The P_{1n} values predicted by Möller in [101] also reproduce these pairing patterns.

7.3.2 Comparisons to theory

In section 2.3.1, it was shown that the models used to calculate the half-lives of nuclei could also be used to calculate the P_{1n} value of nuclei too. In the case of the FRDM+QRPA model, it was shown that this was calculated as the

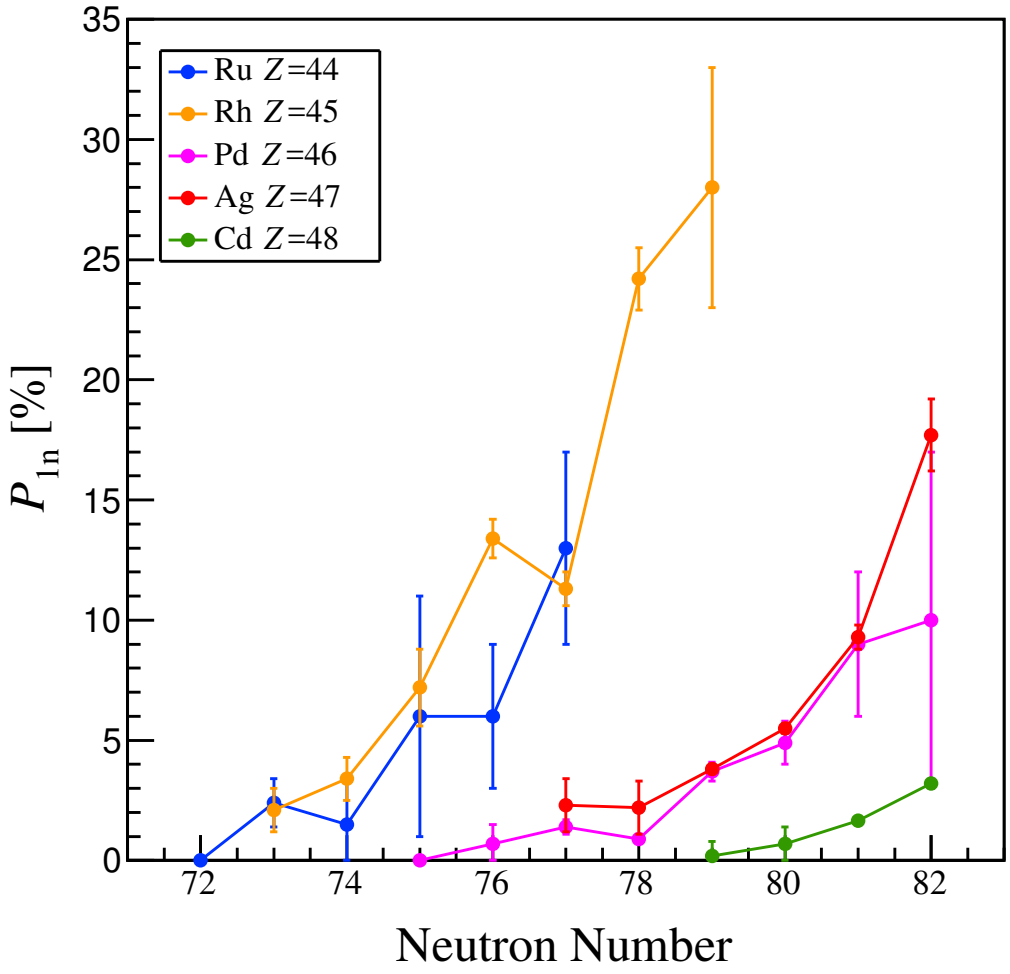

Figure 7.5 *The development of the P_{1n} values measured in this thesis with increasing neutron number for each of the isotopic chains.*

percentage of decays populating an excited state above the daughter's neutron separation energy, and the effects of de-excitation via emission of γ-rays were ignored. In this section the calculated P_{1n} values of the models discussed in section 2.3.1 will be compared to the P_{1n} values measured in this thesis. In addition to the four models that were used in the comparison of half-lives, a fifth model is included. This model is the effective density model (EDM), of Miernik [107], that was also introduced in section 2.3.1. This model differs from both FRDM+QRPA and RHB+*pn*-RQRPA, as it is a phenomenological model and was optimised by fitting parameters to experimentally measured P_n values and extending it to nuclei that there were no experimental measurements of at the time of creation. The comparison with theoretical predictions is split across two figures to try to limit them from being too dense. The first figure, Figure

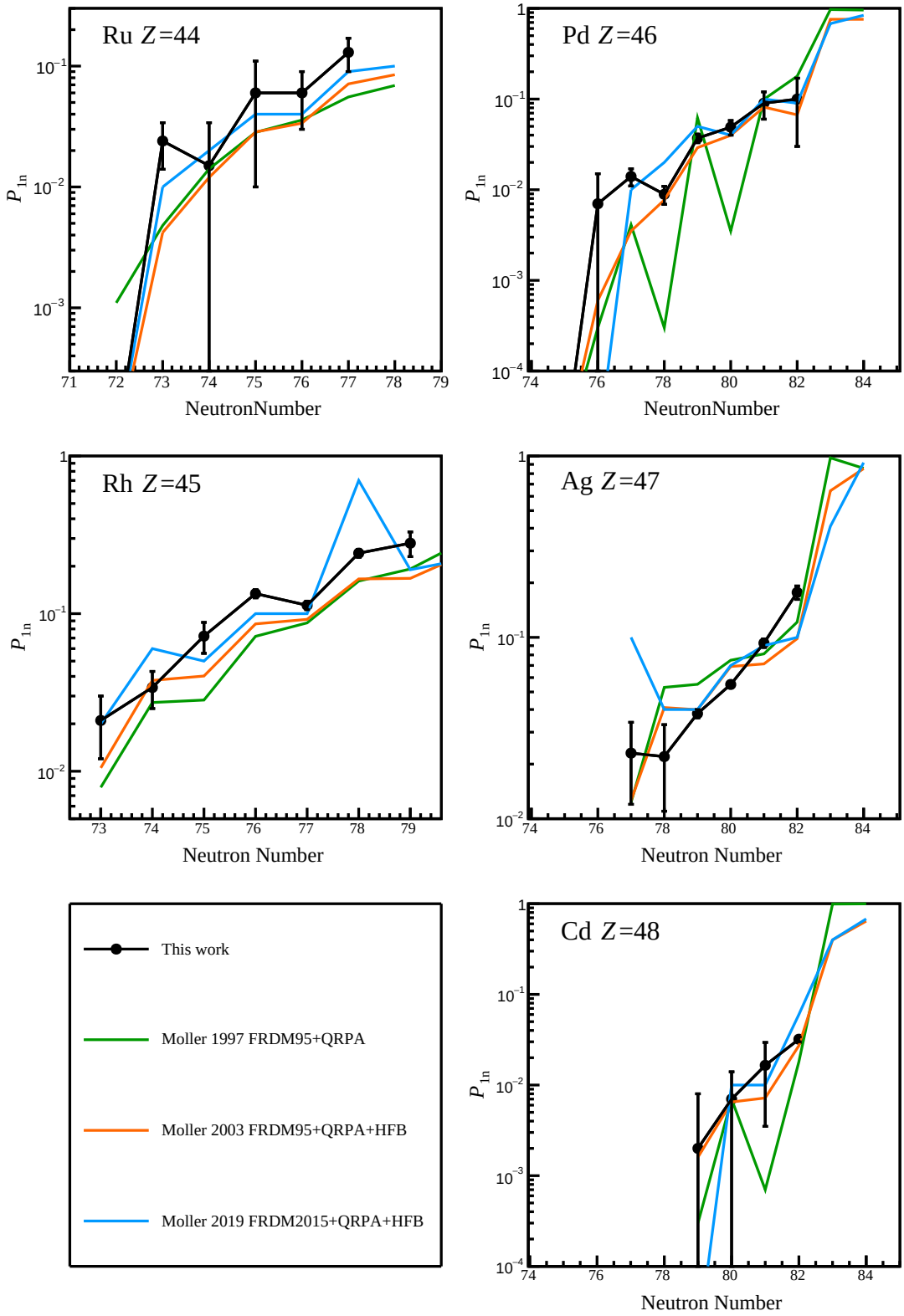

Figure 7.6 *Comparison of the measured β-delayed neutron emission probabilities alongside a selection of theoretical predictions. References for the models are: Möller 1997 [100], Möller 2003 [99], Möller 2019 [101]*

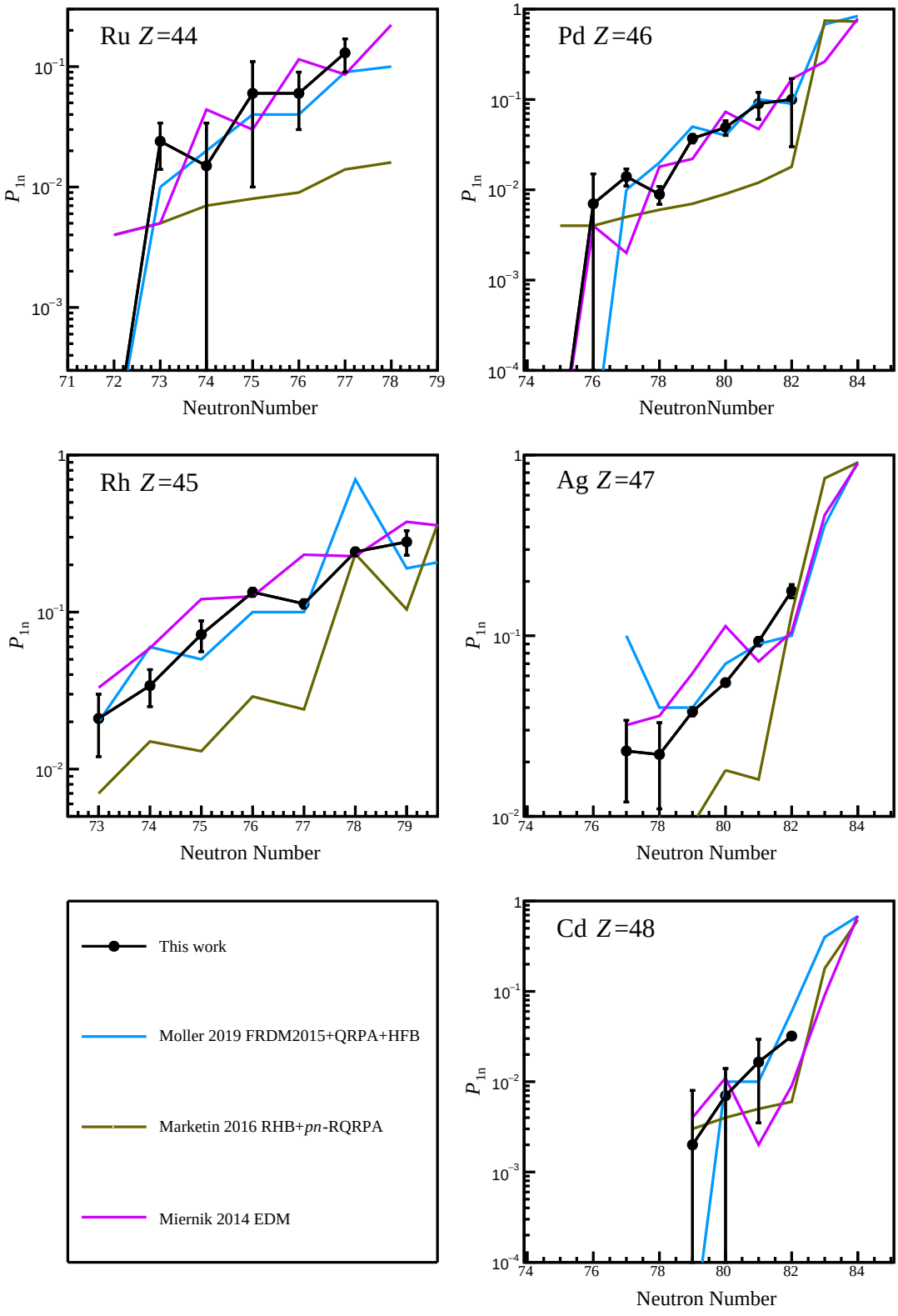

Figure 7.7 *Comparison of the measured β-delayed neutron emission probabilities alongside a selection of theoretical predictions. References for the models are: Möller 2019 [101], Marketin 2016 [106], Miernik 2014 [107].*

7.6, shows the P_{1n} values measured in this thesis along with those calculated in each of the three FRDM+QRPA models, to show the development of the model with each revision. The second figure, Figure 7.7, shows the P_{1n} values measured in this thesis alongside P_{1n} values calculated using the newest revision of the FRDM+QRPA models, the RHB+*pn*-RQRPA model and the EDM. This figure allows comparisons to be made among the three approaches of: hybrid macroscopic-microscopic, fully microscopic and phenomenological in calculating the P_{1n} values of nuclei.

When comparing the P_{1n} values measured in this work to those predicted by FRDM+QRPA in Figure 7.6, good agreement is seen for most nuclei, with the values predicted by FRDM+QRPA reproducing the trend of the half-lives well. It is also seen that typically with each new revision of FRDM+QRPA the half-lives predicted are closer to the measured values, with the 2019 revision reproducing the measured values best. The P_{1n} values predicted by RHB+*pn*-RQRPA, shown in Figure 7.7, show little agreement to the measured values; this is a stark contrast to how it performed in predicting the half-lives where it was seen to perform best out of the models compared. The P_{1n} values calculated are consistently less than the values measured. The values calculated using the EDM are seen to be in better agreement with the measured values than those calculated by RHB+*pn*-RQRPA.

Also included in the figure are the calculations for the P_{1n} values of nuclides with neutron number greater than $N = 82$, the limit of values measured in this work. Beyond $N = 82$ a sharp increase in the P_{1n} is predicted immediately at $N = 83$, a feature common to all models, this is of interest as these are nuclides that β-decay into the closed neutron shell at $N = 82$. This increase could be as a result of the increase in the Q-value for β-decay beyond $N = 82$, for example, the predicted Q_β of $^{130}_{47}\mathrm{Ag}_{83}$ is over 4 MeV larger than that of $^{129}_{47}\mathrm{Ag}_{82}$ in FRDM+QRPA 2019 [101]. A larger Q_β could also make the population of states above the S_n of nuclei more probable, leading to an increased P_{1n} value.

7.3.3 Dependence on $Q_{\beta n}$

As shown in Eq. 2.17, the P_n value of a nuclide in the FRDM+QRPA model is defined as the probability of a decay populating a state above the neutron separation energy of its daughter. For this to occur, the Q-value of the β-decay must be larger than the neutron separation energy of the daughter. Using the

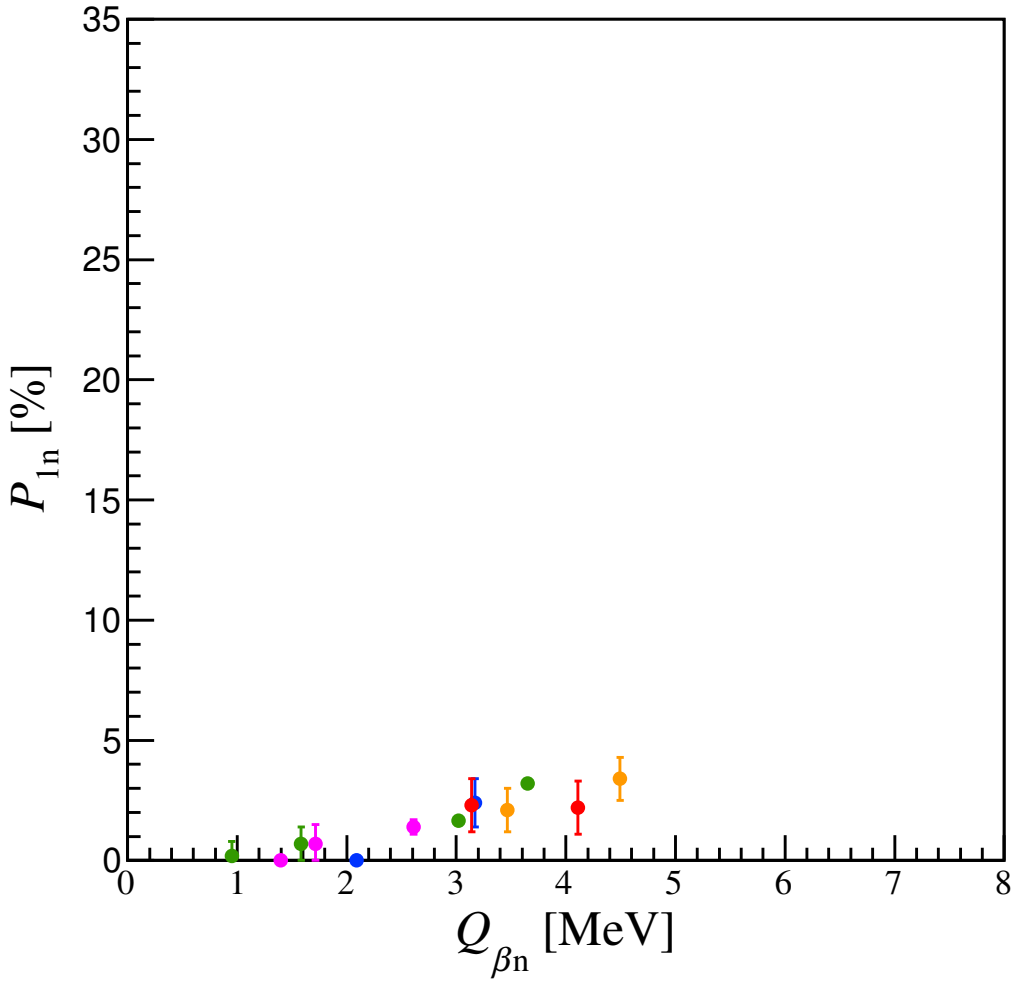

Figure 7.8 *P_n values measured during RIBF128 plotted as a function of experimentally measured $Q_{\beta n}$ values obtained from the 2016 Atomic Mass Evaluation [109]. Colouring of points is the same as was used for P_{1n} vs N.*

definition of neutron separation energy in Eq. 2.5 the $Q_{\beta n}$-value of an nuclide can be calculated as

$$Q_{\beta n}\left({}^{A}_{Z}X\right) = \left[m\left({}^{A}_{Z}X\right) - m\left({}^{A-1}_{Z+1}X\right) - m_n - m_e\right]c^2, \tag{7.1}$$

where m_e is the mass of an electron. Even though the FRDM+QRPA model does not take into account possible de-excitation through γ-ray emission, it might be expected then that larger $Q_{\beta n}$-values may lead to larger P_n values, as there is a greater range of states available above the neutron separation energy. This section investigates if any correlation between these quantities may exist for the P_{1n} values measured in this thesis.

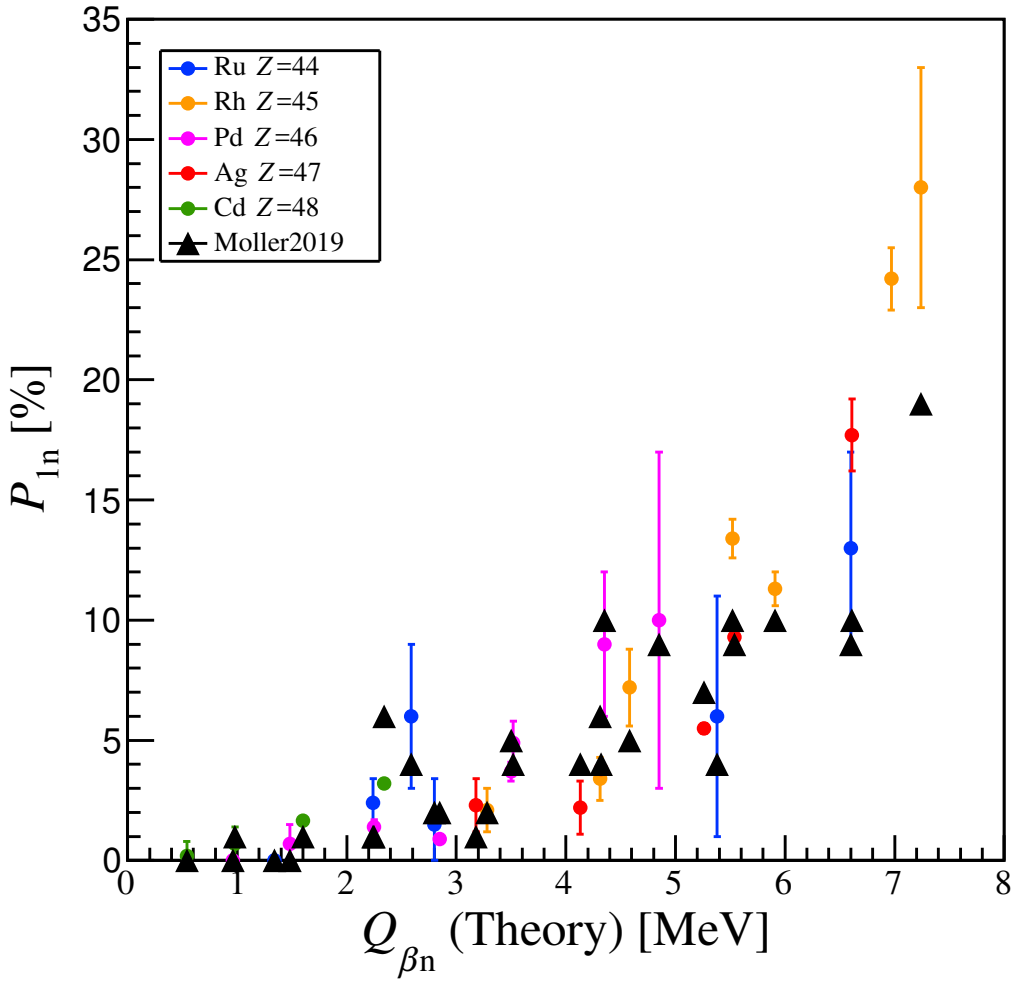

Figure 7.9 *Evolution of experimentally measured P_{1n} values against theoretically calculated $Q_{\beta n}$ values using a FRDM based mass model [101]. Also included are theoretically predicted P_{1n} values from the same reference.*

Atomic masses have been previously measured for a small number of the nuclei presented in Table 7.1, allowing the calculation of the $Q_{\beta n}$-value for each of these isotopes. The P_{1n} values of these nuclides have then been plotted against the nuclides's $Q_{\beta n}$-value to investigate any correlation between the two, this is shown in figure 7.8. From the figure, it is observed that for all of the nuclei plotted β-delayed neutron emission is energetically possible as all nuclides have a positive $Q_{\beta n}$. Despite this, no significant P_{1n} is observed until a $Q_{\beta n}$ of 2.5 MeV is reached at which point ^{123}Pd has a P_{1n} of 1.4%. Beyond this point, a smooth trend of increasing P_{1n} with increasing $Q_{\beta n}$ is observed up to the extent of the currently measured experimental masses.

To test whether this relationship extends to higher $Q_{\beta n}$-values the masses of more neutron-rich nuclides are needed. As these are currently beyond the limit of experimentally measured masses, theoretical predictions are used instead. Figure 7.9 shows the P_{1n} values measured in this work as a function of $Q_{\beta n}$ calculated using the FRDM2015 mass model [112]. Also included in the figure are the theoretical calculations of P_{1n} from FRDM+QRPA2019 [101], which are calculated using the masses from FRDM2015, for comparison. The trend observed using the experimentally measured masses is once again observed at lower $Q_{\beta n}$-values, showing an increase in P_{1n} as the $Q_{\beta n}$ increases. Going beyond 4.5 MeV, the highest experimentally measured $Q_{\beta n}$-value, the trend appears to continue with the rate of increase in P_{1n} increasing at large $Q_{\beta n}$-values for the measured P_{1n}. It is also observed that for small $Q_{\beta n}$-values, the FRDM+QRPA predictions show good agreement with the measured P_{1n} values. However, at larger values of $Q_{\beta n}$, it is observed that the calculated P_{1n} values are often much lower than those measured in this work.

Chapter 8

Astrophysical Implications

In addition to providing reference points for the optimisation of future theoretical models, the half-lives and β-delayed neutron emission probabilities presented in this thesis can be used as direct inputs in r-process reaction network calculations. In this chapter, the impact of these new values on calculated r-process abundances is investigated.

8.1 *SkyNet*: Nuclear reaction network

SkyNet is an open-source nuclear reaction network that evolves the abundances of nuclear species as they undergo nuclear reactions [222]. Multiple astrophysical scenarios can be evolved using the code such as X-ray bursts, hydrostatic carbon-oxygen burning and neutron-rich r-process calculations [223]. Object-orientated C++ is employed to make the program highly modular; this allows the code to perform well under the many astrophysical scenarios. The modularity allows the fine-tuning of physical behaviour to match the required conditions for the various scenarios.

In this thesis *SkyNet* is used to evolve a reaction network for a neutron-rich r-process. The evolution of the network is carried out from a starting point obtained from Nuclear Static Equilibrium (NSE), which is calculated from a user-provided set of initial parameters. Following on from NSE as the temperature drops, the program begins to evolve the reaction network. After the neutron flux powering the r-process ceases, the program follows the decay chains back to

stability, including branching caused by β-delayed neutron emission. The output of the calculations is a list of abundances matched to mass numbers A, which can be compared to the solar r-process abundances.

8.1.1 Input rates

In order to propagate the reaction network, a list of all possible reactions and their accompanying rates is required. The version of *SkyNet* used in this work obtains the reaction rates from the REACLIB [224] database provided by the Joint Institute for Nuclear Astrophysics (JINA). In the database, reaction rates are given as parameters that are used in a parametric fitting formula that depends on temperature. This allows the determination of a reaction rate at a given temperature. To model the heating that is produced by the reactions, the Q-values of the reactions are also included.

In the case of a r-process network calculation, the most significant rates will be the β-decay rates and any β-delayed neutron emission probabilities for exotic nuclei along the r-process path. The β-decay rates will play a key role in determining the path of the r-process during the process, and the β-delayed neutrons will continue to shape the distribution of final abundances after freeze-out. In the base version of REACLIB, these rates and probabilities are obtained from the Möller 2003 [99] gross calculations.

The parameters provided by REACLIB can be converted into a temperature-dependent rate using the following equation [224]:

$$\lambda = \exp\left[a_0 + \sum_{i=1}^{5} a_i T_9^{\frac{2i-5}{3}} + a_6 \ln T_9\right] \tag{8.1}$$

where T_9 is the temperature in GK and a_i is each of the seven parameters, with i running from 0 to 6. From the equation it can be seen that all of the parameters except a_0 have a temperature dependence associated with them. For the case of β-decay, Eq. 8.1 can be simplified to:

$$\lambda = \exp\left[a_0\right] \tag{8.2}$$

where λ now only depends on the term a_0 as β-decay is temperature independent.

The parameter a_0 can then be calculated as:

$$a_0 = \ln \lambda. \tag{8.3}$$

For β-decay we can recall that λ, the decay constant, is given by $\lambda = \ln 2/t_{1/2}$. In REACLIB β-decay and β-delayed neutron emission are treated as two separate decay processes, therefore the total β-decay rate must be split between the two processes. Consequently, a value of λ calculated in this way cannot be used directly in Eq. 8.3 as the branching that occurs during β-delayed neutron emission needs to be accounted for. For example in the case of ^{127}Ag, a half-life of 89.1 ms was measured corresponding to a decay constant of $\lambda = 7.78$ s^{-1}. However the P_{1n} value of ^{127}Ag was measured to be 5.5%, therefore, only 94.5% of β-decays produce ^{126}Cd and the rest produce ^{125}Cd. The two values of λ needed can be calculated as:

$$\lambda_\beta = (1 - P_{1n}) \times \frac{\ln 2}{t_{1/2}} \tag{8.4}$$

$$\lambda_{\beta n} = P_{1n} \times \frac{\ln 2}{t_{1/2}} \tag{8.5}$$

where λ_β is the decay constant for β-decay with no neutron emission and $\lambda_{\beta n}$ is the decay constant for β-decay followed by a single neutron emission. These values can then be used in Eq. 8.3 to calculate the parameters a_0, for each decay process, that will be included in the REACLIB database file.

8.1.2 Input parameters

In addition to the reaction library, four input parameters are required by *SkyNet* to calculate the initial NSE from which the abundances are evolved. For r-process calculations the four parameters required are: the initial electron fraction, Y_e; the initial entropy, s; the expansion timescale, t_{exp} and the initial temperature, T. The electron fraction, initial entropy and initial temperature are the same as those discussed in Chapter 2. The expansion timescale is a parameter which determines how fast the density decreases during nuclear burning [121].

Of these values, it has been shown that the final abundance distribution of the r-process is most sensitive to the electron fraction [223, 225]. This is easily understood as this is equivalent to the proton fraction if the matter is neutrally charged. A low electron fraction, therefore, indicates a considerable fraction of

neutrons which is needed to push the r-process to higher masses.

8.2 Sensitivity study

To test the impact of the newly measured β-decay rates and β-delayed neutron emission probabilities on the final r-process abundance distributions, reaction network calculations were carried out. The calculations were performed using both the newly measured and existing theoretical rates to allow any changes in the final abundance distributions to be compared.

Rather than running the calculations for a single astrophysical environment, multiple calculations were performed covering a wide range of initial parameters. Changes in abundance were calculated for each set of initial conditions. An impact factor was used to quantify the changes in abundance observed across all mass numbers. The impact factor used was the same as defined in Eq. 2.20, allowing for comparisons to be made to the sensitivity studies shown in the introduction.

8.2.1 Choice of values

The final abundances produced by the r-process depend heavily on the initial electron fraction, Y_{e} as this sets the neutron density that drives the process out to neutron-rich nuclei. While the initial electron fraction has the most impact on the final abundance distribution, under certain conditions the initial entropy (s_0) and expansion timescales (t_{exp}) can play a role in determining the abundance distribution [121].

The initial electron fraction was varied over a range of $0.01 \leq Y_{\mathrm{e}} \leq 0.35$, with 0.01 being the most neutron-rich of initial conditions. The upper limit of 0.35 was chosen as it was previously found that for electron fractions greater than 0.35, at the entropies being studied, the $A \sim 130$ peak is not produced and therefore the new values will have no effect on the final r-process abundances.

The range of initial specific entropies was varied between 10 and 100 k_{B} baryon^{-1}, at values of 10, 20, 50 and 100 k_{B} baryon^{-1}. This range was chosen as it is similar to the range used by the creators of *SkyNet* when benchmarking the program against other reaction networks [121]. The largest effect the initial entropy has on the calculations occurs during NSE, where it determines the initial atomic

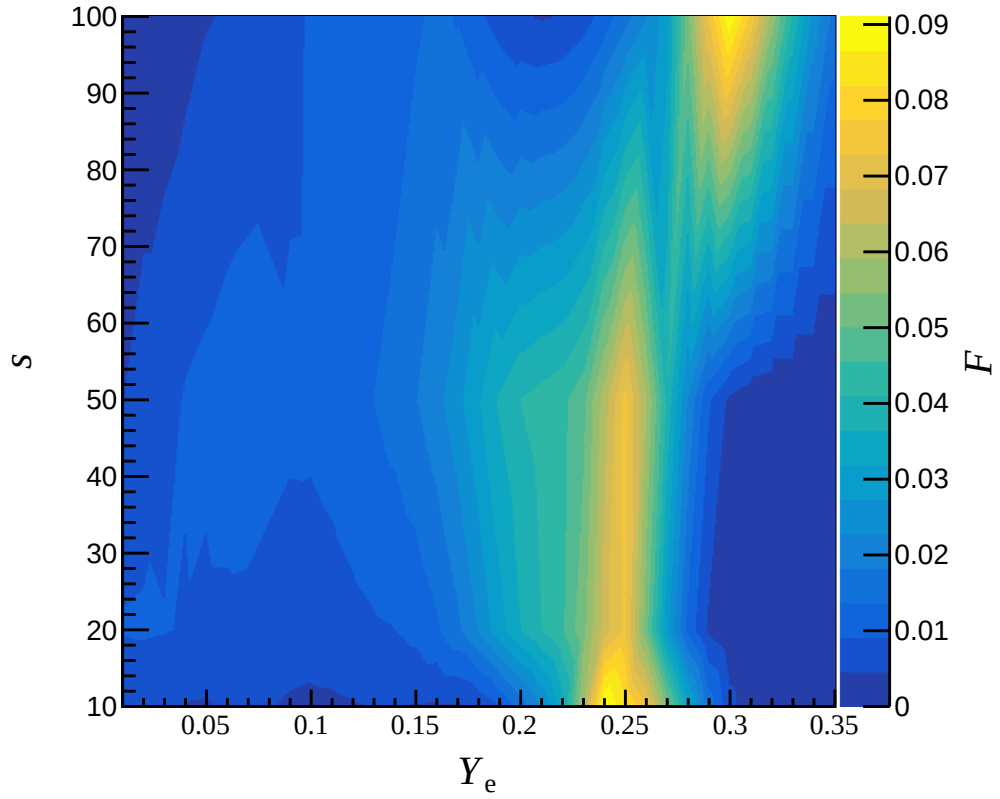

Figure 8.1 *Impact factor F showing the effect of the new β-decay rates and β-delayed neutron probabilities presented in this thesis.*

numbers of the seeds and the availability of free neutrons. Lower entropies will have initial seed nuclei with large atomic numbers but will have fewer free neutrons than are available at higher entropies where the initial seeds are lighter in comparison.

For the current calculations, the initial temperature was the same for all runs at $T_0 = 6.0$ GK. This temperature is high enough that fusion reactions are balanced by their inverse disintegration reactions allowing NSE to form. The expansion timescale was left at its default value of 7.1 ms for all of the runs.

8.2.2 Results

The results of the sensitivity study are shown in Figure 8.1, where the impact factor F is plotted for each of the initial conditions. It can be noted that the overall impact factor F calculated based on these simulations is seen to have less of an impact than in the sensitivity studies shown in Figures 2.5 and 2.6. A

much smaller impact is somewhat expected as the sensitivity studies performed in [95] varied the half-lives by a factor of 10 and tested the complete removal of β-delayed neutron emission for individual nuclides. The changes made to the decay rates and emission probabilities in these calculations were not as significant, as can be seen from Figures 7.4 and 7.6 where the new values are compared to the FRDM2003 rates and probabilities used during the calculations.

For low values of entropy, the maximum impact is seen at $Y_e = 0.24$. The low entropy will mean that the composition of the matter coming out of NSE is predominantly iron-rich; this will limit the neutron to seed ratio available for the r-process. This value of Y_e corresponds to around the maximum electron fraction that the r-process is still capable of reaching the $A \sim 130$ peak before the neutrons are exhausted at this entropy. As the majority of the r-process abundance builds up in the peak when this occurs, a significant impact is seen in the comparison of abundances using the new and baseline rates. At low values of entropy above $Y_e = 0.25$, the impact of the new values is seen to diminish quickly; this can be explained by the r-process path no longer reaching the second r-process peak, and thus the new rates are not encountered. At higher entropies, however, the most substantial impact is observed for $Y_e = 0.30$, this occurs for the same reasons as the peak at Y_e =0.25 at lower entropies. The reason for the shift in Y_e value between entropies can be described by the initial composition of matter, at larger entropies smaller seed nuclei are present, and a more prominent density of free neutrons is available. The greater density of free neutrons enables the second r-process peak to be reached at larger values of Y_e for higher entropies.

8.2.3 Calculated r-process abundances

In this section, the r-process abundances calculated during the sensitivity study are shown. Rather than showing the abundances calculated for all of the runs in the sensitivity study, a few select trajectories are shown in Figure 8.2. The first trajectory shown has initial conditions of Y_e=0.24 and $s = 10$; this trajectory was highlighted during the sensitivity study as showing the most impact for the new rates. It can be seen that for this trajectory, most of the abundance is held within the $A = 130$ peak, and the third r-process peak is no longer formed. The build-up in abundance was expected and given as a possible reason why a significant impact is observed for these conditions. A significant impact is also seen for the initial conditions of $Y_e = 0.30$ and $s = 100$, where the greatest abundance

observed is in the $A = 130$ peak. The main difference between the second and first trajectories is the maximum location of the peak. For the first trajectory, this peak is located at $A = 129$ whereas in the second it is located at $A = 126$. It should be noted that for all of the calculations, the abundances were normalised to the solar r-process abundances presented by Goriely *et al.* [13] at $A = 129$.

For both trajectories that the new rates were shown to have maximum impact on, it has been seen that the abundance distributions were dominated by the production of the second r-process peak and unable to produce the third peak at $A = 194$. In order to better reproduce the full r-process abundance distribution, a third trajectory is shown. This trajectory starts with a more neutron-rich electron fraction of $Y_e = 0.14$ and a moderate entropy of $s = 20\ k_B/b$, these are conditions similar to those predicted by models of binary neutron-star mergers [226]. The more neutron-rich initial conditions allow the production of both the $A = 130$ r-process peak and the third peak at $A = 194$. For this trajectory, the isobars just beyond $A = 130$ are shown to be overproduced as the peak is shifted to the right from the solar r-process abundances. This result appears typical of current r-process calculations performed using *SkyNet* and is observed in references [36, 226]. It has been noted in papers that this shifting of the peaks could be as a result of the β-decay rates predicted by FRDM+QRPA [227], and that faster β-decay rates will help in producing the r-process peaks in their correct locations. It is worth noting then that the maximum impact of β-delayed neutron emission probabilities observed in Figure 2.6 are beyond $N = 82$, where nuclei predominantly have $A \geq 130$, as these studies were also carried out using FRDM+QRPA2003. A build-up of abundance in this region would cause individual P_{1n} values to have a large impact factor as the impact factor used does not take into account the relative abundances of the nuclei. In their paper, the authors note that the global measure F used is not well suited to this kind of sensitivity study, and stated that future works would examine alternative local sensitivity measures to P_n values [95]. To fully investigate the effects of the new half-lives and β-delayed neutron probabilities measured by the BRIKEN collaboration, it will likely require all of the measured rates to be combined. The combination of the results is planned for future works.

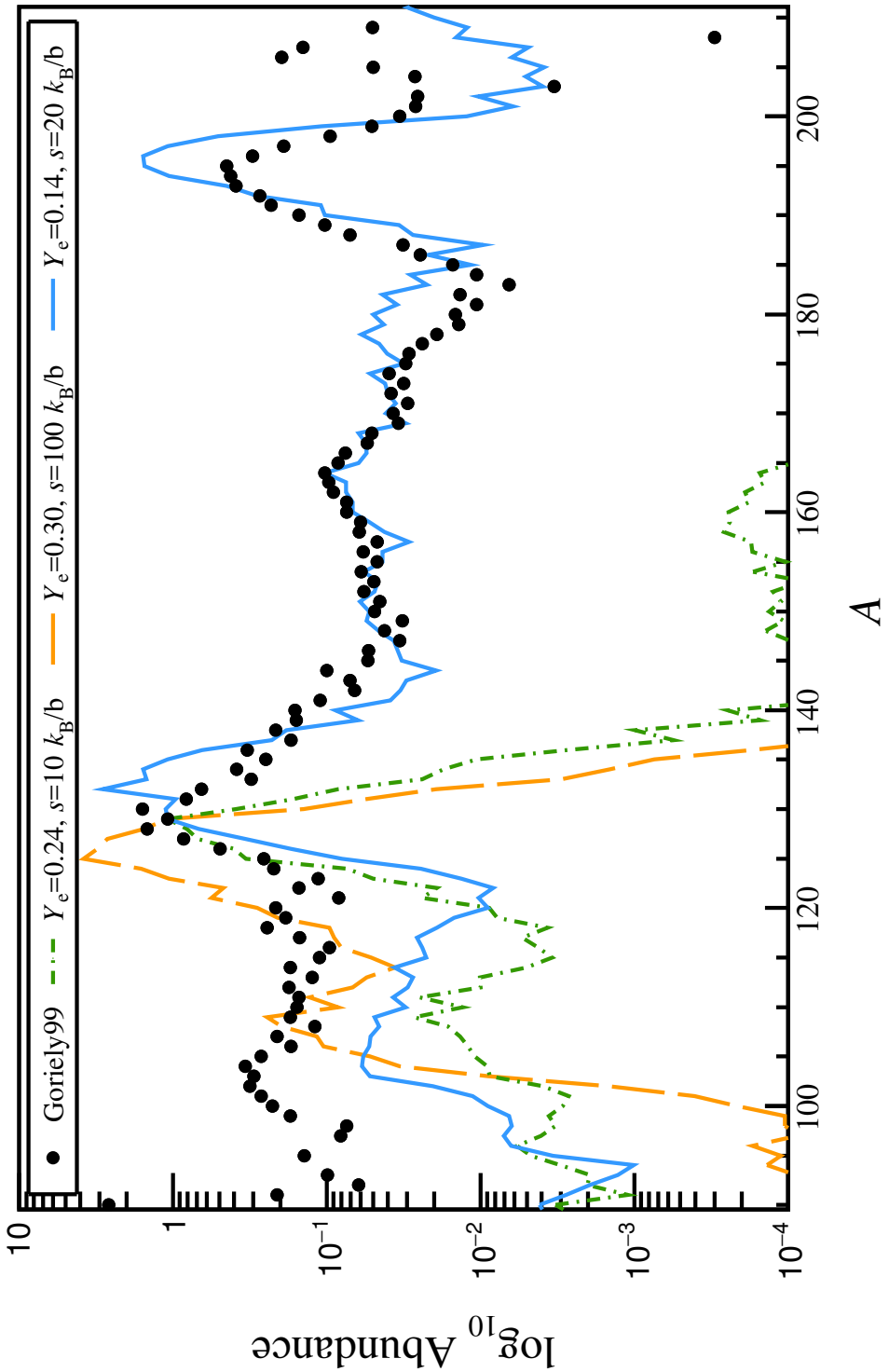

Figure 8.2 *Calculated r-process abundances using SkyNet, updated to include the new rates from this thesis. Three initial trajectories are shown: two highlighted by the sensitivity study performed as being the most impacted by the new rates and a third neutron rich trajectory.*

Chapter 9

Conclusions

The rapid neutron-capture process, or r-process, is thought to be responsible for the production of around half the elements heavier than iron. The main ideas of the r-process were first proposed in 1957, yet our understanding of how and where the process occurs is still lacking. Our ability to model the process computationally is hindered by a lack of experimental data on the nuclear properties of isotopes far from stability, primarily half-lives, β-delayed neutron emission probabilities, and nuclear masses.

This thesis provides much-needed reference data for the β-delayed neutron emission probabilities of isotopes at, or near, the $N = 82$ neutron shell closure. It provides 23 P_{1n} values that have not previously been published in peer-reviewed sources and improves upon the precision of a further four. The analysis methodology employed also allowed the extraction of an isotope's half-life, which resulted in the measurement of 32 half-lives. The half-lives and β-delayed neutron emission probabilities were obtained by measuring β-decay events using the AIDA system in correlation with neutrons measured by the BRIKEN neutron counter array. The experiment was performed at the Radioactive Ion Beam Factory at RIKEN.

The half-lives measured in this thesis are in excellent agreement with literature values, providing a second validation measurement for several isotopes that previously only had one measurement. The new P_{1n} values presented, push out the range of measured values towards much more neutron-rich isotopes than had previously been studied. Comparisons made between the $t_{1/2}$ presented in this thesis and values calculated using theoretical models showed that all

models were able to reproduce the overall trend of a smoothly decreasing half-live with increasing neutron number. However, the half-lives predicted using FRDM+QRPA were seen to show significant discrepancies for isotopes with an even Z, where the calculated half-lives were many times to large. The half-lives calculated using the RHB+pn-RQRPA model were shown to have the best agreement with the measured half-lives across all isotopes studied. However, the P_{1n} values calculated by the RHB+pn-RQRPA model were unable to reproduce the measured P_{1n} values, where the values calculated by the FRDM+QRPA model were seen to be in much better agreement. When plotting β-delayed neutron emission probability against experimentally measured $Q_{\beta n}$-values, a strong dependence was observed between the two values. This dependence was also observed for $Q_{\beta n}$-values calculated using the FRDM2012 mass model.

Calculations of r-process nucleosynthesis were performed using rates obtained from the $t_{1/2}$ and P_{1n} values measured in this thesis, carrying out a sensitivity study to determine initial conditions for the r-process that showed the most sensitivity to these new rates. The initial conditions highlighted by the sensitivity were shown to result in a build-up of abundance in the second r-process abundance peak and were unable to produce the full range of r-process abundances. A third more neutron-rich trajectory was also included, here the abundances were seen to be in much better agreement with the solar r-process abundances, but discrepancies were seen around the $A = 130$ peak. It is expected that the inclusion of rates from the other regions measured in the experiment may improve the shape of the peak, primarily for isotopes with $N > 82$ which analysis is being carried out on.

The $t_{1/2}$ and P_{1n} values measured in this thesis are some of the first values presented using the AIDA and BRIKEN detector systems. Since carrying out this experiment in 2017, further experiments have been performed, covering a wide range of the nuclear chart. As results from these experiments are also published, the list of known P_{xn} emitters will continue to grow, improving the accuracy of r-process calculations.

In addition to the continued work on r-process isotopes as part of the BRIKEN collaboration, AIDA is being used in nuclear structure studies as part of the Digital Total Absorption Spectrometer (DTAS) [228] group at RIBF. A second AIDA assembly is also in commissioning at GSI, as part of the Decay Spectroscopy (DeSpec) group. It is well placed to begin scientific research at the start of 2020 with the coming online of FAIR phase 0.

Appendix A

Previous values from non peer-reviewed sources

While performing a search of the literature, a few sources of previous measurements were found that were not published in peer-reviewed journals. The sources of these measurements were most commonly theses. While the table in Chapter 7 only included previous work that had been peer-reviewed, values from non-peer-reviewed sources are listed here for completeness.

The majority of the values included in this table come from the thesis of Dr Smith, that is on an experiment performed at GSI in 2013. The experiment was performed using a similar setup to the experiment reported in this thesis, in that ions were implanted into a detector stack that was surrounded by ^{3}He tubes located in a HDPE moderator. The ions were supplied as a bunched beam to the experimental setup. The β-background of the silicon detectors is, therefore, not constant and different analysis techniques must be used to subtract the β-background. A different methodology was also used to extract the β-delayed neutron emission probabilities of these nuclides. The experiment was performed alongside another experiment, which has since published the P_{n} values of nuclides above $N = 126$ [181, 229, 230].

The overlap in nuclides measured by Smith and those measured in this thesis covers several nuclides of the elements Rh, Pd and Ag. When comparing the half-lives measured in the Smith experiment to those presented in this thesis, the values measured in this thesis are often the most precise. For some of the less exotic nuclides such as ^{119}Rh and $^{124-125}$Ag agreements in half-life are observed.

However, the differences between the two experiments are seen to increase as the nuclides become more neutron-rich. While there is some agreement between the half-lives, there exists almost no agreement on the β-delayed neutron emission probabilities reported by Smith and those measured in this thesis. The P_{n} values reported by Smith are all larger than the values reported in this thesis, with the increases ranging from a factor of 2 to a factor of 10. One possible explanation for discrepancies between the two experiments is in the statistics available; for example, the number of implants observed for each nuclide were much greater in RIBF128 than is reported by Smith for their experiment. A much larger number of neutrons were then observed in RIBF128, reducing the uncertainty in our measurement and providing a much better ratio of delayed neutrons to background neutrons.

Table A.1 *Half-lives and β-delayed neutron emission probabilities measured in RIBF128 alongside non peer-reviewed literature values.*

	$T_{1/2}$ [ms]		P_{1n} [%]		
Nuclide	This Work	Literature	This Work	Literature	Ref.
^{119}Rh	192(12)	190(10)	3.4(9)	-	[205]
^{120}Rh	150(15)	120(10)	7.2(16)	-	[205]
^{123}Pd	114(2)	170^{+49}_{-52}	1.4(3)	10(6)	[204]
^{124}Pd	94(3)	144^{+17}_{-18}	0.89(3)	17(5)	[204]
^{125}Pd	64.4(17)	61^{+24}_{-23}	3.7(4)	12(4)	[204]
^{126}Pd	51(3)	45^{+11}_{-9}	4.9(9)	22(9)	[204]
^{127}Pd	39(5)	73^{+24}_{-23}	9(3)	< 19	[204]
^{128}Pd	53(10)	< 262	10(7)	-	[204]
^{124}Ag	205(17)	230^{+28}_{-25}	2.3(11)	< 9	[204]
^{125}Ag	146(11)	163^{+11}_{-9}	2.2(11)	11.8(10)	[204]
^{126}Ag	103.2(14)	114(3)	3.8(2)	13.7(11)	[204]
^{127}Ag	89.1(9)	102(5)	5.5(2)	14.6(15)	[204]
^{128}Ag	67.4(16)	73^{+10}_{-9}	9.3(5)	20(5)	[204]
^{129}Ag	57(3)	95^{+35}_{-29}	17.7(15)	< 20	[204]

Bibliography

[1] K. Lodders, Astrophys. Sp. Sci. Proc. , 379 (2010), arXiv:1010.2746 .

[2] J. Abadie, B. P. Abbott, R. Abbott, T. D. Abbott, M. Abernathy, T. Accadia, F. Acernese, C. Adams, R. Adhikari, C. Affeldt, et al., Phys. Rev. D **85**, 122007 (2012), arXiv:1801.08023 .

[3] R. H. Cyburt, B. D. Fields, K. A. Olive, and T.-H. Yeh, Rev. Mod. Phys. **88**, 015004 (2016).

[4] G. Wallerstein, I. Iben, P. Parker, A. M. Boesgaard, G. M. Hale, A. E. Champagne, C. A. Barnes, F. Käppeler, V. V. Smith, R. D. Hoffman, et al., Rev. Mod. Phys. **69**, 995 (1997), arXiv:1997RvMP...69..995W .

[5] E. M. Burbidge, G. R. Burbidge, W. A. Fowler, and F. Hoyle, Rev. Mod. Phys. **29**, 547 (1957).

[6] A. G. W. Cameron, Publ. Astron. Soc. Pacific **69**, 201 (1957).

[7] J. B. Blake and D. N. Schramm, Astrophys. J. **197**, 615 (1975), arXiv:arXiv:1011.1669v3 .

[8] C. Iliadis, *Nuclear Physics of Stars*, 2nd ed. (Wiley, 2007).

[9] A. Abzouzi, M. S. Antony, and V. B. Ndocko Ndongué, J. Radioanal. Nucl. Chem. Lett. **135**, 1 (1989).

[10] S. E. Woosley and W. M. Howard, Astrophys. J. Suppl. Ser. **36**, 285 (1978).

[11] M. Arnould and S. Goriely, Phys. Rep. **384**, 1 (2003).

[12] N. Nishimura, T. Rauscher, R. Hirschi, A. S. J. Murphy, G. Cescutti, and C. Travaglio, Mon. Not. R. Astron. Soc. **474**, 3133 (2018), arXiv:1711.09098 .

[13] S. Goriely, Astron. Astrophys. **342**, 881 (1999).

[14] M. Arnould, S. Goriely, and K. Takahashi, Phys. Rep. **450**, 97 (2007), arXiv:0705.4512 .

[15] R. . R. Griffin, B. Gustafsson, and T. Vieira, Mon. Not. R. Astron. Soc. **198**, 637 (1982).

[16] S. Honda, W. Aoki, T. Kajino, H. Ando, T. C. Beers, H. Izumiura, K. Sadakane, and M. TakadaâĂŘHidai, Astrophys. J. **607**, 474 (2004).

[17] J. Westin, C. Sneden, B. Gustafsson, and J. J. Cowan, Astrophys. J. **530**, 783 (2000).

[18] J. B. Kaler, *Stars*, revised an ed. (Scientific American Library, New York, 1998) p. 273.

[19] J. J. Cowan, C. Sneden, J. E. Lawler, A. Aprahamian, M. Wiescher, K. Langanke, G. Martínez-Pinedo, and F.-K. Thielemann, Making the Heaviest Elements in the Universe: A Review of the Rapid Neutron Capture Process (2019), arXiv:1901.01410 .

[20] T. C. Beers and N. Christlieb, Annu. Rev. Astron. Astrophys. **43**, 531 (2005).

[21] C. Sneden, J. J. Cowan, J. E. Lawler, I. I. Ivans, S. Burles, T. C. Beers, F. Primas, V. Hill, J. W. Truran, G. M. Fuller, et al., Astrophys. J. **591**, 936 (2003), arXiv:0303542 [astro-ph] .

[22] G. J. Wasserburg, M. Busso, and R. Gallino, Astrophys. J. **466**, L109 (1996).

[23] Y. Qian and G. J. Wasserburg, Astrophys. J. **559**, 925 (2001).

[24] F. Montes, T. C. Beers, J. Cowan, T. Elliot, K. Farouqi, R. Gallino, M. Heil, K. Kratz, B. Pfeiffer, M. Pignatari, et al., Astrophys. J. **671**, 1685 (2007).

[25] Y. Qian, P. Vogel, and G. J. Wasserburg, Astrophys. J. **494**, 285 (1998).

[26] S. Woosley and T. Janka, Nat. Phys. **1**, 147 (2005).

[27] H. A. Bethe, Rev. Mod. Phys. **62**, 801 (1990).

[28] J. J. Cowan, A. G. W. Cameron, and J. W. Truran, Astrophys. J. **265**, 429 (1983).

[29] J. Cowan and F. Thielemann, Phys. Today **57**, 47 (2004), arXiv:0309802 [astro-ph] .

[30] S. E. Woosley, J. R. Wilson, G. J. Mathews, R. D. Hoffman, and B. S. Meyer, Astrophys. J. **433**, 229 (1994).

[31] R. C. Duncan, S. L. Shapiro, and I. Wasserman, Astrophys. J. **309**, 141 (1986).

[32] Freiburghaus, Rosswog, and Thielemann, Astrophys. J. **525**, L121 (1999).

[33] B. S. Meyer, Phys. Rep. **227**, 257 (1993).

[34] S. E. Woosley and E. Baron, Astrophys. J. **391**, 228 (1992).

[35] K. Takahashi, J. Witti, and J. H.-T., Astron. Astrophys. **286**, 857 (1994).

[36] L. F. Roberts, J. Lippuner, M. D. Duez, J. A. Faber, F. Foucart, J. C. Lombardi, S. Ning, C. D. Ott, and M. Ponce, Mon. Not. R. Astron. Soc. **464**, 3907 (2017).

[37] L. F. Roberts, S. E. Woosley, and R. D. Hoffman, Astrophys. J. **722**, 954 (2010), arXiv:1004.4916 .

[38] A. Arcones and G. Martínez-Pinedo, Phys. Rev. C - Nucl. Phys. **83**, 1 (2011).

[39] A. Arcones and F.-K. Thielemann, J. Phys. G Nucl. Part. Phys. **40**, 013201 (2013), arXiv:1207.2527 .

[40] K. L. Kratz, W. Akram, K. Farouqi, and O. Hallmann, AIP Conf. Proc. **2076**, 10.1063/1.5091628 (2019).

[41] J. M. Lattimer and D. N. Schramm, Astrophys. J. **192**, L145 (1974).

[42] E. Symbalisty and D. N. Schramm, Astrophys. Lett. **22**, 143 (1982).

[43] S. W. Hawking, Phys. Rev. Lett. **26**, 1344 (1971).

[44] B. Abbott, R. Abbott, T. Abbott, F. Acernese, K. Ackley, C. Adams, T. Adams, P. Addesso, R. Adhikari, V. Adya, et al., Phys. Rev. Lett. **119**, 161101 (2017), arXiv:1710.05832 .

[45] B. P. Abbott, R. Abbott, R. Adhikari, P. Ajith, B. Allen, G. Allen, R. S. Amin, S. B. Anderson, W. G. Anderson, M. A. Arain, et al., Reports Prog. Phys. **72**, 076901 (2009), arXiv:arXiv:0711.3041v2 .

[46] F. Acernese, P. Amico, M. Alshourbagy, S. Aoudia, S. Avino, D. Babusci, G. Ballardin, F. Barone, L. Barsotti, M. Barsuglia, et al., J. Phys. Conf. Ser. **32**, 223 (2006).

[47] E. Nakar and T. Piran, Nature **478**, 82 (2011).

[48] T. Piran, Rev. Mod. Phys. **76**, 1143 (2004), arXiv:0405503 [astro-ph] .

[49] S. Rosswog, M. Liebendoerfer, F. K. Thielemann, M. B. Davies, W. Benz, and T. Piran, Astron. Astrophys. **341**, 44 (1998), arXiv:9811367 [astro-ph] .

[50] Y. Sekiguchi, K. Kiuchi, K. Kyutoku, M. Shibata, and K. Taniguchi, Phys. Rev. D **93**, 124046 (2016), arXiv:1603.01918 .

[51] A. Perego, S. Rosswog, R. M. Cabezon, O. Korobkin, R. Kappeli, A. Arcones, and M. Liebendorfer, Mon. Not. R. Astron. Soc. **443**, 3134 (2014), arXiv:1405.6730 .

[52] B. D. Metzger and R. Fernández, Mon. Not. R. Astron. Soc. **441**, 3444 (2014), arXiv:1402.4803 .

[53] B. D. Metzger, Living Rev. Relativ. **23**, 1 (2020).

[54] J. M. Lattimer, F. Mackie, D. G. Ravenhall, and D. N. Schramm, Astrophys. J. **213**, 225 (1977).

[55] B. D. Metzger, G. Martínez-Pinedo, S. Darbha, E. Quataert, A. Arcones, D. Kasen, R. Thomas, P. Nugent, I. V. Panov, and N. T. Zinner, Mon. Not. R. Astron. Soc. **406**, 2650 (2010), arXiv:1001.5029 .

[56] L. F. Roberts, D. Kasen, W. H. Lee, and E. Ramirez-Ruiz, Astrophys. J. **736**, L21 (2011), arXiv:1104.5504 .

[57] D. A. Coulter, R. J. Foley, C. D. Kilpatrick, M. R. Drout, A. L. Piro, B. J. Shappee, M. R. Siebert, J. D. Simon, N. Ulloa, D. Kasen, et al., Science (80-.). **358**, 1556 (2017), arXiv:1710.05452 .

[58] S. J. Smartt, T.-W. Chen, A. Jerkstrand, M. Coughlin, E. Kankare, S. A. Sim, M. Fraser, C. Inserra, K. Maguire, K. C. Chambers, et al., Nature , 1 (2017), arXiv:1710.05841 .

[59] E. Troja, L. Piro, H. van Eerten, R. T. Wollaeger, M. Im, O. D. Fox, N. R. Butler, S. B. Cenko, T. Sakamoto, C. L. Fryer, et al., Nature 10.1038/nature24290 (2017), arXiv:1710.05433 .

[60] I. Arcavi, G. Hosseinzadeh, D. Andrew Howell, C. Mccully, D. Poznanski, D. Kasen, J. Barnes, M. Zaltzman, S. Vasylyev, D. Maoz, et al., Nat. Publ. Gr. 10.1038/nature24291 (2017), arXiv:1710.05843 .

[61] M. M. Kasliwal, E. Nakar, L. P. Singer, D. L. Kaplan, D. O. Cook, A. Van Sistine, R. M. Lau, C. Fremling, O. Gottlieb, J. E. Jencson, et al., Science (80-.). **358**, 1559 (2017), arXiv:1710.05436 .

[62] D. Kasen, B. Metzger, J. Barnes, E. Quataert, and E. Ramirez-Ruiz, Nat. Publ. Gr. , 1 (2017), arXiv:1710.05463 .

[63] P. S. Cowperthwaite, E. Berger, V. A. Villar, B. D. Metzger, M. Nicholl, R. Chornock, P. K. Blanchard, W. Fong, R. Margutti, M. Soares-Santos, et al., Astrophys. J. **848**, L17 (2017), arXiv:1710.05840 .

[64] M. Nicholl, E. Berger, D. Kasen, B. D. Metzger, J. Elias, C. Briceño, K. D. Alexander, P. K. Blanchard, R. Chornock, P. S. Cowperthwaite, et al., Astrophys. J. **848**, L18 (2017), arXiv:1710.05456 .

[65] R. Chornock, E. Berger, D. Kasen, P. S. Cowperthwaite, M. Nicholl, V. A. Villar, K. D. Alexander, P. K. Blanchard, T. Eftekhari, W. Fong, et al., Astrophys. J. **848**, L19 (2017), arXiv:1710.05454 .

[66] D. Watson, C. J. Hansen, J. Selsing, A. Koch, D. B. Malesani, A. C. Andersen, J. P. U. Fynbo, A. Arcones, A. Bauswein, S. Covino, et al., Nature **574**, 497 (2019), arXiv:1910.10510 .

[67] The LIGO Scientific Collaboration, the Virgo Collaboration, B. P. Abbott, R. Abbott, T. D. Abbott, S. Abraham, F. Acernese, K. Ackley, C. Adams, R. X. Adhikari, et al., ArXiv Prepr. (2020), arXiv:2001.01761 .

[68] Y.-Z. Qian, Astrophys. J. **534**, L67 (2000).

[69] D. Argast, M. Samland, F.-K. Thielemann, and Y.-Z. Qian, Astron. Astrophys. **416**, 997 (2004), arXiv:0309237 [astro-ph] .

[70] M. Safarzadeh, R. Sarmento, and E. Scannapieco, Astrophys. J. **876**, 28 (2019), arXiv:1812.02779 .

[71] P. W. Merrill, Astrophys. J. **116**, 21 (1952), arXiv:arXiv:1011.1669v3 .

[72] B. Coursey, J. Gibson, M. Heitzmann, and J. Leak, Int. J. Appl. Radiat. Isot. **35**, 1103 (1984).

[73] C. Arlandini, F. Kappeler, K. Wisshak, R. Gallino, M. Lugaro, M. Busso, and O. Straniero, Astrophys. J. **525**, 886 (1999), arXiv:9906266 [astro-ph] .

[74] F. Käppeler, R. Gallino, S. Bisterzo, and W. Aoki, Rev. Mod. Phys. **83**, 157 (2011), arXiv:arXiv:1012.5218v1 .

[75] K. S. Krane, *Intoductory Nuclear Physics*, 3rd ed. (John Wiley, Chichester, New York, 1988).

[76] A. G. W. Cameron, Astrophys. J. **121**, 144 (1955).

[77] Z. Bao, H. Beer, F. Käppeler, F. Voss, K. Wisshak, and T. Rauscher, At. Data Nucl. Data Tables **76**, 70 (2000).

[78] U. Abbondanno, G. Aerts, F. Alvarez-Velarde, H. Álvarez-Pol, S. Andriamonje, J. Andrzejewski, G. Badurek, P. Baumann, F. BečváÅŹ, J. Benlliure, et al., Nucl. Phys. A **758**, 501 (2005).

[79] P. A. Seeger, W. A. Fowler, and D. D. Clayton, Astrophys. J. Suppl. Ser. **11**, 121 (1965), arXiv:1965ApJS...11..121S .

[80] The LIGO Scientific Collaboration, the Virgo Collaboration, B. P. Abbott, R. Abbott, T. D. Abbott, S. Abraham, F. Acernese, K. Ackley, C. Adams, R. X. Adhikari, et al., Reports Prog. Phys. **52**, 945 (2020), arXiv:2001.01761 .

[81] F. Kaeppeler, R. Gallino, M. Busso, G. Picchio, and C. M. Raiteri, Astrophys. J. **354**, 630 (1990), arXiv:arXiv:1011.1669v3 .

[82] R. G. Couch, A. B. Schmiedekamp, and W. D. Arnett, Astrophys. J. **190**, 95 (1974), arXiv:arXiv:1011.1669v3 .

[83] F. Käppeler, R. Gallino, S. Bisterzo, and W. Aoki, Rev. Mod. Phys. **83**, 157 (2011), arXiv:1012.5218 .

[84] M. Pignatari, R. Gallino, M. Heil, M. Wiescher, F. Käppeler, F. Herwig, and S. Bisterzo, Astrophys. J. **710**, 1557 (2010).

[85] K.-L. Kratz, J.-P. Bitouzet, F.-K. Thielemann, P. Moeller, and B. Pfeiffer, Astrophys. J. **403**, 216 (1993).

[86] G. J. Mathews and J. J. Cowan, Nature **345**, 491 (1990).

[87] S. Goriely and M. Arnould, Astron. Astrophys. **262**, 73 (1992).

[88] V. Bouquelle, N. Cerf, M. Arnould, T. Tachibana, and S. Goriely, Astron. Astrophys. **305**, 1005 (1996).

[89] W. Hillebrandt, Space Sci. Rev. **21**, 639 (1978).

[90] A. G. W. Cameron, J. J. Cowan, and J. W. Truran, Astrophys. Space Sci. **91**, 235 (1983).

[91] Y. Z. Qian, Prog. Part. Nucl. Phys. **50**, 153 (2003), arXiv:0301422 [astro-ph] .

[92] Y. Z. Qian and G. J. Wasserburg, Phys. Rep. **442**, 237 (2007), arXiv:0708.1767 .

[93] J. J. Cowan, F.-k. Thielemann, and J. W. Truran, Phys. Rep. **208**, 267 (1991).

[94] S. Tsuruta and A. G. W. Cameron, Can. J. Phys. **43**, 2056 (1965).

[95] M. Mumpower, R. Surman, G. McLaughlin, and A. Aprahamian, Prog. Part. Nucl. Phys. **86**, 86 (2016), arXiv:1508.07352 .

[96] E. Caurier and F. Nowacki, Acta Phys. Pol. B **30**, 705 (1999).

[97] E. Caurier, G. Martínez-Pinedo, F. Nowacki, A. Poves, and A. P. Zuker, Rev. Mod. Phys. **77**, 427 (2005), arXiv:0402046v1 [arXiv:nucl-th] .

[98] Q. Zhi, E. Caurier, J. J. Cuenca-García, K. Langanke, G. Martínez-Pinedo, and K. Sieja, Phys. Rev. C **87**, 025803 (2013), arXiv:1301.5225 .

[99] P. Möller, B. Pfeiffer, and K.-L. Kratz, Phys. Rev. C **67**, 055802 (2003).

[100] P. Möller, J. Nix, and K.-L. Kratz, At. Data Nucl. Data Tables **66**, 131 (1997).

[101] P. Möller, M. Mumpower, T. Kawano, and W. Myers, At. Data Nucl. Data Tables **125**, 1 (2019).

[102] C. L. Duke, P. G. Hansen, O. B. Nielsen, and G. Rudstam, Nucl. Physics, Sect. A **151**, 609 (1970).

[103] P. Möller and J. Randrup, Nucl. Physics, Sect. A **514**, 1 (1990).

[104] J. Krumlinde and P. Möller, Nucl. Physics, Sect. A **417**, 419 (1984).

[105] M. R. Mumpower, T. Kawano, and P. Möller, Phys. Rev. C **94**, 064317 (2016), arXiv:arXiv:1608.01956v1 .

[106] T. Marketin, L. Huther, and G. Martínez-Pinedo, Phys. Rev. C **93**, 025805 (2016).

[107] K. Miernik, Phys. Rev. C **90**, 054306 (2014).

[108] S. Goriely, N. Chamel, and J. M. Pearson, Phys. Rev. C **82**, 035804 (2010).

[109] M. Wang, G. Audi, F. G. Kondev, W. Huang, S. Naimi, and X. Xu, Chinese Phys. C **41**, 030003 (2017).

[110] S. Goriely, N. Chamel, and J. M. Pearson, HFB-24 Mass Model, http://www-astro.ulb.ac.be/bruslib/nucdata/hfb24-dat (2015).

[111] P. Möller, J. R. Nix, W. D. Myers, and W. J. Swiatecki, At. Data Nucl. Data Tables **59**, 185 (1995), arXiv:9308022 [nucl-th] .

[112] P. Möller, A. J. Sierk, T. Ichikawa, and H. Sagawa, At. Data Nucl. Data Tables **109-110**, 1 (2016), arXiv:1508.06294 .

[113] S. Goriely, N. Chamel, and J. M. Pearson, Phys. Rev. C **88**, 061302 (2013).

[114] S. Goriely, M. Samyn, P.-H. Heenen, J. M. Pearson, and F. Tondeur, Phys. Rev. C **66**, 024326 (2002).

[115] S. Goriely, F. Tondeur, and J. Pearson, At. Data Nucl. Data Tables **77**, 311 (2001).

[116] S. Goriely, N. Chamel, and J. M. Pearson, Phys. Rev. C - Nucl. Phys. **88**, 1 (2013).

[117] A. Sobiczewski and Y. A. Litvinov, Phys. Rev. C **90**, 017302 (2014).

[118] M. R. Mumpower, R. Surman, D.-L. Fang, M. Beard, P. Möller, T. Kawano, and A. Aprahamian, Phys. Rev. C **92**, 035807 (2015), arXiv:1505.07789 .

[119] M. Mumpower, R. Surman, and A. Aprahamian, J. Phys. Conf. Ser. **599**, 10.1088/1742-6596/599/1/012031 (2015).

[120] R. Surman, M. Mumpower, and G. McLaughlin, in *Proc. 14th Int. Symp. Nucl. Cosm.*, Vol. 010612 (Journal of the Physical Society of Japan, 2017) pp. 1–4.

[121] J. Lippuner and L. F. Roberts, Astrophys. J. **815**, 82 (2015), arXiv:1508.03133 .

[122] C. J. Horowitz, A. Arcones, B. Côté, I. Dillmann, W. Nazarewicz, I. U. Roederer, H. Schatz, A. Aprahamian, D. Atanasov, A. Bauswein, et al., J. Phys. G Nucl. Part. Phys. **46**, 083001 (2019), arXiv:1805.04637 .

[123] M. Mumpower, J. Cass, G. Passucci, R. Surman, and A. Aprahamian, AIP Adv. **4**, 041009 (2014).

[124] R. Surman, M. Mumpower, J. Cass, I. Bentley, A. Aprahamian, and G. C. McLaughlin, EPJ Web Conf. **66**, 07024 (2013), arXiv:1309.0059 .

[125] R. Surman, M. Mumpower, and A. Aprahamian, in *Proc. Conf. Adv. Radioact. Isot. Sci.*, Vol. 010010 (Journal of the Physical Society of Japan, 2015) pp. 1–8.

[126] T. Rauscher, NON-SMOKER: Neutron-capture cross sections, https://nucastro.org/nonsmoker.html (2011).

[127] G. Lorusso, S. Nishimura, Z. Y. Xu, A. Jungclaus, Y. Shimizu, G. S. Simpson, P.-A. Söderström, H. Watanabe, F. Browne, P. Doornenbal, et al., Phys. Rev. Lett. **114**, 192501 (2015).

[128] R. Dunlop, V. Bildstein, I. Dillmann, A. Jungclaus, C. E. Svensson, C. Andreoiu, G. C. Ball, N. Bernier, H. Bidaman, P. Boubel, et al., Phys. Rev. C **93**, 10.1103/physrevc.93.062801 (2016).

[129] R. Dunlop, C. E. Svensson, C. Andreoiu, G. C. Ball, N. Bernier, H. Bidaman, V. Bildstein, M. Bowry, D. S. Cross, I. Dillmann, et al., Phys. Rev. C **99**, 045805 (2019).

[130] J. Hakala, J. Dobaczewski, D. Gorelov, T. Eronen, A. Jokinen, A. Kankainen, V. S. Kolhinen, M. Kortelainen, I. D. Moore, H. Penttilä, et al., Phys. Rev. Lett. **109**, 1 (2012), arXiv:1203.0958 .

[131] J. Van Schelt, D. Lascar, G. Savard, J. A. Clark, P. F. Bertone, S. Caldwell, A. Chaudhuri, A. F. Levand, G. Li, G. E. Morgan, et al., Phys. Rev. Lett. **111**, 1 (2013).

[132] I. Dillmann and A. Tarifeño-Saldivia, Nucl. Phys. News **28**, 28 (2018).

[133] T. J. M. Symons, Y. P. Viyogi, G. D. Westfall, P. Doll, D. E. Greiner, H. Faraggi, P. J. Lindstrom, D. K. Scott, H. J. Crawford, and C. McParland, Phys. Rev. Lett. **42**, 40 (1979).

[134] G. D. Westfall, T. J. M. Symons, D. E. Greiner, H. H. Heckman, P. J. Lindstrom, J. Mahoney, A. C. Shotter, D. K. Scott, H. J. Crawford, C. McParland, et al., Phys. Rev. Lett. **43**, 1859 (1979).

[135] J. R. Alonso, A. Chatterjee, and C. A. Tobias, IEEE Trans. Nucl. Sci. **26**, 3003 (1979).

[136] J. Bowman, W. Swiatecki, and C. Tsang, *Abrasion and ablation of heavy ions*, Tech. Rep. (Lawrence Berkl, 1973).

[137] D. J. Morrissey and B. M. Sherrill, Philos. Trans. R. Soc. A Math. Phys. Eng. Sci. **356**, 1985 (1998).

[138] M. Bernas, S. Czajkowski, P. Armbruster, H. Geissel, P. Dessagne, C. Donzaud, H. R. Faust, E. Hanelt, A. Heinz, M. Hesse, et al., Phys. Lett. B **331**, 19 (1994).

[139] M. Bernas, C. Engelmann, P. Armbruster, S. Czajkowski, F. Ameil, C. Böckstiegel, P. Dessagne, C. Donzaud, H. Geissel, A. Heinz, et al., Phys. Lett. Sect. B Nucl. Elem. Part. High-Energy Phys. **415**, 111 (1997).

[140] M. Bernas, P. Armbruster, S. Czajkowski, C. Donzaud, H. Geissel, F. Ameil, P. Dessagne, C. Engelmann, A. Heinz, Z. Janas, et al., Nucl. Phys. A **616**, 352 (1997).

[141] J. Äystö, A. Astier, T. Enqvist, K. Eskola, Z. Janas, A. Jokinen, K.-L. Kratz, M. Leino, H. Penttilä, B. Pfeiffer, et al., Phys. Rev. Lett. **69**, 1167 (1992).

[142] E. Moll, H. Schrader, G. Siegert, M. Asghar, J. P. Bocquet, G. Bailleul, J. P. Gautheron, J. Greif, G. I. Crawford, C. Chauvin, et al., Nucl. Instruments Methods **123**, 615 (1975).

[143] W. Schwab, M. Bernas, P. Armbruster, S. Czajkowski, P. Dessagne, C. Donzaud, H. Geissel, A. Heinz, C. Kozhuharov, C. Miehé, et al., Eur. Phys. J. A **2**, 179 (1998).

[144] J. W. Norbury, Phys. Rev. C **43**, R368 (1991), arXiv:arXiv:1011.1669v3 .

[145] L. Wilets, E. Guth, and J. S. Tenn, Phys. Rev. **156**, 1349 (1967).

[146] P. Armbruster, M. Bernas, S. Czajkowski, H. Geissel, T. Aumann, P. Dessagne, C. Donzaud, E. Hanelt, A. Heinz, M. Hesse, et al., Zeitschrift für Phys. A Hadron. Nucl. **355**, 191 (1996).

[147] C. Domingo, J. Font, C. Baixeras, L. Font, and F. Fernández, Nucl. Instruments Methods Phys. Res. Sect. B Beam Interact. with Mater. Atoms **146**, 114 (1998).

[148] J. Mompart, C. Domingo, C. Baixeras, and F. Fernández, Nucl. Instruments Methods Phys. Res. Sect. B Beam Interact. with Mater. Atoms **107**, 56 (1996).

[149] N. Fukuda, T. Kubo, T. Ohnishi, N. Inabe, H. Takeda, D. Kameda, and H. Suzuki, Nucl. Instruments Methods Phys. Res. Sect. B Beam Interact. with Mater. Atoms **317**, 323 (2013), arXiv:1310.8351 .

[150] H. Sakurai, Nucl. Phys. A **805**, 526c (2008).

[151] Y. Yano, Nucl. Instruments Methods Phys. Res. Sect. B Beam Interact. with Mater. Atoms **261**, 1009 (2007).

[152] T. Kubo, D. Kameda, H. Suzuki, N. Fukuda, H. Takeda, Y. Yanagisawa, M. Ohtake, K. Kusaka, K. Yoshida, N. Inabe, et al., Prog. Theor. Exp. Phys. **2012**, 1 (2012).

[153] T. Nakagawa, Y. Higurashi, J. Ohnishi, T. Aihara, M. Tamura, A. Uchiyama, H. Okuno, K. Kusaka, M. Kidera, E. Ikezawa, et al., Rev. Sci. Instrum. **81**, 02A320 (2010).

[154] Y. Higurashi, J. Ohnishi, T. Nakagawa, H. Haba, M. Tamura, T. Aihara, M. Fujimaki, M. Komiyama, A. Uchiyama, and O. Kamigaito, Rev. Sci. Instrum. **83**, 02A333 (2012).

[155] H. Sakurai, Eur. Phys. J. A **25**, 403 (2005).

[156] H. Okuno, J. Ohnishi, K. Yamada, N. Fukunishi, K. Ikegami, T. Maie, H. Hasebe, M. Hamanaka, M. Kase, A. Goto, et al., IEEE Trans. Appl. Supercond. **17**, 1063 (2007).

[157] Nishina Center for Accelerator-Based Science, Intoduction to RI Beam Factory and Users' Information, http://www.nishina.riken.jp/RIBF/BigRIPS/intensity.html (2019).

[158] T. Ohnishi, T. Kubo, K. Kusaka, A. Yoshida, K. Yoshida, N. Fukuda, M. Ohtake, Y. Yanagisawa, H. Takeda, D. Kameda, et al., J. Phys. Soc. Japan **77**, 7 (2008).

[159] T. Ohnishi, T. Kubo, K. Kusaka, A. Yoshida, K. Yoshida, M. Ohtake, N. Fukuda, H. Takeda, D. Kameda, K. Tanaka, et al., J. Phys. Soc. Japan **79**, 1 (2010).

[160] T. Sumikama, S. Nishimura, H. Baba, F. Browne, P. Doornenbal, N. Fukuda, S. Franchoo, G. Gey, N. Inabe, T. Isobe, et al., Phys. Rev. C **95**, 051601 (2017).

[161] N. Fukuda, T. Kubo, D. Kameda, N. Inabe, H. Suzuki, Y. Shimizu, H. Takeda, K. Kusaka, Y. Yanagisawa, M. Ohtake, et al., J. Phys. Soc. Japan **87**, 014202 (2018).

[162] Y. Shimizu, T. Kubo, N. Fukuda, N. Inabe, D. Kameda, H. Sato, H. Suzuki, H. Takeda, K. Yoshida, G. Lorusso, et al., J. Phys. Soc. Japan **87**, 014203 (2018).

[163] A. Yoshida, K. Morita, K. Morimoto, D. Kaji, T. Kubo, Y. Takahashi, A. Ozawa, and I. Tanihata, Nucl. Instruments Methods Phys. Res. Sect. A Accel. Spectrometers, Detect. Assoc. Equip. **521**, 65 (2004).

[164] A. Yoshida, T. Suda, T. Ohtsuki, H. Yuki, and T. Kubo, Nucl. Instruments Methods Phys. Res. Sect. A Accel. Spectrometers, Detect. Assoc. Equip. **590**, 204 (2008).

[165] T. Kubo, Nucl. Instruments Methods Phys. Res. Sect. B Beam Interact. with Mater. Atoms **204**, 97 (2003).

[166] T. Kubo, K. Kusaka, K. Yoshida, A. Yoshida, T. Ohnishi, M. Ohtake, Y. Yanagisawa, N. Fukuda, T. Haseyama, Y. Yano, et al., IEEE Trans. Appl. Supercond. **17**, 1069 (2007).

[167] K.-H. Schmidt, E. Hanelt, H. Geissel, G. Münzenberg, and J. Dufour, Nucl. Instruments Methods Phys. Res. Sect. A Accel. Spectrometers, Detect. Assoc. Equip. **260**, 287 (1987).

[168] K. Kimura, T. Izumikawa, R. Koyama, T. Ohnishi, T. Ohtsubo, A. Ozawa, W. Shinozaki, T. Suzuki, M. Takahashi, I. Tanihata, et al., Nucl. Instruments Methods Phys. Res. Sect. A Accel. Spectrometers, Detect. Assoc. Equip. **538**, 608 (2005).

[169] Micron Semiconductors Ltd., BB18 Information Page, http://www.micronsemiconductor.co.uk/product/bb18/ (2019).

[170] P. J. Sellin, *Proton Radioactivity Measurement Using a Double-Sided Silicon Strip Detector*, Ph.D. thesis, University of Edinburgh (1992).

[171] P. Sellin, P. Woods, D. Branford, T. Davinson, N. Davis, D. Ireland, K. Livingston, R. Page, A. Shotter, S. Hofmann, et al., Nucl. Instruments Methods Phys. Res. Sect. A Accel. Spectrometers, Detect. Assoc. Equip. **311**, 217 (1992).

[172] D. Braga, P. Coleman-Smith, T. Davinson, I. Lazarus, R. Page, and S. Thomas, in *2009 IEEE Nucl. Sci. Symp. Conf. Rec.* (IEEE, 2009) pp. 1924–1928.

[173] Nuclear Physics Group - STFC, MIDAS, http://npg.dl.ac.uk/MIDAS/ (2019).

[174] A. Tarifeño-Saldivia, J. Tain, C. Domingo-Pardo, F. Calviño, G. Cortés, V. Phong, A. Riego, J. Agramunt, A. Algora, N. Brewer, et al., J. Instrum. **12** (04).

[175] T. Wilpert, Neutron News **23**, 14 (2012).

[176] C. D. Keith, Z. Chowdhuri, D. R. Rich, W. M. Snow, J. D. Bowman, S. L. Penttilä, D. A. Smith, M. B. Leuschner, V. R. Pomeroy, G. L. Jones, et al., Phys. Rev. C **69**, 034005 (2004).

[177] G. F. Knoll, *Radiation Detection and Measurement*, fourth edi ed. (John Wiley, Hoboken, N.J., 2010) pp. 519–536.

[178] J. Agramunt, J. L. Tain, M. B. Gómez-Hornillos, A. R. Garcia, F. Albiol, A. Algora, R. Caballero-Folch, F. Calviño, D. Cano-Ott, G. Cortés, et al., Nucl. Instruments Methods Phys. Res. Sect. A Accel. Spectrometers, Detect. Assoc. Equip. **807**, 69 (2016).

[179] J. Agramunt, A. R. García, A. Algora, J. Äystö, R. Caballero-Folch, F. Calviño, D. Cano-Ott, G. Cortés, C. Domingo-Pardo, T. Eronen, et al., Nucl. Data Sheets **120**, 74 (2014).

[180] M. B. Gómez-Hornillos, J. Rissanen, J. L. Taín, A. Algora, K. L. Kratz, G. Lhersonneau, B. Pfeiffer, J. Agramunt, D. Cano-Ott, V. Gorlychev, et al., Hyperfine Interact. **223**, 185 (2014).

[181] R. Caballero-Folch, C. Domingo-Pardo, G. Cortès, J. Taín, J. Agramunt, A. Algora, F. Ameil, Y. Ayyad, J. Benlliure, M. Bowry, et al., Nucl. Data Sheets **120**, 81 (2014).

[182] R. Grzywacz, K. P. Rykaczewski, C. J. Gross, M. Madurga, K. Miernik, D. T. Miller, S. V. Paulauskas, S. W. Padgett, C. Rasco, M. Wolińska-Cichocka, et al., Acta Phys. Pol. B **45**, 217 (2014).

[183] K. Miernik, K. P. Rykaczewski, C. J. Gross, R. Grzywacz, M. Madurga, D. Miller, J. C. Batchelder, I. N. Borzov, N. T. Brewer, C. Jost, et al., Phys. Rev. Lett. **111**, 1 (2013).

[184] A. Svirikhin, A. Andreev, V. Dushin, M. Chelnokov, V. Chepigin, M. Gupta, A. Isaev, I. Izosimov, D. Katrasev, A. Kuznetsov, et al., EPJ Web Conf. **62**, 03005 (2013).

[185] S. Agostinelli, J. Allison, K. Amako, J. Apostolakis, H. Araujo, P. Arce, M. Asai, D. Axen, S. Banerjee, G. Barrand, et al., Nucl. Instruments Methods Phys. Res. Sect. A Accel. Spectrometers, Detect. Assoc. Equip. **506**, 250 (2003).

[186] J. Tain, J. Agramunt, D. Ahn, A. Algora, J. Allmond, H. Baba, S. Bae, N. Brewer, R. Caballero Folch, F. Calvino, et al., Acta Phys. Pol. B **49**, 417 (2018).

[187] V. H. Phong, G. Lorusso, T. Davinson, A. Estrade, O. Hall, J. Liu, K. Matsui, F. Montes, S. Nishimura, A. Boso, et al., Phys. Rev. C **100**, 011302 (2019).

[188] S. Shepherd, P. Nolan, D. Cullen, D. Appelbe, J. Simpson, J. Gerl, M. Kaspar, A. Kleinboehl, I. Peter, M. Rejmund, et al., Nucl. Instruments Methods Phys. Res. Sect. A Accel. Spectrometers, Detect. Assoc. Equip. **434**, 373 (1999).

[189] I. Lazarus, E. Appelbe, P. Butler, P. Coleman-Smith, J. Cresswell, S. Freeman, R. Herzberg, I. Hibbert, D. Joss, S. Letts, et al., IEEE Trans. Nucl. Sci. **48**, 567 (2001).

[190] Nuclear Physics Group - STFC, GREAT Data Format (2016).

[191] M. Berger, J. Coursey, M. Zucker, and J. Chang, NISTIR **4999**, 1 (2017).

[192] R. Brun and F. Rademakers, Nucl. Instruments Methods Phys. Res. Sect. A Accel. Spectrometers, Detect. Assoc. Equip. **389**, 81 (1997).

[193] J. Agramunt, J. L. Tain, F. Albiol, A. Algora, E. Estevez, G. Giubrone, M. D. Jordan, F. Molina, B. Rubio, and E. Valencia, AIP Conf. Proc. **1541**, 165 (2013).

[194] S. Innovative systeme, SIS3302 8 Channel 100 MS/S 16-BIT ADC, https://www.struck.de/sis3302.htm (2019).

[195] RIBFDAQ Group, ANAROOT, https://ribf.riken.jp/RIBFDAQ (2013).

[196] J. Agramunt and A. Tolosa-Delgado, Data integration for experiments with independent setups. Nuclear physics in stellar explosions Workshop '18, (p. 56). Hungary: Institute for Nuclear Research of the Hungarian Academy of Sciences. (2018).

[197] O. Hall, A. Estrade, J. Liu, G. Lorusso, K. Matsui, F. Montes, and S. Nishimura, RIKEN Accel. Prog. Rep. **52**, 38 (2019).

[198] H. Bateman, Proc. Camb. Philol. Soc. **15**, 423 (1910).

[199] A. Tolosa-Delgado, J. Agramunt, J. Tain, A. Algora, C. Domingo-Pardo, A. Morales, B. Rubio, A. Tarifeño-Saldivia, F. Calviño, G. Cortes, et al., Nucl. Instruments Methods Phys. Res. Sect. A Accel. Spectrometers, Detect. Assoc. Equip. **925**, 133 (2019), arXiv:1808.00732 .

[200] M. R. Bhat, in *Nucl. Data Sci. Technol.*, edited by S. M. Qaim (Springer Berlin Heidelberg, Berlin, Heidelberg, 1992) pp. 817–821.

[201] I. Dillmann, P. Dimitriou, and B. Singh, Summ. Rep. NDC (NDS)-0683 (2015).

[202] J. Shergur, M. Hannawald, D. Seweryniak, H. Fynbo, U. Koester, A. Woehr, D. Fedorov, V. Fedoseyev, V. Mishin, P. Hoff, et al., Nucl. Phys. A **682**, 493 (2001).

[203] J. Shergur, B. A. Brown, V. Fedoseyev, U. Köster, K.-L. Kratz, D. Seweryniak, W. B. Walters, A. Wöhr, D. Fedorov, M. Hannawald, et al., Phys. Rev. C **65**, 034313 (2002).

[204] K. I. Smith, *β Delayed Neutron Emission Studies of Neutron-Rich Palladium and Silver Isotopes*, Ph.D. thesis, University of Notre Dame (2014).

[205] B. E. Tomlin, *Nuclear structure below ^{132}Sn: An investigation of neutron-rich nuclides via β and isomeric decay*, Ph.D. thesis, Michigan State University (2006).

[206] F. Montes, A. Estrade, P. T. Hosmer, S. N. Liddick, P. F. Mantica, A. C. Morton, W. F. Mueller, M. Ouellette, E. Pellegrini, P. Santi, et al., Phys. Rev. C - Nucl. Phys. **73**, 1 (2006).

[207] A. Jokinen, J. C. Wang, J. Äystö, P. Dendooven, S. Nummela, J. Huikari, V. Kolhinen, A. Nieminen, K. Peräjärvi, and S. Rinta-Antila, Eur. Phys. J. A **9**, 9 (2000).

[208] W. B. Walters, B. E. Tomlin, P. F. Mantica, B. A. Brown, J. R. Stone, A. D. Davies, A. Estrade, P. T. Hosmer, N. Hoteling, S. N. Liddick, et al., Phys. Rev. C **70**, 034314 (2004).

[209] H. Watanabe, G. Lorusso, S. Nishimura, T. Otsuka, K. Ogawa, Z. Y. Xu, T. Sumikama, P.-A. Söderström, P. Doornenbal, Z. Li, et al., Phys. Rev. Lett. **113**, 042502 (2014).

[210] J. C. Batchelder, N. T. Brewer, C. J. Gross, R. Grzywacz, J. H. Hamilton, M. Karny, A. Fijalkowska, S. H. Liu, K. Miernik, S. W. Padgett, et al., Phys. Rev. C **89**, 054321 (2014).

[211] P. L. Reeder, R. A. Warner, and R. L. Gill, Phys. Rev. C **27**, 3002 (1983).

[212] J. C. Hill, F. K. Wohn, Z. Berant, R. L. Gill, R. E. Chrien, C. Chung, and A. Aprahamian, Phys. Rev. C **29**, 1078 (1984).

[213] V. N. Fedoseyev, Y. Jading, O. C. Jonsson, R. Kirchner, K. L. Kratz, M. Krieg, E. Kugler, J. Lettry, T. Mehren, V. I. Mishin, et al., Zeitschrift für Phys. A Hadron. Nucl. **353**, 9 (1995).

[214] T. Kautzsch, W. B. Walters, M. Hannawald, K.-L. Kratz, V. I. Mishin, V. N. Fedoseyev, W. Böhmer, Y. Jading, P. Van Duppen, B. Pfeiffer, et al., Eur. Phys. J. A **9**, 201 (2000).

[215] K. L. Kratz, B. Pfeiffer, F. K. Thielemann, and W. B. Walters, Hyperfine Interact. **129**, 185 (2000).

[216] H. Göktürk, B. Ekström, E. Lund, and B. Fogelberg, Zeitschrift für Phys. A At. Nucl. **324**, 117 (1986).

[217] H. Mach, R. L. Gill, D. D. Warner, A. Piotrowski, and R. Moreh, Phys. Rev. C **34**, 1117 (1986).

[218] J. Taprogge, A. Jungclaus, H. Grawe, S. Nishimura, P. Doornenbal, G. Lorusso, G. S. Simpson, P.-A. Söderström, T. Sumikama, Z. Y. Xu, et al., Phys. Rev. C **91**, 054324 (2015).

[219] M. Hannawald, V. N. Fedoseyev, U. Köster, K. L. Kratz, V. I. Mishin, W. F. Mueller, H. L. Ravn, J. Van Roosbroeck, H. Schatz, V. Sebastian, et al., Decay properties of N=82 to 84 cadmium r-process nuclides (2001).

[220] K. L. Kratz, H. Gabelmann, W. Hillebrandt, B. Pfeiffer, K. Schlösser, and F. K. Thielemann, Zeitschrift für Phys. A At. Nucl. **325**, 489 (1986).

[221] I. N. Borzov, Phys. Rev. C **71**, 065801 (2005).

[222] J. Lippuner, *r-Process nucleosynthesis in neutron star mergers with the new nuclear reaction network SkyNet Thesis by*, Ph.D. thesis, California Institute of Technology (2018).

[223] J. Lippuner and L. F. Roberts, Astrophys. J. Suppl. Ser. **233**, 18 (2017), arXiv:1706.06198 .

[224] R. H. Cyburt, A. M. Amthor, R. Ferguson, Z. Meisel, K. Smith, S. Warren, A. Heger, R. D. Hoffman, T. Rauscher, A. Sakharuk, et al., Astrophys. J. Suppl. Ser. **189**, 240 (2010).

[225] D. Kasen, R. Fernández, and B. D. Metzger, Mon. Not. R. Astron. Soc. **450**, 1777 (2015), arXiv:1411.3726 .

[226] D. M. Siegel and B. D. Metzger, Phys. Rev. Lett. **119**, 1 (2017).

[227] J. D. J. Mendoza-Temis, M.-R. Wu, K. Langanke, G. Martínez-Pinedo, A. Bauswein, and H.-T. Janka, Phys. Rev. C **92**, 055805 (2015), arXiv:1409.6135 .

[228] A. Algora, B. Rubio, and J. L. Tain, Nucl. Phys. News **28**, 12 (2018).

[229] R. Caballero-Folch, C. Domingo-Pardo, J. Agramunt, A. Algora, F. Ameil, A. Arcones, Y. Ayyad, J. Benlliure, I. N. Borzov, M. Bowry, et al., Phys. Rev. Lett. **117**, 1 (2016).

[230] R. Caballero-Folch, C. Domingo-Pardo, J. Agramunt, A. Algora, F. Ameil, Y. Ayyad, J. Benlliure, M. Bowry, F. Calviño, D. Cano-Ott, et al., Phys. Rev. C **95**, 064322 (2017), arXiv:1701.03845 .